Modeling Close Stellar Interactions Using Numerical and Analytical Techniques

by

Jean-Claude Passy
B.Sc., University of Orsay, 2005
Diplôme d'ingénieur, Ecole Nationale de Techniques Avancées, 2008
M.Sc., University of Orsay, 2009

A Dissertation Submitted in Partial Fulfillment of the
Requirements for the Degree of

DOCTOR OF PHILOSOPHY

in the Department of Physics and Astronomy

Modeling Close Stellar Interactions Using Numerical and Analytical Techniques

by

Jean-Claude Passy
B.Sc., University of Orsay, 2005
Diplôme d'ingénieur, Ecole Nationale de Techniques Avancées, 2008
M.Sc., University of Orsay, 2009

Supervisory Committee

Dr. Falk Herwig, Co-supervisor
(Department of Physics and Astronomy, University of Victoria)

Dr. Orsola De Marco, Co-supervisor
(Department of Physics and Astronomy, University of Victoria)

Dr. Julio F. Navarro, Departmental Member
(Department of Physics and Astronomy, University of Victoria)

Dr. Reinhard Illner, Outside Member
(Department of Mathematics, University of Victoria)

Supervisory Committee

Dr. Falk Herwig, Co-supervisor
(Department of Physics and Astronomy, University of Victoria)

Dr. Orsola De Marco, Co-supervisor
(Department of Physics and Astronomy, University of Victoria)

Dr. Julio F. Navarro, Departmental Member
(Department of Physics and Astronomy, University of Victoria)

Dr. Reinhard Illner, Outside Member
(Department of Mathematics, University of Victoria)

ABSTRACT

The common envelope (CE) interaction is a still poorly understood, yet critical phase of evolution in binary systems that is responsible for various astrophysical classes and phenomena. In this thesis, we use various approaches and techniques to investigate different aspects of this interaction, and compare our models to observations.

We start with a semi-empirical analysis of post-CE systems to predict the outcome of a CE interaction. Using detailed stellar evolutionary models, we revise the α equation and calculate the ejection efficiency, α, both from observations and simulations consistently. We find a possible anti-correlation between α and the secondary-to-primary mass ratio, suggesting that the response of the donor star might be important for the envelope ejection.

Secondly, we present a survey of three-dimensional hydrodynamical simulations of the CE evolution using two different numerical techniques, and find very good agreement overall. However, most of the envelope of the donor is still bound at the

end of the simulations and the final orbital separations are larger than the ones of young observed post-CE systems.

Despite these two investigations, questions remain about the nature of the extra mechanism required to eject the envelope. In order to study the dynamical response of the donor, we perform one-dimensional stellar evolution simulations of stars evolving with mass loss rates from 10^{-3} up to a few $M_{\odot}$/yr. For mass-losing giant stars, the evolution is dynamical and not adiabatic, and we find no significant radius increase in any case.

Finally, we investigate whether the substellar companions recently observed in close orbits around evolved stars could have survived the CE interaction, and whether they might have been more massive prior to their engulfment. Using an analytical prescription for the disruption of gravitationally bound objects by ram pressure stripping, we find that the Earth-mass planets around KIC 05807616 could be the remnants of a Jovian-mass planet, and that the other substellar objects are unlikely to have lost significant mass during the CE interaction.

Contents

List of Tables

List of Figures

CO-AUTHORSHIP

The published work in this thesis is contained in Chapter 2 through Chapter 5, and Appendices A and B. At the start of each of these chapters and appendices, I have indicated whether the work presented within is a reprint or a draft based on a paper already published.

The project and articles were developed in collaboration with my supervisors Orsola De Marco and Falk Herwig, and Mordecai-Mark Mac Low.

In addition to writing parts of Chapter 2, I performed the analytical calculations and fits presented in Section 2.2, as well as the stellar evolution calculations for the determination of α. Orsola De Marco, Falk Herwig and I developed the reconstruction technique described in Section 2.3.

Chapter 3 was written entirely by me. I carried out the *Enzo* simulations, and analyzed the *Enzo* and the *SNSPH* simulations. The *SNSPH* simulations were performed by Chris L. Fryer and Steven Diehl.

I carried out and analyzed all the simulations presented in Chapter 4, and wrote the entire paper.

In addition to writing most of Chapter 5, I developed the different formalisms and performed the simulations presented in Section 5.1. The work presented in Section 5.2 is the result of an ongoing collaboration with Greg L. Bryan (Columbia University).

The observations used in Appendix A were acquired in November 2008 by Orsola De Marco and Maxwell Moe. I reduced and analyzed the data obtained during these 8 nights. I determined the photometric magnitudes and uncertainties of the targets, standard and reference stars (Section A.4).

I performed the Enzo simulations presented in Appendix B, and wrote a small part of the paper.

ACKNOWLEDGEMENTS

As my "second mother" likes to say, a PhD is a journey during which the student is supposed to mature as a scientist and a person. Without the help and support of countless people, my journey would not have been a success. I shall here try to thank everyone who matter to me, and without whom none of this work would have been possible.

First of all, I would like to express my gratitude to my supervisors Orsola De Marco, Falk Herwig, and Mordecai-Mark Mac Low. Their passion for science, their knowledge and their kindness have been essential. I have learned a lot from them and the freedom they gave me allowed me to develop the critical thinking and confidence that are necessary to pursue such a career successfully. I am also grateful to the other members of my supervisory committee, Julio F. Navarro and Reinhard Illner, and to my external examiner, Alison Sills, for their helpful questions and feedback that improved this manuscript. I am thankful to the various collaborators I had the opportunity to work with, in particular Chris L. Fryer, Gabriel Rockefeller, Greg L. Bryan, Bill Paxton (not the actor), George H. Jacoby, David J. Frew, and Colin P. McNally.

I feel very fortunate to have been able to complete my PhD at two amazing institutions: the American Museum of Natural History in New York City, and the University of Victoria. I have become very attached to these two places and consider them now as my "homes."

For team AMNH, I would like to thank:

- our department administrator Gwen King, for her kindness and her help throughout the years;
- Colin P. McNally, for helpful discussions, fun times, and for his flowers and his state-of-the-art 3D visualization toolkit;
- Kelle Cruz, for her friendship;
- Matt Wilde and David Zurek, for good discussions (sometimes about science) and too many sports games watched at the bar or at our desks.

For team UVic, I am grateful to:

- Jolene Bales, Amanda Bluck, Monica Lee, and Michelle Shen, for helping me to solve my numerous administrative issues;

- the Star Talk group, for many interesting discussions;
- Don Vandenberg, for being such an inspiring man and scientist;
- The UVic astrograds, in particular my officemates Azadeh Fattahi, Sheona Urquhart, Chris Barber, Chris Bildfell and Razzi Movassaghi, for making office 403 the best office in the entire department;
- Chris Bildfell, for sometimes letting me beat him at basketball;
- Masen Lamb, for being himself;
- Razzi Movassaghi, for being the best worst friend I have ever had;
- Yasser Hajivalizadeh, for checking his emails once per month;
- Hannah Broekhoven-Fiene and Charli Sakari, for proof-reading my thesis, being great mock-committee members, playing pranks on me, being there for me, etc... In a word, for being true friends;

Finally, I would like to give my greatest thanks to:

- my high school teacher Emmanuel Lesueur, for helping me to go through the difficult times of adolescence, as well as my college physics teacher Mr. Massias, for passing on his love for physics and science;
- George H. Jacoby, for being not only a great collaborator and mentor, but also a close friend, for going grocery shopping with me in Tucson on Senior Discount Day, and almost fighting a sweaty guy in Sydney with me;
- Shamsky B. M. for showing me the path. I am still two behind, but I am getting there;
- my brother Pierre-Luc Passy, for offering me a stunning framed picture taken by Apollo 11. And also for being a great brother;
- Ja-Mei, whose love and understanding have been unwavering since the day I met her. I am thankful for everything she has given me, and feel very fortunate to have her in my life.

I am forever indebted to my parents, for the love, support and guidance they provided me since I was born. I could not have done this without them.

DEDICATION

To my parents, with love.

Chapter 1

Introduction

Unlike our Sun, a large fraction of stars in the Universe are found with at least one stellar companion. The stars within these multiple systems may interact in various ways, which will inevitably alter the evolution that they would have if they were isolated. One of these interactions is the *common envelope* (CE) *evolution* during which the two stars of a binary system find themselves embedded in a common extended envelope.

Historically, the CE phase was introduced as an attempt to explain the formation of *cataclysmic variables*, which are short-period systems that contain a white dwarf[1] accreting matter from a main sequence star. The fundamental discovery regarding the nature of cataclysmic variables was made by Walker (1954), who for the first time probed binarity of a nova. It was in the early 1960's that cataclysmic variables were suggested to be binary systems (see, e.g., Kraft, 1962). However, a viable scenario for the formation of these short-period systems with an evolved component was still missing. A key discovery was the photometric detection of V 471'Tau, a detached binary composed by a 0.6 $M_{\odot}$ white dwarf and a 0.8 $M_{\odot}$ dwarf star with a 3 $R_{\odot}$ orbital separation (Nelson & Young, 1970)[2]. J. P. Ostriker and B. Paczynski then introduced the concept of CE evolution in order to explain the formation of cataclysmic variables. Paczynski (1976) described this phase in his abstract as follows:

[1] A white dwarf is the remnant of a low- or intermediate mass star. We discuss this subject further in Section 1.2.5.

[2] The most recent parameters for V 471'Tau are $M_1 = 0.84\ M_{\odot}$, $M_2 = 0.93\ M_{\odot}$ and $a = 3.3\ R_{\odot}$ (see Chapter 2).

> *When a contact binary expands so much that the stellar surface moves beyond the outer Lagrangian point, a common envelope binary is formed. The suggestion is made that while the two dense stellar nuclei spiral towards each other, the envelope expands and is eventually lost. Most of the angular momentum is lost with the envelope, and therefore the final orbital period may be orders of magnitude shorter than the initial period. V 471 Tau could have formed from a binary with a ten year orbital period. Most probably, cataclysmic variables are products of the evolution of systems like V 471 Tau.*

Since then, a significant amount of work on the CE interaction has been carried out, in particular computationally (see, e.g., Taam et al., 1978; Bodenheimer & Taam, 1984; Sandquist et al., 1998; Ricker & Taam, 2008). For a review, see Taam & Sandquist (2000). Indeed, a numerical approach is necessary for the study of the CE evolution, as direct observations of this evolutionary phase are challenging due to the short timescales involved ($\approx$ a few years, see Chapter 3). However the recent eruption of V1309 Scorpii might have been in response to a CE phase that led to the merger of a contact binary (Tylenda et al., 2011). With the advent of wide, time-dependent surveys, it is likely that such transient interactions will be observed routinely in the near future.

1.1 Motivations

The CE evolution is now widely accepted as a mechanism required in the formation of numerous astrophysical objects and phenomena. First of all, the CE interaction is an essential ingredient for the formation of compact binaries, which contain at least one evolved component and have orbital separations of a few solar radii. Types of compact binaries include:

- cataclysmic variables: white dwarfs accreting material from main sequence donors (Figure 1.1). These systems have orbital periods between 80 min and $\approx$ 6 hr. Their period evolve due to magnetic braking and gravitational radiation (Knigge, 2011);
- symbiotic binaries: white dwarfs accreting from giant donors. Due to the large radii of the giant donors, these systems are the interacting binaries with the

longest separations, and some of them show ellipsoidal variability (Mikołajewska, 2007);

- AM CVn binaries: systems similar to cataclysmic variables but with the white dwarf accreting helium-rich material from a helium donor. They have extremely short orbital periods ranging from 5 min to $\approx$ 1 hr (Solheim, 2010);
- double degenerate binaries: short-period systems composed of two white dwarfs (Webbink, 1984).

These systems are believed to be all possible progenitors of Type Ia (Maoz & Mannucci, 2012) or Type .Ia (Bildsten et al., 2007) supernovae. The existence of such systems for which the radius of the precursor of the evolved star was larger than today's orbital separation, suggests that they have gone through at least one CE interaction.

Figure 1.1 Artistic view of a cataclysmic variable (left) and image of the extended hydrogen-alpha emission of GK Persei, also called Nova Persei 1901 (right). Credits: http://www.optcorp.com (left) and Adam Block/Mount Lemmon SkyCenter/University of Arizona (right).

More generally, the CE interaction will strongly impact all binary populations of intermediate (e.g., Politano et al., 2010) or massive stars (e.g., Belczynski et al., 2008). The CE interaction is expected to happen quite often: Sana et al. (2012) estimated that $\approx$ 40% of all O-type stars would go through a CE phase. Results deduced from

population synthesis studies are therefore highly dependent on the treatment of the CE phase (Meng et al., 2011). For example, Yungelson et al. (1993) investigated the formation of planetary nebulae (PNe) using population synthesis models and showed how the period distribution of the different populations of binary nuclei of PNe depends on the prescription used for the CE interaction. As we can see on Figure 1.2, the peak of the orbital distribution of the different populations depends strongly on the efficiency of the ejection. A deeper understanding of the physics of the CE interaction is thus required in order to build more accurate models that can be directly compared to observables, such as the Type Ia supernova birth rate.

The CE interaction is also believed to be responsible for the formation of peculiar objects such as:

- subdwarf O/B (sdO/sdB) stars: extreme horizontal branch stars with very thin hydrogen-rich envelopes. Although a single star scenario involving a late helium-flash during the cooling of a carbon-oxygen white dwarf has been proposed (Sweigart, 1997), the three preferred channels for the formation of sdB/sdO stars require binary interactions: either a CE ejection, stable Roche lobe[3] overflow (RLOF) mass transfer, or the merger of two helium white dwarfs (Han et al., 2002, 2003). Soker (1998) also proposed that even a CE interaction with a planetary companion might create a sdB/sdO star. Results from population synthesis suggest that the CE ejection channel is the main contributor and produces populations with a mass distribution peaking at 0.46 $M_{\odot}$ (Han et al., 2002, 2003). Observations are in good agreement with this results (Morales-Rueda et al., 2004), and are consistent with a binary fraction $\approx 100\%$ (Maxted et al., 2001) with primarily F- to K-type companions (Girven et al., 2012).

- blue stragglers: main sequence stars that are bluer and/or brighter than the main sequence turnoff in a cluster. Some are also found in the field, notably through their low Li abundance (Ryan et al., 2000; Carney et al., 2004). Stellar collision and/or mass transfer in a binary system are thought to be the formation channels of these objects (Sills et al., 2009; Sills, 2010);

- γ-ray bursts: flashes of gamma rays that are among the most energetic phenomena in the universe ($\approx 10^{53}$ ergs), and almost always of extragalactic origin.

[3]In a binary system, the Roche lobe associated to a given star is the boundary beyond which matter is not gravitationally bound to the star. We discuss this subject in detail in Section 1.3.2.

A sub-category of γ-ray bursts called *long-soft γ-ray bursts* are believed to be associated to core-collapse supernovae. Fryer & Heger (2005) argue that in the collapsar model (a single star collapsing to a black hole), the star does not have enough angular momentum to create a black hole that rotates fast enough to support the accretion disk supposed to power the γ-ray burst. They therefore suggest a formation channel where two nearly equal-mass massive stars enter two successive CE phases, after which the two helium cores will merge and form remnants that can rotate 3-10 times faster than single stars. Once they collapse, these remnants will lead to the formation of black holes with higher spin rates, which should be able to support the accretion disk and produce a jet.

Furthermore, there is no general consensus yet about what shapes non-spherical PNe (Figure 1.3), which represent 80% of PN morphologies (Mastrodemos & Morris, 1998, 1999; García-Arredondo & Frank, 2004; Parker et al., 2006; Edgar et al., 2008; Miszalski et al., 2009). Although models can reproduce elliptical and bipolar shapes, they assume that magnetic fields can be sustained over the high mass-loss period at the end of the asymptotic giant branch (AGB) phase, an assumption that is now rejected (Soker, 2006; Nordhaus et al., 2006). A plausible alternative is that a companion is responsible for the shaping of the AGB outflow, in some cases through a CE interaction. This hypothesis leads to the corollary that PNe form preferentially around binaries. For a review, see De Marco (2009).

Finally, several substellar companions have recently been discovered in compact orbits around evolved stars. Maxted et al. (2006) detected a 0.053 $M_{\odot}$ brown dwarf orbiting the 0.39 $M_{\odot}$ white dwarf WD 0137-349 with a 0.64 $R_{\odot}$ orbital separation. A similar system composed of the sdB star SDSS J08205+0008 and a small companion – most likely a brown dwarf – in a 2.3-hour orbit was discovered by Geier et al. (2011). Setiawan et al. (2011) discovered a Jupiter-mass object orbiting the red horizontal branch star HIP 13044 with a 24.95-$R_{\odot}$ separation. Charpinet et al. (2011) reported the detection of two nearly Earth-sized planets orbiting the sdB star KIC 05807616 at distances 1.290 and 1.636 $R_{\odot}$. Again, the existence of these systems for which the radius of the precursor of the primary was larger than today's orbital separation, suggests that the planets have gone through a CE interaction and have been engulfed by their giant host star. The fact that such low-mass companions survive the CE phase tells us that our understanding of the CE energetics is incomplete.

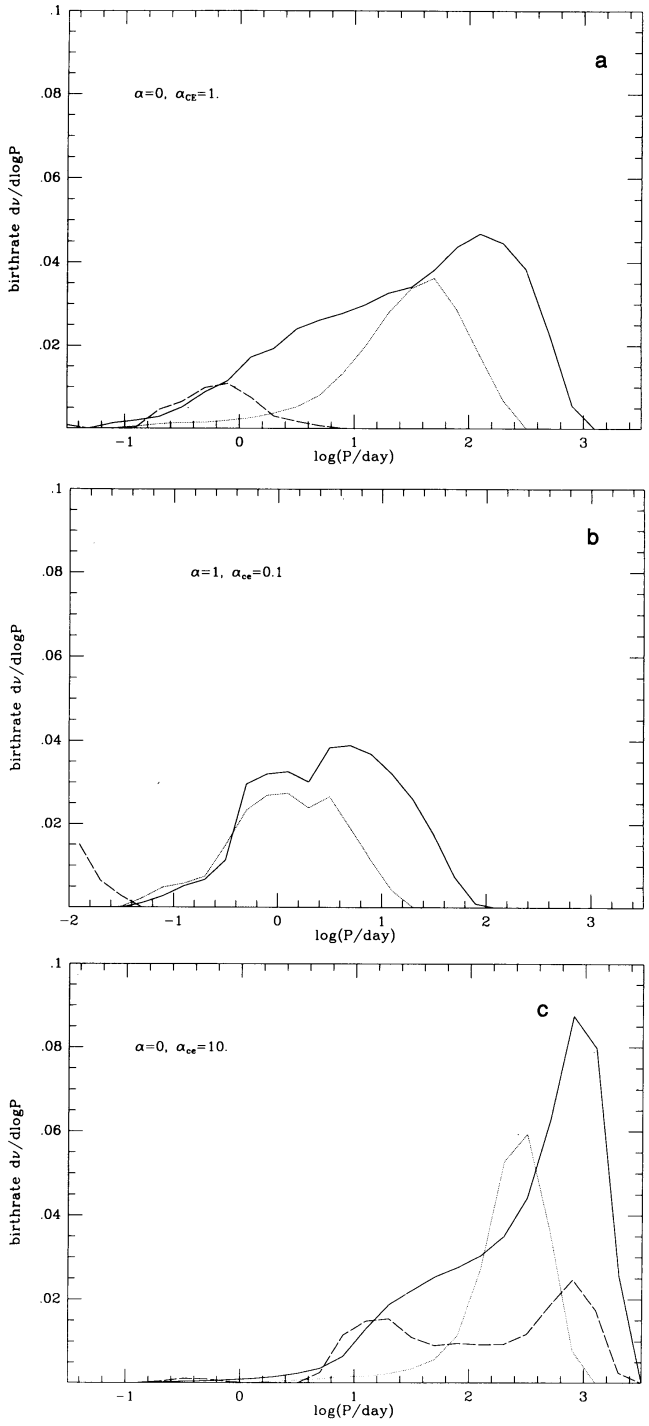

Figure 1.2 Period distribution of PN nuclei versus the orbital period of different populations: carbon-oxygen white dwarf with a main sequence companion (solid line), helium white dwarf with a main sequence companion (dotted line), and double white dwarfs systems (dashed line). Each panel corresponds to a different initial distribution of binaries $f(q) \propto q^{\alpha}$ and/or a different efficiency of the CE ejection, α_{CE}, which we discuss in Chapter 2. Figure from Yungelson et al. (1993), reproduced by permission of the AAS.

These few examples show how critical the CE interaction is for any study involving binaries. Although this phenomenon was predicted a few decades ago, many questions still remain unsolved, as we will see in Section 1.4.3. Before that, we first recall, in Section 1.2, some basics of single stellar evolution, necessary in order to fully understand the CE interaction. We then discuss binarity in Section 1.3, explain what observational techniques are used to detect binary systems, and introduce some key concepts necessary to understand how the CE evolution starts. Finally, we focus on the CE evolution itself and present the outline of this thesis in Section 1.4.

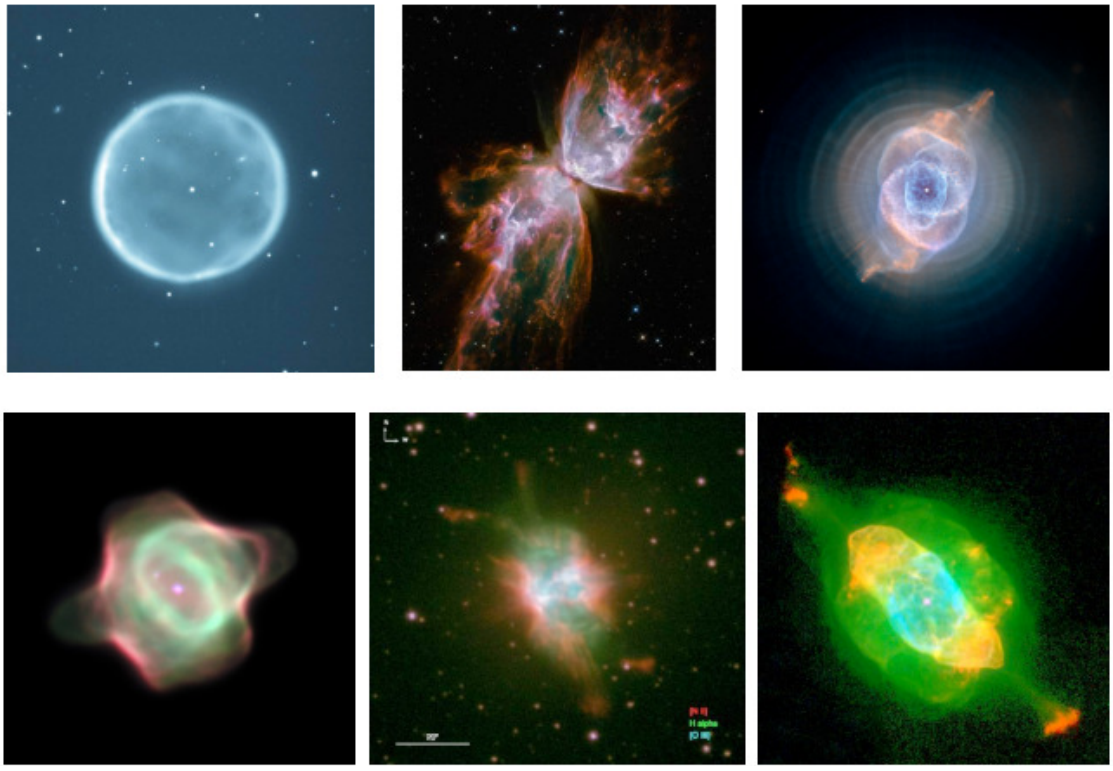

Figure 1.3 A large variety of PN morphologies. Most PN are non-spherical, unlike Abell 39 (top left), such as the "butterfly nebula" (NGC 6302, top middle) and NGC 6543 (top right). The central star of the "stingray nebula" (Hen 1357, bottom left) has a binary companion that is visible above and to the left. Some PNe even exhibit jets like NGC 6778 (also known to have a binary central star, bottom middle) and NGC 7009 (bottom right). Credits: George Jacoby (Abell 39), Guerrero & Miranda (2012, NGC 6778) and hubblesite.org (NGC 6302, NGC 6543, Hen 1357, NGC 7009).

1.2 Stellar evolution of single stars

1.2.1 The governing equations

Stars seem eternal to us because they evolve on timescales that are far longer than those humans are familiar with. Stars exist and behave according to two different levels of physics:

- *macrophysics*, which includes gravity, the dynamics of gases, and energy transport;
- *microphysics*, which encompasses nuclear fusion, the state of the gas, and chemical composition.

All the processes mentioned above depend on each other. Assuming spherical symmetry, they are described by the following system of differential equations in the Eulerian description:

$$\frac{dm}{dr} = 4\pi r^2 \rho \tag{1.1}$$

$$\frac{dP}{dr} = -G\frac{m\rho}{r^2} \tag{1.2}$$

$$\frac{dT}{dr} = -\frac{Gm\rho}{r^2}\frac{T}{P}\nabla \quad \text{with} \quad \nabla = \begin{cases} \nabla_{\text{rad}} \equiv \dfrac{3\bar{\kappa}}{16\pi acG}\dfrac{LP}{mT^4} & \text{(Radiative zone)} \\ \nabla_{\text{ad}} + \nabla_{\text{sup-ad}} & \text{(Convective zone)} \end{cases} \tag{1.3}$$

$$\frac{dL}{dr} = 4\pi r^2 \rho \left(\epsilon_{\text{nuc}} - \epsilon_\nu + \epsilon_{\text{gr}}\right) \tag{1.4}$$

where r is the radial distance from the center of the star, m is the mass coordinate, ρ is the density, P is the pressure, T is the temperature, $\bar{\kappa}$ is the Rosseland mean opacity, L is the luminosity, ∇ is the temperature gradient, ∇_{rad} is the radiative gradient, ∇_{ad} is the adiabatic gradient, ϵ_{nuc} is the specific rate of nuclear energy production, ϵ_ν is the specific rate of energy loss due to neutrinos, and ϵ_{gr} is the specific rate of change of gravitational energy due to contraction or expansion. G, a and c are the gravitational constant, the radiation constant and the speed of light, respectively.

Using the first law of thermodynamics, one can write $\epsilon_{\rm gr} = -c_P\dot{T} + \frac{1}{\rho}\dot{P}$, where c_p is the specific heat at constant pressure. For a derivation of these equations, see, e.g., Kippenhahn & Weigert (1994).

The temperature gradient depends on how energy is transported. In a convection zone, the temperature gradient is most of the time adiabatic ($\nabla = \nabla_{\rm ad}$). However, as one approaches the stellar surface, the gradient becomes superadiabatic: the convective velocity increases and the convective transport becomes inefficient due to the low density environment. The superadiabacity is reflected by the extra term $\nabla_{\rm sup-ad}$ in Equation (1.3). We study this question in detail in Chapter 4.

Equations (1.1), (1.2), (1.3) and (1.4) are called the *mass continuity*, *hydrostatic equilibrium*, *energy transport* and *energy generation* equations, respectively, and together form the set of *stellar structure equations*.

1.2.2 The Virial theorem

One of the most important consequence of hydrostatic equilibrium is certainly the *Virial theorem*. Multiplying Equation (1.2) by $4\pi r^3$ and integrating over the stellar interior leads to the famous relation:

$$2U + \Omega = 0 \ , \tag{1.5}$$

where U is the internal energy of the star, and $\Omega = -\int \frac{Gmdm}{r}$ is its gravitational binding energy. Equation (1.5) assumes a monoatomic ideal gas with $\gamma = 5/3$. One should emphasize that the Virial theorem applies *globally*, not locally. Also, Equation (1.5) would contain additional terms if more forces – such as magnetic fields – were considered in Equation (1.2). The constant factors would also be modified if the state of the gas were different. For instance, a pure photon gas has $P = aT^4/3$ and $P/\rho = u/3$ where u is the internal energy per unit mass. The Virial theorem for such a gas would become $U + \Omega = 0$.

Using Equation (1.5), the total energy of the star is:

$$E_{\rm tot} \equiv U + \Omega = -U = \frac{\Omega}{2} < 0 \ . \tag{1.6}$$

The luminosity of the star is the total energy lost by radiation per unit time, and so according to the conservation of energy:

$$L = -\dot{E}_{\rm tot} = \dot{U} = -\dot{\Omega}/2 \ . \tag{1.7}$$

If the star contracts, half of the energy released is radiated away and the other half is stored into internal energy. Surprisingly, the star heats up while losing energy: it has therefore a *negative* specific heat. This is a general property of self-gravitating systems.

1.2.3 Timescales

The stellar structure equations presented in Section 1.2.1 introduce various timescales on which stars evolve. Usually these timescales differ by orders of magnitude, which allows assumptions to be made when one studies how stars react to perturbations. Assuming a star with mass M, radius R and luminosity L, we describe these different timescales and compare them in Table 1.1 for various stars at different stage of their evolution.

Dynamical timescale. The first timescale is the timescale on which a star reacts when its hydrostatic equilibrium is perturbed. If one includes the acceleration term $\rho\frac{d^2r}{dt^2}$ in Equation (1.2), the resulting timescale on which the star reacts is

$$t_{\rm dyn} \sim \sqrt{\frac{R^3}{GM}} \sim 0.44 \left(\frac{R}{\rm R_\odot}\right)^{3/2} \left(\frac{\rm M_\odot}{M}\right)^{1/2} \ \text{hr.} \tag{1.8}$$

Thermal timescale. Another timescale is the time required for a star to react when its thermal equilibrium is disturbed, which is also the time needed by the star to radiate all its energy away. Following Equation (1.7), one can define the thermal or Kelvin-Helmholtz timescale

$$t_{\rm KH} \sim \frac{|\Omega|}{L} \sim \frac{GM^2}{2RL} \sim 1.5 \times 10^7 \ \left(\frac{R}{\rm R_\odot}\right)^{-1} \left(\frac{L}{\rm L_\odot}\right)^{-1} \left(\frac{M}{\rm M_\odot}\right)^{2} \ \text{yr.} \tag{1.9}$$

Nuclear timescale. Finally, one can consider the timescale for which nuclear burning will balance energy loss. The main reaction is the fusion of four hydrogen atoms into one helium atom. The mass excess is $\Delta m = 0.007u$ so the nuclear energy that can be released is $E_{\rm nuc} = 0.007 f M c^2$ where f is the fraction of the total mass of the star that can be fused. Assuming that approximatively 10% of the stellar mass is fused, one derives

Table 1.1. Timescales

Star	$M/\mathrm{M}_\odot$	$R/\mathrm{R}_\odot$	$L/\mathrm{L}_\odot$	t_{dyn}	t_{KH} (yr)	t_{nuc} (yr)
Sun	1	1	1	27 min	1.5(7)	1.0(10)
Gliese 185	0.47	0.63	0.063	19 min	8.7(7)	7.7(10)
β Pictoris	2.1	1.7	20	41 min	2.0(6)	1.1(9)
Φ_1 Orionis	18	7.4	20 000	2.1 hr	3.4(4)	9.3(6)
Arcturus	1.1	25.7	170	2.3 day	4.3(3)	6.7(7)
Mira	1.18	400	9 000	4.4 month	6.1	1.4(6)
Antares	12.4	883	57 500	4.5 month	4.7(1)	2.2(6)

Note. — Different timescales for the Sun, low-mass (Gliese 185), intermediate-mass (β Pictoris) and massive (Φ_1 Orionis) main sequence stars, a red giant branch star (Arcturus), an asymptotic giant branch star (Mira) and a supergiant star (Antares).

$$t_{\mathrm{nuc}} \sim \frac{E_{\mathrm{nuc}}}{L} \sim 10^{10} \frac{M}{\mathrm{M}_\odot} \left(\frac{L}{\mathrm{L}_\odot} \right)^{-1} \ \mathrm{yr}. \tag{1.10}$$

1.2.4 Complete Evolution

As mentioned earlier, the differential equations governing stellar evolution are coupled, which makes them impossible to solve analytically in most cases. We therefore use stellar evolution codes such as MESA (Module for Experiment in Stellar Astrophysics, Paxton et al., 2011) to solve the system of Equations (1.1-1.4). We show in Figure 1.4 the evolutionary tracks in the Hertzsprung-Russell (HR) diagram of stars with different masses, computed with MESA. We outline below the different phases of evolution for stars of mass between 0.8 and $\approx 8\ M_\odot$.

Pre-main sequence. A molecular cloud in which gravity dominates over thermal and magnetic pressure collapses on a dynamical timescale. A quasi-static protostar is formed. The central temperature is not high enough to ignite hydrogen fusion so the protostar keeps contracting, this time on a Kelvin-Helmholtz timescale. The opacity is large enough such that the star is fully convective: the protostar evolves

down the *Hayashi* track, the limit on the HR diagram on the cool side of which a star cannot be in hydrostatic equilibrium. As the central temperature increases, the opacity decreases, a radiative core develops, and the pre-main sequence star moves to the left part of the HR diagram.

Main sequence. Once the temperature at the centre is high enough (typically about 10^7 K), hydrogen-burning is ignited. The pre-main-sequence star becomes a zero-age main-sequence star and evolves on a nuclear timescale. Protostars smaller than $\approx 0.08\ M_\odot$ are not massive enough to fuse hydrogen, and will become brown dwarfs.

Subgiant branch. The main sequence phase stops when hydrogen-burning ceases in the stellar core. The core contracts and hydrogen is still fused in a thick shell surrounding the core and below the star's envelope. The core mass increases and the core becomes isothermal. For stars more massive than $\approx 2\ M_\odot$, the core mass fraction eventually reaches the Schönberg-Chandrasekhar limit

$$q_{SC} = 0.37 \left(\frac{\mu_{\rm env}}{\mu_c} \right)^2 \tag{1.11}$$

where $\mu_{\rm env}$ and μ_c are the mean molecular weights of the envelope and the core, respectively. For a hydrogen-rich envelope with solar composition and a helium core ($\mu_c = 4/3$), one finds $q_{SC} \approx 0.1$. At this point the core becomes too massive to support the envelope: it contracts rapidly on a Kelvin-Helmholtz timescale in a quasi-static way. A temperature gradient is established in the core. This temperature gradient (as well as degeneracy pressure for low-mass stars) adds to the pressure gradient to keep the star in hydrostatic equilibrium. A derivation of Equation (1.11) can be found, e.g., in Kippenhahn & Weigert (1994).

Red giant branch (RGB). At the end of the subgiant branch, the envelope temperature has decreased so its opacity has increased. Radiative transport is not efficient enough so the envelope becomes convective, starting from the surface. The hydrogen-burning shell becomes thinner and adds mass to the helium core. As a result, the core contracts and the envelope expands. This behavior can be understood by the *mirror principle*, which states that if a star has an active shell-burning source, the burning shell acts like a mirror between the core and the envelope. Thus core con-

traction leads to the envelope expansion, and vice versa. The temperature of the hydrogen-burning shell increases, as well as the rate of energy released by the shell. Consequently, the convective envelope expands inwards and when it reaches its deepest extent, the products of nuclear fusion are brought to the surface, changing the surface abundances: this process is known as the *first dredge-up*. Through the CNO cycle, the primordial ^{12}C has been transformed into ^{13}C by $^{12}\mathrm{C}(p,\gamma)^{13}\mathrm{N}(e^+,\nu)^{13}\mathrm{C}$, and into ^{14}N via a proton capture and a β decay. As a consequence, the surface abundance of ^{12}C decreases, while ^{14}N increases (Wallerstein et al., 1997). As the bottom of the convective envelope moves outwards, the hydrogen-burning shell eventually encounters the chemical discontinuity left behind by the retracting envelope, where the hydrogen abundance is greater. As a result, the shell burns at a slower rate, resulting in a decrease of the luminosity. This phase is called the *RGB bump*.

Horizontal branch. At the tip of the RGB, helium burning is ignited either explosively through the *helium core flash* (for stars with $M_{\mathrm{ini}} \lesssim 2\ M_\odot$), which occurs when the temperature of the core is about 10^8 K and can reach $\sim 10^{11}\ L_\odot$, or quiescently for higher mass stars. The core expands while the stellar radius shrinks. The star now has a helium-burning core with a hydrogen-burning shell.

Asymptotic giant branch. After helium has been exhausted in the core, an evolutionary phase similar to the RGB phase takes place, but with a hydrogen-burning as well as a helium-burning shell. A *second dredge-up* takes place at this point, leading to an increase of the ^{14}N surface abundance. Eventually, the helium-burning shell gets thinner and becomes thermally unstable, leading to *thermal pulses*. The different phases taking place during a thermal pulse are described below:

- the outer hydrogen-burning shell adds ashes to the intershell region, increasing pressure and temperature of the intershell region;
- eventually, a thermonuclear runaway, the *helium-shell flash*, occurs. The helium-shell flash can reach a luminosity of $10^8\ L_\odot$ for about a year;
- the energy released by the helium-shell flash drives the expansion of the intershell region and of the entire star, which therefore cools off. The hydrogen-burning shell extinguishes;

- the convective envelope extends inwards, in some cases beyond the hydrogen-burning shell, bringing material from the intershell region to the surface: this phase is called the *third dredge-up*;

- the star contracts back at the end of the pulse. The helium-burning shell becomes inactive while the hydrogen-burning shell reignites. A phase of stable hydrogen-shell burning called the *interpulse* period starts until the next thermal pulse. The duration of this interpulse phase can vary between $\lesssim 1\,000$ yr and a few 10 000 yr.

The third dredge-up is responsible for the formation of carbon-rich stars, which initially were oxygen-rich due to the interstellar medium. For stars with $M_{\rm ini} \gtrsim 5\ M_\odot$, the temperature at the base of the envelope during the interpulse period can be high enough to ignite hydrogen-burning through the CNO cycle. This process is called *hot bottom burning*. As a consequence, the luminosity increases, the carbon surface abundance decreases – thus preventing massive stars from becoming carbon-rich – and the N surface abundance increases.

Post-AGB evolution The mass loss rate increases during the thermal pulses. Once the envelope mass becomes quite small, typically between 10^{-3} and $10^{-2}\ M_\odot$, the star shrinks and leaves the AGB. The envelope mass decreases so the star moves to higher temperatures at a constant luminosity. When the effective temperature reaches a few $\approx 10\,000$K, the star develops a fast radiation-driven wind and the strong UV flux from the star destroys dust grains and ionizes the circumstellar material. The star now appears as a planetary nebula that can be observed in recombination lines such as Hα, [N II] or [O III]. The H-burning shell extinguishes when the envelope drops below $\approx 10^{-5}\ M_\odot$ ($T_{\rm eff} \sim 10^5$K), at which point the central star becomes a white dwarf and fades away. In some cases the star can experience a final thermal pulse during its post-AGB evolution and become a *born again* AGB star. About 10% of all post-AGB stars are expected to experience such a late He-shell flash (Wallerstein et al., 1997). Sakurai-type objects (Herwig, 2001) and R Coronae Borealis stars (Clayton, 2012) are some possible examples of born again stars.

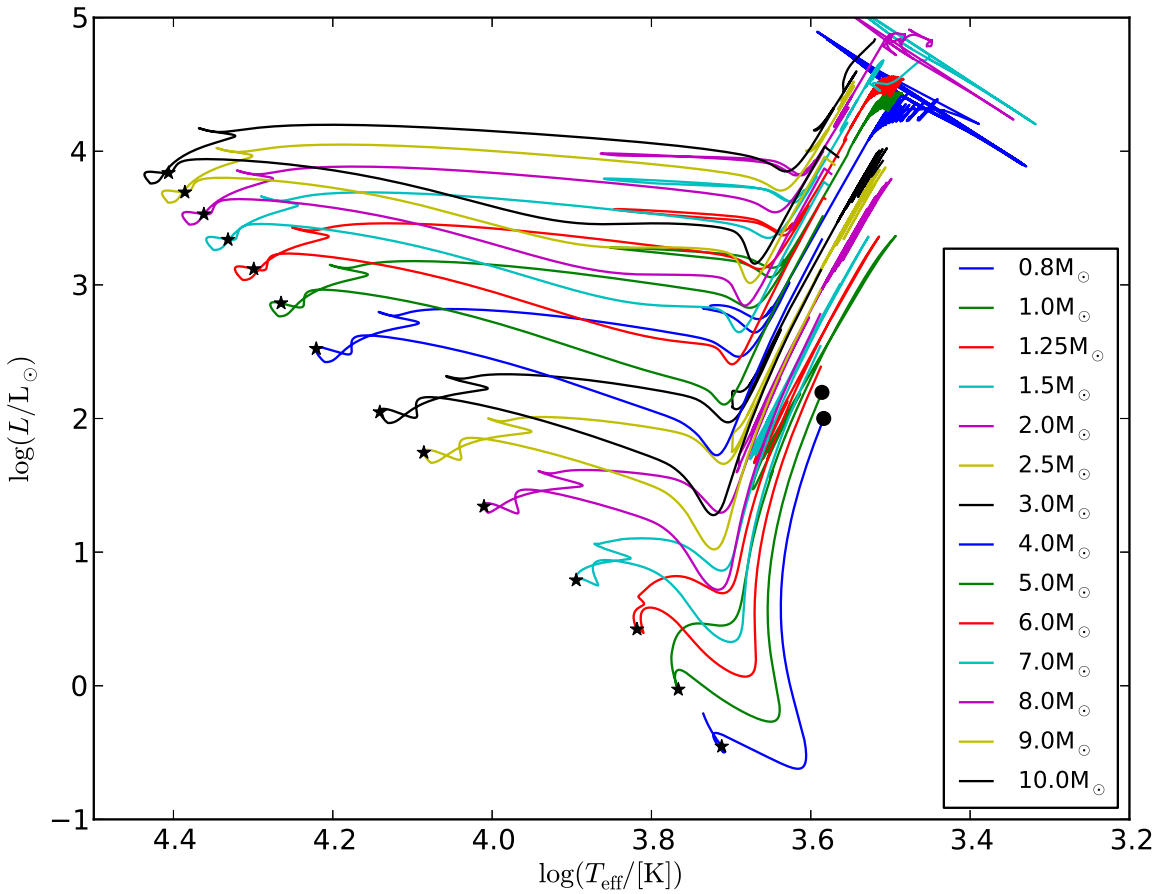

Figure 1.4 HR diagram showing the temporal evolution of stars with a range of initial masses and a metallicity $Z = 0.01$. For each individual track, the zero-age main sequence stage is showed by an asterisk. As an example, we show the start of the pre-main sequence phase for the 0.8 and 1.0 $M_{\odot}$ models (filled circles). The erratic behavior at the end of the AGB phase (top right corner) is due to non-physical pulsations.

1.2.5 Classification

Stars are usually classified spectroscopically and photometrically. These observational classifications give us information about a particular object *at a given time*. However, another possibility is to classify stars theoretically according to their inferred evolution.

Stars have different characteristics such as mass, size, luminosity or metallicity, to name a few. Although varying these parameters will impact the entire stellar evolution, the stellar mass is the main parameter that governs the evolution. One can therefore classify stars according to their initial mass $M_{\rm ini}$ in an approximate manner, as shown in Figure 1.5.

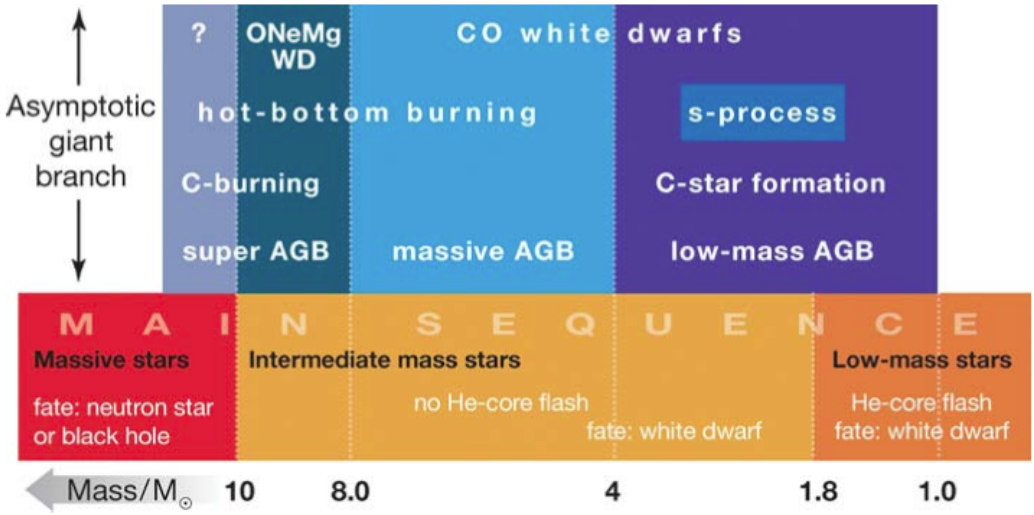

Figure 1.5 Classification of stars by mass, from Herwig (2005). The lower part shows mass designation according to initial mass. Approximate limiting masses between different regimes are given at the bottom. These estimates are dependent on physics assumptions and input of models, as well as on metallicity. The different regimes have been labeled with some characterizing properties, where time increases upwards. The evolutionary fate of super-AGB stars is still uncertain. Reproduced by permission of the Copyright Clearance Center.

Very-low-mass stars. Stars with $M_{\rm ini} \lesssim 0.8\ M_{\odot}$. They have not had the time to evolve past the main sequence in a Hubble time.

Low-mass stars. Stars with $0.8 \lesssim M_{\rm ini}/M_{\odot} \lesssim 2$. After the main sequence phase, they develop a degenerate helium core on the red giant branch. Helium burning is

ignited explosively in a *helium core flash*. They end their lives as carbon-oxygen white dwarfs.

Intermediate mass stars. Stars with $2 \lesssim M_{\rm ini}/M_\odot \lesssim 8$. Similar to low-mass stars except that helium burning is ignited quiescently in a non-degenerate core.

Massive stars. Stars with $M_{\rm ini} \gtrsim 8\ M_\odot$. They ignite carbon burning in a non-degenerate core. A small range ($M_{\rm ini} \approx 8-10\ M_\odot$) of these stars might end their lives as ONeMg white dwarfs. Higher masses ignite burning of heavier elements until an iron core is formed, which eventually collapses into a neutron star ($M_{\rm ini} \lesssim 15-20\ M_\odot$) or a black hole for higher masses (Woosley et al., 2002).

In what follows and in this thesis, we will only consider low- and intermediate-mass stars.

1.3 Binarity

The evolution described in Section 1.2.4 does not take into account the influence of a potential nearby companion. Unlike our Sun, a large fraction of stars in the Universe is found in binary or multiple systems. Indeed, Duquennoy & Mayor (1991) concluded that 60% of F and G stars are in multiple systems, while a more recent study found the multiplicity of F- to K-type stars to be $\approx 45\%$ (Raghavan et al., 2010). More massive objects could have a binary fraction of nearly 100%, while cool M and later types could have a binary fraction on the order of 40% (Bouy, 2011). Although this number is rather unknown because of completeness, observational studies show a clear correlation between the binary fraction and the mass of the primary (Bouy, 2011, and references herein). The period distribution of binary F,G and K stars is a Gaussian peaking at around 180 yr; unequal mass systems also seem to be favoured (Duquennoy & Mayor, 1991; Bouy, 2011).

If the components of a binary system are close enough they might interact through various mechanisms, and alter the orbital parameters and their individual evolution. One of these mechanisms is tidal interaction (Zahn, 1989), which can modify not only the shape of the stellar components and their individual evolution, but also circularize the orbit (Zahn & Bouchet, 1989). Binarity might also enhance mass loss and result in mass transfer, therefore producing systems that cannot be explained by standard evolution (Tout & Eggleton, 1988). From a numerical point of view, mass

transfer in binaries is a challenging process to model (Lajoie & Sills, 2011a,b). In this thesis we focus on more extreme interactions, which we describe in Section 1.3.3 and Section 1.4.

Although multiplicity properties are mostly dictated early in the star formation process, they might change during the evolution depending on the environment. For instance, the binary fraction of open clusters is in general quite large, similar to that for the solar neighborhood. On the other hand most globular clusters, in particular those with dense cores, are found to have low binary fractions and exhibit a correlation between the binary fraction and the fraction of blue stragglers (Sollima et al., 2008; Milone et al., 2012). The dynamical evolution of binary stars in clusters has been studied using either an hybrid approach combining Monte Carlo and population synthesis techniques (Ivanova et al., 2005; Ivanova, 2011), or N-body simulations (Hurley et al., 2007). Both methods yield different results[4] which cannot be really compared as the initial conditions and the range of applicability of these techniques are drastically different (Fregeau, 2007a). Moreover, these numerical results are difficult to compare to direct observations as there are significant uncertainties regarding what stage of evolution the cluster is at, and what is the true binary fraction of the cluster. For instance, Fregeau (2007b) suggested that most globular clusters are in the core contraction phase rather than the binary burning phase, unlike previously thought. Another difficulty resides in the discrepancy between the observed binary fraction, and the one predicted by models: the observed binary fraction might be significantly underestimated, as it does not take into account compact object–compact object and main sequence–compact object binaries (Fregeau et al., 2009). Nevertheless, what causes the low binary fraction in globular clusters, still remains unclear.

1.3.1 Methods of detection

Binaries are usually classified according to their method of detection. We mention here the usual methods to probe binarity. A more detailed description can be found, e.g., in Jorissen & Frankowski (2008).

Visual binaries. Visual binaries are systems in which each component can be resolved individually. Long term observations allow determinations of the orbital

[4]The N-body simulations show an increase of the *hard* binary fraction with time while the binary fraction decreases in the Monte Carlo simulations. For more details, see Figure 1 in Fregeau (2007a)

parameters for systems whose motion on the plane of the sky can be detected over reasonably short times. A famous example of a visual binary is α Centauri. This method works only for nearby objects with a relatively long orbital period ($\gtrsim 1$ yr). If the distance to the binary is known, the separations between the stellar components and masses can each be derived.

Photometric binaries. Most binary systems are too distant and/or have too short of an orbital separation to be resolved. Another method to detect them is through photometric measurements. These systems show variation in their light curves because:

- the stellar components fully or partially eclipse one another, in which case these systems are known as *eclipsing binaries*;
- one or both stellar components are deformed due to tides; these systems are called *ellipsoidal variables*;
- the hotter component irradiates the cooler component.

The transit technique probes eclipsing binary systems with shorter orbital periods, typically below ≈ 1 yr. If the radius of the eclipsed star is known, the orbital separation and the sum of the masses can be derived.

Spectroscopic binaries. Binarity can also be probed by measuring the Doppler shift of spectral lines of one or both stellar components, as they orbit each other. Masses can be calculated within a factor $\sin i$, where i is the inclination angle of the orbital plane axis with respect to the line of sight.

Astrometric binaries. If the orbital separation is too wide or one component too faint for the binary to be detected, an unseen companion can be detected by probing the wobbling motion on the celestial sphere of the bright star around the center of mass of the system.

In some specific cases, there are other photometric techniques to detect binarity, such as the detection from rapid rotation velocities, X-ray emission or composite spectra and/or magnitudes. We apply this last technique to the study of central stars of PNe in Appendix A.

1.3.2 The Roche analysis

The problem of binary interactions was first studied in the 19th century by the French mathematician Edouard Roche. Let us consider two stars of masses M_1 and M_2 orbiting around a common centre of mass (CM). In the frame of reference rotating with the binary system, the effects of both gravitational fields and the centrifugal force are described by the effective *Roche* potential:

$$\Phi_{\rm R}(\mathbf{r}) = -\frac{GM_1}{|\mathbf{r}-\mathbf{r_1}|} - \frac{GM_2}{|\mathbf{r}-\mathbf{r_2}|} - \frac{1}{2}(\mathbf{\Omega}\times\mathbf{r})^2 \tag{1.12}$$

where $\mathbf{\Omega}, \mathbf{r_1}, \mathbf{r_2}$ are the angular velocity and the position vectors of the two stars, respectively. The last term on the right-hand-side is the centrifugal force. The equipotential lines in the orbital plane for a specific system are shown in Fig. 1.6. For each star, the contour that crosses between the two stars forms two lobes called the *Roche lobes*. An approximation of the Roche lobe radius for M_1 is $R_{1,L} = ar_{1,L}$ where a is the separation and $r_{1,L}$ is the effective Roche lobe radius around M_1 given by Eggleton (1983) and Webbink (2008):

$$r_{1,L} \sim \frac{0.49q^{-2/3}}{0.6q^{-2/3} + \ln(1+q^{-1/3})}, \tag{1.13}$$

where $q = M_2/M_1$. Another simpler fitting formula can be found in Eggleton (2006):

$$r_{1,L} \sim 0.44\frac{q^{-1/3}}{(1+1/q)^{0.2}} \qquad \text{for } 0.1 \lesssim q \lesssim 10. \tag{1.14}$$

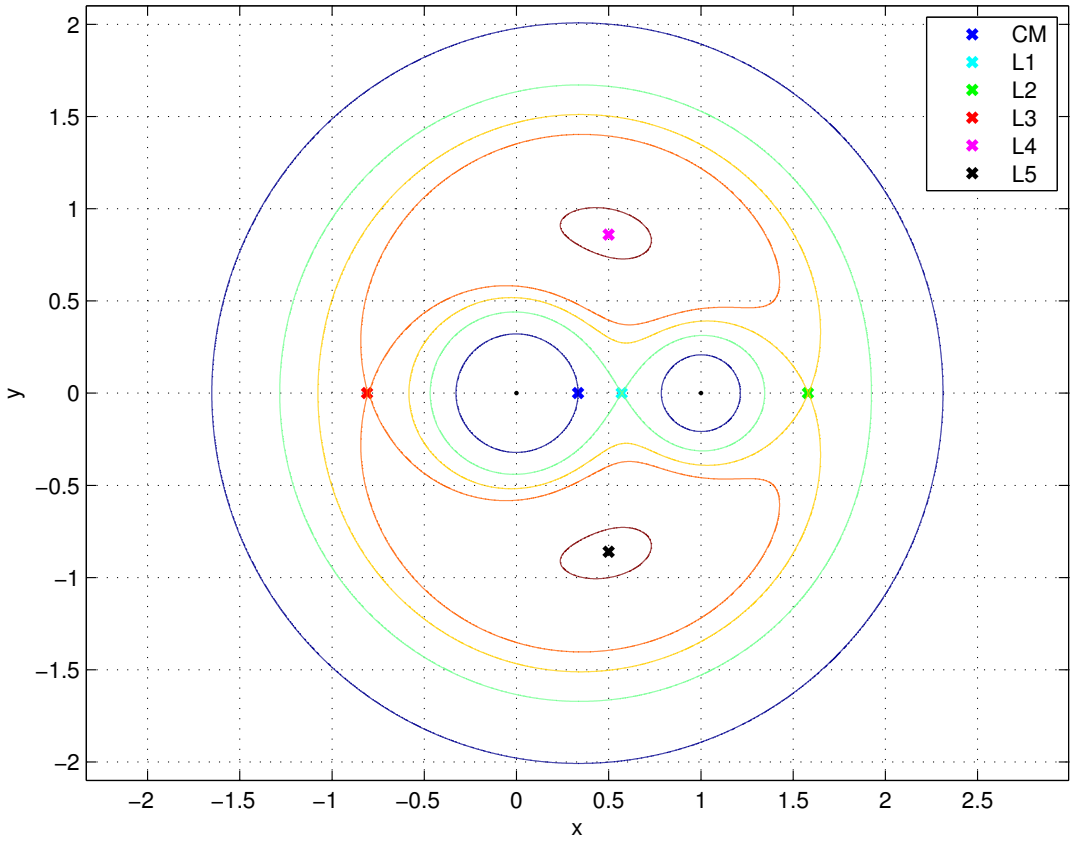

Figure 1.6 Equipotential contours (in the rotating frame) on the orbital plane of a binary system with $M_1 = 1$, $M_2 = 0.5$ and $A = 1$ (dimensionless), as well as the location of the center of mass of the system (CM) and the Lagrangian points $(L_i)_{i\leq 5}$. Computer program written with *MATLAB*.

1.3.3 Roche lobe overflow

Let us assume that M_1 evolves and becomes a giant star; usually M_1 would be the more massive component of the binary system, but we study here the general case. The stellar radius increases with time (Figure 1.7) and if the orbital separation is small enough, the star eventually fills its Roche Lobe and mass transfer onto the companion starts due to RLOF . In order to determine whether the mass transfer is stable, one must compare how the radius of the donor M_1 and its Roche lobe change with mass loss. One therefore introduces the so-called *radius-mass exponents*:

$$\xi \equiv \frac{d\ln R_1}{d\ln M_1} \; ; \; \xi_L \equiv \frac{d\ln R_{1,L}}{d\ln M_1}. \tag{1.15}$$

Note that $\xi \geq 0$ means that the radius shrinks when the star loses mass. The condition $\xi \geq \xi_L$ implies that mass transfer is stable. In the case of a conservative mass transfer, i.e. when the total mass and angular momentum of the system are conserved, one can use Equation (1.14) to show that:

$$\xi_L = 2.13q - 1.67 \qquad \text{for } 0.1 \lesssim q \lesssim 10. \tag{1.16}$$

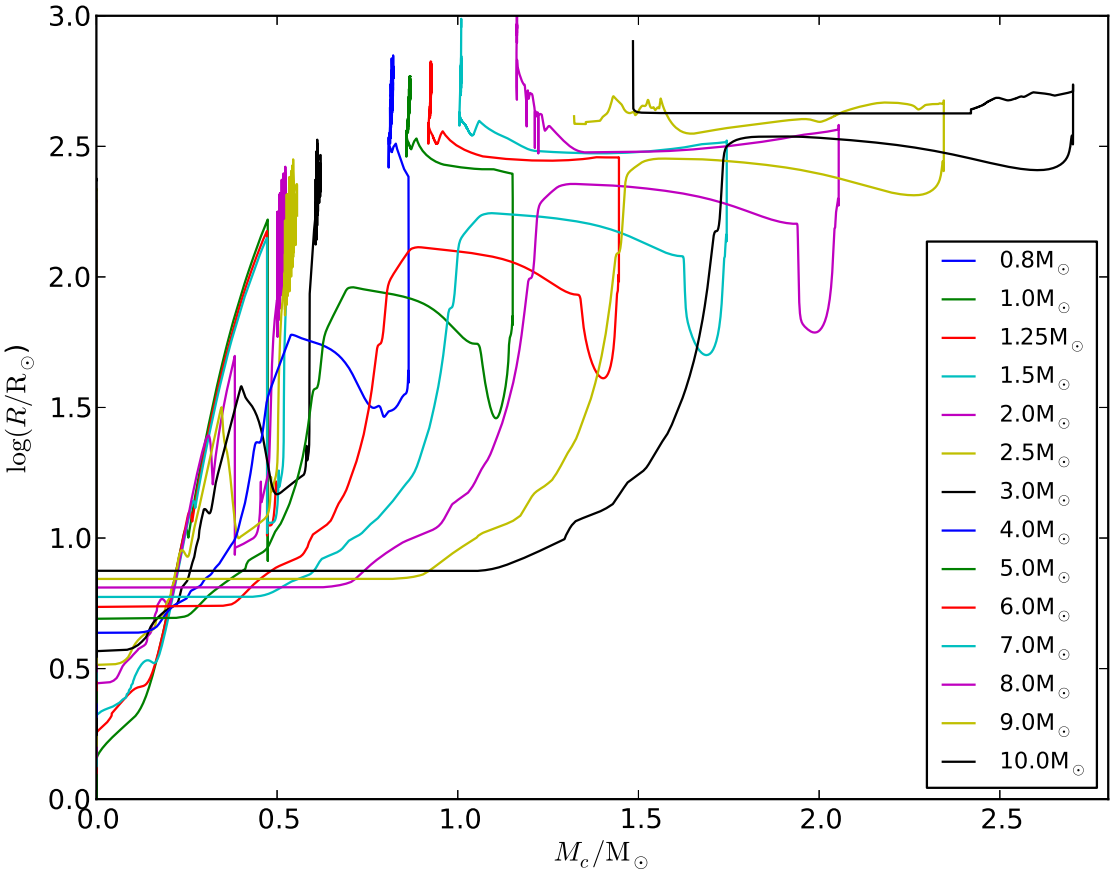

Figure 1.7 The evolution of the stellar radius as a function of the core mass for the models presented in Figure 1.4.

1.4 Common envelope evolution

The CE phase is an evolutionary phase during which the secondary star, which we shall call the *accretor*, spirals inside the envelope of the primary, or *donor*. During the CE phase the secondary may also fills its own Roche lobe because it cannot accrete

all the matter coming from the donor star. Consequently, the stellar components orbit inside a common extended envelope. As we mentioned earlier, the CE phase was originally described by Paczynski (1976) to explain the formation of compact binaries. For a general review of the topic see, e.g., Iben & Livio (1993) and Taam & Sandquist (2000).

1.4.1 The onset of the common envelope evolution

There are two different mechanisms leading to the onset of a CE evolution.

The first one is the start of unstable mass transfer from the expanding primary to the secondary due to RLOF (Hjellming & Webbink, 1987; Hurley et al., 2002). It occurs when the radius of the donor grows faster than its Roche lobe ($\xi < \xi_L$). Thus, the condition for unstable mass transfer relies strongly on how the donor responds to mass loss. We discuss this subject further in Chapter 4.

The second mechanism is the development of a tidal or *Darwin* instability that occurs if there is not enough angular momentum in the orbit to maintain the primary's envelope in tidal synchronization (Darwin, 1879). Assuming that the total angular momentum is conserved, one can show that instability occurs when

$$J_1 > \frac{1}{3} J_{\rm orb}, \tag{1.17}$$

where J_1 is the spin angular momentum of the primary, and $J_{\rm orb}$ the orbital angular momentum. Instability usually happens for $M_1/M_2 \gtrsim 5 - 6$ (Taam & Sandquist, 2000).

1.4.2 The physics of the common envelope evolution

Once the CE phase has started, the companion, surrounded by the primary's stellar gas, exchanges momentum and energy with this gas through strong drag forces. The drag forces have two components:

- the *gravitational* drag, which includes dynamical friction between the cores and the surrounding gas, as well as non-axisymmetric tidal effects;
- the *hydrodynamic* drag due to ram pressure forces acting on the companion and the giant core.

Ricker & Taam (2008) showed that not only does the gravitational component always dominate over the hydrodynamic one, but also that the mass accretion rate onto the companion is negligible, even smaller than the rate expected in a Bondi-Hoyle formalism (see Chapter 5). Note that a Bondi-Hoyle formalism is not strictly applicable here as it assumes neither a density nor a velocity gradient, as well as no external gravitational field. Some of these assumptions are obviously violated in the vicinity of a companion embedded in a CE.

As a result of gravitational drag, the orbital separation shrinks rapidly while the envelope is ejected. The evolution is highly dynamical and stops when no more drag forces act on the two cores. We will see in Chapter 3 that this dynamical phase is quite short, typically ≈ 1 yr, which is the main reason why it has so far been seldom observed directly.

Another physical process has been suggested for transferring energy and angular momentum during this dynamical phase. Using an evolutionary code, Meyer & Meyer-Hofmeister (1979) derived the energy dissipation rate considering turbulent convection only. Their model overestimates the in-spiral timescale as gravitational drag is showed to be dominant in numerical simulations (Ricker & Taam, 2008; Passy et al., 2012; Ricker & Taam, 2012). Furthermore, the flow is laminar on the scales used in hydrodynamical simulations. Consequently, their turbulent viscosity is also overestimated (Ricker & Taam, 2012). However, once the dynamical phase stops (and assuming that the envelope has not been fully ejected) a much longer non-dynamical phase might take place in which turbulent convection is important (Podsiadlowski, 2001). We discuss this subsequent phase in Chapter 3.

1.4.3 Remaining questions

Although the CE phase has been studied for over 30 years, many questions remain unanswered.

First of all, the mechanisms for the transfer of energy taking place during the CE interaction, leading eventually to the ejection of the envelope, are not yet completely understood. Although it has been shown that the CE evolution is driven mainly by gravitational drag (Ricker & Taam, 2008), the existence of low-mass companions having survived a CE phase suggest that some extra energy sources are required for the envelope to be fully ejected. Webbink (2008) suggests that the missing energy comes from recombination of the envelope, but this question is still debated.

Although some numerical studies of the CE interaction have already been carried out (see, e.g., Bodenheimer & Taam, 1984; Sandquist et al., 1998; Ricker & Taam, 2008, 2012), a direct comparison of the results obtained using different techniques has never been carried out. There are also very few studies that connect simulations and observations in a meaningful way (see, e.g., Sandquist et al., 2000). Additionally, parameter space has been barely explored.

The conditions for a successful CE phase, i.e. for which the companion does not merge with the primary's core and the envelope is ejected, are still unknown. One would like to be able to predict for any given system entering a CE whether the envelope will be ejected and, in this case, what the final separation of the surviving binary would be. The case of possible substellar companions is of particular interest as they must not only find a way to eject the envelope, but also to survive destruction as they travel through the dense envelope of the giant star.

Eventually, these results should be compared directly to observational data, for validation, and to the analytical/empirical work previously done (Tutukov & Yungelson, 1979; Nelemans et al., 2000), in order to improve the prescriptions for the CE phase used in population synthesis codes.

Finally, the era of transient astronomy is upon us thanks to ongoing and upcoming surveys such as the Palomar Transient Factory (PTF, Rau et al., 2009) or the Large Synoptic Survey Telescope (LSST, Ivezic et al., 2008). Accurate numerical models are therefore needed in order to predict the light curves that will be observed by these surveys, and to explain a variety of transient events.

1.5 Thesis outline

1.5.1 Chapter 2: On the α-formalism for the Common Envelope Interaction

We first use an empirical/analytical approach in order to statistically predict the outcome of a CE evolution. We consider the α-formalism, a common way to parametrize the CE interaction in binary population synthesis studies, where the α parameter describes the fraction of orbital energy released by the companion that is available to eject the giant star's envelope. Using new stellar evolutionary calculations, we rewrite and improve the α equation. Then we determine α both from simulations and observations in a self consistent manner, thus gaining a better understanding of

the uncertainties. Finally, we discuss the dependency of α on the orbital parameters.

1.5.2 Chapter 3: Hydrodynamics Simulations of the Common Envelope Phase

We then compare the results discussed in Chapter 2 to numerical models. Therefore, we perform three-dimensional simulations of the in-spiral phase of the CE interaction of a red giant branch star and a companion star with different masses. We compare the results obtained using different numerical techniques and resolutions, with observed systems thought to have gone through a CE interaction, and discuss the role of recombination in the evolution.

1.5.3 Chapter 4: The Response of Giant Stars To Dynamical-Timescale Mass Loss

Despite the different investigations presented in Chapters 2 and 3, questions remain about the extra mechanism required to fully eject the giant's envelope. Following the suggestion made in Chapter 2 that the dynamical response of the giant donor might facilitate the envelope's ejection, we study the response of giant stars to high mass loss rates. We carry out one-dimensional simulations using a stellar evolution code, and compare our results with previous studies. We discuss the assumptions made in some previous work and the implications of our results on the CE evolution.=

1.5.4 Chapter 5: The Common Envelope Phase with Planetary Companions

Motivated by recent observations of low-mass companions in close orbit around evolved stars, we study in Chapter 5 the case of CE interactions happening between a giant star and a substellar companion. We first consider whether these companions could have lost significant amounts of mass during the phase when they orbited through the envelope of the giant. We apply an analytical criterion to determine whether mass loss may have played a role in the histories of these brown dwarfs and planets. Then we describe a numerical algorithm that we have implemented, which is necessary to perform simulations with such low-mass secondaries.

1.5.5 Chapter 6: Summary and Conclusions

We summarize and conclude in Chapter 6.

1.5.6 Appendix A: The binary fraction of planetary nebula central stars. I. A high-precision, I-band excess search

Paczynski (1976) concluded the abstract to his paper suggesting that the "observational discovery of a short period binary being a nucleus of a planetary nebula would provide very important support for the evolutionary scenario presented in [Paczynski (1976)]." Using observational data obtained with the 2.1m telescope at Kitt Peak National Observatory, we test the binarity of 27 central stars of planetary nebula using the IR-excess method, and compare our results with predictions.

1.5.7 Appendix B: A Well-Posed Kelvin-Helmholtz Instability Test and Comparison

Kelvin-Helmoltz Instability is among the most important tests used to compare the accuracy and performance of hydrodynamical codes (Chapter 3). Also, Kelvin-Helmoltz Instability might play a significant role in the destruction of the companion during the CE phase (Chapter 5). Recently, there has been a significant level of discussion of the correct treatment of Kelvin-Helmholtz instability in the astrophysical community. We pose a stringent test of the initial growth of the instability, and carry out simulations with five different codes. We compare the behavior of the different methods, and comment on the tendency of some of them to produce secondary Kelvin-Helmholtz billows.

Chapter 2

On the α-formalism for the Common Envelope Interaction

Originally published as De Marco, O., Passy, J.-C., Moe, M., Herwig, F., Mac Low, M.-M., & Paxton, B. 2011, MNRAS, 411, 2277

Abstract

The α-formalism is a common way to parametrize the common envelope interaction between a giant star and a more compact companion. The α parameter describes the fraction of orbital energy released by the companion that is available to eject the giant star's envelope. By using new, detailed stellar evolutionary calculations we derive a user-friendly prescription for the λ parameter and an improved approximation for the envelope binding energy, thus revising the α equation. We then determine α both from simulations and observations in a self consistent manner. By using our own stellar structure models as well as population considerations to reconstruct the primary's parameters at the time of the common envelope interaction, we gain a deeper understanding of the uncertainties. We find that systems with very low values of q (the ratio of the companion's mass to the mass of the primary at the time of the common envelope interaction) have *higher* values of α. A fit to the data suggests that lower mass companions are left at comparable or larger orbital separations to more massive companions. We conjecture that lower mass companions take longer than a stellar dynamical time to spiral in to the giant's core, and that this is key to allowing the giant to use its own thermal energy to help unbind its envelope. As a result, although systems with light companions might not have enough orbital energy

to unbind the common envelope, they might stimulate a stellar reaction that results in the common envelope ejection.

2.1 Introduction

Common envelope (CE) binary interactions occur when expanding stars transfer mass to a companion at a rate so high that the companion cannot accrete it. This results in the companion being engulfed by the envelope of the primary (Paczynski, 1976). The companion's orbital energy and angular momentum are then transferred to the envelope via an as yet poorly characterized mechanism. This can result in the ejection of the envelope and in a much reduced orbital separation. If the companion cannot eject the CE, it merges with the core of the primary. The CE interaction is thought to last for only a few years, and it is therefore likely that we have never witnessed it directly, although some claims have been made, e.g., for V Hya (Kahane & Jura, 1996). The existence of companions in close orbits around evolved stars, whose precursor's radius was larger than today's orbital separation, vouches for such interactions having taken place.

The CE interaction is thus thought to be responsible for short period binaries such as cataclysmic variables (CV; King, 1988; Warner, 1995), close binary central stars of planetary nebula (PN; De Marco 2009), subdwarf B binaries (Han et al., 2002, 2003), low mass X-ray binaries (Charles & Coe, 2006), the progenitors of Type Ia supernovae (Belczynski et al., 2005) and other classes of binaries and single stars thought to have suffered a merger (such as FK Comae stars; Bopp & Stencel 1981). The specific characteristics exhibited by these binary classes, as well as their relative population sizes are dictated by the period and mass ratio distribution of the progenitor binary population, as well as by the details of the physical interaction during the CE phase.

The CE interaction can be parametrized in terms of the binding and orbital energy sources at play (e.g., Webbink, 1984, 2008), and the post-CE period has been expressed as a function of how efficiently orbital energy can be used to unbind the CE. The efficiency parameter, α, was thus introduced:

$$\alpha = \frac{E_{\rm bin}}{\Delta E_{\rm orb}}, \tag{2.1}$$

where E_{bin} is the gravitational binding energy of the envelope and ΔE_{orb} is the amount of orbital energy released during the companion's in-spiral. The expressions used for

binding and orbital energies in the literature have varied. As a result, the conclusions reached in the numerous papers discussing the CE interaction by means of the α-formalism are difficult to compare. The first motivation of this paper is therefore to choose a formalism by revisiting past choices.

Several papers (e.g., Maxted et al., 2006; Afşar & Ibanoğlu, 2008; Zorotovic et al., 2010) use individual post-CE binaries to derive α. Their observed primary and secondary masses, together with their orbital periods, provide us with parameters of the post-CE systems. Based on the primary mass, one can reconstruct the mass and radius of the primary at the time of the CE interaction and, with this information, a value of α can be derived. However, this method has many hidden uncertainties, and the values of α derived in this way are, once again, only indicative. We therefore use our preferred α-formalism to re-evaluate the value of α for observations and simulations in a homogeneous way and with an increased attention to the sources of uncertainty.

The values of α determined by simulations, (e.g., Sandquist et al., 1998) have their own flavour of hidden caveats and are not easily comparable with those derived from observations. We therefore use the better-understood simulations from the literature to gain insight in how the values of α determined in this way compare with those derived from observations.

In § 2.2 we discuss the α-formalism in the literature and derive our preferred form. We also discuss the value of λ, often used in parametrizing the envelope binding energy. In § 2.3 we calculate the value of α for a set of simulations and observations in a self consistent manner. We then (§ 2.4) discuss the dependence of α on stellar and system parameters. We conclude and summarise in § 2.5.

2.2 The α equation

In this section we determine the best form of the α equation (Eq. 2.1).

2.2.1 The α-formalism in the literature

The original α equation can be found in Tutukov & Yungelson (1979), who used:

$$\Psi \frac{M^2}{R} = \beta \frac{M_{\rm He} m}{2R_{\rm He}}, \tag{2.2}$$

where we have maintained the original symbols to emphasize the subtly different assumptions made in each equation. β is the binding energy parameter equivalent to α, $M_{\rm He}$ and $R_{\rm He}$ are the post-CE primary's core mass and radius, respectively, m is the companion's mass, M and R are the mass and radius of the primary at the time of the CE interaction. The value of Ψ was taken to be 0.5 to account for the fact that the radius of the primary at the start of the *dynamically-significant* part of the CE interaction was thought to be twice as large as it was at the beginning of the CE interaction.

Later Iben & Tutukov (1984) used a similar expression but modified the symbols:

$$\frac{M_1^2}{A} = \alpha \frac{M_{1,R} M_2}{A_f}, \tag{2.3}$$

where M_1 is the primary mass at the time of the CE and $M_{1,\rm R}$ is the primary (remnant) mass after the CE interaction. Remembering that there is a factor of 1/2 on both sides of Eq. 2.3 we see that A, the initial binary separation, has replaced the initial primary radius (a reasonable assumption) and that A_f, the final binary separation, has taken the place of the primary core radius, a choice that seems sensible, as the final binary separation should be larger than the primary's core radius.

In the same year, Webbink (1984) rewrote the expression as:

$$-G\frac{M_1 M_{1,e}}{\lambda R_{1,L}} = -\alpha_{CE} G \left[\frac{M_{1,c} M_2}{2A_f} - \frac{M_1 M_2}{2A_i} \right], \tag{2.4}$$

where we have adopted the symbols used by Webbink (2008): $M_{1,c}$ and $M_{1,e}$ are the primary's core and envelope masses, respectively, A_i is the inital binary separation, $R_{1,L}$ is the Roche lobe of the primary at the onset of mass transfer and where λ is a number of order unity which depends on the mass distribution of the primary's envelope (λR is effectively the mass-weighted mean radius of the envelope). The symbol λ was actually introduced by de Kool et al. (1987) as an addition to the Webbink (1984) equation and has been included in the equation ever since. Eq. 2.4 contains a term for the orbital energy at the beginning of the CE interaction, a term that others have neglected, on the ground that its value is far smaller than that of the final orbital energy, due to the considerable in-spiral that happens during the interaction.

Yungelson et al. (1993) rewrote the α equation in the following way:

$$\frac{(M_1 - M_{1,R})(M_1 + M_2)}{A_0} = -\alpha M_{1,R} M_2 \left[(\frac{1}{A_f} - \frac{1}{A_0}) \right], \tag{2.5}$$

where all symbols have been previously defined and A_0 is the binary separation at the beginning of the *dynamically-significant* part of the CE interaction. Eq. 2.5 actually contains a factor of 0.5 on both sides of the equality, which was cancelled out by Yungelson et al. (1993), but that must be there for the expression of the orbital energy to be correct. This factor implies that the size of the primary at the start of the dynamically-significant part of the CE interaction is $2 \times A_0$ (Eq. 2.3). Using this expression will therefore result in smaller values of α (as also noticed by Han et al. 1995). Aside from the difference in primary radius, Eq. 2.5 is different from that of Webbink (1984) also because the binding energy of the envelope is more negative: the giant's envelope during the CE is bound also by the gravitational attraction of the companion within it.

Pre-empting our derivation in § 2.2.2, in this work we will use:

$$-G\frac{M_e(\frac{M_e}{2} + M_c)}{\lambda R} = -\alpha G \left[\frac{M_c M_2}{2A_f} - \frac{(M_c + M_e)M_2}{2A_i} \right] \tag{2.6}$$

where M_c and M_e are now the giant primary's core mass (which is assumed to be the same as the mass of the primary after the CE interaction) and the primary's envelope mass (which is assumed to be ejected by the interaction), respectively. In § 2.2.3 we will use the virial theorem to show that the energy budget should include a factor of 0.5 on the left-hand-side of Eq. 2.6, corresponding to the thermal energy of the gas lessening the stellar envelope's gravitational potential well. For now, however, we have presented the α equation using only the traditionally-included energy sources. The thermal energy source will be discussed further in § 2.2.3, § 2.3.4 and § 2.5.

In the case of observed systems (§ 2.3.2), we assume that the primary is filling its Roche lobe radius at the beginning of the CE interaction (i.e., $R = R_{1,RL}$) and that $A_i = R_{1,RL}/r_{1,RL}$, where (Eggleton, 1983; Webbink, 2008):

$$r_{1,\mathrm{RL}} \sim \frac{0.49 q^{-2/3}}{0.6 q^{-2/3} + \ln(1 + q^{-1/3})} \tag{2.7}$$

and $q = M_2/M_1$[1]. Our expression is almost identical to that of Webbink (1984),

[1]Different studies substitute the Roche Lobe radius for A_i, instead of the actual separation between primary and secondary at the time of Roche lobe overflow. The initial orbital energy term is mostly negligible compared to the final orbital energy one though, so specific choices of the initial

except that our binding energy is somewhat lower.

Clearly, irrespective of which formalism one uses, it is paramount that values of α calculated with one formalism not be used as input to a different formalism in order to derive, for instance, values for the final orbital separation.

2.2.2 The binding energy term

Several authors (e.g., Han et al., 1995) chose not to use an approximation for the binding energy of the envelope, but instead integrate the envelope mass from stellar structure calculations. As we will see in § 2.2.5 this choice does not necessarily lead to a more accurate value of α. So, here we determine as accurate an approximation to the binding energy as possible.

The binding energy of a star is:

$$E_{\rm bin} \equiv -\int \frac{Gm}{r} dm. \tag{2.8}$$

In the case of giants, the small and dense core is surrounded by a vast envelope whose density rapidly falls with radius. Therefore we model the core as a point mass and the envelope as a shell of homogeneous density

$$\rho = \frac{M_e}{4\pi(\lambda R)^2},$$

located at a distance λR from the core. The factor $\lambda < 1$ accounts for the fact that, in the shell approximation of the real envelope, the shell is located at the mass-averaged stellar radius. Using this assumption we calculate separately the envelope binding energy deriving from the attraction of the core, $E_{\rm ce}$, and that deriving from the attraction of the envelope onto itself, $E_{\rm ee}$:

$$E_{\rm bin} = E_{\rm ce} + E_{\rm ee}. \tag{2.9}$$

The core-envelope binding energy can be easily calculated:

$$E_{\rm ce} = -G\int \frac{M_c dm}{\lambda R} = -G\frac{M_c M_e}{\lambda R}, \tag{2.10}$$

where dm is a parcel of envelope mass sitting at distance λR from the core, and the integration is over the entire envelope, approximated as a shell with radius λR. The

orbital separation are not fundamental.

self-gravity of the envelope results in:

$$E_{\rm ee} = -\frac{G}{2}\int\int \frac{dm^{'}dm}{|\mathbf{r}-\mathbf{r}^{'}|}, \tag{2.11}$$

where dm and $dm^{'}$ are mass parcels in the envelope shell separated by a distance $|\mathbf{r}-\mathbf{r}^{'}|$. The factor $\frac{1}{2}$ prevents double counting the interaction between parcels. Since we have made the assumption that all mass parcels are in a shell with radius λR, $|\mathbf{r}^{'}| = |\mathbf{r}| = \lambda R$, the denominator is:

$$\frac{1}{|\mathbf{r}-\mathbf{r}^{'}|} = \frac{1}{\lambda R}\sum_{n=0}^{\infty} P_n(\cos\psi) \sim \frac{1}{\lambda R}\left(1-(\cos\psi)\right), \tag{2.12}$$

where P_n is the Legendre polynomial. For the final step, we only consider $P_0 = 1$ and $P_1 = \cos\psi$, where ψ is the angle between $\mathbf{r}$ and $\mathbf{r}^{'}$ and we neglect orders $n > 1$. Because of symmetry, the term including $\cos\psi$ vanishes. Substituting Eq. 2.12 into Eq. 2.11, we obtain the binding energy of the envelope in the shell approximation:

$$E_{\rm bin} \sim -G\frac{M_e(\frac{M_e}{2}+M_c)}{\lambda R}. \tag{2.13}$$

This expression is different from all of the ones used before (the numerator of our expression is the lowest) although our expression is actually quite similar to that used by Webbink (1984).

2.2.3 The thermal energy

The virial theorem can be used to quantify another source of energy that may play a role in the CE interaction, namely the thermal energy of the envelope (Webbink, 2008). The familiar identity $2K + U$=0, where K is the total thermal, or kinetic energy[2] of the star and U is its potential (binding) energy, accurately represents the global properties of the entire star. If we only include the stellar envelope, rather than the entire star, the virial theorem takes a slightly different form (for the derivation see Webbink 2008):

$$2K_{\rm env} + 4\pi R_c^3 P_c + E_{\rm bin,env} = 0, \tag{2.14}$$

[2]Throughout this paper we will keep referring to the energy due to the thermal motion of the particles as the thermal energy. This will avoid confusion with the energy stored in the bonds of atoms and molecules, called the internal energy by Webbink (2008).

	RGB	AGB
$2U_{\rm env}$ (ergs)	0.9983×10^{48}	2.7101×10^{47}
$4\pi R_c^3 P_c$ (ergs)	0.0532×10^{48}	0.1365×10^{47}
$2U_{\rm env} + 4\pi R_c^3 P_c$ (ergs)	1.0516×10^{48}	2.8466×10^{47}
$E_{\rm bin,env}$ (ergs)	-1.0433×10^{48}	-2.8348×10^{47}
error without extra term	4 %	4 %
error with extra term	0.8 %	0.4 %

Table 2.1 Error on the virial theorem calculations for the entire star using the 2 $M_\odot$ model. The R_c values are defined by the left over mass criterion in § 2.2.5.

where $K_{\rm env}$ is the thermal energy of the envelope only, and we now use $E_{\rm bin,env}$ to represent the binding energy of the envelope only; R_c and P_c are the values of the radius and the pressure at the core-envelope boundary, respectively (defined in § 2.2.5).

We can show that the extra term ($4\pi R_c^3 P_c$) can be neglected, by integrating stellar structure models (whose details will be given in § 2.2.5). We use a 2 $M_\odot$ main sequence model evolved to the RGB and AGB phases. The total stellar binding energy is integrated using the denominator in Eq. 2.16. A similar equation is used to determine the total thermal energy of the stellar models:

$$U = \sum_{r_i=R_c}^{R} \frac{3}{2} P(r_i) 4\pi r_i^2 \Delta r_i, \tag{2.15}$$

where r_i is the radius of the i^{th} concentric shell, Δr_i are the shell's thickness, and $P(r_i)$ is the pressure in the shell. R_c is the core-envelope boundary radius chosen according to the criteria explained in § 2.2.5.

We see (Table 2.1) that the first two terms in Eq. 2.14 do equate to the third term to within less than 1% for both the RGB and AGB models. We also see that not including the second term, still results in an acceptable equality between twice the thermal energy and the gravitational binding energy of the envelope. In this way we have a very simple way to account for the thermal energy of the stellar envelope in the CE energy budget: the thermal energy is simply one half of the binding energy. Since the two energy sources have opposite signs, the effect of accounting for the thermal energy is to "fill" the stellar envelope potential well, or make the envelope lighter.

Finally, one should remember that there is another possible energy source: the dissociation and ionisation energy of the envelope. This was discussed by Han et al. (1995) and Webbink (2008). We will return to this topic in § 2.4.

Criterion:	Density	X_H=0.1	Shell	Remnant Env.
		RGB		
M_c ($M_\odot$)	0.314	0.313	0.313	0.314
R_c ($R_\odot$)	0.044	0.031	0.032	0.040
X_H	0.70	**0.1**	0.23	0.69
$E_{\rm bin}/10^{47}$(ergs)	−9.14	−9.62	−9.55	−9.23
λ	0.40	0.38	0.38	0.39
		AGB		
M_c ($M_\odot$)	0.537	0.534	0.534	0.534
R_c ($R_\odot$)	0.233	0.037	0.038	0.040
X_H	0.70	**0.1**	0.28	0.52
$E_{\rm bin}/10^{47}$(ergs)	−2.05	−3.06	−3.00	−2.92
λ	0.32	0.21	0.22	0.22

Table 2.2 Parameters at the core-envelope boundary according to different criteria for the 2 $M_\odot$ model on the RGB (M_1=2.0 $M_\odot$, R = 20 $R_\odot$) and AGB (M_1=1.93 $M_\odot$, R = 100 $R_\odot$).

2.2.4 The core-envelope boundary and the value of λ for different stellar models and evolutionary stages.

To locate the core-envelope boundary one could use a criterion based on density alone (called "Density" in Table 2.2), such as the radius value that minimizes $dm/d\log r$. This criterion leads to a larger radius than any criteria based on a physical argument. Aside from the criterion we have adopted (dubbed "Remnant Envelope" in Table 2.2, see also § 2.2.5), there are two additional criteria that lead to similar values of λ: (i) the radius where the abundance of hydrogen is 0.1 (this is the criterion adopted by Dewi & Tauris 2000), and (ii) the largest radius where the nuclear reaction rate decreases below a given threshold value (just outside the hydrogen-burning shell; dubbed "Shell" in Table 2.2).

Although the abundance criterion leads to a lower value of the core-envelope boundary radius, a glance at Table 2.2 shows us that the resulting values of λ are quite similar. There we list the values of the core mass, core radius and hydrogen abundance of the 2 $M_\odot$ MESA model for two key evolutionary phases, when the star is half way up the RGB (M=2.0 $M_\odot$, R=20 $R_\odot$ and τ=1.0 Gyr) and at the start of the thermally-pulsating AGB (M=1.93 $M_\odot$, R=100 $R_\odot$ and τ=1.2 Gyr), along with the derived values of the envelope binding energy and of λ.

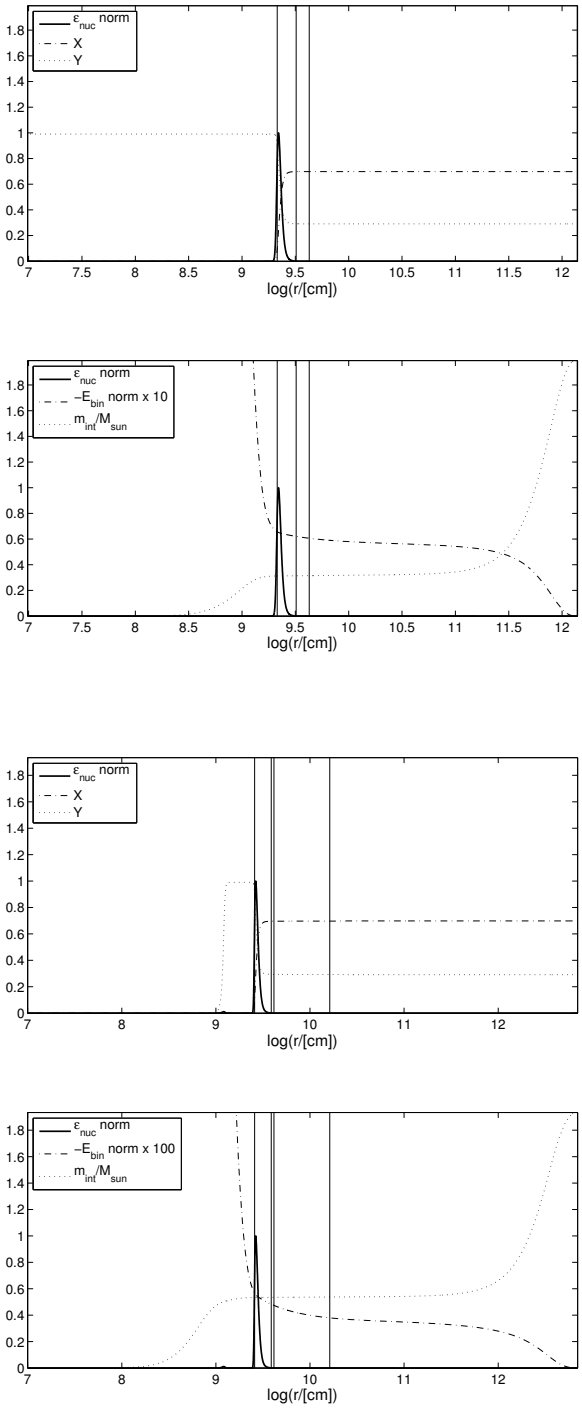

Figure 2.1 Stellar structures for an RGB star (upper panels) which had a main sequence mass of 2 $M_{\odot}$ and its AGB counterpart (bottom panels; for additional model parameters see Table 2.2). Vertical solid lines represent the core/envelope boundaries chosen according to the "$X_H = 0.1$" criterion (leftmost vertical line), "shell" criterion and "remnant envelope" criterion (second and third vertical lines from the left - overlapping in the left panels) and "density" criterion (rightmost vertical line).

2.2.5 The stellar structure parameter λ

To determine a suitable value of λ we use a 2 $M_\odot$ model calculated with the code Modules for Experiments in Stellar Astrophysics (MESA[3]; Paxton et al. 2011), evolving from the main sequence to the tip of the AGB. This new stellar evolutionary code compares well with EVOL (e.g. Herwig, 2004).

By equating the envelope binding energy obtained by numerical integration of the stellar structure and that obtained by the approximation in Eq. 2.13, we calculate λ in this way:

$$\lambda = \frac{-(GM_e/R)(M_e/2 + M_c)}{-4\pi G \sum_{r_i=R_c}^{R} m_{\rm int}(r_i)\rho_i r_i \Delta r_i}, \tag{2.16}$$

where ρ_i is the density and radius of a shell of material of thickness Δr_i and $m_{\rm int}$ is the mass internal to that radius.

The choice of a core radius based only on density (e.g., where $dm/d\log r$ reaches a minimum, see also Tauris & Dewi 2001 and Bisscheroux 1998) locates a core-envelope boundary that is quite different from any boundary located on physical grounds. We therefore chose the core-envelope boundary to be at the radius where the nuclear burning reaches a maximum *plus* the thickness of a remaining envelope of mass 10^{-3} $M_\odot$ for the 2.0 $M_\odot$ AGB model described above and 10^{-2} $M_\odot$ for the corresponding RGB model. This criterion is motivated by the fact that AGB and RGB stars depart their respective giant branches by contracting, when the envelope mass decreases below a threshold value (or, for RGB stars, when core helium is ignited; Bloecker, 1995a; Castellani et al., 2006). In a CE situation, such contraction would detach the primary from its Roche lobe and dictate the end of the interaction. This criterion leads to very similar core-envelope boundaries and values of λ to the criteria of Dewi & Tauris (2000).

With this choice of core-envelope boundary, we carried out stellar evolution calculations for main sequence masses of 1, 1.5, 2, 2.5, 3, 4 and 5 $M_\odot$. For each of these models, we determined λ for a few stellar structure models clustered on the RGB and AGB. The results are summarized in Table 2.3. For each main sequence mass, we list the numbers of stellar structures used in determining the average value of λ, the smallest and largest stellar radius for the models in each cluster and finally the average value of λ as well as the 1-σ spread of values. The minimum and maximum radii

[3]mesa.sourceforge.net

on the RGB and AGB for each model cluster were chosen as follows: the minimum radii were those of the first model that had developed a clear shell burning structure (hydrogen for the RGB and helium for the AGB). The maximum values were the maximum RGB and AGB radius values for the respective models. The value of λ does not vary significantly within each cluster, despite the relatively large radius range, because the mass is centrally concentrated.

We have fitted the average λ values as a function of main sequence mass (Fig. 2.2) and obtained the resulting fit parameters:

$$\lambda_{\rm RGB} = (0.547 \pm 0.068) \times \left(\frac{M_{\rm MS}}{\rm M_\odot}\right)^{(2.11\pm0.12)} \times \exp\left(-M_{\rm MS}/M_\odot\right) \tag{2.17}$$

and

$$\lambda_{\rm AGB} = (0.237 \pm 0.021) + (0.032 \pm 0.006) \times \frac{M_{\rm MS}}{\rm M_\odot}, \tag{2.18}$$

which are valid for 1.0 $M_\odot \leq M_{\rm MS} \leq$ 5.0 $M_\odot$. By calculating the value of λ for each of our systems using the expression:

$$\lambda^{-1} \sim 3.000 - 3.816M_e + 1.041M_e^2 + 0.067M_e^3 + 0.136M_e^4$$

of Webbink (2008), we obtain much larger values.

Finally, we comment on the fact that in our static calculation of the binding energy we assume that the envelope that needs to be ejected is the same as the mass above the core-envelope boundary just discussed. This assumption does not take into account that in an evolving, mass-losing and expanding giant, the actual mass left on the star after termination of the AGB may not be exactly that which we accounted for in our static calculation. Deloye & Taam (2010) calculate the adiabatic mass-loss response of the primary. They explain that massive stars – they show the case of a 10 $M_\odot$ – have a shallow entropy gradient in the core/envelope region, and this can lead to a 30% difference between the donor's post-CE remnant mass and M_c. However, for the lower mass stars we are interested in, the gradient is much steeper and the two masses are similar. The other concern is that the binding energy as we calculate it, does not take into account the work done by the envelope throughout the adiabatic mass-loss. However, according to Ge et al. (2010), including this effect does not make a large difference on the binding energy (see their Section 4 and their Equations 62

$M_{\rm MS}$ ($M_\odot$)	# of models in cluster	$R_{\rm min}$ ($R_\odot$)	$R_{\rm max}$ ($R_\odot$)	λ
		RGB		
1	6	20	120	0.175 ± 0.055
1.5	6	20	120	0.275 ± 0.049
2	4	20	80	0.352 ± 0.030
2.5	5	10	30	0.300 ± 0.028
3	4	10	40	0.218 ± 0.063
4	5	10	50	0.146 ± 0.032
5	4	20	80	0.121 ± 0.014
		AGB		
1	4	150	300	0.203 ± 0.073
1.5	6	150	400	0.291 ± 0.047
2	7	50	350	0.302 ± 0.052
2.5	6	50	300	0.344 ± 0.039
3	7	50	350	0.330 ± 0.047
4	9	100	500	0.369 ± 0.047
5	8	150	500	0.393 ± 0.027

Table 2.3 Average values of λ calculated for clusters of models equally distributed in radius between $R_{\rm min}$ and $R_{\rm max}$, on the RGB and AGB

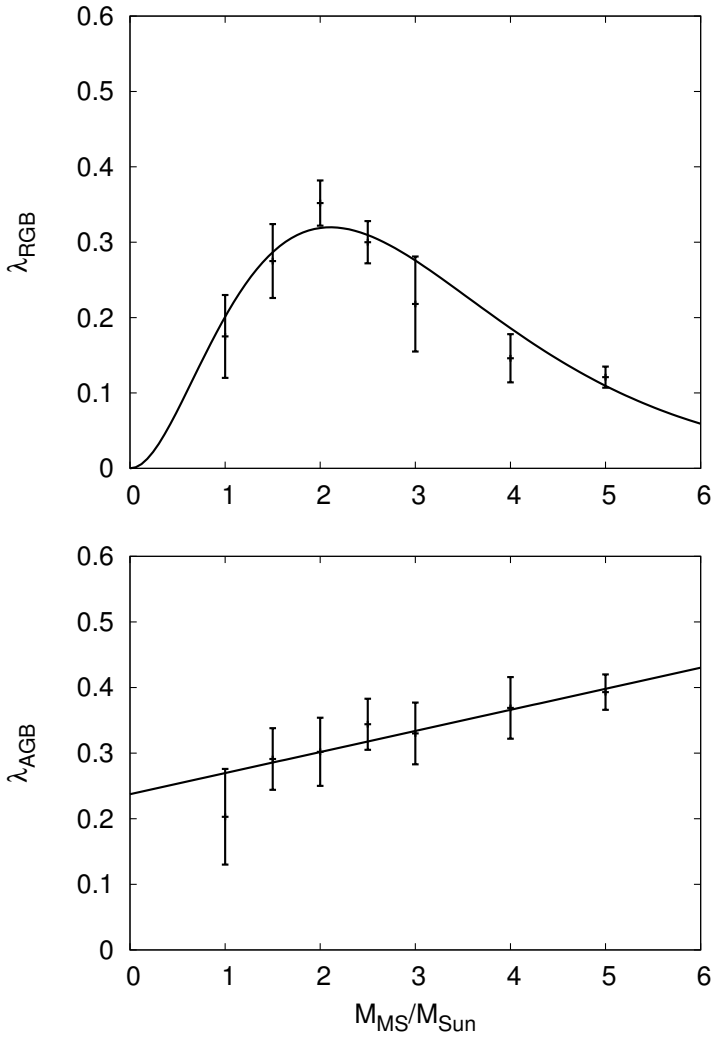

Figure 2.2 The average value of λ (symbols with error bars) calculated for clusters of models on the RGB (top panel) and AGB (bottom panel) as a function of main sequence mass, along with the best fits (solid lines)

and 83).

2.3 The determination of α using simulations and observations

Here we calculate α for observed post-CE binary systems as well as for a set of CE simulations. To do so, we use our approximation (Eq. 2.6) together with the value of λ determined from the fits in § 2.2.5 (Eqs. 2.17 and 2.18).

2.3.1 The pre-CE giant reconstruction technique

We assume that observed post-CE systems with $M_c \geq 0.47\ M_\odot$ have suffered a CE interaction on the AGB and those with $M_c < 0.47\ M_\odot$ have suffered an interaction on the RGB. The latter assumption is not strictly correct, because more massive primaries can have a core mass >0.47 $M_\odot$ during the RGB ascent (see for instance the 5 $M_\odot$ model in Fig. 2.6). However, our assumption is approximately correct because lower mass stars ($\lesssim 2.5\ M_\odot$), which are statistically more common, have cores in the 0.47-0.62 $M_\odot$ range only during their AGB ascent. In § 2.3.4 we discuss this topic further.

Of the post-AGB primaries ($M_c \geq 0.47\ M_\odot$), some are surrounded by a PN, guaranteeing that the system only emerged from the CE interaction recently (or the PN, which has a lifetime of $\lesssim$100 000 years, would not be visible). When a PN is lacking, there is a chance that the time since the CE interaction might be sufficiently long to have allowed the evolution of the system's orbital period. In order to avoid such systems we use the binary post-CE list of Schreiber & Gänsicke (2003) and Zorotovic et al. (2010), who determined which post-CE systems have the same period today as they had when they emerged from the CE.

Once the RGB or AGB origin of the primary is determined, the radius and mass of the giant at the time of the CE interaction can be estimated. For post-RGB primaries, the radius has traditionally been obtained by the core mass-radius relation of Iben & Tutukov (1985, $R \sim 10^{3.5} M_c^4$). RGB masses at the time of the CE interaction cannot be determined from the core mass alone, so a range has to be adopted (e.g., Nelemans et al., 2000)

To determine the pre-CE radius and mass for primaries that went through the interaction on the AGB, several studies (e.g., Afşar & Ibanoğlu, 2008) used the core

mass-luminosity relation for post-AGB stars (e.g., Vassiliadis & Wood, 1994, $L/\mathrm{L}_{\odot} = 56694(M_c/\mathrm{M}_{\odot} - 0.5)$) to determine the luminosity of the primary at the time of the CE interaction. They then used the initial-to-final mass relation to determine the main sequence progenitor mass of today's primary, to then determine the mass of the primary at the time of the CE interaction (e.g., Vassiliadis & Wood, 1994). Once the primary's mass and luminosity at the time of the CE interaction have been determined, the radius can be found using the fitting relation of Hurley et al. (2000, $R = 1.125 M_1^{-0.33}(L^{0.4} + 0.383 L^{0.76})$). This method cannot be applied to primary stars with core mass $\lesssim 0.55\ M_{\odot}$, because below that value the core mass-luminosity relation of Vassiliadis & Wood (1994) becomes extremely imprecise and for core masses $\leq 0.5\ M_{\odot}$, the stellar luminosity becomes negative. Finally, using the initial-to-final mass relation in this way is incorrect, because the CE interaction interrupted the evolution of the primary and the growth of its core, resulting in a less massive core (i.e., smaller final mass) than if the star had been single.

By studying the relations used in the past one realises that reconstructing the giant's mass and radius using only the mass of the post-CE primary (assumed to have been the mass of the core of the giant), is fundamentally a statistical process. Each relation appears to state that the error on a given quantity, e.g., the giant radius at the time of the CE interaction, depends solely on the error on the measured core mass. However, this error propagation does not include the error in the fit, i.e., the error in the relations themselves. Nor is the error in the assumptions used to establish the relations quantified. We therefore diverge from previous methods, and recalculate the fitting relations from stellar evolution models. This allows us to better quantify the true uncertainty on the entire reconstruction process. In our reconstruction technique, we make use of two sets of stellar evolution calculations. The first set is from the detailed calculations of MESA for $Z = 0.01$ (§ 2.2.5). The second set is from the computations of Bertelli et al. (2008), who calculated an extensive grid of models including their metallicity dependence.

The primary mass at the time of the CE interaction

To determine the mass of the primary at the time of the CE interaction for the post-AGB group, we start by determining the mass of the main sequence progenitors. To do so we use the initial-to-final mass relation (IFMR) determined with the MESA code. The final mass is assumed to be the mass of the core at the first thermal pulse.

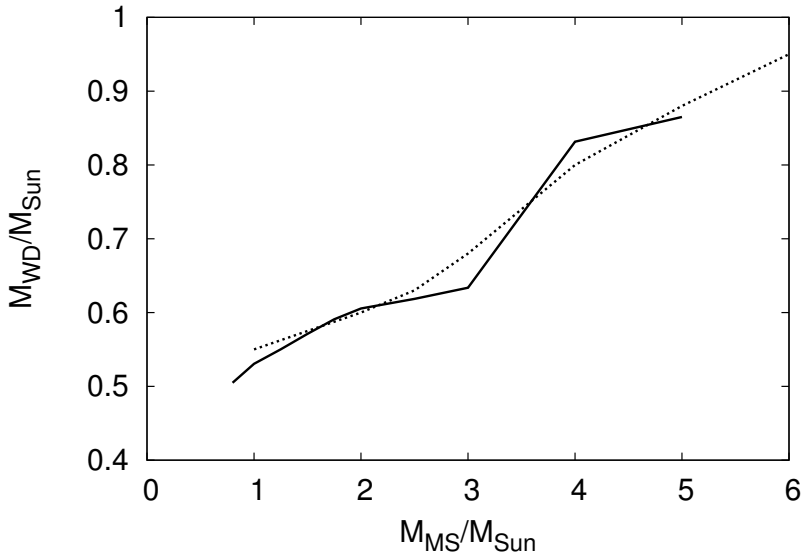

Figure 2.3 A comparison of the MESA code initial-to-final mass relation (solid line) and that determined empirically by Weidemann (2000, dashed line).

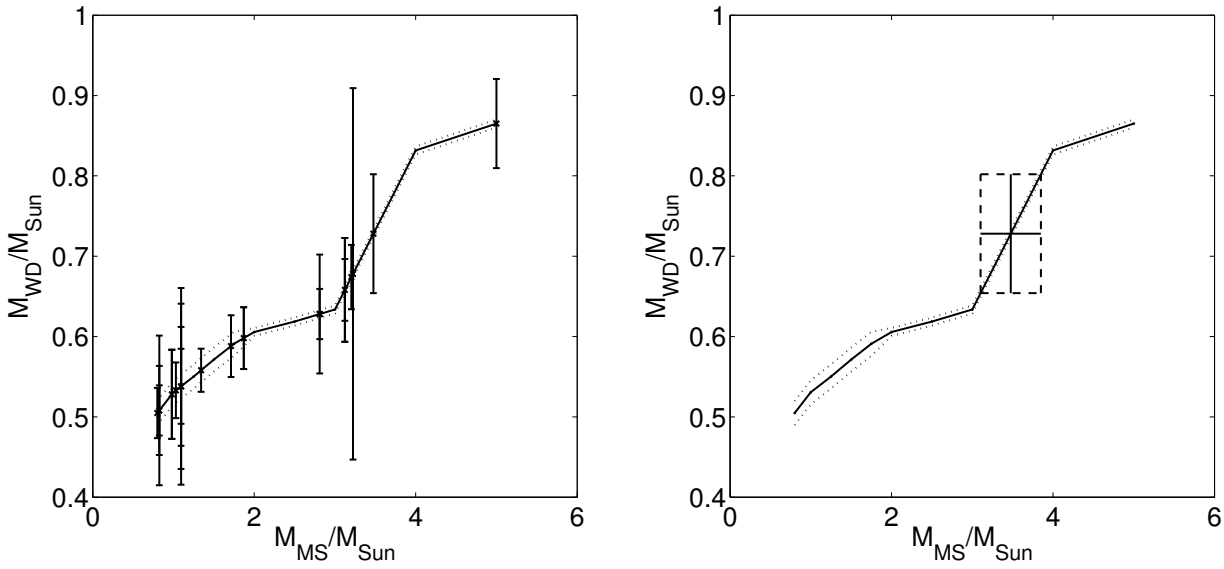

Figure 2.4 Left: the initial-to-final mass relation (IFMR) determined from the MESA code calculations, plotted together with the data and their error bars (Table 2.4). The dotted lines delimit the estimated error on the IFMR itself. Right: the IFMR plotted with the data point for BE UMa to exemplify our determination of the error on the derived main sequence masses.

Although this may appear as an under estimate of the final mass, it is accurate for core mass values $\lesssim 0.52\ M_\odot$, because low mass stars with low mass cores have low mass envelopes which get depleted rapidly by mass loss and do not give the core time to grow. Our assumption also results in good accuracy for masses $\gtrsim 0.58\ M_\odot$, because high mass stars suffer substantial dredge-up so that the core does not grow appreciably during thermal pulses. For values between 0.52 and 0.58 $M_\odot$, the core could grow slightly above the value that we are using, resulting in a slight overestimate of the initial mass. However this uncertainty is very small compared to the very large uncertainty on the core mass, as we explain below.

Older predictions for the IFMR (e.g., Bloecker, 1995a; Vassiliadis & Wood, 1994) compare well to the MESA IFMR for lower initial masses ($\lesssim$3 $M_\odot$), while for the larger initial masses the more recent MESA IFMR yields higher WD masses (also observed by Han et al. 1994). The reason is that the new MESA models include convective core overshooting during the main sequence, which increases the core mass predictions compared to the older models. However, at low initial mass, models now show efficient third dredge-up, which compensates for the core mass increase from core overshooting. For more massive AGB stars the third dredge-up does not play a significant role in the core mass prediction, and the core mass difference from core overshooting assumptions can be observed. The MESA IFMR compares well with the observationally derived IFMR of Weidemann (2000, Fig. 2.3), although the observational IFMR has a large scatter.

For each system's primary we obtained the main sequence mass of its progenitor by direct interpolation. The metallicity dependence of the IFMR is small, as can be seen by a fit to the Bertelli et al. (2008) models ($M_{WD}/M_\odot = 0.451 + 0.091 M_{\rm MS}/M_\odot - 0.044 \log Z/Z_\odot$) and we ignore it.

Before we can use the IFMR, we need to account for the fact that the IFMR relates the final WD mass, $M_{\rm WD}$, to its main sequence mass, $M_{\rm MS}$, only if the star evolved to the *natural* termination of its AGB life. The CE interaction interrupted the regular AGB evolution and core growth, so that the post-CE primary mass, M_c, is smaller than it would have been had the primary been single ($M_{\rm WD}$). This mass discrepancy is determined for each Bertelli et al. (2008) model, assuming that a CE will terminate the AGB evolution at a random value of R, between the maximum RGB radius and the maximum AGB radius. We use Bertelli et al. (2008) models in the mass range 0.8–2.5 $M_\odot$, and metallicity range $Z = 10^{-4} - 0.07$. On average, models depart the AGB with a mass that is $0.028 \pm 0.024\ M_\odot$ lower than if the AGB evolution had

progressed till its natural termination. The error in this value is dominated by the lack of knowledge of the precise stage at which the system departs the AGB.

We can now calculate the WD mass of each of our post-AGB, post-CE primaries and use the IFMR to determine the main sequence mass of its progenitor. The error on the WD masses is determined from the error on the measured post-CE primary masses and the error on the core growth estimation, added in quadrature. In Fig. 2.4 (left) we show the MESA IFMR with our interpolated data points and their error bars. To determine the error on the main sequence masses thus obtained, we projected the errors calculated on $M_{\rm WD}$ on the IFMR itself, as demonstrated in Fig. 2.4 (right). For three data points at the higher (V471 Tau) and lower (SDSS J0110+1326 and RR Cae) extremes of the IFMR, the errors were assumed to be the same as the *relative* error of HS 0705+6700 and SDSS J1548+4057, for the low and high mass, respectively, because these two systems have the same measurement errors and similar core mass values.

Using this error estimation method, we are not taking into account the error on the IFMR itself (plotted as a dotted curve in Fig. 2.4, from approximate estimates). If we had, the errors on the determined main sequence masses would have been only marginally larger.

The last step in the main sequence mass determination is carried out by using conditional probability considerations. For each of the three populations of post-CE binaries (the central stars of PN, the post-AGB stars with no PN and the post-RGB stars) we know the main sequence mass distribution of the progenitors from population considerations and observations (see below). To exploit this extra knowledge, we convert the progenitor main sequence mass of each system's primary, determined above from the WD mass alone (dotted vertical lines in Fig. 2.5), into a Gaussian probability distribution function (PDF), by using the error estimates (dotted curves in Fig. 2.5). We then multiply each PDF with the main sequence mass distribution for the parent population (also called the prior in Bayesian statistics; dashed curves in Fig. 2.5). This procedure results in a PDF for the "conditional" values of the main sequence masses of each of our post-CE primaries (solid curves in Fig. 2.5), from which we can determine a mean value (solid vertical lines in Fig. 2.5) and a new error estimate. These are the values we adopt for the primary progenitors' main sequence masses. We note that two identical primary masses (M_c) that have different error estimates will result in two different "conditional" main sequence progenitor masses, because of the Bayesian statistical treatment (compare HW Vir, HS0705+6700 and

MS Peg in Table 2.4). In Fig. 2.5 we show two specific cases, one for a central stars of PN, and one for a post-AGB system with no PN.

In Fig. 2.5 (dashed lines) the prior distributions are the main sequence mass distribution of the parent populations. For the central stars of PN, the progenitor main sequence mass distribution is known from population synthesis as well as observations (Moe & De Marco, 2006, dashed line in the left panel of Fig. 2.5). For the post-AGB stars with no PN, the main sequence mass distribution of the progenitors can be determined using the WD mass distribution (Kepler et al., 2007) and using the IFMR to translate the WD mass distribution into a main sequence mass distribution. The WD mass distribution of Kepler et al. (2007) is fitted by three Gaussian curves with different means and standard deviations. The Gaussian curve with the lowest mean mass corresponds to the helium WDs and we ignore it. To represent the WD mass distribution corresponding to the post-AGB stars (with no PN), we only use the remaining two Gaussian curves combined (with mean masses of 0.578 and 0.678 $M_{\odot}$, respectively, standard deviations 0.047 and 0.148 $M_{\odot}$, respectively and relative strength 2.9:1)[4].

For the post-RGB group we cannot use the IFMR, because the primaries have not been through the AGB evolution. For all post-RGB primaries, we therefore use the initial mass function ($\propto M^{-2.35}$; Kroupa 2000), truncated between 0.78 and 2.3 $M_{\odot}$ (Nelemans et al., 2000). This distribution results in a mean value accompanied by an error (1.19$\pm$0.40 $M_{\odot}$).

Once we have calculated the primaries' progenitors main sequence masses, we can derive the mass of the primary at the time of the CE interaction (M_1), by determining how much mass the star lost between the main sequence and the time of the CE interaction on the RGB or AGB. The stellar evolutionary calculations of Bertelli et al. (2008) for a range of masses and metallicities are used once again to average the RGB and AGB stellar masses using uniform weighting with respect to radius (for the AGB, we used only the values for which the radius was larger than the maximum radius attained on the RGB). The values thus obtained are $M_1/M_{\rm MS} = 0.98\pm0.02$ for post-RGB stars and 0.87$\pm$0.07 for post-AGB stars, where the errors are derived from

[4]We note that this prior is not entirely correct, because CE interactions on the AGB happen slightly more frequently to relatively more massive stars. This is because lower mass stars grow to relatively larger radii while on the RGB, increasing the chance that an interaction will happen on the RGB rather than the AGB. As a result the priors for the post-AGB, post-CE binary populations should be slightly weighted towards more massive stars. To calculate the correct priors would entail a complete population study, which we have not carried out here.

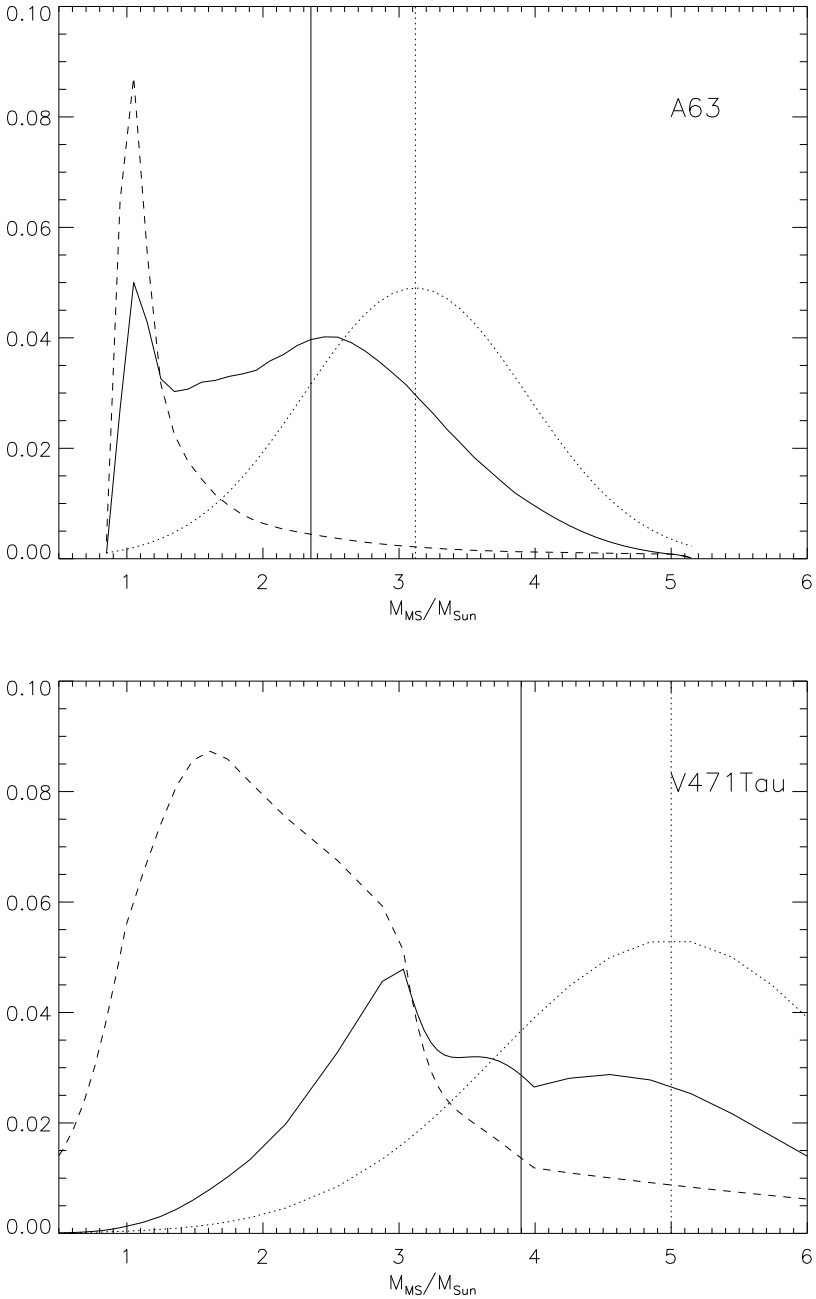

Figure 2.5 The main sequence mass (solid vertical lines) determined for two of our post-CE primaries: A 63, a central star of PN (top) and V471 Tau, a post-AGB star (bottom). These masses are the means derived from statistical distributions (solid curves), that are the result of a convolution of the Gaussian mass obtained from the IFMR (dotted curve with the mean plotted as dotted vertical lines) and the Baysian prior distributions (dashed lines). These latter distributions are the mass distributions of the progenitors of the two types of objects, the central stars of PN (top) and the post-AGB stars with no PN (bottom).

the scatter on the fit. We then considered that the presence of a companion would stimulate mass-loss prior to the CE interaction (e.g., Bear & Soker, 2010), so we lowered these numbers slightly and raised the uncertainty: $M_1/M_{\rm MS} = 0.90\pm0.10$ for RGB systems and 0.75 ± 0.15 for AGB ones. Once again, the dependence on the mass and metallicity is not what dominates the error, but rather the lack of knowledge of what stage during the RGB or AGB evolution the systems enter the CE phase.

The primary radius at the time of the CE interaction

We next determined the radii of the giants at the time of the CE interaction. From the MESA calculations we know the radius evolution as a function of the mass of the hydrogen-exhausted core (Fig. 2.6). We first selected the track corresponding to the main sequence progenitor's mass of each of our post-CE primary stars (§ 2.3.1); we then read from the plot the radius corresponding to today's core mass. This is the radius of the giant at the time of the CE interaction. The error on this radius has to be determined taking into account the errors for both the measured core mass *and* the derived main sequence mass. Considering each error bar in turn results in new radius values, from which we can estimate the final error on the radius. There is, however, one additional complication. The radius evolution of each model is complex and non-monotonic. This means that we need to use logical arguments to consider each radius value obtained in this way: a star can only be caught in a CE interaction while its radius is growing *and* if it is larger than at any time in the past. Once all these conditions are accounted for, it is found that the range of possible radii corresponding to each of our systems is quite large and that it is no less accurate to use fits of the core mass vs. radius values from the Bertelli et al. (2008) calculations, for the usual ranges of masses and metallicities:

$$R = 440 R_\odot (M_{\rm MS}/M_\odot)^{-0.47} (M_c/(0.6 M_\odot))^{5.1} (Z/Z_\odot)^{0.15}, \tag{2.19}$$

where the *rms* error on the fit is $\pm 50\ \ R_\odot$. Or, evaluating R in terms of M_1 instead of $M_{\rm MS}$:

$$R = 440 R_\odot (M_1/M_\odot)^{-0.54} (M_c/(0.6 M_\odot))^{5.0} (Z/Z_\odot)^{0.14}, \tag{2.20}$$

with the same fit scatter. We note that this relation applies equally to the post-RGB and post-AGB stars, although the fit was technically carried out for the AGB phase only. These fits are over-plotted on the detailed MESA calculation in Fig. 2.6. As can

be seen from Fig. 2.6, the radius values implied by our approximate fits and the range of radii one would derive using the detailed MESA tracks become quite different for larger main sequence masses. The most massive of our systems, V 471 Tau, with a core mass of 0.84 $M_{\odot}$, has a conditional main sequence mass of 3.9 $M_{\odot}$. Using the MESA tracks one derives a radius at the time of the CE interaction of 435±100 $R_{\odot}$. The value derived instead from the fits is 570±62 (see Table 2.4). These two values are quite different, although they are consistent within the uncertainties. Pre-empting our results from § 2.3.4, the MESA radius value results in α=0.28±0.16, while using the radius fit from Eq. 2.20 α=0.21±0.15. We therefore see that even for the worse case scenario of the system with the largest mass, the advantage of using the detailed MESA code for this purpose is limited.

Finally, as we did for the case of the main sequence mass, we combine these radius values and their formal errors with the prior knowledge that for our primaries' progenitor populations, the radii of the RGB primaries should be in the range 10–300 $R_{\odot}$, while for the AGB primaries they should be in the range 50–650 $R_{\odot}$(Bertelli et al., 2008), in the usual mass and metallicity ranges. The maximum RGB radius of 300 $R_{\odot}$, and maximum AGB radius of 650 $R_{\odot}$, are the maximum radii achieved by any model in the set considered. The minimum radius value adopted for the AGB (50 $R_{\odot}$) was selected because it is the smallest of all maximum RGB radii, achieved by any of the considered models. The minimum RGB radius (10 $R_{\odot}$) is the approximate radius that separates Hertzsprung gap from RGB models for the Bertelli et al. (2008) tracks. Convolution with the prior results in a new radius value and a new error, according to Bayesian statistics.

2.3.2 Observed systems used in the determination of α

In Table 2.4 we list the values of M_c, M_2, P and A_f determined from observations as well as the values of M_1 and R deduced from stellar evolution in § 2.3.1. References for the observed values can be obtained from De Marco (2009), for central stars of PN. Of all the ∼40 post-CE binary central stars listed by De Marco (2009) only 6 central stars with non-degenerate secondaries have sufficient information to be useful in the present study. For the observed post-CE binary in the centre of PN NGC 6337 we list two sets of parameters in Tables 2.4 and 2.5. When we fit the value of α (§ 2.3.4), we use only one set (that with $M_2 = 0.35\ M_{\odot}$). The fit with the alternative

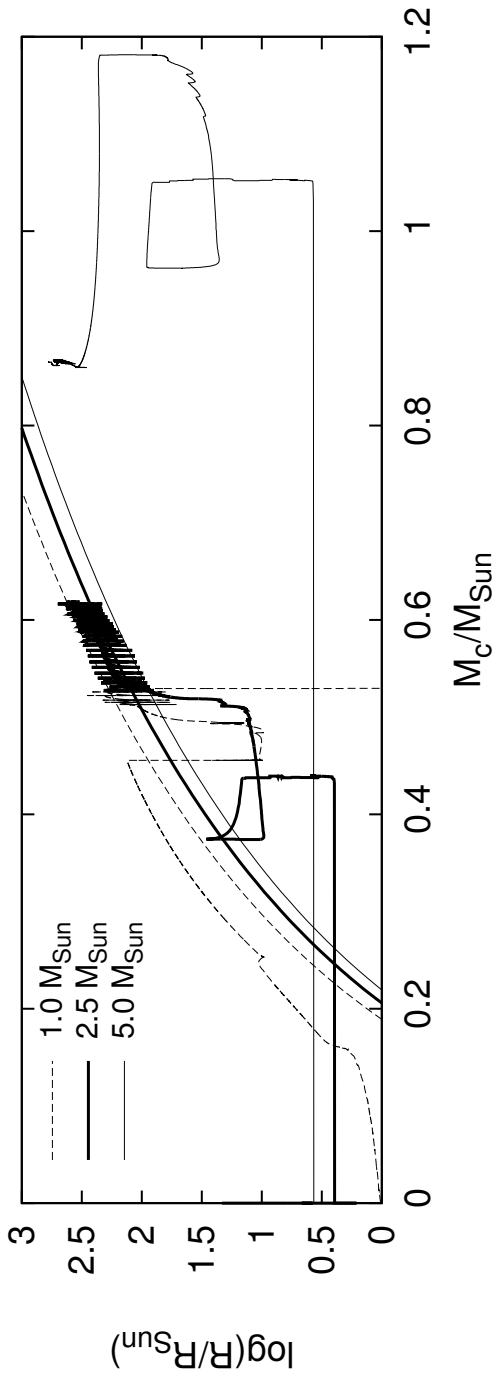

Figure 2.6 Stellar evolutionary tracks on the core mass vs. stellar radius plane for 1 $M_\odot$, 2.5 $M_\odot$ and 5 $M_\odot$(thick solid, dashed and thin solid lines, respectively) calculated with the MESA code, accompanied by fits to the Bertelli et al. (2008) tracks (smooth curves, Eq. 2.19) for the same three masses.

set, results in very similar fit parameters. Finally, for the binary system in the PN HFG 1 there also are two sets of parameters (De Marco, 2009). We use the set with the most massive companion, $M_2 = 1.09\ M_\odot$, because a recent analysis of X-ray radiation (Montez et al., 2010) finds this system's companion to be coronally active and the only way to reproduce the X-ray luminosity is to have a companion at least as massive as a $\sim 1\ M_\odot$ main sequence star.

Other post-CE binaries are primarily from the list of Schreiber & Gänsicke (2003, where we selected only those systems that have not suffered substantial reduction of the orbital period after emerging from the CE). Wherever parameters have been updated by new measurements of Zorotovic et al. (2010), we have adopted the revisions. From the extensive list of *Sloan Digital Sky Survey* post-CE binaries in Zorotovic et al. (2010), we only use the systems SDSS J1548+4057, SDSS J0110+1326 and SDSS J1435+3733 (for more discussion, see § 2.5). Finally, we have also considered AA Dor and HD 149382, because of their low mass secondaries. Whenever errors were not given in the cited references, we have assumed an error of 20% on both primary and secondary masses. In Table 2.5 we list the calculated values of q $(=M_2/M_1)$ and α, determined using Eq. 2.6, along with their uncertainties, both in linear and logarithmic form. We also list values of α determined using the Webbink (2008) relation.

2.3.3 The simulations used in the determination of α

Hydrodynamic simulations, carried out both with smooth particle hydrodynamics (e.g. Terman & Taam, 1996) or grid methods (e.g., Sandquist et al., 1998), are a tool to determine the value of α *ab initio*. These simulations start by mapping a giant star into the simulation domain. The quantities describing the star (i.e., density, temperature, internal energy, etc.) are calculated using a one-dimensional stellar evolution model. The companion is represented by a point mass, as is the compact core of the giant. The physics included in the simulation is typically only the gravitational attraction of all the masses involved. The interaction timescale is short enough that radiation transport can be neglected (e.g., see discussion in Sandquist et al. 1998). The in-spiral of the companion is typically followed until the resolution of the grid becomes insufficient, which may or may not be at the termination of the CE interaction (i.e., when sufficient mass has become unbound from the system to

Name	Type[1]	M_c ($M_\odot$)	M_2 ($M_\odot$)	P (days)	A_f ($R_\odot$)	M_{MS} ($M_\odot$)	M_1 ($M_\odot$)	R ($R_\odot$)
BE UMa	CSPN	0.70± 0.07	0.36± 0.07	2.29	7.5± 0.7	3.4± 0.4	2.5± 0.6	440± 131
A 46	CSPN	0.51± 0.07	0.15± 0.02	0.47	2.2± 0.2	1.2± 0.3	0.90± 0.29	239± 140
A 63	CSPN	0.63± 0.06	0.29± 0.04	0.46	2.4± 0.2	2.4± 0.9	1.8± 0.8	376± 140
HFG 1	CSPN	0.57± 0.10	1.1± 0.1	0.58	3.5± 0.4	1.4± 0.5	1.1± 0.4	316± 172
DS 1	CSPN	0.63± 0.03	0.23± 0.01	0.36	2.0± 0.1	3.0± 0.4	2.2± 0.5	348± 93
NGC 6337	CSPN	0.60± 0.07	0.35± 0.04	0.17	1.3± 0.1	1.8± 0.8	1.4± 0.7	346± 152
			(0.20±0.03)		(1.2±0.1)			
V471 Tau	pAGB	0.84± 0.05	0.93± 0.10	0.52	3.3± 0.2	3.9± 1.3	2.9± 1.1	570± 62
UZ Sex	pAGB	0.65± 0.23	0.22± 0.05	0.60	2.8± 0.8	2.4± 1.1	1.8± 0.9	322± 194
SDSS J1548+4057	pAGB	0.65± 0.03	0.17± 0.03	0.19	1.3± 0.1	3.1± 0.2	2.3± 0.5	383± 99
RE J1016-053	pAGB	0.60± 0.02	0.15± 0.02	0.79	3.3± 0.1	2.6± 0.5	1.9± 0.6	288± 66
Feige 24	pAGB	0.57± 0.03	0.39± 0.02	4.23	10.9± 0.4	1.9± 0.6	1.4± 0.5	266± 85
IN CMa	pAGB	0.57± 0.03	0.43± 0.03	1.26	4.9± 0.2	1.9± 0.6	1.4± 0.5	266± 85
RE J2013+400	pAGB	0.56± 0.03	0.18± 0.04	0.71	3.0± 0.2	1.8± 0.6	1.4± 0.5	250± 81
NN Ser	pAGB	0.53± 0.01	0.12± 0.03	0.13	0.94± 0.05	1.4± 0.3	1.1± 0.3	199± 38
GK Vir	pAGB	0.51± 0.04	0.10± 0.01	0.34	1.7± 0.1	1.3± 0.4	1.0± 0.3	197± 84
Hz 9	pAGB	0.51± 0.10	0.28± 0.04	0.56	2.6± 0.4	1.7± 0.7	1.2± 0.5	245± 161
AA Dor	pAGB	0.51± 0.12	0.085± 0.027	0.26	1.4± 0.3	1.7± 0.7	1.3± 0.6	256± 172
BPM 6502	pAGB	0.50± 0.05	0.17± 0.01	0.34	1.8± 0.1	1.2± 0.4	0.90± 0.32	198± 101
PG 1017-086	pAGB	0.50± 0.05	0.078± 0.006	0.07	0.64± 0.05	1.2± 0.4	0.90± 0.32	198± 101
NY Vir	pAGB	0.50± 0.05	0.15± 0.02	0.10	0.79± 0.07	1.2± 0.4	0.90± 0.32	198± 101
SDSS J1435+3733	pAGB	0.50± 0.03	0.22± 0.03	0.13	0.95± 0.05	1.1± 0.3	0.85± 0.27	181± 54
HW Vir	pAGB	0.48± 0.09	0.14± 0.02	0.12	0.86± 0.13	1.2± 0.4	0.90± 0.36	224± 150
HS 0705+6700	pAGB	0.48± 0.05	0.13± 0.03	0.10	0.75± 0.07	1.0± 0.3	0.74± 0.25	181± 95
MS Peg	pAGB	0.48± 0.02	0.22± 0.02	0.17	1.1± 0.0	0.88± 0.14	0.66± 0.17	154± 39
SDSS J0110+1326	pAGB	0.47± 0.02	0.31± 0.05	0.33	1.9± 0.1	0.85± 0.13	0.64± 0.16	141± 36
LM Com	pRGB	0.45± 0.05	0.28± 0.05	0.26	1.5± 0.1	1.2± 0.4	1.1± 0.4	116± 61
RR Cae	pRGB	0.44± 0.02	0.18± 0.01	0.30	1.6± 0.1	1.2± 0.4	1.1± 0.4	89± 29
HD 149382	pRGB	0.47± 0.12	0.015± 0.007	2.39	5.9± 1.5	1.2± 0.4	1.1± 0.4	136± 91
HR Cam	pRGB	0.41± 0.01	0.10± 0.01	0.10	0.72± 0.02	1.2± 0.4	1.1± 0.4	59± 13
CC Cet	pRGB	0.39± 0.10	0.18± 0.05	0.28	1.5± 0.3	1.2± 0.4	1.1± 0.4	96± 82
WD 0137-349	pRGB	0.39± 0.04	0.052± 0.005	0.08	0.60± 0.05	1.2± 0.4	1.1± 0.4	54± 26
DeMa [2]	Sim	0.60	0.10	30	36	1.20	1.0	645
Sand1-2 [2]	Sim	0.70	0.40	1.08	4.56	3.18	2.8	190
Sand3 [2]	Sim	1.00	0.40	0.90	4.39	5.29	4.6	190
Sand4 [2]	Sim	1.00	0.60	0.96	4.79	5.29	4.6	190
Sand5 [2]	Sim	0.94	0.60	2.48	8.90	5.31	4.6	353

[1]CSPN: the primary is a central star of PN and went through the AGB evolution; pAGB: the primary does not have a PN, but we consider it as a post-AGB star; pRGB: the primary is considered as having suffered a CE interaction on the RGB and never having ascended the AGB; Sim: simulations.
[2]DeMa: De Marco et al. (2003). Sand: Sandquist et al. (1998), simulations. The number indicates the particular simulation, and follows the scheme of their Table 1. See also text in § 2.3.3.

Table 2.4 The observationally-derived quantities for our post-CE systems (M_c, M_2 and P) listed alongside the quantities derived from orbital, stellar evolution and population considerations (A_f, M_1 and R). Simulation inputs (M_c, M_2, M_1 and R) and outputs (P and A_f) are also listed. All these quantities are inputs to the α equation (Eq. 2.6). Parameters in brackets are an alternative set not used in the fits (see § 2.3.2)

Name	Type[1]	$\log q$	$\log \alpha$	q	α	α(Web)
BE UMa	CSPN	-0.85± 0.12	0.08± 0.25	0.14± 0.04	1.2± 0.7	1.1
A 46	CSPN	-0.78± 0.13	-0.45± 0.34	0.17± 0.05	0.35± 0.31	0.24
A 63	CSPN	-0.78± 0.17	-0.54± 0.34	0.16± 0.06	0.29± 0.25	0.23
HFG 1	CSPN	0.01± 0.16	-1.06± 0.35	1.0± 0.4	0.087± 0.080	0.043
DS 1	CSPN	-0.99± 0.10	-0.29± 0.23	0.10± 0.02	0.51± 0.28	0.46
NGC 6337	CSPN	-0.59± 0.18	-1.01± 0.36	0.26± 0.11	0.10± 0.09	0.068
		(-0.83± 0.19)	(-0.83±0.34)	(0.15±0.06)	(0.15±0.14)	(0.11)
V471 Tau	pAGB	-0.50± 0.15	-0.68± 0.30	0.32± 0.11	0.21± 0.15	0.17
UZ Sex	pAGB	-0.91± 0.20	-0.24± 0.45	0.12± 0.06	0.57± 0.70	0.37
SDSS J1548+4057	pAGB	-1.13± 0.10	-0.32± 0.22	0.074± 0.018	0.48± 0.26	0.31
RE J1016-053	pAGB	-1.11± 0.12	0.13± 0.25	0.078± 0.023	1.3± 0.8	0.85
Feige 24	pAGB	-0.56± 0.14	0.08± 0.29	0.27± 0.09	1.2± 0.9	0.86
IN CMa	pAGB	-0.52± 0.14	-0.32± 0.30	0.30± 0.10	0.47± 0.35	0.35
RE J2013+400	pAGB	-0.88± 0.16	-0.16± 0.31	0.13± 0.05	0.69± 0.53	0.44
NN Ser	pAGB	-0.94± 0.15	-0.54± 0.25	0.11± 0.04	0.29± 0.18	0.17
GK Vir	pAGB	-0.98± 0.13	-0.22± 0.30	0.10± 0.03	0.60± 0.45	0.34
Hz 9	pAGB	-0.65± 0.17	-0.40± 0.41	0.22± 0.09	0.40± 0.43	0.28
AA Dor	pAGB	-1.17± 0.20	-0.16± 0.44	0.07± 0.03	0.69± 0.81	0.40
BPM 6502	pAGB	-0.72± 0.13	-0.47± 0.33	0.19± 0.06	0.34± 0.28	0.21
PG 1017-086	pAGB	-1.06± 0.14	-0.60± 0.33	0.087± 0.027	0.25± 0.21	0.14
NY Vir	pAGB	-0.78± 0.14	-0.78± 0.33	0.17± 0.06	0.17± 0.14	0.10
SDSS J1435+3733	pAGB	-0.59± 0.13	-0.87± 0.27	0.26± 0.08	0.13± 0.09	0.084
HW Vir	pAGB	-0.81± 0.16	-0.73± 0.40	0.16± 0.06	0.19± 0.20	0.11
HS 0705+6700	pAGB	-0.76± 0.15	-0.82± 0.34	0.18± 0.06	0.15± 0.13	0.087
MS Peg	pAGB	-0.48± 0.11	-0.91± 0.27	0.33± 0.08	0.12± 0.08	0.074
SDSS J0110+1326	pAGB	-0.31± 0.12	-0.82± 0.28	0.49± 0.13	0.15± 0.11	0.10
LM Com	pRGB	-0.58± 0.15	-0.43± 0.34	0.26± 0.09	0.37± 0.32	0.26
RR Cae	pRGB	-0.77± 0.14	-0.09± 0.29	0.17± 0.05	0.81± 0.57	0.54
HD 149382	pRGB	-1.85± 0.21	1.52± 0.47	0.014± 0.007	33± 43	16
HR Cam	pRGB	-1.03± 0.14	0.04± 0.27	0.093± 0.030	1.1± 0.7	0.68
CC Cet	pRGB	-0.77± 0.17	-0.09± 0.45	0.17± 0.07	0.82± 1.02	0.56
WD 0137-349	pRGB	-1.31± 0.14	0.30± 0.33	0.049± 0.016	2.0± 1.7	1.2
DeMa [2]	Sim	-1.02	0.53	0.096	3.4	1.8
Sand1-2 [2]	Sim	-0.84	0.34	0.14	2.2	1.6
Sand3 [2]	Sim	-1.06	0.96	0.087	9.0	6.3
Sand4 [2]	Sim	-0.88	0.82	0.13	6.6	4.8
Sand5 [2]	Sim	-0.89	0.86	0.13	7.2	5.4

[1,2]: see comments to Table 3

Table 2.5 The determined values of α, using our equation as well as that of Webbink (1984, 2008). Parameters in brackets are from an alternative sets of inputs (see Table 2.4 and § 2.3.2).

dictate the collapse of the primary and its detachment from its Roche lobe). At the end of a simulation, α can be determined by using Eq. 2.6.

We determined α from five simulations, four from Sandquist et al. (1998) and one from De Marco et al. (2003). All simulations were carried out with the Burkert & Bodenheimer (1993) code, as modified by Sandquist et al. (1998). Relevant parameters are taken from the listed publications and are reproduced in Tables 2.4 where, for the Sandquist et al. (1998) simulations, we use the same labels as in their Table 1. Their simulations 1 and 2 were identical, except for the giant envelope's rotation being either zero or synchronized with the companion's orbital motion. For these two simulations we take the average of their post-CE binary periods.

All simulations considered were stopped after orbital decay time-scales lengthened considerably, when only a very small amount of envelope mass was left inside the orbit of the companion ($\sim 10^{-4}$ – 10^{-3} $M_{\odot}$). However, in all cases a considerable amount of envelope gas was still bound to the system albeit at some distance from the core (usually outside the original giant radius and with small binding energy). Because of this left over bound envelope, we may not assume that the separation of the binary at the end of the simulation is the actual post-CE binary separation. Any envelope still bound to the system at the end of the CE will fall back onto the system to form a circumbinary disk that might have some dynamical effect on the binary period. To understand this eventuality will require further numerical simulations.

The simulations of Yorke et al. (1995) started the interaction with the companion well inside the AGB stellar envelope. This results in a negative value of α because $M_c/A_f < (M_c + M_e)/A_i$. Although they justified this initial setup by noting that spin-up only becomes important within their initial radius, when the timescale for orbital decay exceeds the orbital period, they also stated that a value for α cannot be trivially derived from their simulations, but that the values can be estimated between 0.3 and 0.6. Since it is not clear how these values were determined, we did not use their models.

Finally, we did not use the simulations of Terman & Taam (1996). They considered a 5 $M_{\odot}$ AGB giant in two different evolutionary stages. The less evolved AGB star, still at the very base of the AGB, and still undergoing core helium burning, was used to simulate a CE interaction with a 0.5 $M_{\odot}$ companion and presumably resulted in a merger. The more evolved of the two stars was used to simulate CE interactions with 0.5 and 1.0 $M_{\odot}$ main sequence companions. In neither case was the simulation followed till the end of the interaction, and a substantial amount of envelope remained

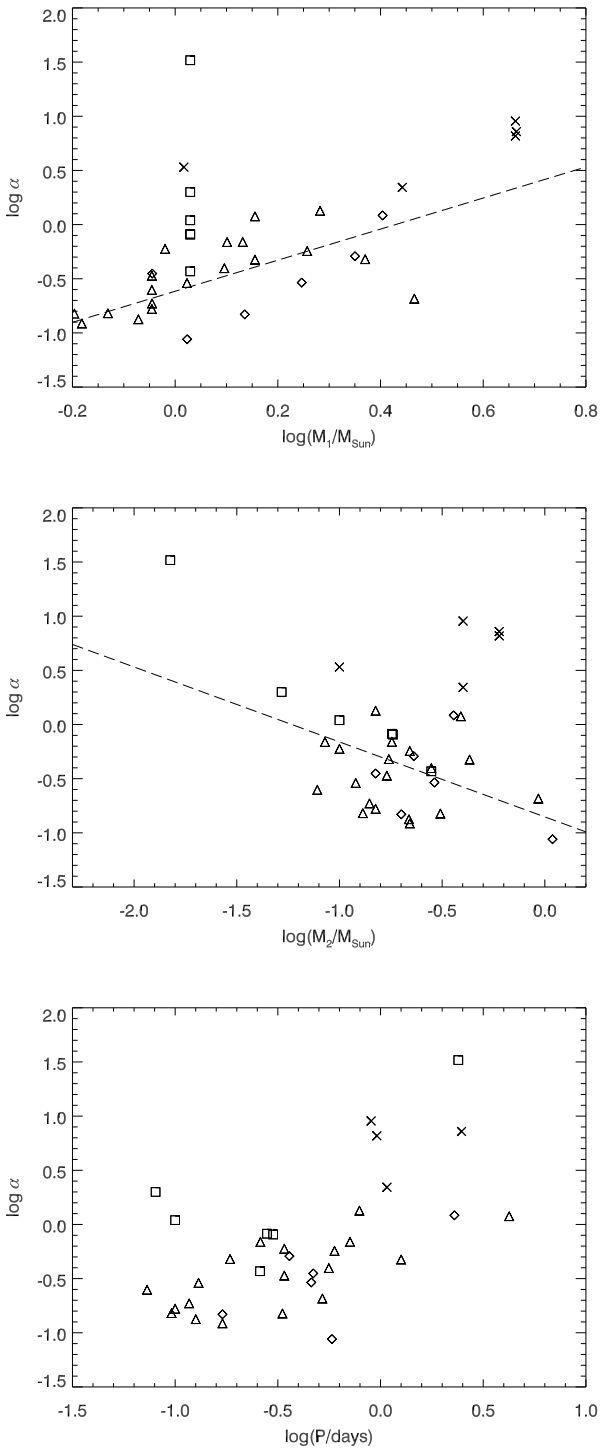

Figure 2.7 A plot of log α as a function of log M_1 (top), log M_2 (middle) and logarithm of the period (bottom). The symbols are the same as in Fig. 2.8. Error bars were omitted for clarity but were used in the linear fits (dashed lines). Post-RGB systems were not fitted in the upper panel. Simulations (crosses) were never fitted.

bound to the system at the end of the simulation. However, the orbital decay timescale had considerably slowed down and envelope mass was still being unbound. The authors therefore concluded that the system would survive, albeit with a smaller orbital separation than that reached by the end of the simulation.

2.3.4 Results

Here, we finally calculate the values of α from observations and simulations (Table 2.5, where we report both linear and logarithmic values). The error bars on α are significant but realistic.

$\alpha > 1$.

For six observed systems and all the simulations α exceeds unity. The physical interpretation of this is that the specific CE interaction under consideration has benefited from more energy than the orbital energy supplied by the companion. Several authors (e.g., Han et al., 1995; Webbink, 2008) discuss thermal energy as well as the dissociation and ionisation energies as additional sources of energy in the α equation. In § 2.2.3 we discussed the thermal energy and showed that we can use the virial theorem to gauge its value, which is exactly half of the binding energy. If we include the thermal energy in this way, all values of α will be below unity, except for the system with a substellar companion (HD 149382, discussed further in § 2.4) and the simulations.

A possible $\log q$ vs. $\log\ \alpha$ anti-correlation

In Fig. 2.7 we explore possible correlations between α and other relevant parameters. The simulations' α values are plotted (cross symbols) but not fitted, because it is impossible to determine their error bars in a way that is consistent with the observations. We fit $\log M_1$ vs. $\log\alpha$ for post-AGB and CSPN systems (not for post-RGB primaries, because for those stars we had to adopt a single mass value). We find a very marginal correlation (correlation coefficient, r=0.56). On the $\log M_2$ vs. $\log\alpha$ plane we see a slightly better anti-correlation with $r = -0.79$ (post-RGB systems are fitted here). Fits to the data and their errors result in reduced χ^2=0.77 and 1.79 for the M_1 and M_2 cases, respectively. The correlation between $\log\alpha$ and the period is extremely weak ($r = 0.33$).

			Linear fit			Constant fit		
	n^a	r^a	$\log \alpha =$	χ^2/ν^b	pte^a	$\alpha =$	χ^2/ν^c	pte^a
All data	31	–0.78	$(-1.4 \pm 0.2) - (1.2 \pm 0.2) \log q$	0.78	0.79	0.43±0.08	1.9	0
As above, no HD 149382	30	–0.64	$(-1.2 \pm 0.2) - (1.0 \pm 0.3) \log q$	0.75	0.83	0.41±0.06	1.4	0.06
Only CSPN and pRGB	12	–0.92	$(-1.4 \pm 0.3) - (1.4 \pm 0.3) \log q$	0.54	0.86	0.63±0.12	2.8	0
As above, no HD 149382	11	–0.83	$(-1.2 \pm 0.3) - (1.2 \pm 0.4) \log q$	0.53	0.85	0.54±0.11	1.7	0

[a] n: size of the dataset. r: correlation coefficient. pte: probability to exceed.
[b] Degrees of freedom, $\nu = n - 2$.
[c] Degrees of freedom, $\nu = n - 1$.

Table 2.6 Statistical properties of the fits to $\log q$ vs. $\log \alpha$.

A fit to logα as a function of log($q = M_2/M_1$) is plotted in Fig. 2.8. In Table 2.6 we list the parameters of the linear fit with their errors, along with the number of data points, reduced χ^2 value, probability to exceed[5] and the correlation coefficient r; we then list constant α fits, along with their reduced χ^2 and probability to exceed. First, we fit all of our data together, except for the simulations, as before. The data is reasonably anti-correlated. We then exclude the outlier (HD 149382 [$q = 0.014$, $\alpha = 33$]); the anti-correlation is somewhat degraded, although these two fits are very equivalent from a statistical point of view. Both have a reduced χ^2 below unity and a probability to exceed of 0.8, meaning that the errors may have been overestimated or too many degrees of freedom have been considered in the fit. However, a constant α fit never represents the data better, with a probability to exceed of zero, which means that random deviations would always explain the data better than the constant α fit.

To investigate further our data, we eliminated groups of systems to determine whether this would improve the statistics of the anti-correlation among the remaining data. By fitting only post-RGB and central stars of PN systems one can improve the anti-correlation (Fig. 2.8, bottom panel). On the other hand the probability to exceed reduces further and since the constant α fit is not better, we once again have to conclude that the errors have been overestimated for this fit. The improved anti-correlation might derive from the fact that in our reconstruction technique we have assumed that any primary with mass larger than 0.47 $M_\odot$, went through the AGB evolution. That assumption results in a specific primary mass at the time of the CE interaction (§ 2.3.1). It is however possible, that some of these primaries are actually post-RGB objects descending from *more massive* stars, as we described in § 2.3.1. More massive stars develop a helium core more massive than 0.47 $M_\odot$ before ascending the RGB. Once they expand, they may suffer a CE interaction on the RGB that truncates the RGB evolution by ejecting the envelope. These massive, post-RGB, post-CE primaries would later ignite core helium, thus developing a CO core, but with an envelope mass low enough to make them appear as hot sub-dwarfs with a close companion. It is therefore possible that these objects' masses and radii at the time of the CE interaction might have been significantly miscalculated, resulting in the observed large scatter on the $\log q$ vs. $\log \alpha$ plot in Fig. 2.8 (top panel). On the other hand, the central stars of PN are (almost) guaranteed to have been on the

[5]The probability to exceed is the probability that a set of randomly sampled data from a normal distribution produces a reduced χ^2 that exceeds the one determined. This value should be as close as possible to 0.5, corresponding to a reduced χ^2 of approximately unity, where the exact value depends on the number of degrees of freedom (Bevington & Robinson, 2003).

AGB, and the systems with $M_c < 0.47\ M_\odot$ are post-RGB stars, making these two groups less prone to error.

The values of α derived by Sandquist et al. (1998) are approximately a factor of four lower than those we derive. They used the formalism of Tutukov & Yungelson (1979), except that they revised the expression for the orbital energy to include the orbital energy value at the time of the CE interaction, unlike Tutukov & Yungelson (1979). Sandquist et al. (1998) also derived the binding energy as the *difference* between the binding energy at the beginning and at the end of the CE interaction, where they integrated the stellar structure for the initial value and used the simulation output to determine the remaining binding energy from the left over bound envelope in the system. Although we suspect that the leftover envelope binding energy is low, they do not report the actual value. It is not possible at this point to account exactly for this discrepancy. However a large part of it is certainly due to the fact that Tutukov & Yungelson (1979), like Yungelson et al. (1993) (Eqs. 2.2 and 2.5), use a far larger radius of the primary at the time of the CE interaction, reducing the value of α (see § 2.2.1).

2.4 The stellar response and the thermal energy

In § 2.2.3 we discussed using the virial theorem to quantify the entire energy budget of the envelope. If we accounted for the thermal energy of the envelope in this way, we would multiply the envelope binding energy by a factor of 0.5, which would lower all α values by a factor of two, and bring all but one of the observed systems below unity.

It is possible that the anti-correlation in the data, where some of the systems with low q value appear to *need* the thermal energy, while others do not, may hold some clues. Since the virial theorem is based on the principle of hydrostatic equilibrium, and since adjustments to hydrostatic equilibrium take place on the stellar dynamical timescale, we may hypothesise that the timescales of envelope penetration and inspiral vary as a function of q.

The equation of hydrostatic equilibrium dictates that, during their giant phases, stars expand upon losing mass because the pressure gradient overcomes gravity. When the envelope mass is reduced below a certain threshold by mass-loss, the gravity term dominates and the star shrinks rapidly - this is the phase when the star leaves the RGB or AGB and moves to the left of the Hertzsprung-Russell diagram. If a small

companion triggers additional mass-loss while in the outer parts of the envelope, it will also trigger expansion and reduction of the envelope binding energy, because of radius relaxation. This means that relatively light companions could unbind an envelope that is in principle too heavy for them to lift.

The time over which stars respond to changes is the stellar dynamical time. For a 100 $R_{\odot}$ RGB star this is approximately two weeks, while for a 500 $R_{\odot}$ AGB star it is of the order of a few months to a year. The latter vaue is similar to the CE interaction timescale determined by the few simulations carried out so far (e.g., Sandquist et al., 1998; De Marco et al., 2003). On these grounds *we suggest that if the in-spiral of the companion takes longer than a dynamical time the giant can use its own thermal energy to help unbind the envelope, but if it takes less, this energy source will not be available.* It may be possible that when q is smaller it takes the companion longer to plunge into the primary envelope, thus giving the primary star more time to respond by expanding and reducing its own envelope binding energy. In other words, for slower changes the star has time to become virialised, which results in a stellar expansion, i.e., the star is tapping its own thermal energy.

This idea is supported by the calculation of Nordhaus & Blackman (2006, their Figure 2) that shows that lower mass companions take longer to in-spiral. This also makes sense in view of the fact that the transfer of orbital energy to the envelope is via gravitational drag (Ricker & Taam, 2008): the companion creates a dense wake that slows it down and makes it fall in towards the giant's core. Such a wake would be less massive for lower mass companions. This suggestion can also explain the simulations' above-unity α values. Hydrodynamic simulations do not include the stellar energy source, but as long as the CE in-spiral timescale is shorter than the thermal timescale, the simulated star will behave physically.

HD 149382, with a sub-stellar companion, remains troublesome. Its value of α is so high that it cannot be explained simply by invoking the thermal response of the star. One could invoke additional sources of energy such as dissociation and ionisation energies, but it seems suspicious that such source should only be invoked for the lightest companion. It is possible that a third body was present in these systems, such as another planet. We could also question the precision of the determined parameters; however we note that with such a low mass companion, there is no reasonable way of reducing the value of α. To test this we increased that primary mass from 0.41 $M_{\odot}$(the middle of the calculated range) to 0.47 $M_{\odot}$, suggested by Geier et al. (2010) as a more likely value and we determined α under the assumption

that HD 149382 is a post-RGB system as well as a post-AGB one. The smallest value of α (10) is obtained for a post-AGB object and the reduction from the value of 33 (Table 2.5) is due primarily to the fact that the radius would be larger for a larger core mass. In our log–log fit this does not alter appreciably the fit parameters and the anti-correlation is preserved.

2.5 Summary and discussion

In this paper we have compared different derivations of the CE efficiency equations used in the literature, and have derived a more accurate form. Our approximation is quite similar to that of Webbink (1984), although our binding energy is more negative, resulting in higher values of α.

We have then used this approximation to determine the value of α for a set of observed post-CE systems as well as a set of simulations. In so doing we have revealed the difficulties inherent in deriving α values from observations: the methods available to reconstruct the parameters of the primary at the time of the CE interaction do not lead to accurate values. As a result the errors on the determined α are large.

We have also found some evidence for an anti-correlation between $\log(q = M_2/M_1)$ and $\log \alpha$, such that $\alpha \approx (0.05 \pm 0.02) \times q^{(-1.2 \pm 0.4)}$. Considering the exponent of q is $\lesssim -1$, this implies that smaller mass companions are left with comparable, if not longer post-CE periods than their more massive counterparts. One way this could be achieved is if smaller companions took longer than the primary's dynamical time to penetrate into the CE than larger ones, giving their primary star an opportunity to react and use its own thermal energy to expand, thus helping to eject the envelope. Since the CE timescales seem to be similar to the stellar dynamical time scale (of the order of a year; Sandquist et al., 1998; De Marco et al., 2003) this suggestion is plausible.

The energetics of the CE interaction are complex, however, and it is not enough to state that ionization and dissociation energies could be available, one has to also show that once tapped, these sources aid the envelope ejection process, a thing that was questioned by Soker & Harpaz (2003) who argued that the opacity of the envelope would be too low. Several other mechanisms could play a role in the common envelope ejections (e.g., excitation of pulsation waves; Soker, 1992), which may also depend on the in-spiral time scales.

Politano & Weiler (2007) and Davis et al. (2010) calculated population synthesis

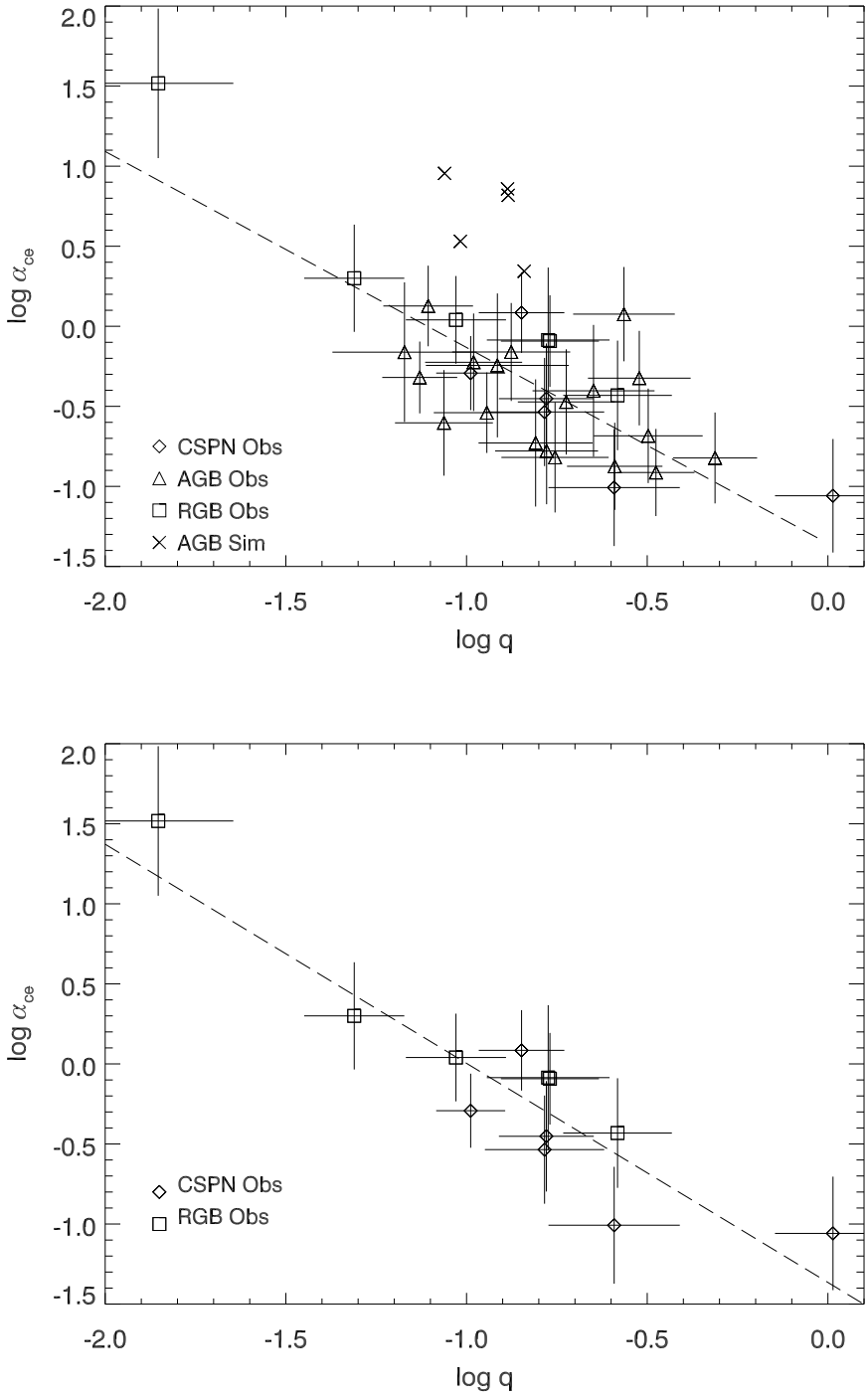

Figure 2.8 A plot of $\log(q = M_2/M_1)$ vs. $\log \alpha$. The simulations (crosses) are not fitted as the errors could not be determined. Top panel: all data is presented. Bottom panel: same as the top panel but without the post-AGB systems with no PN. The dashed lines are least square fits to the data.

models under the assumption of a constant α, or α proportional to the secondary mass. Politano & Weiler (2007) compared the predicted post-CE period distribution, secondary and primary mass distributions with observations of present day post-CE systems and cataclysmic variables. The predicted distributions are not strongly dependent on the prescription of α they used, leaving α unconstrained. Their period distribution for current day post-CE systems predicts many more systems at longer periods than observed (e.g., Miszalski et al. (2009) or Schreiber et al. (2008) and Schreiber et al. (2009)). The predicted secondary mass distribution seems also in contrast with observations that show that the most represented companion mass has spectral type M3.5, similarly to the distribution of field main sequence stars (Farihi et al., 2005). Politano & Weiler (2007) claim that the large fraction of brighter companions they predict would be missed by surveys because they would outshine the WD primary. However Holberg et al. (2008) shows that the companions that would be missed because they outshine the primary WD are brighter than mid-to-late K stars. This means that if the real companion mass distribution were that predicted by the models of Politano & Weiler (2007), we would have detected more companions with mass larger than $\sim$0.4 $M_{\odot}$.

Davis et al. (2010) predict the space density of post-CE systems, the distribution of secondary masses and the period distribution. The latter two predictions do not match observations. Davis et al. (2010) claim that similarly to observations they predict a steep decline of the systems with secondary masses $<$0.35 $M_{\odot}$. However, as we can see from the exhaustive compilation of Zorotovic et al. (2010), the number of systems with secondary mass below that threshold is very large. Finally, as is the case for the Politano & Weiler (2007) models, the predicted period distribution peaks at longer periods and is very broad, contrary to the observed ones, whose distribution peaks at periods shorter than a day and is very narrow. The period distribution is likely to become the best observation against which to test our population synthesis models in the future.

2.5.1 A comparison of this work to that carried out by Zorotovic et al. (2010)

While this paper was in review we became aware of a publication by Zorotovic et al. (2010), in which the authors determined the values of α for a set of post-CE WDs and drew conclusions from their findings in much the same way as we have done here.

Some of their conclusions are similar to our own, while others differ.

Both our and their data derive from that of Schreiber & Gänsicke (2003). However, they added 35 systems that their group has newly discovered. On the other hand, they excluded subdwarf primaries, such as all central stars of PN, and the systems with low mass secondaries (AA Dor and HD 149382). We have insured that for all the objects in common we used the same parameters.

Zorotovic et al. (2010) remarked that α values from simulations are in the range determined by their technique for the observed systems. We maintain instead that there is no way of comparing α values from simulations to those obtained by system reconstruction, without fully understanding what α formalism was adopted by the simulation studies and subject to the caveats of the simulations. This is why we have selected those simulations that we understand the best and re-determined their α values using the same formalism used for the observed systems.

Zorotovic et al. (2010) compared three α formalisms, the Yungelson et al. (1993) formalism, the Webbink (1984) formalism and a hybrid form between the two formalisms adopted by Hurley et al. (2002). Differences between α values obtained with these formalism are in line with our discussion in § 2.2.1. However, in contrast to Zorotovic et al. (2010) we have argued that it is possible to select the best formalism on physical grounds. In the end they adopted the formalism of Webbink (1984), making a comparison with our own work straight forward.

We agree with Zorotovic et al. (2010) on the treatment of λ, i.e., that one should calculate it according to what stellar structure one is examining. On the other hand, they did not disclose what values they used for those cases when they calculated λ using stellar structure calculations, only mentioning that the calculation was performed. They used the hydrogen abundance criterion for the core-envelope boundary, rather than the remnant envelope criterion, but that does not change significantly the resulting value of λ.

The primary reconstruction technique is usually the hardest part to compare. Zorotovic et al. (2010) used the stellar evolution fitting formulae of Hurley et al. (2000) to determine core mass, radii and luminosities as a function of time for a range of main sequence masses. Each measured primary mass (M_c) has multiple matching parameter sets (L, R and $M_{\rm MS}$); each set can be used to determine α. In this way each observed system will have a range of α values. We, on the other hand, determined only one value of α, but our error bar encompasses similar ranges to those determined by Zorotovic et al. (2010).

For example, Zorotovic et al. (2010) did not use the IFMR to determine $M_{\rm MS}$ for their systems, but instead determined a range of main sequence masses which, sometime during their evolution, will attain the same core mass as that of the primary of the observed systems. This is equivalent to using the IFMR implied by the fitting formulae, along with the uncertainty in those very relations and the measurement errors (the error propagation is not discussed in their paper, nor the uncertainties in the fitting relations). In the end, the largest difference between the two methods is likely to lie in the difference between the Hurley et al. (2000) fitting formulae and our MESA evolutionary sequences and fits to the Bertelli et al. (2008) tracks.

The Zorotovic et al. (2010) reconstruction technique does not pre-select whether the system went through a CE interaction on the RGB or AGB. Indeed several of their systems may have gone through such interaction in either phase. We find that all our post-RGB systems are post-RGB systems also in their scheme, while those of our systems with M_c in the range 0.47-0.55 $M_{\odot}$, which are post-AGB in our scheme (recall our criterion: $M_c > 0.47\ M_{\odot}$), have a chance to have gone through a CE interaction on the RGB. We pointed out (§ 2.3.4) that our conclusions remain true, and in fact become even stronger if we eliminate the entire class of post-AGB stars with no PN, leaving the central stars of PN (not addressed by Zorotovic et al. (2010)) and the post-RGB stars (which are post-RGB stars also in Zorotovic et al. (2010)).

After determining ranges of α values for each star, Zorotovic et al. (2010) determined the most likely values within those ranges by carrying out a population synthesis exercise. We have effectively carried out a similar exercise by using Baysian statistics in the determination of mass and radius of the primary at the time of the CE, by calculating the differences between $M_{\rm MS}$ and M_1 and between M_{WD} and M_c using statistical arguments. Interestingly, the conclusions drawn in the two papers are similar: α values for post-RGB stars are higher. A very weak to no correlation of α with M_2 exists (Fig. 2.7, middle panel). Post-AGB systems display a mild correlation between period and α, while post-RGB systems do not (Fig. 2.7, bottom panel). Zorotovic et al. (2010) did not test possible correlation between q and α nor did they carry out a statistical treatment of their data. In addition, they did not list their mean α values nor the corresponding stellar parameters, making it difficult to carry out a more thorough comparison.

Chapter 3

Hydrodynamics Simulations of the Common Envelope Phase

Originally published as Passy, J.-C., De Marco, O., Fryer, C. L., Herwig, F., Diehl, S., Oishi, J. S., Mac Low, M.-M., Bryan, G. L., & Rockefeller, G. 2012, ApJ, 744, 52

Abstract

We use three-dimensional hydrodynamical simulations to study the rapid infall phase of the common envelope interaction of a red giant branch star of mass equal to 0.88 $M_{\odot}$ and a companion star of mass ranging from 0.9 down to 0.1 $M_{\odot}$. We first compare the results obtained using two different numerical techniques with different resolutions, and find overall very good agreement. We then compare the outcomes of those simulations with observed systems thought to have gone through a common envelope. The simulations fail to reproduce those systems in the sense that most of the envelope of the donor remains bound at the end of the simulations and the final orbital separations between the donor's remnant and the companion, ranging from 26.8 down to 5.9 $R_{\odot}$, are larger than the ones observed. We suggest that this discrepancy vouches for recombination playing an essential role in the ejection of the envelope and/or significant shrinkage of the orbit happening in the subsequent phase.

3.1 Introduction

Around 60% of F and G stars are binaries, of which about 30% have separations smaller than 30 AU and will interact during the primary's evolution (Duquennoy & Mayor, 1991). During the giant phases of the primary, companions closer than ~ 5 AU enter a strong interaction phase with the primary and, under certain circumstances, a common envelope (CE) may form around the two stars. The secondary star spirals inside the envelope of the primary and may also fill its own Roche lobe because it cannot accrete all the matter coming from the donor star. This process is called a *common envelope interaction* and was originally described by Paczynski (1976). For a general review of the topic see, e.g., Iben & Livio (1993). There are two different processes leading to the onset of a CE phase: the start of unstable mass transfer from the expanding primary to the secondary (Hjellming & Webbink, 1987; Hurley et al., 2002) and the development of a tidal instability that occurs if there is not enough angular momentum in the orbit to maintain the primary's envelope in synchronization (Darwin, 1879). The post-CE system will be either a compact binary system, if there is enough energy to eject the primary's envelope, or a merger, if not.

The CE interaction is an essential ingredient for any binary population synthesis study of intermediate (e.g., Politano et al., 2010) or massive stars (e.g., Belczynski et al., 2008). Compact binaries are believed to be formed through at least one CE phase. Among them are symbiotic binaries, supersoft X-ray sources, cataclysmic variables and double white dwarfs, which are all possible supernova Type Ia progenitors. As Meng et al. (2011) pointed out, results deduced from population synthesis studies such as the Type Ia supernova birth rate are highly dependent on the physics of the CE phase. Therefore, it is paramount to understand more accurately the CE interaction in order to identify the formation channels of such supernovae and to compare observations with predictive models. Moreover, many substellar companions to evolved stars have recently been discovered with small orbital separations. Maxted et al. (2006) found a brown dwarf orbiting a white dwarf with a 116 min period, while Setiawan et al. (2011) discovered a system composed of a Jupiter-like object orbiting an horizontal branch star with a 16.2 day period. We therefore know that substellar companions can survive a CE interaction, but what is the minimum mass of the companion that can eject the envelope? Is the ejected envelope entirely unbound or will some of it eventually fall back and form a circumbinary disk? Were the substellar companions present before and survived the CE or were they formed later on in such

a disk (Perets, 2010)? Those questions remain unanswered.

Although the CE process was outlined more than 30 years ago, it is still far from understood quantitatively. Numerical simulations suggest that the typical duration of the entire CE phase is short — less than 10^3 years — which makes CE ejections unlikely to be observed. However, one can use observations of post-CE binaries to better understand CE evolution. With the use of stellar models, the initial configuration of such systems can be approximately determined from the final configuration. Using either the α-formalism (Webbink, 1984, but see De Marco et al. 2011) or the γ-formalism (Nelemans et al., 2000) the relevant parameters can be constrained and the CE ejection efficiency can be predicted. Using this approach, De Marco et al. (2011) suggested an anti-correlation between α, the CE efficiency parameter, and the secondary to primary mass ratio.

The entire CE evolution can be divided into three different phases (Podsiadlowski, 2001) with different timescales, length scales and physics involved. These differences are the reasons why reproducing the entire CE evolution of a given system accurately is challenging. Therefore, one usually treats one phase after the other with different methods. In this paper, we focus only on the rapid infall phase, which has a short timescale ($\sim 1-10$ years), and in which the evolution is driven by drag forces. Several numerical hydrodynamic studies of the CE interaction have been carried out in the past (for an exhaustive list, see Taam & Sandquist, 2000), including a series of ten papers starting with the two-dimensional calculation of the interaction of a 16 $M_\odot$ supergiant and a 1 $M_\odot$ neutron star (Bodenheimer & Taam, 1984), and most recently treating three-dimensional simulations of the CE interaction between 3 or 5 $M_\odot$ giant stars and 0.4 or 0.6 $M_\odot$ main sequence (MS) companions (Sandquist et al., 1998). The latter study has been extended first by Sandquist et al. (2000) to 1 $M_\odot$ and 2 $M_\odot$ red giant branch (RGB) stars with companion masses ranging from 0.1 to 0.45 $M_\odot$, then by De Marco et al. (2003) to a 1 $M_\odot$ asymptotic giant branch star with a 0.1 or 0.2 $M_\odot$ companion. Ricker & Taam (2008) computed high resolution simulations of the CE phase between a 1.05 $M_\odot$ RGB star and a 0.6 $M_\odot$ compact companion, and concluded that the gravitational component of the drag dominates over the hydrodynamical component (also see Taam & Ricker, 2010; Ricker & Taam, 2012).

A direct comparison of the results obtained using different numerical methods has however never been carried out. Although analytical/empirical work has included discussion regarding observational data, there are only a couple of publications that

connect simulations and observations in a meaningful way (see e.g., Sandquist et al., 2000). Those are, as we will explain in §3.2 and §3.4, key steps to better understand the implications of CE interactions and the physical processes driving them. In this paper we therefore present numerical simulations with two different algorithms of the CE interaction of a 0.88 $M_{\odot}$ RGB star with a MS companion. Different companion masses from 0.1 $M_{\odot}$ to 0.9 $M_{\odot}$ are considered. The simulations are carried out with both an Eulerian code (*Enzo* in uniform-grid mode, O'Shea et al. (2004) and *enzo.googlecode.com*) and a Lagrangian code (*SNSPH*, Fryer et al. 2006), and for different resolutions. We describe the numerical methods and the initial conditions of our 15 simulations in §3.2 and §3.3. We describe and discuss the results in §3.4 and §3.5, and finally conclude and summarize in §3.6.

3.2 The codes

In this section we describe the numerical methods we use. We first compare the code algorithms and explain why a code-to-code comparison is necessary. Then, we describe both codes in detail and finally discuss different ways to compare resolution.

3.2.1 Eulerian vs Lagrangian codes

Although they are meant to simulate similar astrophysical situations, high order Eulerian grid codes and Lagrangian smoothed-particle hydrodynamics (SPH) codes differ fundamentally, with each having advantages and disadvantages. Among other studies, Davies et al. (1993), Frenk et al. (1999), Agertz et al. (2006) and Tasker et al. (2008) aim at identifying these differences. On the one hand, high-order Eulerian grid codes have a better wavenumber resolution than SPH codes for an equal number of cells and particles and are more accurate at resolving the rarefied regions since, unlike SPH, the resolution does not depend on the density of the gas; Eulerian codes also better resolve shocks (Tasker et al., 2008) compared to SPH codes; and finally, SPH noise dominates subsonic flows and therefore makes it difficult for SPH codes to follow perturbations in flows with Mach numbers under unity. On the other hand, SPH codes don't diffuse material properties, and inherently conserve mass, momentum and energy (Rosswog, 2009). While the treatment of boundary conditions can be challenging in grid-based codes when the flow expands beyond the computational domain, SPH easily handles vacuum conditions. It is still unclear which method is

the most appropriate to simulate CE interactions. Therefore, we use both methods and confront the results from both codes in order to draw conclusions about their physical relevance.

3.2.2 Input physics

Both codes solve the fully compressible hydrodynamics equations with self-gravity included. These equations can be written using an Eulerian formulation:

$$\frac{\partial \rho}{\partial t} + \nabla \cdot (\rho \mathbf{v}) = 0 \tag{3.1}$$

$$\frac{\partial \mathbf{v}}{\partial t} + (\mathbf{v} \cdot \nabla)\mathbf{v} = -\frac{1}{\rho}\nabla p - \nabla \Phi \tag{3.2}$$

$$\frac{\partial u}{\partial t} + \mathbf{v} \cdot \nabla u = -\frac{1}{\rho}\nabla \cdot (p\mathbf{v}) - \mathbf{v} \cdot \nabla \Phi \tag{3.3}$$

$$u_{int} = \frac{1}{\gamma - 1}\frac{p}{\rho} \tag{3.4}$$

$$\Delta \Phi = 4\pi G \rho \tag{3.5}$$

where $\rho, \mathbf{v}, p, \Phi, u, u_{int}, \gamma$ are the density, velocity, pressure, gravitational potential, specific total energy, specific internal energy and adiabatic index of the gas, respectively. The total energy is the sum of the internal energy, and the macroscopic kinetic energy:

$$u = u_{int} + \mathbf{v}^2/2. \tag{3.6}$$

Equations (3.1), (3.2) and (3.3) express mass continuity, conservation of momentum and conservation of energy, respectively. Both codes evolve the internal energy rather than the total energy. An ideal gas equation of state (Eq. 3.4) for a monoatomic gas ($\gamma = 5/3$) closes the system composed by equations (3.1)-(3.3). Such an equation of state represents an adequate approximation of the deep convective envelope of RGB stars (Hjellming & Webbink, 1987) although it ignores some physical processes such as radiation pressure and ionization. We discuss this point in detail in §3.5.2. Finally, the gravitational potential is calculated using the Poisson equation (Eq. 3.5).

3.2.3 The *Enzo* code

Enzo is a three-dimensional, adaptive mesh refinement hybrid (hydrodynamics + N-body) grid-based code (Bryan et al., 1995; O'Shea et al., 2004) that we use in uniform-grid mode only. It is primarily designed to simulate cosmological structure formation (Norman et al., 2007). However, its numerous features make it useful for reproducing many different astrophysical situations, including CE interactions.

The Euler equations (Eqs. 3.1–3.3) are solved using the van Leer (1977) second-order advection method also implemented in *Zeus* (Stone & Norman, 1992). Although those equations can also be solved in *Enzo* by a third-order piecewise parabolic method that better resolves shocks and turbulence, our tests show that it slows down the computation by a factor 2. As we will point out in §3.4, there are neither strong shocks nor important turbulence in our simulations so we favor efficiency and use the van Leer solver. The Poisson equation is solved using fast-Fourier transforms.

In the case of a CE interaction between a RGB star and a MS companion, the radius of the secondary — typically 0.5 $R_\odot$ — is small compared to the primary's radius ($\sim$ 100 $R_\odot$), so we can legitimately model the companion as a point mass particle. Furthermore, as shown in Fig. 3.3, the primary's core is also small ($\sim$ 0.01 $R_\odot$) and dense, so it can also be modeled as a point mass.

Enzo usually models collisionless particles as a continuous mass field appropriate for computing the gravitational potential in the case that each particle represents many actual particles, such as in cosmological simulations with dark matter. In that case their mass is deposited in the 8 nearest cells and added to the gas density of those cells to find the total density for use in solving the Poisson equation (Eq. 3.5). In a simple two-body interaction between 1 $M_\odot$ and 0.1 $M_\odot$ objects in a one year circular orbit without gas, this method does not provide the accuracy required by our problem because of the spreading out of the mass of the point source, leading to an inaccurate gravitational potential. Indeed, a 1 % error in the orbit is reached after only 6 orbits. Consequently, we implemented, as a new type of particle, point mass (PM) particles. These particles create a potential that is added analytically to the gas potential calculated using the Poisson equation. Using an analytic potential yields an accuracy of the orbit more than two orders of magnitude better than with the default particles. The gravitational potential created by a PM particle is smoothed according to the prescription of Ruffert (1993), used in Sandquist et al. (1998):

$$\Phi_{PM}(r) = \frac{-GM_{PM}}{\sqrt{r^2 + \epsilon^2\delta^2 \exp\left[-r^2/(\epsilon\delta)^2\right]}} \tag{3.7}$$

where M_{PM} is the mass of the particle, r is the distance from the particle, δ is the size of a cell and $\epsilon = 1.5$. The point mass particles are advanced using a leapfrog algorithm. Time stepping is determined by taking the minimum time step between the Courant conditions for the gas, the particles and the acceleration field:

$$\delta t_{gas} = \min_{\text{cells}} \left(\frac{C_1 \delta}{c_s + \max(|v_x|, |v_y|, |v_z|)} \right) \tag{3.8}$$

$$\delta t_{part} = \min_{\text{particles}} \left(\frac{C_2 \delta}{\max(|V_x|, |V_y|, |V_z|)} \right) \tag{3.9}$$

$$\delta t_{accel} = \min_{\text{cells}} \left(\sqrt{\frac{\delta}{\max(|g_x|, |g_y|, |g_z|)}} \right) \tag{3.10}$$

where $C_1 = 0.4$ is the Courant factor, $C_2 = 0.4$ is the particle Courant factor, c_s is the sound speed, $\mathbf{v} = (v_x, v_y, v_z)$ is the velocity of the gas, $\mathbf{V} = (V_x, V_y, V_z)$ is the velocity of a particle and $\mathbf{g} = (g_x, g_y, g_z)$ is the acceleration field.

Finally, we remark that the current *Enzo* Poisson solver prevented us from using nested or adaptive grids that would have allowed us to increase resolution locally. The inaccurate treatment of boundary conditions within the refined grids prevented us from stabilizing the RGB progenitor in a multi-grid initial setup. We are currently developing a new Poisson solver that will allow us to use nested grids as well as adaptive mesh refinement and carry out better-resolved simulations.

3.2.4 The *SNSPH* code

SNSPH (Fryer, Rockefeller, & Warren, 2006) is a three-dimensional, parallel SPH code using tree gravity. It uses a regular Monaghan cubic spline kernel (Monaghan, 1992). For the artificial viscosity we use the sum of a bulk viscosity and a von Neumann and Richtmyer viscosity (Rosswog, 2009). The particles are organized into a parallel hashed oct-tree as described in Warren & Salmon (1993). The gravitational potential of a SPH particle, i, is smoothed using the following formula:

$$\Phi_i(x_i = r_i/h_i) = \begin{cases} -Gm_i/h_i \times (\frac{2}{3}x_i^3 - \frac{3}{10}x_i^4 + \frac{1}{10}x_i^5 - 1.4) & \\ & \text{if} \quad 0 \leq \mathrm{x} \leq 1 \\ -Gm_i/r_i \times \left[(\frac{4}{3}x_i^2 - x_i^3 + \frac{3}{10}x_i^4 - \frac{1}{30}x_i^5 - 1.6)/h_i + 1/15r_i\right] & \\ & \text{if} \quad 1 \leq \mathrm{x} \leq 2 \\ -Gm_i/r_i & \text{otherwise} \end{cases} \tag{3.11}$$

where h_i, m_i and r_i are the smoothing length, the particle mass and the distance from the particle, respectively. We compare both numerical potentials to the theoretical potential in Fig. 3.1. For a given smoothing length, h_i, the Monaghan (1992) potential used in our *SNSPH* simulations is deeper than the Ruffert (1993) one used in our *Enzo* simulations. Also, the Monaghan (1992) potential is exact at distances larger than $2h_i$ whereas the Ruffert (1993) potential only asymptotically tends to the exact potential.

SNSPH uses the fast multipole method to calculate gravitational accelerations (Warren & Salmon, 1993). The SPH particles are also advanced using an leapfrog algorithm. Finally, in order to keep the same overall spatial coverage, the smoothing length varies according to the formula from Benz (1990):

$$\frac{h_i(t)}{h_i(0)} = \left(\frac{\rho_i(0)}{\rho_i(t)}\right)^{1/3}. \tag{3.12}$$

3.2.5 Resolution comparison

There is no ideal way to compare the resolution between SPH and uniform-grid codes. However, a few criteria can give us a general idea of how to relate them.

As mentioned by Davies et al. (1993), a first global criterion would be to compare the total number of SPH particles N_{part} with the total number of cells originally inside the progenitor:

$$N_{cells} = \frac{V_1}{V_G} \times N_{tot} \sim 4.19 \times \left(\frac{R_1}{L}\right)^3 N_{tot}, \tag{3.13}$$

where N_{tot}, V_1, V_G, R_1 and L are the total number of cells, the volume of the primary, the volume of the grid, the radius of the primary and the linear dimension of the

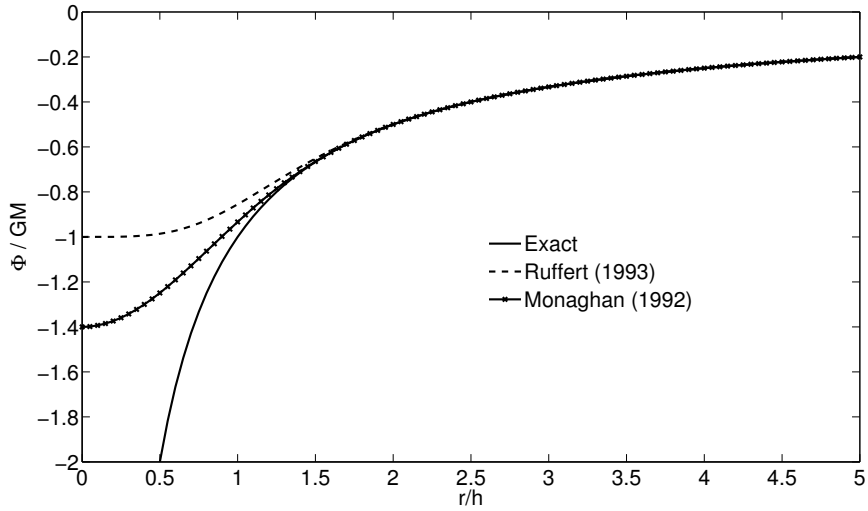

Figure 3.1 Comparison between the different potentials in arbitrary units with $h_i = \epsilon\delta = 1$. Plotted are the theoretical potential (solid line), the Ruffert (1993) potential used in *Enzo* (dashed line) and the Monaghan (1992) one used in *SNSPH* (dash-cross line).

grid, respectively. As time goes by, the gas will however fill a larger fraction of the numerical grid and thus increase the number of relevant cells, but not the real resolution of the simulation.

A more local criterion is to compare the size of an *Enzo* grid cell, δ, with the SPH smoothing length, which varies in space and time. Indeed, if the companion does not sink much into the primary's envelope and does not modify the inner part of the smoothing length distribution too much, then the resolution deep inside the progenitor does not matter. Therefore, we compare the smoothing length distribution of the SPH model to the cell size of the Eulerian grid. As shown in Fig. 3.2, the smoothing length at small radii does not vary, so an *Enzo* run with a 128^3 grid will be under-resolved compared to our canonical 500 000 (roughly 80^3) particle SPH run no matter how deep the companion penetrates while a run with a 256^3 grid would be equivalent to our SPH runs if the separation between the primary core and the companion always exceeds 20 $R_\odot$. This local criterion for the resolution is not perfect either since it does not take into account the variation of the smoothing length throughout the SPH simulation.

Again, comparing the resolution between uniform-grid and SPH codes is quite

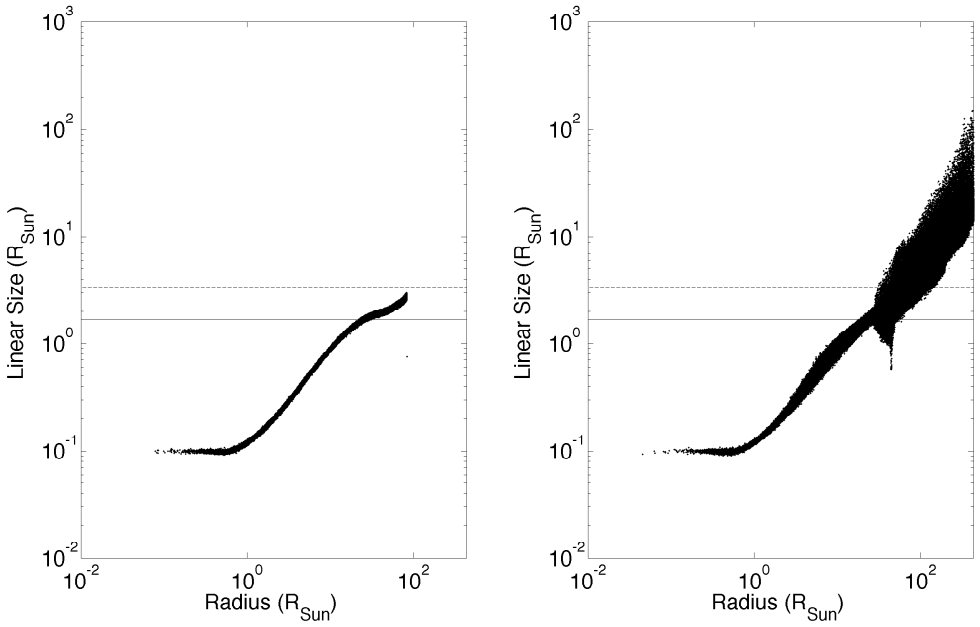

Figure 3.2 Resolution comparison between the *SNSPH* smoothing length field (dots) for a run with 500 000 particles, and the *Enzo* size of a grid cell for the 128^3 (dash line) and the 256^3 (solid line) runs for the initial (left) and final (right) particle distributions.

challenging and both methods have, in the situation we are interested in, strengths and weaknesses: SPH will under-resolve the low-density outer parts of the envelope, where the smoothing length dramatically increases, while it will be more accurate in the later phase of the evolution when the separation between the primary's core and the secondary will typically sink below a few cells. Therefore, comparing SPH and grid-based simulations is paramount in order to state which one is more adapted to our problem, and the combination of both global and local criteria is the best way to compare the resolutions of both methods.

3.3 The simulations

We perform 5 *SNSPH* and 12 *Enzo* simulations of CE interactions with a 0.88 $M_\odot$ RGB primary that are summarized in Table 3.1. The *SNSPH* simulations are computed using 500 000 particles whose initial smoothing length follows the radial profile shown in Fig. 3.2. The *Enzo* simulations are performed using either a 128^3 or a 256^3

grid. In both cases, the linear size of the computational domain is $L = 3 \times 10^{13}$ cm. We consider companion masses of 0.9, 0.6, 0.3, 0.15 and 0.1 $M_\odot$. Giant stars are slow rotators with rotational velocities of the order of a few $\mathrm{km\,s^{-1}}$ (de Medeiros & Mayor, 1999). Although it is expected that a close companion will, through the action of tides and the transport of angular momentum in the primary envelope, spin up the envelope during the pre-CE phase, the actual rotation of the primary at the onset of the CE interaction is hard to quantify. Moreover, even if the primary was uniformly rotating at 50 $\mathrm{km\,s^{-1}}$, its rotational energy would be

$$E_{rot} = \frac{1}{2} r_g M_1 R_1^2 \omega^2 \sim 2.2 \times 10^{44} \text{ ergs} \tag{3.14}$$

where ω, r_g, M_1 and R_1 are the angular velocity, the radius of gyration, the mass and the radius of the primary, respectively. For RGB stars r_g is typically about 0.1 (Taam & Sandquist, 2000). This rotational energy does not affect the energetics of the system since it is more than two orders of magnitude smaller than the binding energy of the primary (see below). Consequently, we assume that the primary is initially non-rotating. Finally, the companion is at the start placed at the surface of the primary in a circular orbit. We thus have three different simulations for each initial companion mass - one with SNSPH, and two with *Enzo* on 128^3 and 256^3 grids. Additionally, we also run two *Enzo* simulations in order to study the dependency of the final parameters on the initial conditions. We consider the 128^3 *Enzo* simulation with a 0.3 $M_\odot$ companion (Enzo3) as the reference and run identical simulations increasing, by 5 %, either the initial velocity of the companion (Enzo11) or the initial separation (Enzo12). All the runs follow the evolution of the system for about 1 000 days.

As a primary, we use a one-dimensional model of a star with a MS mass of 1 $M_\odot$. Using the stellar evolution code EVOL (Herwig, 2000), this progenitor was evolved to the RGB phase until the core reached $M_c = 0.392$ $M_\odot$. At that time, the radius of the star was 83 $R_\odot$ and its total mass was $M_1 = 0.88$ $M_\odot$ due to mass loss, which was treated using the Reimers formalism with $\eta = 0.5$. We adapt this model by using the density and pressure profiles, but computing the internal energy using Eq. 3.4. A sample of relevant profiles are plotted in Fig. 3.3.

We now explain how this stellar model is modified in order to be compatible with an input suitable for each of our codes. For the *SNSPH* simulations, the initial particle configuration is a weighted Voronoi tesselation (WVT) similar to that described by Diehl & Statler (2005). As we have explained in §3.2.1 one limitation of SPH codes

Table 3.1. Main parameters for the different simulations

Name	N_{part} or N_{cells}	M_2 ($M_\odot$)	A_0 ($R_\odot$)	P_0 (days)	v_0/v_{circ}	A_f ($R_\odot$)	P_f (days)
SPH1	500 000	0.9	83	66	1	26.8	13.5
SPH2	500 000	0.6	83	72	1	20.6	10.1
SPH3	500 000	0.3	83	81	1	11.3	5.5
SPH4	500 000	0.15	83	86	1	7.3	3.0
SPH5	500 000	0.1	83	88	1	6.1	2.2
Enzo1	128^3	0.9	91	75	1	28.1	15.5
Enzo2	128^3	0.6	91	83	1	20.0	11.0
Enzo3	128^3	0.3	91	93	1	11.7	5.6
Enzo4	128^3	0.15	91	99	1	8.6	3.4
Enzo5	128^3	0.1	91	102	1	8.5	3.3
Enzo6	256^3	0.9	85	68	1	25.5	13.2
Enzo7	256^3	0.6	85	75	1	19.2	9.8
Enzo8	256^3	0.3	85	84	1	11.2	5.4
Enzo9	256^3	0.15	85	89	1	6.9	2.8
Enzo10	256^3	0.1	85	92	1	5.7	2.1
Enzo11	128^3	0.3	91	93	1.05	12.0	4.6
Enzo12	128^3	0.3	95.5	99	1	12.2	5.0

Note. — Reported are the name of the system, the mass of the stellar component (M_c), the mass of the companion (M_2), the orbital period (P) and the observed orbital separation (A), as presented in the reference papers. Uncertainties can be found in the corresponding papers.

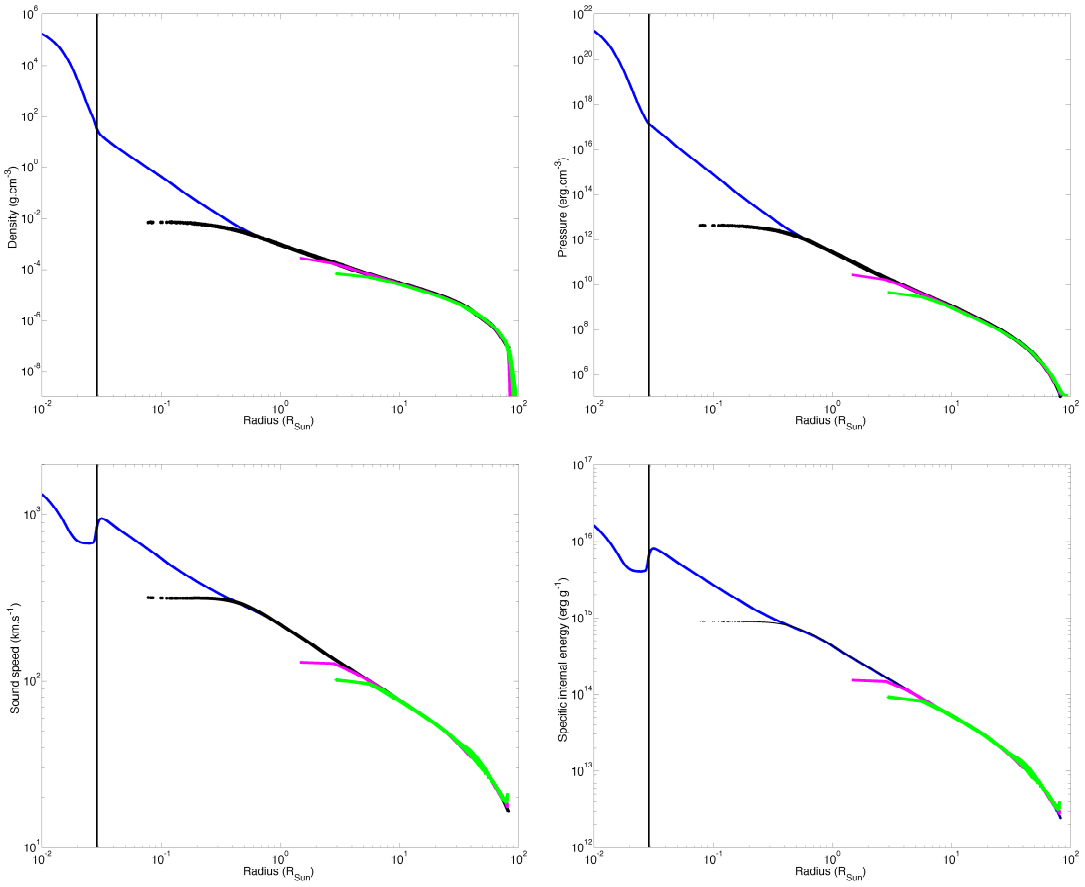

Figure 3.3 Comparison between the EVOL stellar evolution model (blue), the SPH initial model computed with 500 000 particles (black) and the *Enzo* initial models for a 128^3 (green) and a 256^3 (purple) unigrid. The vertical line represents the core-envelope boundary according to the criterion of De Marco et al. (2011).

is the large number of particles required by dense regions such as the core of the primary. Since the time step induced by a particle i can be roughly estimated by $h_i/c_{s,i}$ where $c_{s,i}$ is the local sound speed, a small smoothing length will require a small time step resulting in a high computational cost. Since the equation of state changes significantly around the helium core, we represent the core by a particle with mass M_c. The associated smoothing length is $h_c = 0.1\ R_\odot$. We add SPH particles in the region around the core such that the density values and gradient profiles connect smoothly at the core/envelope boundary ($r = 2h_c = 0.2\ R_\odot$). In this way, we obtain the profile shown in Fig. 3.3. Since the density profile has been changed, one must modify the gravitational acceleration accordingly. Assuming hydrostatic equilibrium

in spherical symmetry, we integrate the pressure gradient choosing the integration constant to match the true profile outside the core (at $r = 0.2\ R_\odot$). The specific energy profile is computed using Eq. 3.4. Finally, the acceleration of a SPH particle is due either to gravity or to gas pressure. These two components are computed using the same particle mass for all particles except the core and the companion, for which we distinguish between the gravitational and SPH masses. The gravitational mass of the core is M_c and its SPH mass is set to balance the gravitational acceleration of the envelope and prevent the star from collapsing. As for the companion, we treat it as an N-body particle so its SPH mass is 0 $M_\odot$.

For the *Enzo* simulations, the grid is initialized using the stellar model of the primary with the addition of a PM particle that represents its core. We fill the computational domain with a constant background density to prevent the star from expanding and set the ratio between the background density and the minimum density of a cell that belongs to the primary to 10^{-4}. This setup is not initially numerically stable. The star tends to expand, so we let the initial configuration evolve for a few dynamical times in the absence of the companion, while damping the velocity field by a factor of 2 after each cycle. Finally, we evolve this relaxed model normally for another few dynamical times to obtain a numerically stable model. As a side effect of the relaxation to hydrostatic equilibrium, the *Enzo* models are a little bit bigger — the lower the resolution, the larger the radius of the primary is — thus the initial orbital separations between the models are slightly different (Table 3.1).

3.4 Results

In this section, we describe the results obtained from our 15 simulations. Since the qualitative behavior is the same in all of them, we discuss in detail the 0.6 $M_\odot$ case (SPH2, Enzo2 and Enzo7).

3.4.1 Description of the rapid infall phase

As explained in §3.3, the companion is placed at the surface of the primary. Thus, the primary extends beyond its Roche lobe and unstable mass transfer starts immediately. The companion, surrounded by stellar matter, exchanges momentum and energy with this gas through drag. The orbital separation shrinks on a dynamical timescale and its evolution for the 256^3 *Enzo* simulations is shown in Fig. 3.4. Although the orbit

is initially circular, it quickly develops eccentricity due to the geometry of the gas ejection. In order to define quantitatively the end of the rapid infall phase and the final orbital separation *ad hoc*, we consider the evolution of the orbital decay (Fig. 3.5). As expected, the orbital decay is initially quite high (~ 0.01 day^{-1}), decreases as less gas is available for the companion to exchange energy with, and eventually reaches a plateau. We decide to define the end of the rapid infall phase to be at the start of this plateau, which occurs at about 280 days for the 0.6 $M_{\odot}$ companion (Fig. 3.5). All the simulations show the same trend and the lighter the companion, the deeper it falls and the longer it needs to reach its final orbital separation. The duration of the rapid infall phase is 260, 280, 280, 300 and 340 days, for the 0.9, 0.6, 0.3, 0.15 and 0.1 $M_{\odot}$ companion, respectively.

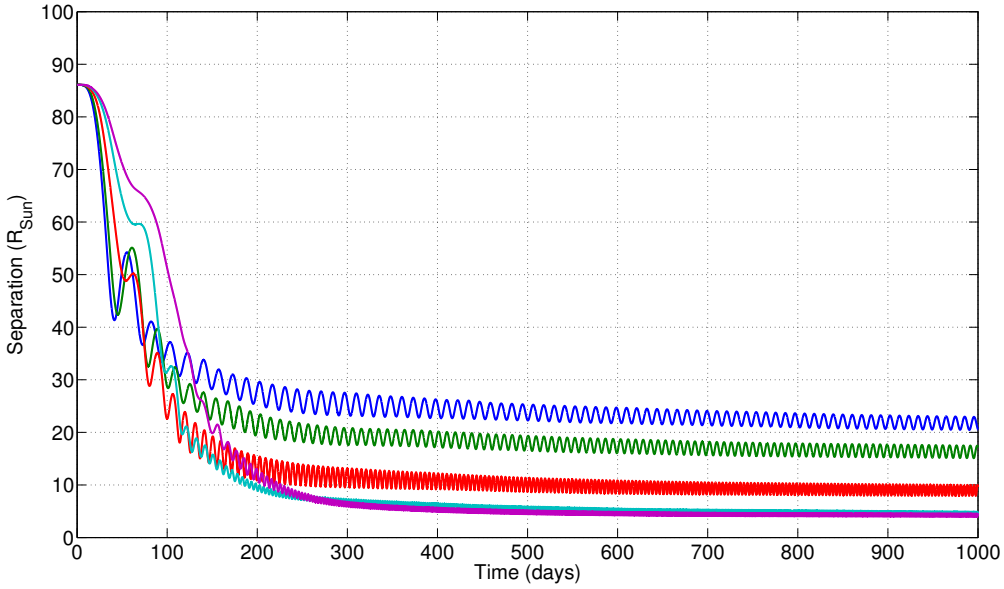

Figure 3.4 Separation between the primary core and the companion as a function of time for the 256^3 *Enzo* simulations. The companion masses are 0.9 (blue), 0.6 (green), 0.3 (red), 0.15 (cyan) and 0.1 (purple) $M_{\odot}$.

As orbital energy is transferred to the envelope, the latter is ejected, initially in the orbital plane; at later phases there is an almost equal distribution of matter into the polar direction as well (Fig. 3.6). Overall, almost 90% of the envelope is ejected within an angle of 30° on each side of the equatorial plane. We compare the orbital velocity of the companion (Fig. 3.7) with the local sound speed of the gas (Fig. 3.3,

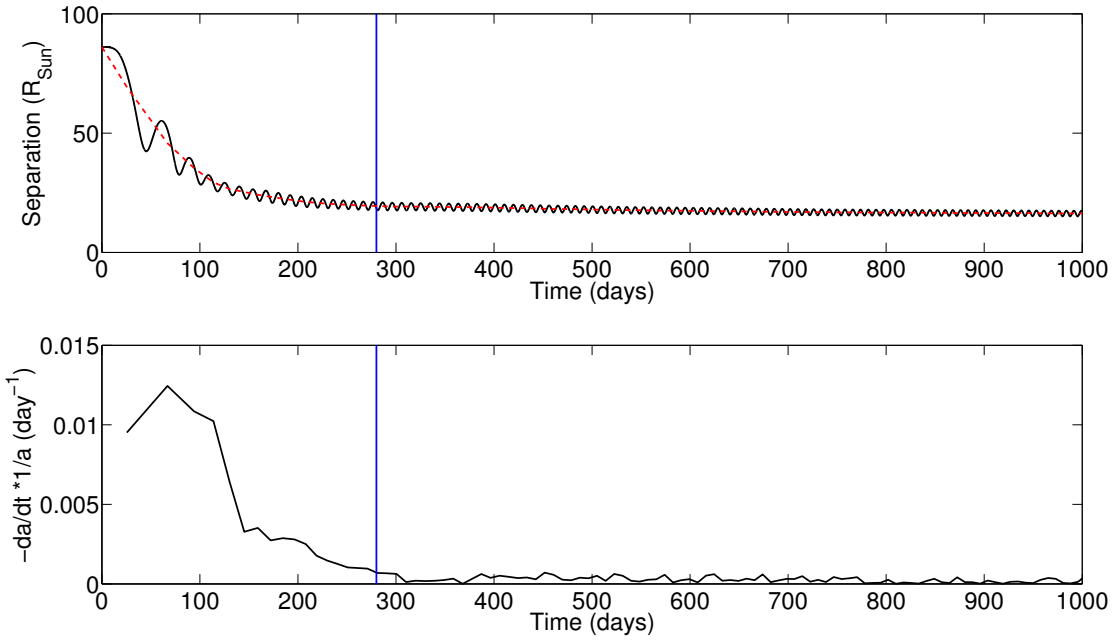

Figure 3.5 Evolution of the separation (top) and of the orbital decay (bottom) for Enzo7. The orbital decay is computed using orbital separations averaged over each cycle (red dashed line). The blue vertical line shows the time when we define the end of the rapid infall phase.

bottom left panel). The former does not exceed 50 $\mathrm{km\,s^{-1}}$ while the highest sound speed encountered is about 60 $\mathrm{km\,s^{-1}}$. The companion moves only slightly above or below the local sound speed. We therefore conclude that the SPH noise could not significantly influence the solution. Also, since the motion of the companion is not highly supersonic, the shocks are not strong and we can use *Enzo* with the faster Zeus solver.

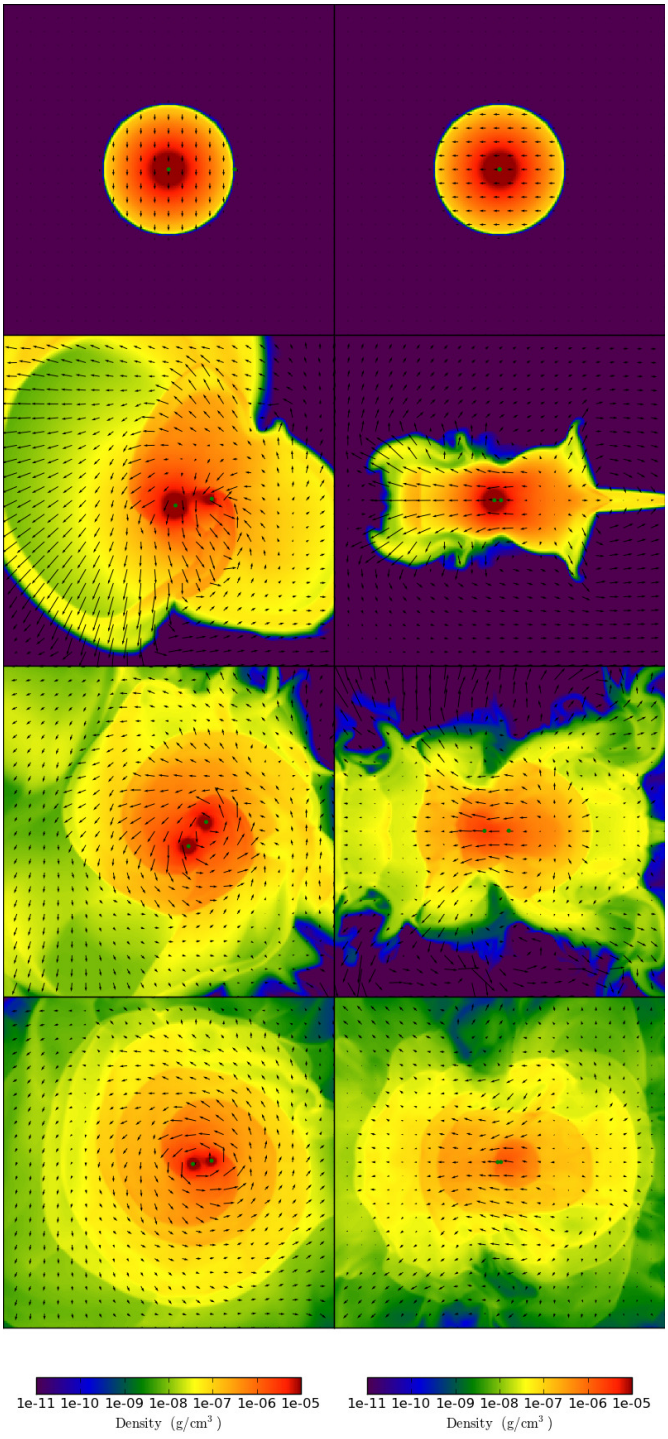

Figure 3.6 Density slices in the orbital plane (left) and in the perpendicular plane (right) at 0, 50, 85 and 130 days (from top to bottom) for the Enzo7 simulation. The scale used for the velocity vector field is the same on each frame and is such that the velocity shown on the top panel equals the initial orbital velocity of the primary ($\sim$ 23 $\mathrm{km\,s^{-1}}$).

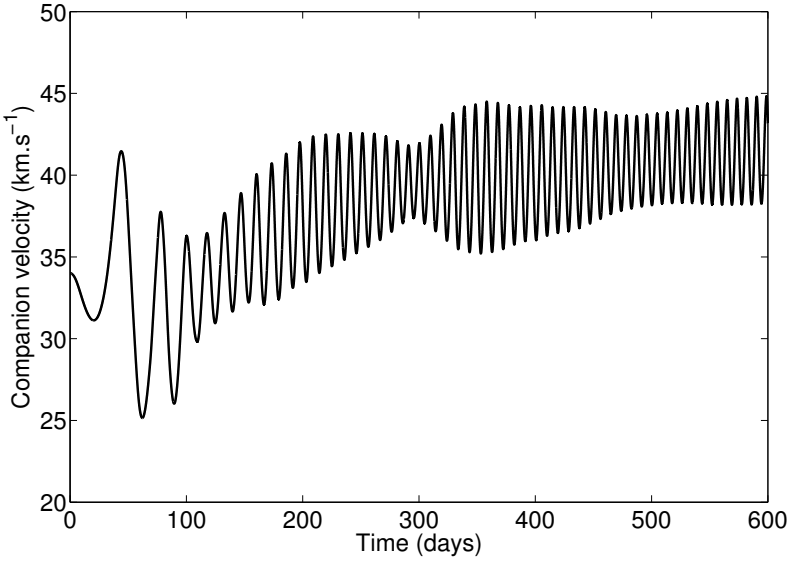

Figure 3.7 Evolution of the companion velocity for the Enzo7 simulation.

Unlike the SPH computational domain, the *Enzo* grid is spatially limited. Thus, the evolution of the gas that leaves the grid cannot be followed. Therefore, we use the SPH2 simulation to study the global evolution of the angular momentum and the energy of the system.

We compute the angular momentum using the center of mass of the SPH particles as the center of reference. As shown in Fig. 3.8 for the 0.6 $M_{\odot}$ companion case, the total angular momentum of the system is conserved to less than 1%. Since the ejection of the gas is asymmetric, the center of reference is eventually located outside the orbit. Consequently, studying the orbital components individually is irrelevant as the sign of each component changes during a single orbit. Therefore, we study their sum $J_{\rm orb}$ instead. During the first 50 days, angular momentum from the orbit almost equally spins up the envelope and unbinds mass from the outer layers. Later on, no more additional mass gets unbound (see § 3.5.1) and the angular momentum lost from the orbit spins up the bound envelope only. Since the unbound mass is located at large distances from the primary's core, there is no more exchange of angular momentum between the unbound mass and the rest of the system. After $\sim$ 150 days, there is no more angular momentum exchange in the system. The primary's core and the companion — which are the main contributors to the calculation of the centre of mass — switch positions twice per orbit, which leads to small periodic motions of

the center of mass. These periodic displacements are the causes for the small angular momentum fluctuations of the orbital components and the bound mass occurring after 100 days.

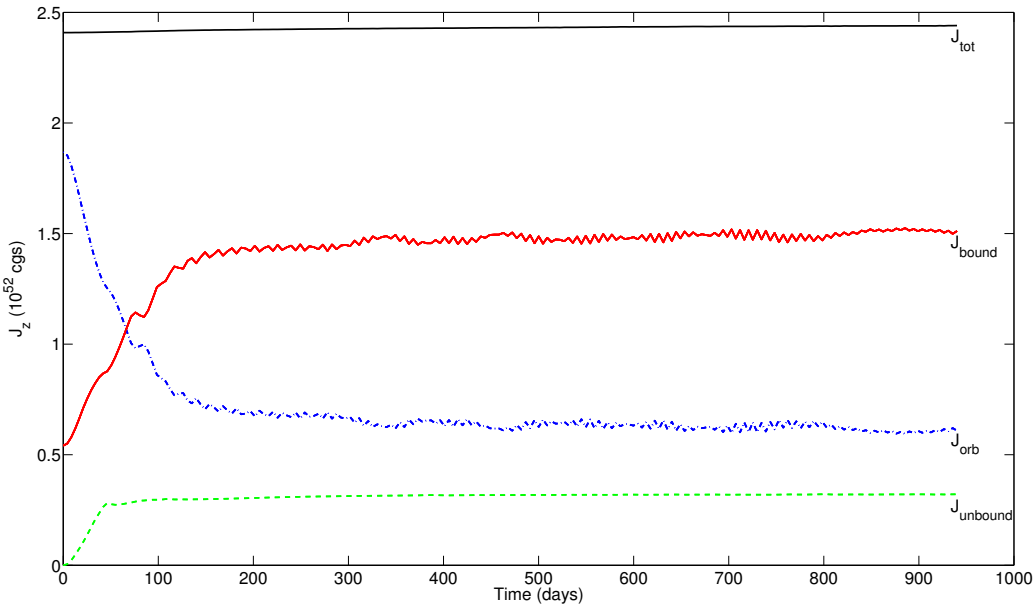

Figure 3.8 Evolution of the z-component of the total angular momentum ($J_{\rm tot}$), the angular momentum of the core and the companion ($J_{\rm orb}$), the angular momentum of the bound mass ($J_{\rm bound}$) and the angular momentum of the unbound mass ($J_{\rm unbound}$) for the SPH2 simulation.

We plot the various energy components in Fig. 3.9. We start by explaining the different components of potential, thermal and kinetic energies represent and how they are computed. Among numerous other attributes, each particle i possesses a specific gravitational potential energy ϕ_i, a specific thermal energy u_i and a specific macroscopic kinetic energy k_i. By definition,

$$\phi_i = \sum_{\text{j particles, j}\neq\text{i}} -G\frac{M_j^{\rm grav}}{r_{ij}} \tag{3.15}$$

where G is the gravitational constant, $M_j^{\rm grav}$ is the gravitational mass of particle j and r_{ij} is the distance between particles i and j. We compute these different components using the gravitational mass of the particle for the gravitational potential energy and the macroscopic kinetic energy, and the SPH mass for the thermal energy (see §3.3):

$$\Phi_i = M_i^{\rm grav} \phi_i \tag{3.16}$$

$$K_i = M_i^{\rm grav} k_i \tag{3.17}$$

$$U_i = M_i^{\rm sph} u_i \tag{3.18}$$

where $M_i^{\rm sph}$ is the SPH mass of particle i used to compute its acceleration due to pressure. We recall that both masses are identical for all particles except the primary's core and the secondary. Thus, the total gravitational potential energy of the system is

$$\Phi_{\rm tot} = \frac{1}{2} \sum_{\text{i particles}} \Phi_i \tag{3.19}$$

Finally, we subtract the contribution of the secondary from the total potential energy in order to calculate the binding energy of the envelope:

$$\Phi_{\rm env} = \Phi_{\rm tot} - M_2^{\rm grav} \phi_2 \tag{3.20}$$

where the subscript "2" stands for the secondary.

During the first 200 days when most of the in-spiral happens, the total internal energy of the system decreases by more than a factor of two: the envelope expands and therefore cools. The energy released is transferred mostly into macroscopic kinetic energy of the gas: the envelope is lifted up, accelerated and the outermost part of the envelope becomes unbound in the first 50 days. At later times, more energy is transferred from the orbit to the envelope but no more material becomes unbound. One can easily note in Fig. 3.9 how the variations of the orbital energy of the core-secondary system and of the total energy of the envelope balance each other. The total energy of the envelope remains negative throughout the simulation. We follow the evolution of the unbound particles and determine their initial position in the envelope. Fig. 3.10 shows the cumulative mass of the particles that will eventually get unbound as a function of their initial distance from the core. It confirms that the unbound mass was initially located in the outer part of the envelope and that almost all gas located initially closer than 40 $R_\odot$ from the primary's core remains bound at the end of the simulations.

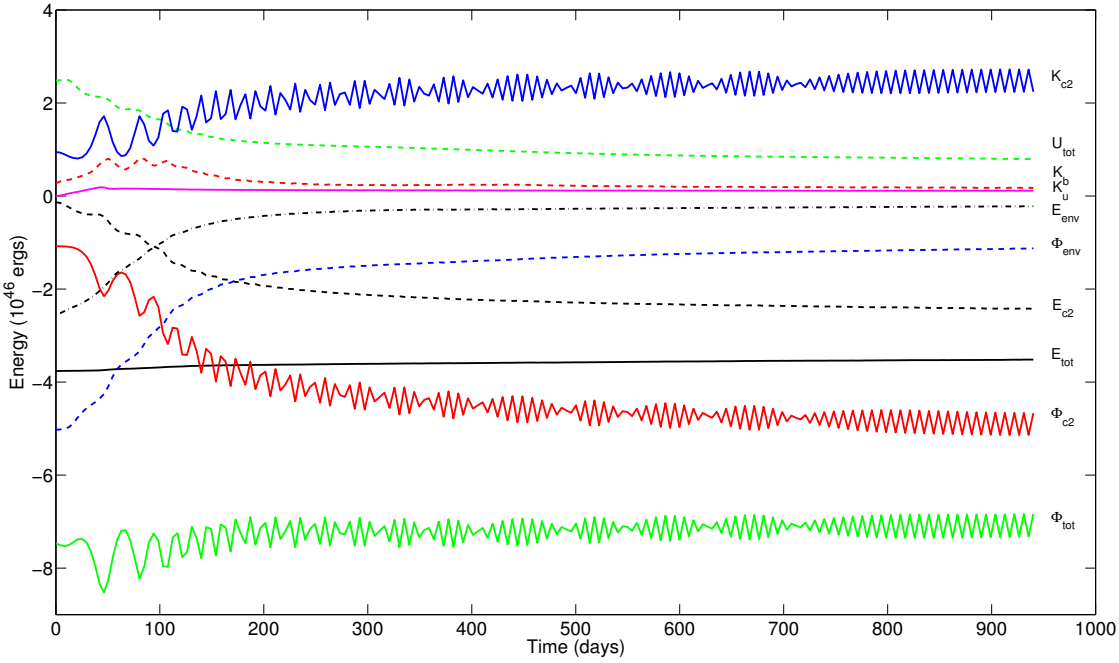

Figure 3.9 Energy components for the SPH2 simulations. Plotted are the total energy ($E_{\rm tot}$), the total gravitational potential energy $\Phi_{\rm tot}$, the internal energy of the system ($U_{\rm tot}$), the gravitational potential energy of the envelope ($\Phi_{\rm env}$), the gravitational potential energy from the core-companion interaction ($\Phi_{\rm c2}$), the kinetic energy of the core and the companion ($K_{\rm c2}$), the kinetic energy of the bound mass ($K_{\rm b}$), the kinetic energy of the unbound mass ($K_{\rm u}$), the orbital energy of the core-companion system ($E_{\rm c2}$) and the total energy of the envelope ($E_{\rm env} \equiv \Phi_{\rm env} + U_{\rm tot} + K_{\rm b}$). The beat frequency seen on K_{c2} and Φ_{c2} are due to the non-synchronization between the orbital period and the data dumping frequency.

3.4.2 Code comparison

The fact that a code solves the equations in an accurate and precise way in a particular situation does not necessary mean it will do so in another regime. Thus, a direct comparison of simulations of the CE interaction using two different numerical methods is a good solution for testing the ability of the two methods to model this problem. One can see in Fig. 3.11 and Table 3.1 that for each binary system, the final separations in the *Enzo* simulations are very close to those obtained with the equivalent *SNSPH* simulations. We may then compare the mass evolution of the material in the volume defined by the *Enzo* grid, the matter within the initial volume of the primary, and within the current separation. For the 0.6 $M_{\odot}$ companion (Fig. 3.12),

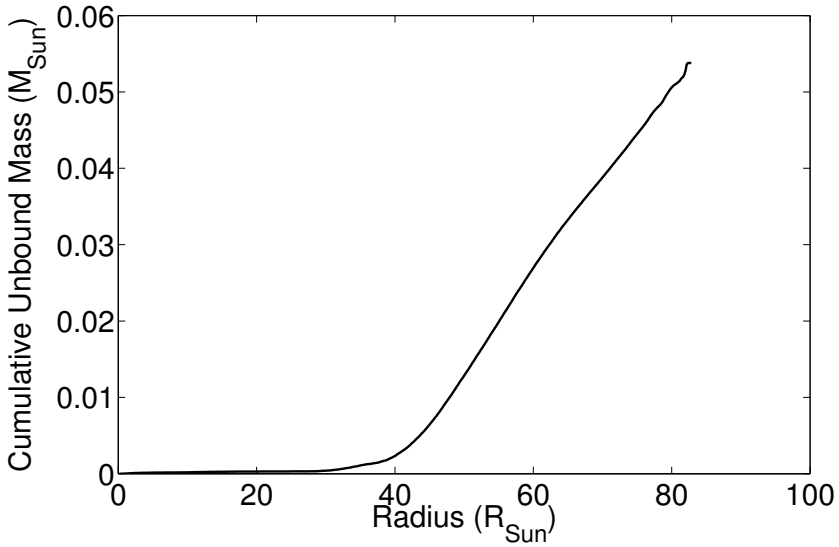

Figure 3.10 Initial distribution within the envelope of the mass that will eventually get unbound for SPH2.

both the mass within the *Enzo* grid and the mass within the initial volume of the progenitor agree well between the *Enzo* and the *SNSPH* runs. For the mass within the orbit we notice a difference of $\sim 10^{-2}\ M_{\odot}$ between the *Enzo* and the *SNSPH* runs. This difference is large compared with the mass of a SPH particle ($\sim 10^{-6}\ M_{\odot}$) and is due to how accurately accretion of the gas by the core and the companion is resolved by the two codes. We have plotted, in Fig. 3.13, density profiles at different times along the line joining the primary core and the secondary, for the three simulations with the 0.9 $M_{\odot}$ companion. Accretion onto the secondary is better resolved in the SPH simulations in which the maximum density of the matter accreted by the companion is about $10^{-3}\ \mathrm{g\,cm^{-3}}$. This maximum value depends on the resolution of the runs. In the single-grid *Enzo* runs, accretion is poorly resolved due to the low number of cells resolving the local region around each particle. Although mass is still accreted around the particles, it eventually becomes dispersed. For the SPH runs, around 60 particles interact within a smoothing length so the accretion zone is well resolved. On the other hand, the cell width of the *Enzo* 256^3 runs is about 1.6 $R_{\odot}$ so the accretion zone cannot be resolved although it is still better than for the *Enzo* 128^3 simulations as can be seen from comparing the different density profiles at 50 days (Fig. 3.13). However, the accurate simulation of accretion onto the secondary is not crucial for the global evolution of the system: as we mentioned earlier, the evolution

is not driven by accretion but by drag forces. Although the density of the matter accreted by the companion differs by up to 3 orders of magnitudes between the two methods, the accreted mass is negligible compared with the companion mass and the final orbital separations are very similar.

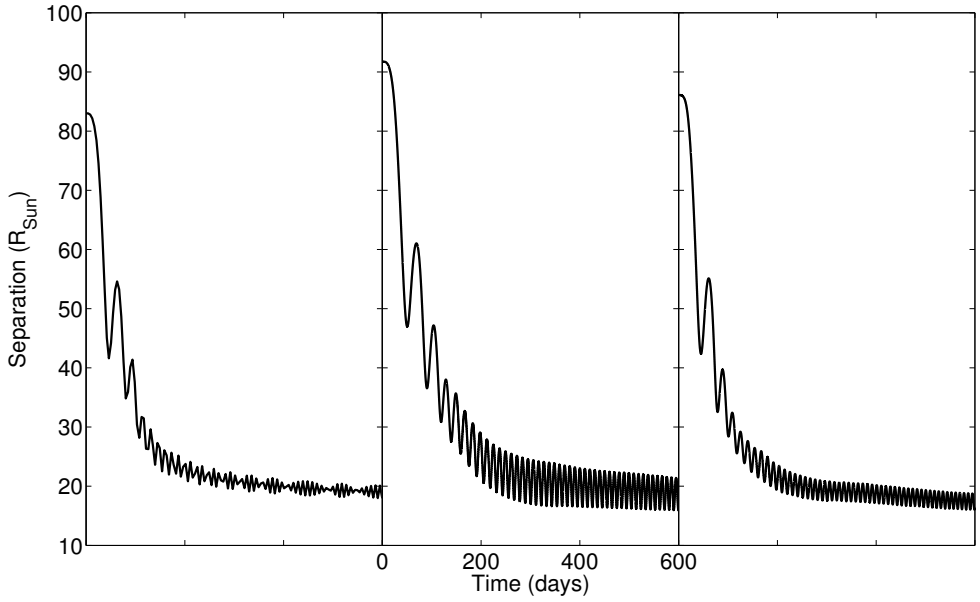

Figure 3.11 Separation between the core of the primary and the 0.6 $M_{\odot}$ companion as a function of time for the SPH2 (left), Enzo2 (middle) and Enzo7 (right) simulations. Again, the beat frequency seen in the SPH simulation is due to the non-synchronization between the orbital period and the dumping frequency.

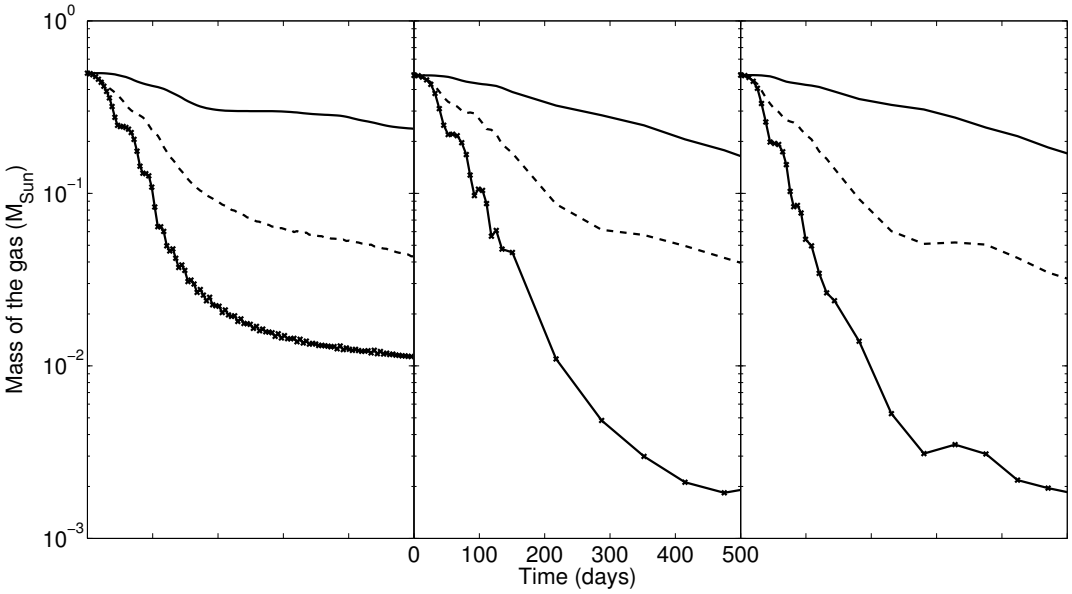

Figure 3.12 Each panel shows the mass within the equivalent *Enzo* grid (plain), the initial volume of the primary (dash) and the orbit (cross-solid) as a function of time for the SPH2 (left), Enzo2 (middle) and Enzo7 (right) simulations.

Ricker & Taam (2008) used the FLASH code (Fryxell et al., 2000) to study the CE evolution of a binary system consisting of a 1.05 $M_\odot$ RGB star having a 0.36 $M_\odot$ core and a 0.6 $M_\odot$ companion. Their implementation is somewhat different from ours since they treat the red giant core and the companion as spherical clouds of particles. In spite of those differences, their progenitor is almost identical to ours and they find a final separation of 20 $R_\odot$ which falls within the range of the results given by our simulations SPH2, Enzo2 and Enzo7. Moreover, one can see in Fig. 3.7 that for the 0.6 $M_\odot$ companion, the velocity of the companion stays below 50 $\mathrm{km\,s^{-1}}$ and therefore, the gas flows are subsonic except in the outer layers. This conclusion was also reached by Ricker & Taam (2008).

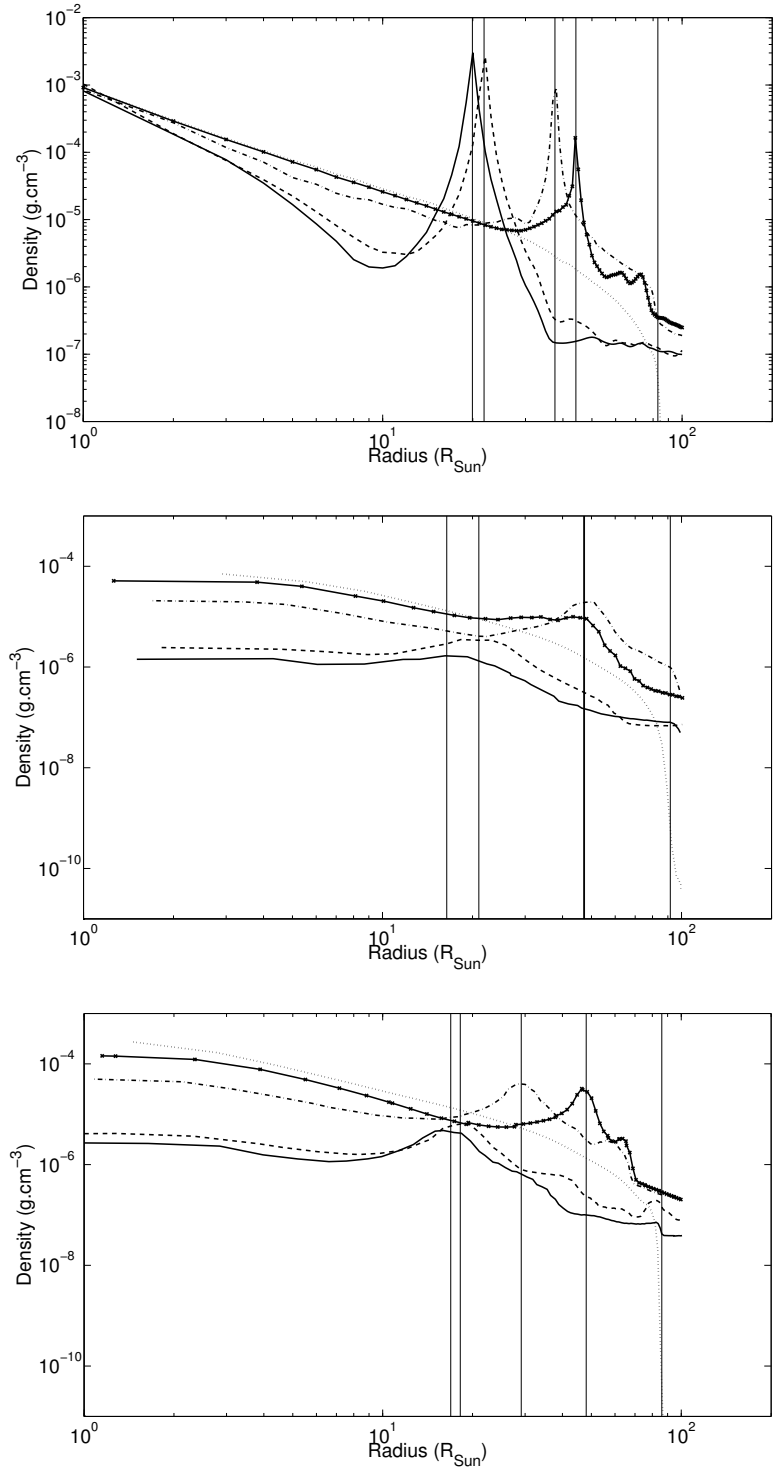

Figure 3.13 Density profiles along the line joining the core and the 0.6 $M_{\odot}$ companion at 0 (dotted line), 50 (dash-cross line), 100 (dash-dot line), 300 (dashed line) and 500 (solid line) days for SPH2 (top), Enzo2 (middle) and Enzo7 (bottom). The vertical lines show the position of the companion.

3.4.3 The impact of initial conditions

In order to determine the sensitivity of the final state of the system to the initial parameters, we start with the Enzo3 simulation and increase by 5% either the initial velocity of the secondary (Enzo11) or the initial separation between the two particles (Enzo12), which correspond to initial eccentricities of 0.10 (Enzo11) and 0.05 (Enzo12). The evolution of the separation for those three simulations is compared in Fig. 3.14. For Enzo11 and Enzo12, the ratio of the initial velocity of the companion to the velocity required for a circular orbit is higher than one ($v_0/v_{circ} > 1$), so the separation must first increase. The larger the orbital separation, the more delayed the rapid infall phase is and the later the system reaches its final separation. The final separations for Enzo3, Enzo11 and Enzo12 are 11.7, 12.0 and 12.2 $R_\odot$, respectively, and the final eccentricities are 0.09, 0.17 and 0.18, respectively. As expected, the companion that moves outwards the farthest initially, sinks into the envelope with a higher orbital decay velocity. Therefore, it attains a more eccentric orbit and completes fewer revolutions around the primary core (Fig. 3.14). However, the standard deviation of the final separation between the three simulations ($\sigma \sim 0.2\ R_\odot$) is more than 10 times smaller than the width of a cell. Consequently, we conclude that the final results are quite insensitive to the initial conditions at the level tested.

3.4.4 Gravitational vs Hydrodynamic drag

The drag exerted on the companion has two components: gravitational and hydrodynamical. The former is due to gravitational forces from matter flowing past the companion and colliding with its wake (Bondi & Hoyle, 1944; Iben & Livio, 1993), while the latter is due to ram pressure forces on the companion. The hydrodynamical contribution can be estimated as:

$$F_{\rm hydro} \sim \rho \mathbf{v}_2^2 \times \pi R_2^2 \tag{3.21}$$

where R_2 is the radius of the secondary, $\mathbf{v}_2$ is the relative velocity between the secondary and the envelope, and we have taken the coefficient of drag to be unity for simplicity. In a similar manner, the gravitational drag is approximated by (Iben & Livio, 1993):

$$F_{\rm grav} \sim \rho \mathbf{v}_2^2 \times \pi R_A^2 \tag{3.22}$$

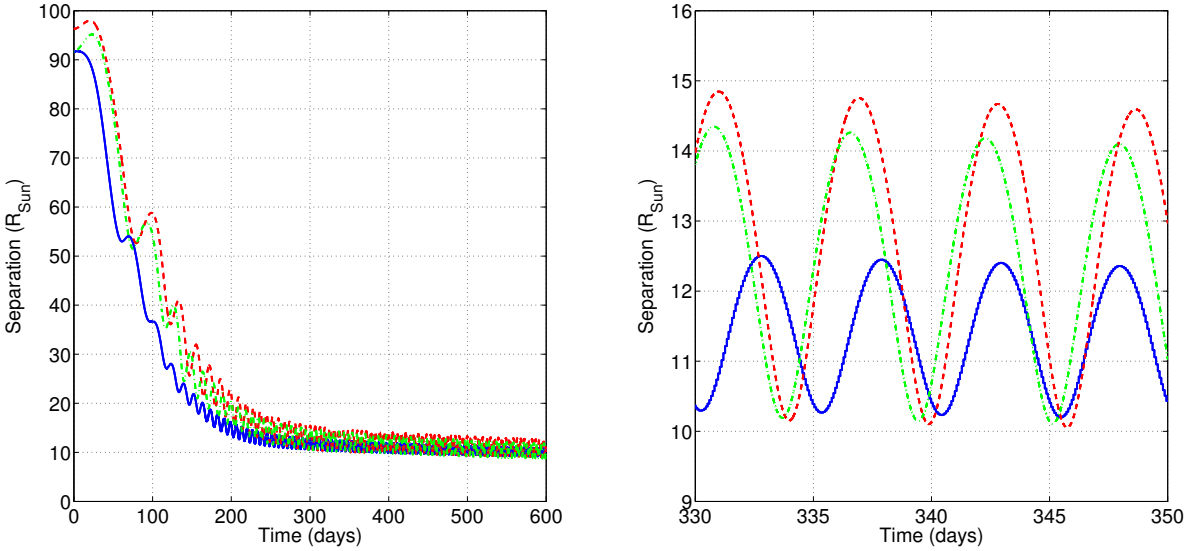

Figure 3.14 Left: separation between the core of the primary and the companion as a function of time for the Enzo3 (solid blue), Enzo11 (dashed red) and Enzo12 (dash-dot green) simulations. Right: a detail of the comparison from the left panel at ~ 340 days.

where the accretion radius R_A is defined as:

$$R_A = \frac{2GM_2}{\mathbf{v}_2^2 + c_s^2} \tag{3.23}$$

where c_s is the sound speed of the medium. Choosing $|\mathbf{v}| = 2c_s = 80 \ \ \mathrm{km\,s^{-1}}$ with an 0.6 $M_\odot$ companion yields $R_A \sim 30\ R_\odot$. Assuming $R_2 \sim 1\ R_\odot$, we conclude that the hydrodynamical drag is of the order of almost 1 000 times smaller than the gravitational drag, thus negligible.

This conclusion is also confirmed by the outcomes of our simulations. Indeed, the primary's core and the companion are treated as point masses and are not pressure sources, except for the primary's core in the *SNSPH* simulations. Instead of being caused by the finite size of the particles, hydrodynamical drag in the models is thus due to the matter accreted around them. We pointed out earlier that the accuracy with which accretion was treated was different between the two different models because of the different finest resolutions and softenings used: accretion is poorly modeled in the *Enzo* simulations whereas in the *SNSPH* simulations, the companion builds up a sphere of accreted matter about a few $R_\odot$ wide around itself (Fig. 3.13). This should lead to differences in the magnitude of hydrodynamic drag

forces. Nevertheless, the consistency of the results suggests that the hydrodynamic drag is unimportant in the evolution of the system, confirming the results of Ricker & Taam (2008).

3.5 Discussion

3.5.1 Comparison of simulations and observations

We now compare the numerical results with a sample of 61 observed post-CE systems listed in Zorotovic et al. (2010) and De Marco et al. (2011).

Final separations

For a given companion mass (or alternatively mass ratio q) we obtain 3 values for the final separation A_f, one for each simulation carried out with that companion mass (Table 3.1 and Fig. 3.15). One can distinguish between these values at high q ($q \geq 0.34$), which correspond to "heavy" companions ($M_2 \geq 0.3\ M_\odot$), and the ones at low q ($q < 0.34$) corresponding to "light" companions ($M_2 < 0.3\ M_\odot$). At high q, the values of A_f are very similar and the standard deviation is more than 20 times smaller than the average value of A_f. At low q, the companion sinks deeper and as a consequence, the resolution used in the 128^3 *Enzo* simulations is not sufficient. However, as one increases the resolution to 256^3 cells, the final separations converge to the solutions given by the *SNSPH* simulations.

Fig. 3.16 shows the distribution of orbital separations reached by the 61 post-CE systems. For all these systems, there has been no substantial orbital shrinkage due to phenomena such as magnetic braking or radiation of gravitational waves (see discussion in Schreiber & Gänsicke, 2003). Although they cover a significant range in secondary masses, going from a 1.1 $M_\odot$ MS star down to a 0.05 $M_\odot$ brown dwarf, all of them have separations smaller than 11 $R_\odot$. Furthermore, 87% of those systems have separations smaller than 4 $R_\odot$, which is smaller than any value obtained in our simulations. This is even more obviously shown in Fig. 3.17, where the final separations for simulations presented here and in the literature are compared to the orbital separations of the observed post-CE systems. Although a couple of observed systems have $q \geq 0.5$, one clearly sees that the simulations with $M_2 = 0.9$ and 0.6 $M_\odot$ leave the companion far out. Systems with lower mass companions ($M_2 \leq 0.3\ M_\odot$) have by and large lower orbital separations than in our simulations. The simulations

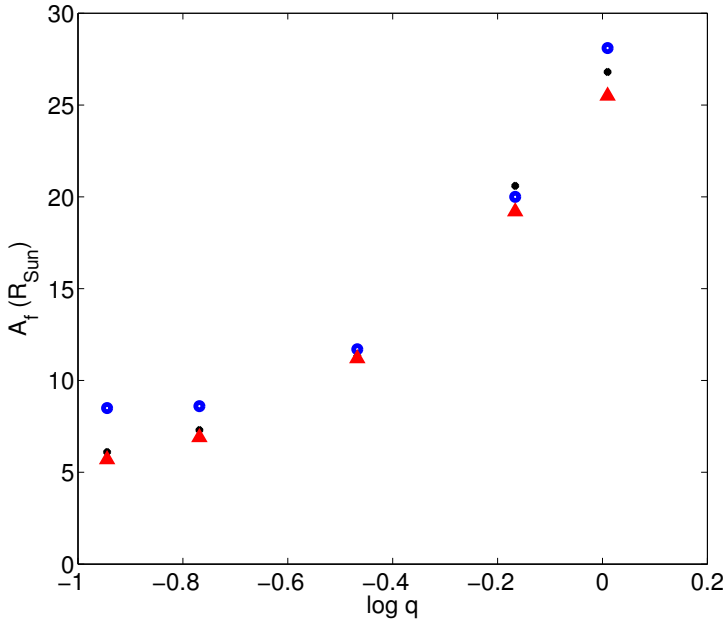

Figure 3.15 Final separations as a function of the mass ratio q for the *SNSPH* (black cross), *Enzo* 128^3 (blue circle) and *Enzo* 256^3 (red triangle) simulations.

of Sandquist et al. (1998) and Ricker & Taam (2008) shown in Fig. 3.17 give results consistent with ours. All these numerical simulations suggest that the separations between the secondary and the primary's remnant at the end of the simulated rapid infall phase are too large to explain the orbital separation of the currently observed post-CE systems. This suggests that further evolution of the orbital separation must occur during the phase immediately following the rapid infall phase. We discuss this point further in §3.5.2.

The state of the envelope at the end of the simulations

As shown in Table 3.2, most of the primary's envelope remains bound in all of our simulations. We study the situation in detail for our canonical model with the 0.6 $M_\odot$ companion here. The evolution of the mass for different components is plotted in Fig. 3.18. It first confirms that some envelope mass is unbound only during the first 50 days, after which neither angular momentum (Fig. 3.8) nor kinetic energy (Fig. 3.9) are exchanged between the unbound mass and the rest of the system. It also shows that more than 85 % of the mass remains bound at the end of the simulation. This

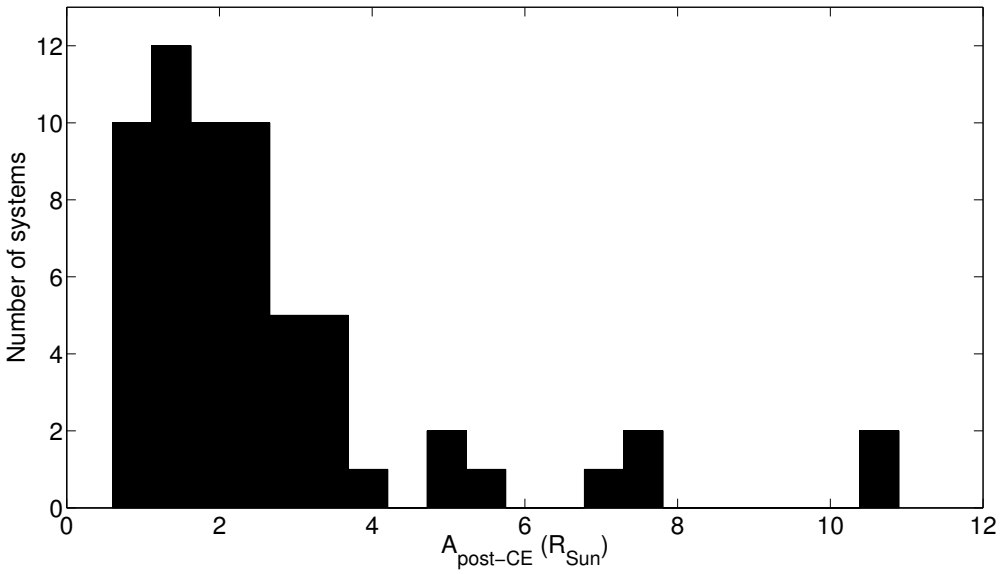

Figure 3.16 Distribution of post-CE systems as a function of their observed orbital separation from Zorotovic et al. (2010) and De Marco et al. (2011).

outcome, already pointed out by Sandquist et al. (1998), is quite intriguing, since the post-CE binaries observed must have succeeded in ejecting their envelope. After about 400 days, most of the envelope mass in our models has been moved to a larger radius ($\sim 100\ R_\odot$, see bottom panel in Fig. 3.19), well outside the orbit of the primary core and the companion but remaining bound.

We now investigate how bound the final system is. We consider the center of mass of the system composed by the secondary and the mass within the current orbit as the center of our frame of reference. Then, we partition the domain into concentric shells with identical thickness, calculate the average radial velocity of each shell and compare it to the escape velocity at that location. Fig. 3.19 shows the escape velocity and the average radial velocity of the shells. The radial velocity is always positive and is similar to the space velocity at radii larger than 600 $R_\odot$, as expected for envelope ejection. At radii smaller than 300 $R_\odot$, the radial velocity is much smaller than the space velocity, suggesting that orbital motions dominate at those radii. All the mass within 10^3 $R_\odot$ is bound, which corresponds to more than 85% of the envelope mass. The remaining mass is found at radii between 10^3 and 6×10^3 $R_\odot$, where the radial velocities are typically between 25 and 75 $\mathrm{km\,s^{-1}}$. Those particles were initially in the outer parts of the giant star, and were the first to encounter the secondary. At

Table 3.2. Amount of the envelope mass still bound at the end of the *SNSPH* simulations.

Name	M_2 ($M_\odot$)	$M_{\rm bound}$ ($M_\odot$)[a]
SPH1	0.9	0.44
SPH2	0.6	0.44
SPH3	0.3	0.45
SPH4	0.15	0.46
SPH5	0.1	0.48

[a]At the start of the simulations, $M_{\rm bound}$ equals the total envelope mass $M_e \equiv M_1 - M_c = 0.49\ M_\odot$

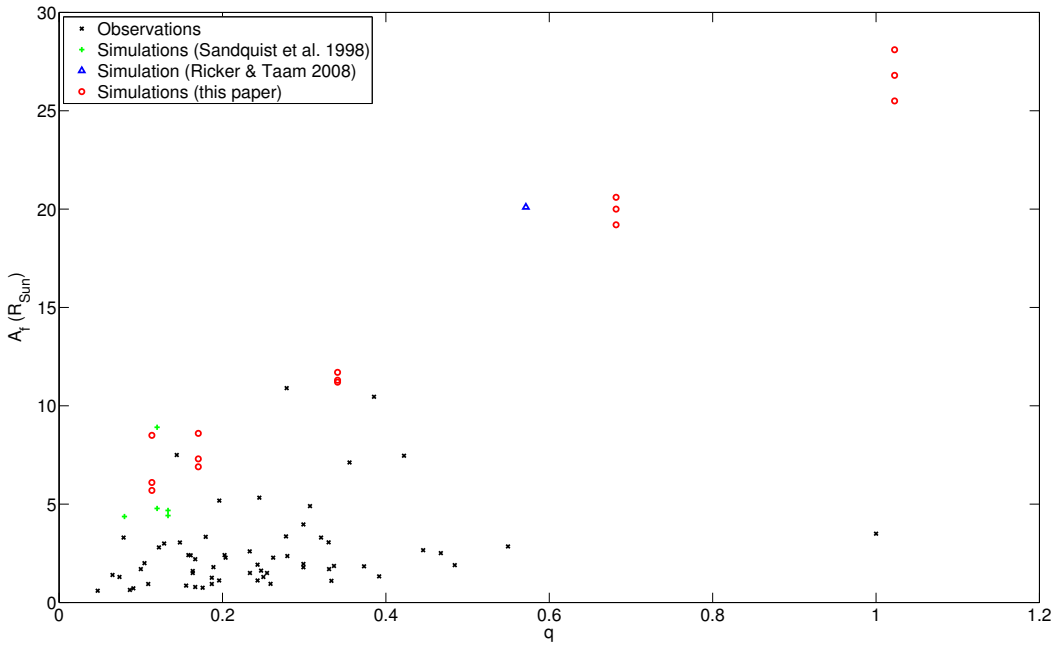

Figure 3.17 Comparison between the orbital separations of observed post-CE systems (black dot) and the final separations reached at the end of the simulations (red circle), as well as the ones by Sandquist et al. (1998) (green circles) and by Ricker & Taam (2008) (blue triangle).

that time of the in-spiral, the shock was slightly supersonic ($V_2 \sim 35$ km s^{-1} and $c_s \sim 20$ km s^{-1}). This regime of evolution is thus different from later phases when the secondary sinks deeper into the primary's envelope, where its velocity does not really increase (Fig. 3.7) but the sound speed of the medium does (Fig. 3.3).

We can measure how much extra energy would be required to unbind the envelope at each radius, using the definition

$$E_{\rm extra} = \sum_i \frac{1}{2} M_i \left(v_{e,i} - v_{r,i}\right)^2 \tag{3.24}$$

where $v_{e,i}$ and $v_{r,i}$ are the escape velocity at the location of the i-th shell and its average radial velocity, respectively. One finds $E_{\rm extra} \sim 8.4 \times 10^{45}$ ergs which represents just over 10% of the initial binding energy of the primary envelope. Thus, a relatively small additional input of energy could be sufficient to completely unbind the remaining envelope material.

We have compared here the final separations deduced from observations and those determined from the simulations. We have purposefully stayed away from calculating

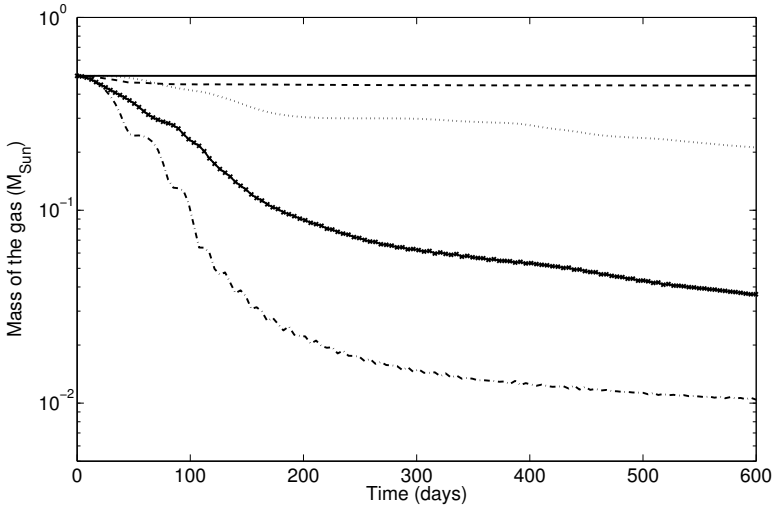

Figure 3.18 Evolution of the total mass (solid line), the bound mass (dashed line), the mass within the volume of the *Enzo* grid (dotted line), the mass within the initial volume of the primary (dash-cross line) and the mass within the orbital separation (dash-dot line) for the SPH2 simulation.

the ejection efficiency α (Webbink, 1984; De Marco et al., 2011). Indeed, we question what the relevance of calculating α is when the envelope has not yet been fully ejected, true both in the Sandquist et al. (1998) and our simulations. We therefore defer for the moment the task of calculating α from simulations — a long term goal of this project — until the simulations are more advanced.

In conclusion, the hydrodynamic simulations do not reproduce the post-CE systems in the sense that the system is left at too large separations and the envelope is not unbound at the end of the rapid infall phase. This means that either physical processes that are not accounted for in the simulations are responsible for the envelope ejection, or the envelope ejection and a significant reduction of the orbit actually happens during the later subsequent slow in-spiral phase. We discuss both possibilities in the following section.

3.5.2 Reproducing the observations

In this section we first study and quantify physical processes that are not taken into account in our hydrodynamic simulations and that might be responsible for ejecting the envelope. Then, we focus on the subsequent slow in-spiral phase and investigate

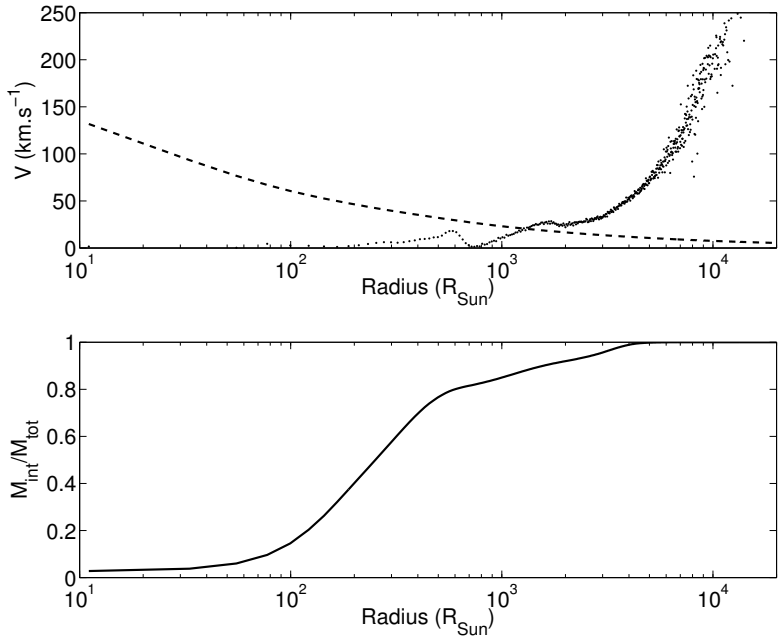

Figure 3.19 Top: Comparison between the escape velocity (dashed line) and the radial velocity (black dots) of the final system for the SPH2 simulation. Bottom: Mass enclosed as a function of radius.

whether the envelope can be ejected and the separation significantly reduced during this subsequent phase.

Rotation of the primary

The envelope of the progenitor is initially non-rotating and although the calculation done in §3.3 shows that, regardless of the initial rotation velocity of the envelope, its rotational energy is negligible in comparison with its binding energy, we suspected at first that the absence of rotation might be the reason for most of the envelope to remain bound. However, Sandquist et al. (1998) carried out two identical simulations where they modified the initial rotation state of the primary from a giant star in synchronization with the orbit to a non-rotating one (their simulations 1 and 2). In both cases, the evolution of the bound mass and the final orbital parameters are similar. It thus does not seem that changing the initial rotation of the primary leads to a different CE outcome.

Physics not included in the simulations

The hydrodynamics codes use an ideal gas equation of state (§3.2.1) which, by definition, does not include variable abundances and the different ionization layers of the envelope. Han et al. (1995) suggested that recombination might play a role in CE interactions. As the outer parts of the envelope expand and cool, ions recombine with electrons, releasing energy that could aid in unbinding the envelope. Although it is unclear how efficient this process is and how much of the initial recombination budget can be used, one can calculate an upper limit on how much energy can be injected into the envelope by recombination.

According to our stellar evolution model, the hydrogen fraction within the convective envelope of our RGB star is $X \sim 0.68$. The mass of the envelope is $M_e = 0.49\ M_\odot$ and each proton recombining with an electron produces an energy $E_0 = 13.6$ eV. We also have to calculate how much of the envelope is ionized. Therefore, we calculate the partition functions Z for hydrogen. The hydrogen ion has no degeneracy so $Z_2 = 1$. The partition function for the hydrogen atom at temperature T is

$$Z_1 = \sum_{n=1}^{\infty} 2n^2 \exp \frac{E_0(1/n^2 - 1)}{kT} \tag{3.25}$$

where $k = 8.6173 \times 10^{-5}$ eV K^{-1} is the Boltzmann constant. We truncate the sum in Eq. 3.25 at the first integer $n_{\max}$ such that the distance at which the electron orbits the proton for this quantum number is larger than $l_{\max} = 10^{-6}$ cm, i.e. $a_0 n_{\max}^2 > l_{\max}$, where $a_0 = 5.2918 \times 10^9$ cm is the Bohr radius (Miranda, 2001). We then use the Saha formula to calculate the ratio of ionized to neutral hydrogen (Carroll & Ostlie, 2006):

$$N_2/N_1 = \frac{2Z_2}{n_e Z_1} \left(\frac{2\pi m_e kT}{h^2} \right)^{3/2} \exp\left(-E_0/kT\right) \tag{3.26}$$

where n_e is the number density of free electrons and m_e is the electron mass. We find that 91% of the envelope is ionized. Consequently, the recombination of the whole ionized envelope would produce an extra energy

$$E_{\rm recomb} = 0.91 \times X M_e \frac{N_A}{M_H} \times 13.6 \text{ eV} \tag{3.27}$$

where N_A is the Avogadro number and M_H the atomic mass of hydrogen. One finds $E_{\rm recomb} \sim 1.18 \times 10^{46}$ ergs, which is slightly higher than the extra energy $E_{\rm extra}$

required to eject the envelope in our canonical model (§3.5.1). Thus, we conclude that recombination in the envelope could substantially aid in unbinding it.

Another source of energy could be radiation pressure. For low- and intermediate-mass giants in hydrostatic equilibrium, radiation pressure ($P_{rad} \equiv aT^4/3$, where a is the radiation constant) is negligible compared to gas pressure (Eq. 3.4): for our primary, $P_{rad}/P_{gas} \lesssim 0.01$ except in a small zone ($0.1\ R_\odot \leq r \leq 10\ R_\odot$), where $P_{rad}/P_{gas} \lesssim 0.1$. However, the deep in-spiral of the companion within the primary's envelope will induce local shock heating. The increase of temperature is proportional to the square of the Mach number (Tarbell et al., 1999), so even if the companion is orbiting at twice the local sound speed, the radiation pressure to gas pressure after the shock becomes:

$$\left(\frac{P_{rad}}{P_{gas}}\right)^{\text{after}} \propto \left(\frac{P_{rad}}{P_{gas}}\right)^{\text{before}} (M^2)^3 = 6.4 \tag{3.28}$$

Therefore, including radiation pressure in the equation of state will increase the total pressure locally and might reduce the energy required to eject the envelope. However, it is possible that this effect is globally small, since this extra heating source is probably very localized around the companion.

The post-rapid-infall phase

At the end of the rapid infall phase, the orbit is stable until the end of the simulations (a few more years). Consequently, there is no further hydrodynamical coupling between the extended envelope and the surviving binary. We now investigate whether the envelope is likely to be ejected during this slower in-spiral phase.

Although the resolution of the simulations prevents us from quantifying how much envelope will be left around the core of the primary, one can still describe qualitatively what the evolution of the primary's remnant will be. Fig. 3.18 shows that less than $10^{-2}\ M_\odot$ is left around the primary's core, so the primary will depart the giant branch (Bloecker 1995a, but see also the discussion in De Marco et al. 2011). Then two scenarios might occur depending on how long the partially ejected envelope will take to fall back.

If the star is given enough time to transit to the blue due to hydrogen burning at the base of the envelope before the lifted envelope falls back, the star will readjust on its thermal timescale of the remaining envelope, and eventually end its life as a Helium white dwarf. This transition will last $\sim 10^3$ years during which the star will

have a luminosity between 300 and 1 000 $L_\odot$ (Iben & Tutukov, 1993, their Fig. 1), which is consistent with the more recent work of Driebe et al. (1998) (their Fig. 1). If we assume the remnant to have a luminosity $L_c \sim 500\ L_\odot$, we can compare the gravitational acceleration of a gas particle with the radiation acceleration defined by

$$a_{rad} = \frac{L_c}{4\pi r^2}\frac{\kappa}{c} \tag{3.29}$$

where r is the distance between the gas particle and the core, $\kappa = 0.4\ \mathrm{cm}^2\, g^{-1}$ is the opacity for Thompson scattering for hydrogen, and c is the speed of light. We still find the radiation acceleration to be overall almost two orders of magnitude smaller than the gravitational acceleration.

If, on the contrary, the envelope falls back before the primary's remnant had crossed the Hertzsprung-Russell diagram, a circumbinary disk will form (Kashi & Soker, 2011). They refer to the numerical work done by Artymowicz et al. (1991), which suggests that in such a configuration, the binary separation will decrease due to Lindblad resonances — mainly — as well as viscous tides. Although this mechanism has the advantage of explaining how the orbital separation will diminish during the subsequent phase, the ability of radiation to eject the gas will even be reduced in comparison with the previous situation, so it is not clear how the latter will eventually be unbound.

In conclusion, radiation acceleration alone does not seem to be responsible for unbinding the remaining gas, regardless of the time the partially ejected envelope will remain suspended for.

3.6 Summary

In this work we have carried out three-dimensional hydrodynamic simulations of the CE interaction between a 0.88 $M_\odot$ RGB star and companions with mass ranging from 0.1 to 0.9 $M_\odot$. We have used both an Eulerian grid code (*Enzo*) and a Lagrangian SPH code (*SNSPH*) with various resolutions. They both have advantages and disadvantages and can be used for different purposes: while one might rather use SPH to study the accretion around the secondary, even a uniform grid code is more suitable in resolving the low-density extended envelope. Of course, adaptive mesh refinement combines the advantages of both of these methods at the cost of increased code complexity.

We first compared the outcomes of those simulations with each other. We found that the results are very similar for companion masses $M_2 \gtrsim 0.3\ M_\odot$. We thus conclude that in this regime, the resolutions used are sufficient to study the global evolution of the system during the rapid infall phase of the interaction, which is driven mainly by gravitational drag. For lower companion masses ($M_2 \lesssim 0.3\ M_\odot$) that penetrate deeper in the giant's envelope, the 128^3 *Enzo* runs are under-resolved but the *Enzo* results converge to the solutions from the *SNSPH* simulations.

We then compared the outcomes of our simulations with observed post-CE systems. The final separations are found to be systematically higher than those deduced from observations, as is the case for the past simulations by Sandquist et al. (1998), De Marco et al. (2003) and Ricker & Taam (2008). Moreover, mass is only unbound during the early stages of the interaction ($\sim$ 50 days for the 0.6 $M_\odot$ companion) and most of the envelope remains bound at the end of the simulations, as was the case for the earlier simulations of Sandquist et al. (1998). We investigated whether there might be additional processes that were not accounted for in the simulations. We found that recombination can contribute significantly, but stellar rotation and radiation pressure play only marginal roles. Finally, we wondered whether the bound envelope is a result of imprecise simulations or a real physical feature. If the latter, then one would have to follow the subsequent evolution of the system to determine the actual outcome of the CE. Fall back disks may form and even have an impact on the inner binary (Artymowicz et al., 1991, Kashi & Soker 2011).

After the submission of this paper, Ricker and Taam made their paper Ricker & Taam (2012) available. This paper continues the work introduced in Ricker & Taam (2008). In their simulation, only about 25 % of the primary's envelope is unbound. Although this value is slightly higher than ours, it is in agreement with our work in the sense that most of the envelope remains bound. They also claim that the ejection occurs mostly in the orbital plane, as it is the case in our simulations. However, the extended envelope at the end of their simulation is rotating much faster than it is expanding which is in contradiction with our results (§ 3.5.1) but might be due to the fact that their primary is initially rotating.

Chapter 4

The Response of Giant Stars To Dynamical-Timescale Mass Loss

Originally published as Passy, J.-C., Herwig, F., & Paxton, B. 2012, ApJ, 760, 90

Abstract

We study the response of giant stars to mass loss. One-dimensional simulations of red and asymptotic giant branch stars with mass loss rates from 10^{-3} up to a few $M_{\odot}$/yr show in no case any significant radius increase. The largest radius increase of 0.2% was found in the case with the lowest mass loss rate. For dynamical-timescale mass loss rates, that may be encountered during a common envelope phase, the evolution is not adiabatic. The superadiabatic outer layer of the giant's envelope has a local thermal timescale comparable to the dynamical timescale. Therefore, this layer has enough time to readjust thermally. Moreover, the giant star is driven out of hydrostatic equilibrium and evolves dynamically. In these cases no increase of the stellar radius with respect to its initial value is found. If the mass loss rate is high enough, the superadiabaticity of the outer layer is lost progressively and a radiative zone forms due to a combination of thermal and dynamical readjustment. Conditions for unstable mass transfer based on adiabatic mass loss models that predict a significant radius increase, may need to be re-evaluated.

4.1 Introduction

Understanding how stars respond when they lose mass is a key ingredient on which binary evolution models depend. This response is particularly important in the context of interacting binaries with a donor filling its Roche lobe on a giant branch. In the oversimplifying case of conservative mass transfer, the orbital separation shrinks if the giant donor is more massive than the companion. If in the meantime the giant star expands or does not contract faster than the orbit shrinks, this positive feedback leads to an increase of the mass transfer rate. The stellar response to mass loss therefore dictates, along with how angular momentum is lost, whether or not a given system enters a common envelope phase (Paczynski, 1976). Consequently, it significantly affects the results of population synthesis studies (see, e.g., Politano et al., 2010).

Also, detailed 3D hydrodynamical simulations of the dynamical common envelope phase have shown that a giant's simulated envelope material is significantly lifted, but most of it does not reach escape velocity under the present modeling assumptions (Passy et al., 2012; Ricker & Taam, 2012). De Marco et al. (2011) suggested that an expansion of the giant as a result of mass loss (Hjellming & Webbink, 1987; Ge et al., 2010) might contribute to the envelope ejection. Such an expansion of mass-losing giants was recently questioned in a *Letter* by Woods & Ivanova (2011).

Therefore, we study the radius response of mass-losing giants again, with detailed microphysics, using the one-dimensional stellar evolution code MESA (Module for Experiment in Stellar Astrophysics, Paxton et al., 2011). Such a tool – although it neglects three-dimensional effects – allows us to remove one or more simplifying assumptions adopted in some previous studies, which we mention in the next paragraphs.

For a star following a polytropic stratification of index n with an adiabatic index $\gamma = 1 + 1/n$, the Lane-Emden equation leads to the *mass-radius relation* between a standard solution of radius R_0 and mass M_0, and a perturbed polytrope of radius R and mass M:

$$\frac{R}{R_0} = \left(\frac{M}{M_0}\right)^{\frac{1-n}{3-n}}. \tag{4.1}$$

Note that Equation (4.1) is only valid for a fixed adiabat throughout the stellar interior. For the complete derivation, see, e.g., Hjellming & Webbink (1987) or Carroll

& Ostlie (2006). For an ideal gas equation of state, the specific entropy follows a simple expression:

$$s(m) = s_0 + (1 + 1/n - \gamma)c_v \ln(\rho) \tag{4.2}$$

where s_0 is a constant and c_v is the specific heat at constant volume. Perfect monoatomic gases have $\gamma = 5/3$, and so a convective region ($ds/dm = 0$) can be modeled with a polytrope of index $n = 3/2$. Using this value in Equation (4.1) leads to $R/R_0 = (M/M_0)^{-1/3}$ and the conclusion that fully convective stars expand when they lose mass.

Later on, Hjellming & Webbink (1987) investigated the stability of polytropes, condensed polytropes (a polytropic envelope with a core modeled by a point mass) and composite polytropes (an envelope and a core with different polytropic indices) for convective ($\gamma = 1 + 1/n$) and radiative ($\gamma > 1 + 1/n$) regions. They evolved their models in the adiabatic regime, which means that they assumed hydrostatic equilibrium and an adiabatic evolution such that the entropy profile remains constant in Lagrangian coordinates. For the condensed polytropes, they showed (their Equation 40) that the *adiabatic radius-mass exponent*, $\xi_{\rm ad}$, asymptotically approaches

$$\xi_{\rm ad} \equiv \left(\frac{d\ln R}{d\ln M}\right)_{\rm ad} = \frac{1}{3-n}\left(1 - n + \frac{m_c}{1-m_c}\right) \tag{4.3}$$

where m_c is the ratio between the core mass and the total mass of the star. Equation (4.3) describes the behavior of $\xi_{\rm ad}$ in the limit $m_c \to 1$ but one also recovers the appropriate $\xi_{\rm ad}$ for a complete polytrope for any value of n ($m_c = 0$, Equation 4.1). However, the response of stars to very high mass loss rates may not be hydrostatic. Moreover, Equation (4.3) is only valid for condensed polytropes which are models that neglect radiation pressure and do not reproduce the superadiabatic regime that is encountered in the outer layers of giants.

Ge et al. (2010) also studied the response of mass-losing stars in the adiabatic limit but used a detailed equation of state instead of a polytropic stratification. The star was assumed to stay in hydrostatic equilibrium, and its response to mass loss was assumed to be fully adiabatic. The entropy and composition profiles were fixed and the local value of these profiles during the evolution was obtained by interpolation from the initial model. For their 1 $M_\odot$ giant star model, the stellar radius increased by 30%. The study concluded that instability in the mass transfer occurs rapidly for donors with a convective envelope, if at all, while donors with a radiative envelope

may encounter a delayed dynamical instability. Deloye & Taam (2010) used a similar approach to study the common envelope outcomes of 10 $M_\odot$ donors. They found that the mass of the remnant can vary by 20% depending on when the common envelope phase happens and on the initial mass ratio.

All the models above yield a paradigm in which giants expand as a result of mass loss, such that mass loss that starts in semi-detached binaries with a giant donor tends to be unstable. However, for typical mass loss rates encountered at the onset of a common envelope interaction ($\dot{M} \lesssim 1\ M_\odot$/yr, Passy et al. 2012), the donor does not stay in hydrostatic equilibrium. Moreover, an adiabatic evolution assumes that mass loss happens on a timescale shorter than the thermal timescale of the mass-losing star throughout its interior.

Recently, Woods & Ivanova (2011) showed that the evolution could be locally non-adiabatic, since the outer superadiabatic layer of giant stars has a thermal timescale so short that it might readjust and reconstruct faster than it is stripped away. They present the evolutionary sequence of a 5 $M_\odot$ giant star for various mass loss rates, and show that the star grows mildly in radius during its evolution (their Figure 3). They also calculate the critical mass ratio for stable mass transfer for different donors. These values are only indicative but show that the response of the mass-losing star evolves with mass loss and cannot be parametrized using only the binary and stellar parameters.

In this paper we present models of mass-losing stars by removing some of the assumptions made in previous investigations. We obtain these models using the stellar evolution code MESA. The numerical method is described in Section 4.2. We present the simulations in Section 4.3 and verify our method with low-mass zero-age main sequence (ZAMS) models in Section 4.4. We then study in detail the dynamical response of red giant branch (RGB) and asymptotic giant branch (AGB) stars, and describe the physical processes involved, in Section 4.5. A summary and conclusions are provided in Section 5.1.4.

4.2 Numerical method

MESA is a parallel one-dimensional stellar evolution code that uses adaptive mesh refinement and adaptive time stepping. In this section, we outline the basic features of this code. More details can be found in Paxton et al. (2011).

In hydrodynamic mode, the full set of differential equations of stellar evolution is

solved in the Lagrangian description:

$$v = r\frac{d\ln r}{dt} \tag{4.4}$$

$$\frac{d\ln r}{dm} = \frac{1}{4\pi r^3\rho} \tag{4.5}$$

$$\frac{dv}{dt} = -4\pi r^2\frac{dP}{dm} - \frac{Gm}{r^2} \tag{4.6}$$

$$\frac{d\ln T}{dm} = \frac{d\ln P}{dm}\nabla \tag{4.7}$$

$$\frac{dl}{dm} = \epsilon_{\rm nuc} - \epsilon_\nu - c_P T\left[(1-\nabla_{\rm ad}\chi_T)\frac{d\ln T}{dt} - \nabla_{\rm ad}\chi_\rho\frac{d\ln\rho}{dt}\right] \tag{4.8}$$

where the mass m is the independent variable and r, ρ, P, T, l, $\nabla \equiv d\ln T/d\ln P$, $\epsilon_{\rm nuc}$, ϵ_ν, c_P, $\nabla_{\rm ad} \equiv (d\ln T/d\ln P)_s$, s, v and G are the radius, the density, the pressure, the temperature, the luminosity, the temperature gradient, the nuclear energy generation rate, the neutrino loss rate, the specific heat at constant pressure, the adiabatic gradient, the specific entropy, the velocity and the gravitational constant, respectively. In addition, $\chi_T \equiv (d\ln P/d\ln T)_\rho$ and $\chi_\rho \equiv (d\ln P/d\ln\rho)_T$. To close this set of equations, we obtained the equation of state from a set of tables computed with the *FreeEOS*[1] code, developed by Alan Irwin, in the EOS4 configuration.

In order to improve numerical stability we use some artificial viscosity following the treatment by Weaver et al. (1978, their Equation 3). Aside from providing better stability for the code, artificial viscosity had no effect on the evolution based on comparison of sequences carried out with or without artificial viscosity.

Different options have been explored for modeling stellar mass loss. We first directly set the mass loss rate $\dot{M}$ to a constant value regardless of the evolutionary stage. In order to show the robustness of the results, we also study how the models respond to a variable mass loss rate, for instance a scaled up wind model (Reimers, 1975):

$$\dot{M} = \eta_{\rm R}\times 4\times 10^{-13}\left(\frac{L}{L_\odot}\right)\left(\frac{R}{R_\odot}\right)\left(\frac{M_\odot}{M}\right) \quad [M_\odot/{\rm yr}] \tag{4.9}$$

where L is the luminosity and $\eta_{\rm R}$ is a dimensionless constant. We select values of $\eta_{\rm R}$

[1] http://freeeos.sourceforge.net/

to model very high mass loss rates. Typical models for RGB winds use values of $\eta_{\rm R}$ around 0.5.

4.3 The simulations

We perform 21 MESA simulations (Table 4.1). We first investigate the behavior of low-mass ZAMS stars (models 1 to 4) in order to verify our method through a comparison with the results of Ge et al. (2010) for such models. We then study the stellar response of a 0.89 $M_\odot$ RGB star (models 5 to 9) in hydrodynamic mode for various mass loss rates. Models 10 to 13 are equivalent to models 5 to 8 except that they are carried out in hydrostatic mode, such that dynamical effects are isolated. Additional sequences for a 0.74 $M_\odot$ AGB star (models 14 and 15) and for a 5 $M_\odot$ RGB star (models 16 to 18) allow comparison with the results of Woods & Ivanova (2011). We also verify that changing the atmosphere boundary conditions from the "simple atmosphere" default option to the "Eddington grey" option (model 19) does not modify the outcome of our simulations (these options are described in Paxton et al., 2011). In order to verify that the initial response of the star is captured accurately in our simulations, we finally examine extra models (models 20 and 21) which are similar to models 8 and 17, but with an initial timestep smaller by an order of magnitude. Time-stepping automatically readjusts and we find no difference between the corresponding models.

4.4 Low-mass zero age main sequence stars

Low-mass ZAMS stars provide a simple case to compare our method — solving the full set of stellar equations — with the method used in Ge et al. (2010) — assuming an adiabatic evolution (c.f. Section 4.1). Indeed, the global thermal timescale of a 0.3 $M_\odot$ ZAMS star is

$$t_{\rm KH} \equiv \frac{GM^2}{RL} \approx 7.7 \times 10^8 \text{ years}, \tag{4.10}$$

which is several orders of magnitude longer than the duration of the different sequences for the mass loss rates considered (Table 4.1). Consequently, the star does not have enough time to readjust thermally throughout its entire interior. Moreover, one can calculate the local thermal timescale of the outer part of the star (Woods &

Table 4.1. The main parameters for the simulations

Model	$M_{\rm MS}/{\rm M}_\odot$	$M_0/{\rm M}_\odot$	$M_c/{\rm M}_\odot$	$R_0/{\rm R}_\odot$	$L_0/{\rm L}_\odot$	$\dot{M}$	Hydro
1	0.30	0.30	-	0.28	1.3×10^{-2}	$10^{-2}\ M_\odot$/yr	No
2	0.40	0.40	-	0.35	2.3×10^{-2}	$10^{-2}\ M_\odot$/yr	No
3	0.50	0.50	-	0.45	4.1×10^{-2}	$10^{-2}\ M_\odot$/yr	No
4	0.30	0.30	-	0.28	1.3×10^{-2}	$0.1\ M_\odot$/yr	No
5	1.00	0.89	0.41	102	1.20×10^{3}	$10^{-3}\ M_\odot$/yr	Yes
6	1.00	0.89	0.41	102	1.20×10^{3}	$10^{-2}\ M_\odot$/yr	Yes
7	1.00	0.89	0.41	102	1.20×10^{3}	$0.1\ M_\odot$/yr	Yes
8	1.00	0.89	0.41	102	1.20×10^{3}	$1.0\ M_\odot$/yr	Yes
9	1.00	0.89	0.41	102	1.20×10^{3}	$\eta_{\rm R} = 10^{6}$	Yes
10	1.00	0.89	0.41	102	1.20×10^{3}	$10^{-3}\ M_\odot$/yr	No
11	1.00	0.89	0.41	102	1.20×10^{3}	$10^{-2}\ M_\odot$/yr	No
12	1.00	0.89	0.41	102	1.20×10^{3}	$0.1\ M_\odot$/yr	No
13	1.00	0.89	0.41	102	1.20×10^{3}	$1.0\ M_\odot$/yr	No
14	1.00	0.74	0.52	111	1.37×10^{3}	$0.5\ M_\odot$/yr	Yes
15	1.00	0.74	0.52	111	1.37×10^{3}	$1.0\ M_\odot$/yr	Yes
16	5.00	4.99	0.61	50	8.85×10^{2}	$10^{-2}\ M_\odot$/yr	Yes
17	5.00	4.99	0.61	50	8.85×10^{2}	$1.0\ M_\odot$/yr	Yes
18	5.00	4.99	0.61	50	8.85×10^{2}	$\eta_{\rm R} = 2 \times 10^{7}$	Yes
19[a]	1.00	0.89	0.41	102	1.20×10^{3}	$0.1\ M_\odot$/yr	Yes
20[b]	1.00	0.89	0.41	102	1.20×10^{3}	$1.0\ M_\odot$/yr	Yes
21[c]	5.00	4.99	0.61	50	8.85×10^{2}	$1.0\ M_\odot$/yr	Yes

Note. — The main parameters for the simulations: the model number, the main sequence mass of the star ($M_{\rm MS}$), the stellar (M_0) and core (M_c) masses, radius (R_0), and luminosity (L_0) at the start of the mass loss phase, the mass loss rate or Reimers parameter ($\dot{M}$), and whether or not the model is carried out in hydrodynamic mode.

[a]Similar to model 7 but with different boundary conditions.

[b]Similar to model 8 but with an initial timestep ten times smaller.

[c]Similar to model 17 but with an initial timestep ten times smaller.

Ivanova, 2011):

$$t_{\rm KH,loc}(m) \equiv \int_m^M u(m^{'})/L(m^{'})\ dm^{'} \tag{4.11}$$

where u is the internal energy per unit mass and m is the mass coordinate. Equation (4.11) implicitly assumes that one can parse the stellar interior at any mass coordinate into an outer and an inner zone, and that the outer zone can thermally readjust independently. This might not strictly be the case in a convective region where convective overturn is usually shorter than the thermal timescale of a given zone, thus stabilizes thermal perturbations on a timescale shorter than the thermal timescale of the zone. Figure 4.1 shows that even the outermost 0.01% of the mass needs about 1000 years to thermally readjust to the perturbations induced by mass loss. Again, this timescale is much longer than the duration of the simulations (25 years for the 0.3 $M_{\odot}$ ZAMS star with a mass loss rate of 10^{-2} $M_{\odot}$/yr, model 1), and so the outer layers cannot thermally readjust. The evolution of the mass-losing star is thus adiabatic, both locally and globally. Among low-mass ZAMS stars, those with lower mass have deeper convective envelopes. The lowest-mass ZAMS stars ($M \lesssim 0.3\ M_{\odot}$) are fully convective, and so should be well approximated by a polytropic expansion ($\xi_{\rm ad} = -1/3$, Equation 4.3).

We carry out simulations where the mass-losing star is a ZAMS star with a mass ranging from 0.3 to 0.5 $M_{\odot}$ (models 1 to 4). The resolution is approximately 1000 zones. We reproduce the results from Ge et al. 2010 quite accurately (their Figure 3). For all models, the radius of the mass-losing star increases as mass is lost (Figure 4.2), in particular the 0.3 $M_{\odot}$ model, which is almost fully convective and therefore behaves most like a polytrope (Equation 4.1). One should emphasize that the small difference between the 0.3 $M_{\odot}$ model and the polytropic limit arise from deviations of the stellar structure from a complete polytrope. We try different mass loss rates of 10^{-2} and 10^{-1} $M_{\odot}$/yr for the 0.3 $M_{\odot}$ star (models 1 and 4, respectively) and find no difference whatsoever. The evolution for both mass loss rates is much too rapid to allow any local thermal readjustment of the outer parts of the star (Figure 4.1). In conclusion, the evolution of low-mass ZAMS stars is fully adiabatic. Thus, the approximation by Ge et al. (2010) is appropriate for these low-mass main-sequence stars.

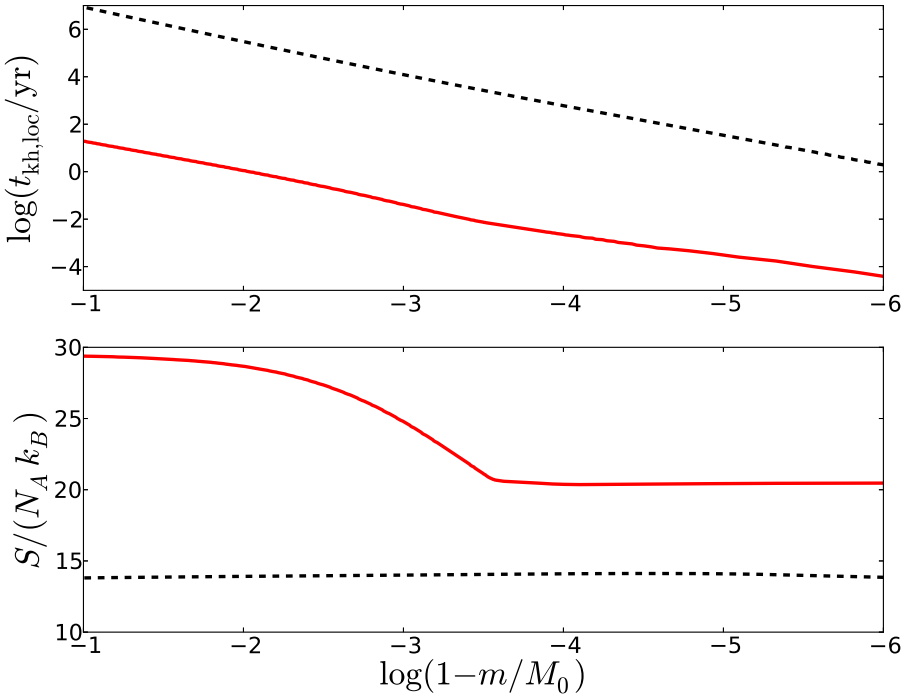

Figure 4.1 The local thermal timescale (top) and specific entropy (bottom) in the outermost 10% of the stellar mass for the $M_0 = 0.3\ M_\odot$ ZAMS star (dashed black, models 1 and 4) and the $M_0 = 0.89\ M_\odot$ RGB star (solid red, models 5 to 8 and 14).

4.5 Giant stars

The case of giant stars is somewhat more complicated. Giant stars have a convective envelope in which the entropy profile is flat. For intermediate-mass giant stars, the global thermal timescale of the star is still large in comparison with its dynamical timescale, and so the stellar interior cannot thermally readjust during most simulations. However, intermediate-mass giants also possess a cool, low-density outer layer in which convection is very inefficient. The local thermal timescale of this superadiabatic layer is very short in comparison with the global thermal timescale of the star: the outermost 1% of the mass thermally readjusts in approximately one year (Figure 4.1). Therefore, the layer might have enough time to thermally readjust locally, depending on how the local thermal timescale of the superadiabatic layer and the time needed to strip it away compare. Assuming that the layer has a mass $m_{\rm shell}$, its local thermal timescale is $t_{\rm KH,loc}(m_{\rm shell})$ and it takes $m_{\rm shell}/\dot{M}$ to remove it. This leads to a critical mass loss rate:

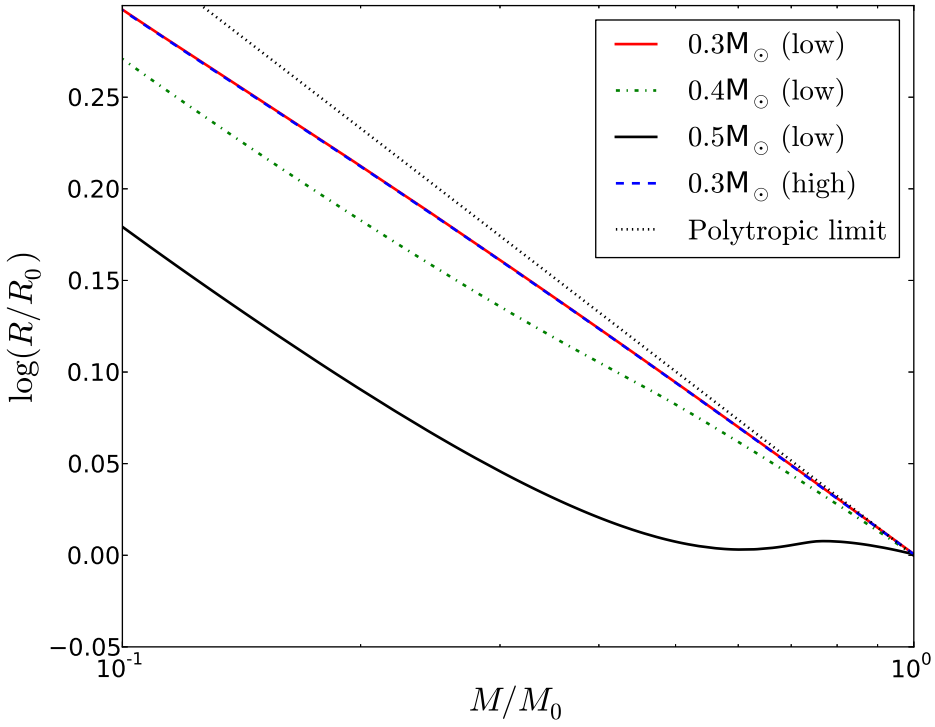

Figure 4.2 The evolution of the stellar radius as a function of stellar mass in terms of the initial radius (R_0) and mass (M_0) of the ZAMS models (1 to 4) with mass loss rates $\dot{M} = 10^{-2}\ M_\odot$/yr (low) and $\dot{M} = 0.1\ M_\odot$/yr (high). Also shown is the evolution in the polytropic limit (Equation 4.1).

$$\dot{M}_{\rm crit} \approx \frac{m_{\rm shell}}{t_{\rm KH,loc}(m_{\rm shell})} \tag{4.12}$$

which gives the threshold for the readjustment of the superadiabatic layer. If $\dot{M} \ll \dot{M}_{\rm crit}$, the superadiabaticity cannot be removed and the outer layer thermally readjusts. If $\dot{M} \gtrsim \dot{M}_{\rm crit}$, the outer layer does not have time to readjust and superadiabaticity is lost progressively. The higher the mass loss rate, the sooner the superadiabatic layer disappears entirely, after which the star evolves adiabatically. A similar argument has been made by Woods & Ivanova (2011), except that we consider here the time required to remove the superadiabatic layer rather than the time to strip away the entire star, as they did in their Equation 3. There is no unique definition of this outer layer, but for our 0.89 $M_\odot$ RGB model one can estimate from the entropy profile that $m_{\rm shell}$ is about $10^{-3}\ M_\odot$ and $t_{\rm KH,loc}(m_{\rm shell}) \approx 0.04$ year, which leads to a critical value for the mass loss rate $\dot{M}_{\rm crit} \approx 2.5 \times 10^{-2}\ M_\odot$/yr.

4.5.1 The canonical case of a 0.89 $M_{\odot}$ red giant branch star

In this section, we first study the canonical case of a 0.89 $M_{\odot}$ RGB star, and compare our results to the adiabatic models from Ge et al. (2010). We carry out hydrodynamic simulations with constant mass loss rates ranging from 10^{-3} to 1 $M_{\odot}$/yr (models 5 to 8) and one model with a varying mass loss rate (model 9). We also carry out their hydrostatic counterparts (models 10 to 13) in order to compare with previously published models, and to demonstrate the error a hydrostatic assumption causes. The resolution for all the one-dimensional models discussed here is approximately 2500 zones.

We plot in Figure 4.3 the evolution of the stellar mass and the mass loss rate for models 5 to 9, while the evolution of the stellar radius for models 5 to 14 is shown in Figure 4.4. Mass-losing giants barely expand, if at all. The difference between the hydrodynamic and the hydrostatic models for the lowest mass loss rate ($\dot{M} = 10^{-3}$ $M_{\odot}$/yr, models 5 and 10) is hardly noticeable. This is due to the fact that for such a low mass loss rate, the star is barely driven out of hydrostatic equilibrium. A comparison between the acceleration ($a = dv/dt$) and the gravitational acceleration ($g = Gm/r^2$) profiles confirms that this model stays in hydrostatic equilibrium (Figure 4.5). If one increases the mass loss rate to 10^{-2} $M_{\odot}$/yr, some marginal differences arise in the very early phase of evolution between the hydrodynamic and the hydrostatic models. This is the threshold for which hydrodynamic effects can no longer be neglected, as the acceleration in the outer parts of the giant represents almost 1% of the gravitational force at that location. These effects naturally increase as the mass loss rate increases.

Hydrodynamic models for which dynamical effects cannot be neglected (models 6 to 9) all contract in the early evolutionary phase. The higher the mass loss rate, the more the stellar radius decreases (Figure 4.4). Later on, differences arise as stars with high mass loss rates keep contracting while stars with lower $\dot{M}$ first re-expand slightly and then contract again. For the model with $\dot{M} = 10^{-2}$ $M_{\odot}$/yr (model 6), the radius of the star grows by less than 5%. We certainly do not see the 30% expansion found in Ge et al. (2010) for a 1 $M_{\odot}$ giant star (their Figure 6). Model 8, for which the shrinkage is most dramatic, considers a typical mass loss rate that is encountered during a common envelope evolution. On the other hand, the equivalent hydrostatic "test" models (models 11 to 13) all show an expansion of the radius, with the higher mass loss rates leading to the largest increases. This behavior is

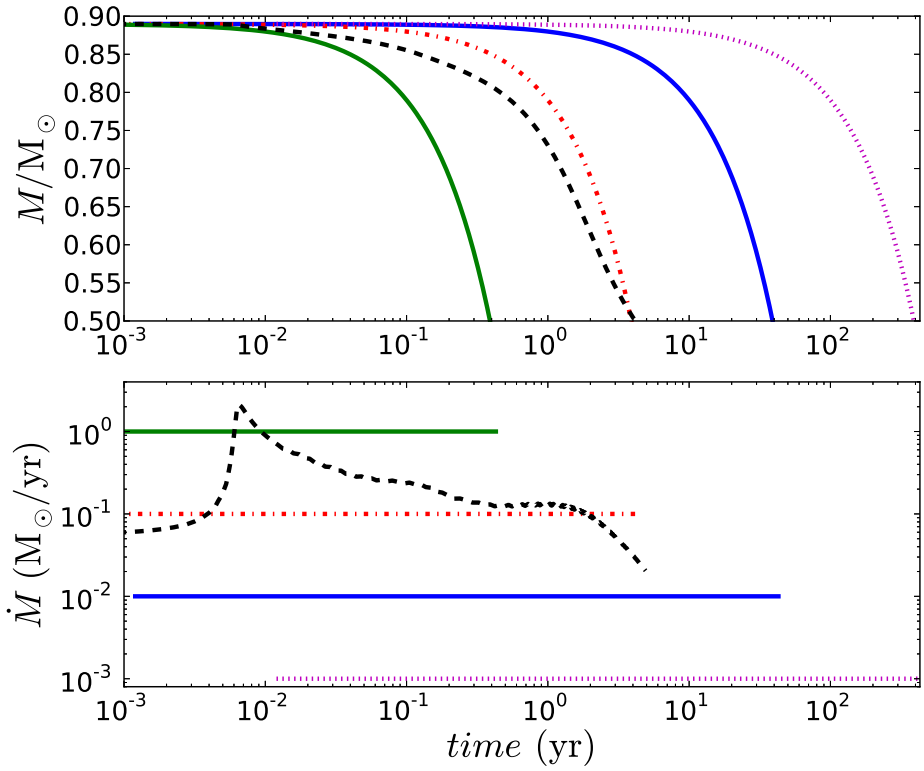

Figure 4.3 The evolution of the mass (top) and the mass loss rate (bottom) for the 0.89 $M_\odot$ RGB star with mass loss rates of 10^{-3} $M_\odot$/yr (dotted magenta, model 5), 10^{-2} $M_\odot$/yr (solid blue, model 6), 0.1 $M_\odot$/yr (dash-dotted red, model 7), 1 $M_\odot$/yr (solid green, model 8), and variable (dashed black, model 9).

similar to sequences by Woods & Ivanova (2011, their Figure 3). This comparison demonstrates that dynamical aspects play a critical role in the stellar response of our model. Some energy that would be transformed into internal energy or expansion work in the hydrostatic assumption can now go into kinetic energy.

In order to understand the reasons for these different behaviors, we plot in Figure 4.6 entropy profiles at different times for models 6, 7 and 8. The evolution of the entropy differs significantly between cases with different mass loss rates. For the lowest mass loss rate ($\dot{M} = 10^{-2}$ $M_\odot$/yr, model 6), the entire interior has enough time to adjust thermally. After 40% of the initial stellar mass has been lost, the star has still the entropy profile similar to the one of a giant star stratification. For the intermediate mass loss rate ($\dot{M} = 0.1$ $M_\odot$/yr, model 7), very little of the outer layer loses its superadiabaticity in the early phase. Eventually, the interior of the star has not changed except in the outermost parts. Moreover, the superadiabatic layer is

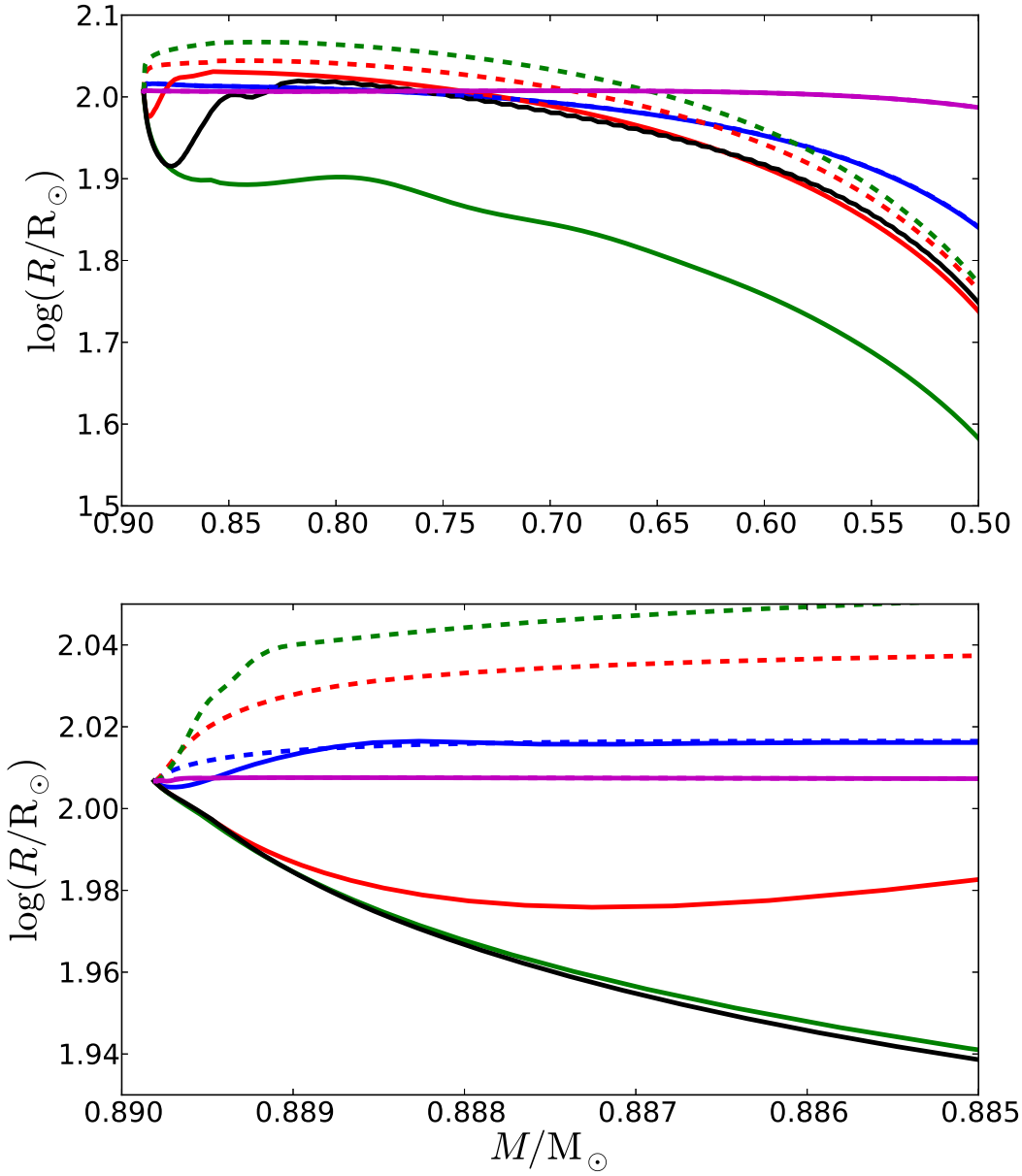

Figure 4.4 Top: evolution of the stellar radius as a function of stellar mass for the 0.89 $M_{\odot}$ RGB star with mass loss rates of 10^{-3} $M_{\odot}$/yr (magenta), 10^{-2} $M_{\odot}$/yr (blue), 0.1 $M_{\odot}$/yr (red), 1 $M_{\odot}$/yr (green), and variable (black). Both hydrodynamic (solid) and hydrostatic sequences (dashed) are shown. Bottom: a close-up of the early evolution of the sequences shown above.

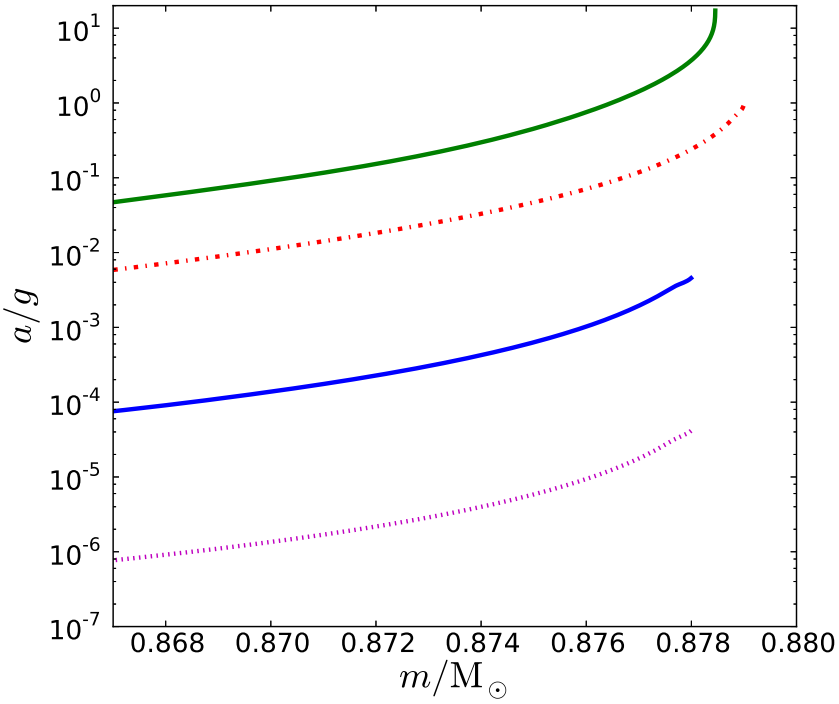

Figure 4.5 Ratio between the acceleration and the gravitational acceleration after the 0.89 $M_{\odot}$ RGB star star has lost about 10^{-2} $M_{\odot}$. The mass loss rate is (from bottom to top) 10^{-3} $M_{\odot}$/yr (dotted magenta, model 5), 10^{-2} $M_{\odot}$/yr (solid blue, model 6), 0.1 $M_{\odot}$/yr (dash-dotted red, model 7), and 1 $M_{\odot}$/yr (solid green, model 8).

much less prominent than for a regular giant star stratification, and a radiative zone has developed just beneath it. In the highest mass loss rate case ($\dot{M}$ = 1 $M_{\odot}$/yr, model 8), one can see the superadiabaticity being removed very early in the evolution and the build-up of a radiative zone. Eventually, the surface is not superadiabatic anymore. The entropy profile of the interior layers has not changed and the mass for which the entropy drops is negligible. Only a small radiative zone remains on top of the convective zone (Figure 4.6, middle and bottom panels).

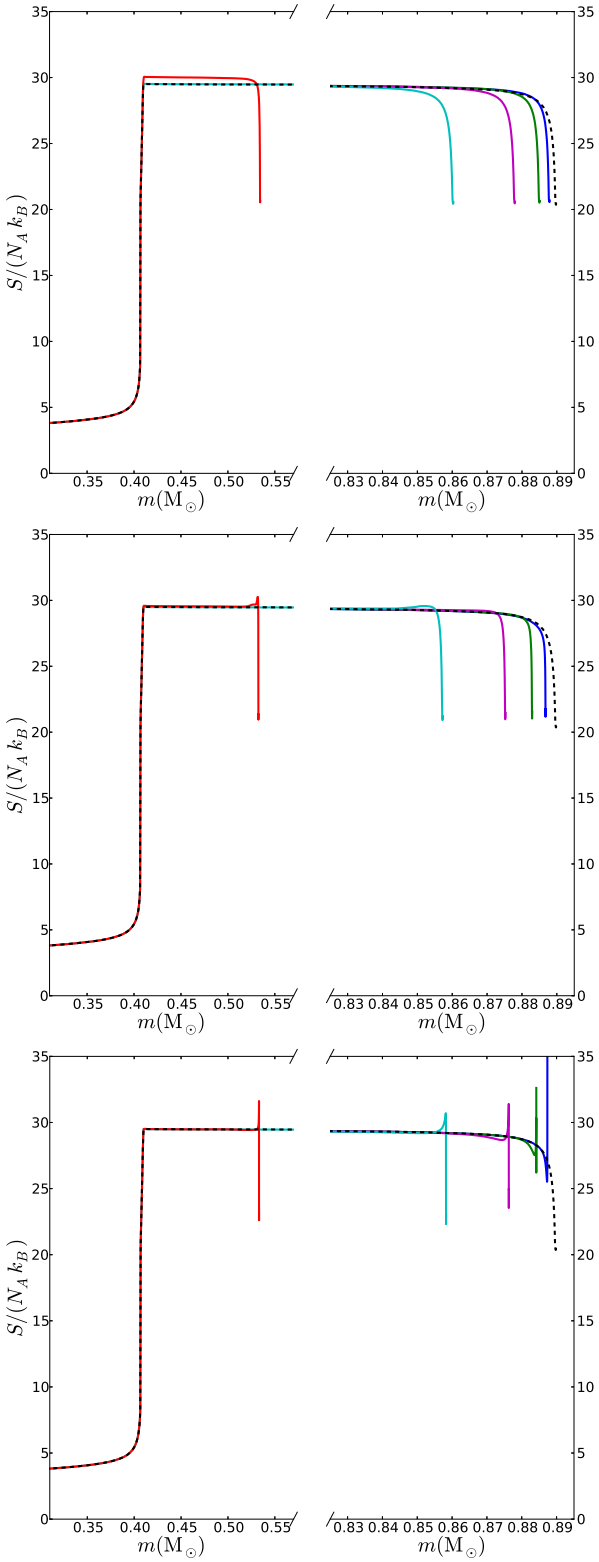

Figure 4.6 Entropy profiles at the onset of mass loss (dashed black), during the early evolutionary phase (solid colors, right panels) and after the 0.89 $M_\odot$ RGB star has lost about 40% of its mass (red, left panels). The mass loss rate is 10^{-2} $M_\odot$/yr (model 6, top), 0.1 $M_\odot$/yr (model 7, middle) and 1 $M_\odot$/yr (model 8, bottom).

The evolution of the radius profile as a function of mass for the hydrodynamic case shows that while some material close to the surface always moves out, the radius continuously decreases (Figure 4.7). A certain kinetic energy is associated with this local outward motion which, in the case of hydrostatic models, goes into expansion work (potential energy). As a result the latter models increase their radius.

We can try to explain the formation of the radiative layer mentioned above by considering a tiny "sub-layer" at a constant mass coordinate, located within the superadiabatic layer of the mass-losing star (Figure 4.8). As the above layers are removed, the sub-layer can as a result more easily radiate some of its energy outwards: the temperature decreases while the local density stays almost constant. The thermal timescale is shorter in this phase than the dynamical timescale. Later on, the density profile readjusts and the density of the sub-layer drops significantly while its temperature only decreases by a small amount. Now the thermal timescale is longer than the local dynamical timescale. These two phases are also seen in the various entropy profiles (Figure 4.9). First, the temperature in the sub-layer decreases while the density stays almost constant, leading to a decrease of the entropy. Then, the density drops while the temperature only marginally decreases, which leads to an increasing entropy. This suggests that the readjustment of the star happens in two (nearly) distinct phases: first a thermal readjustment during which some of the energy of the layers is radiated away, then a dynamical readjustment during which the density in the outer layers decreases leading to the formation of the radiative layer.

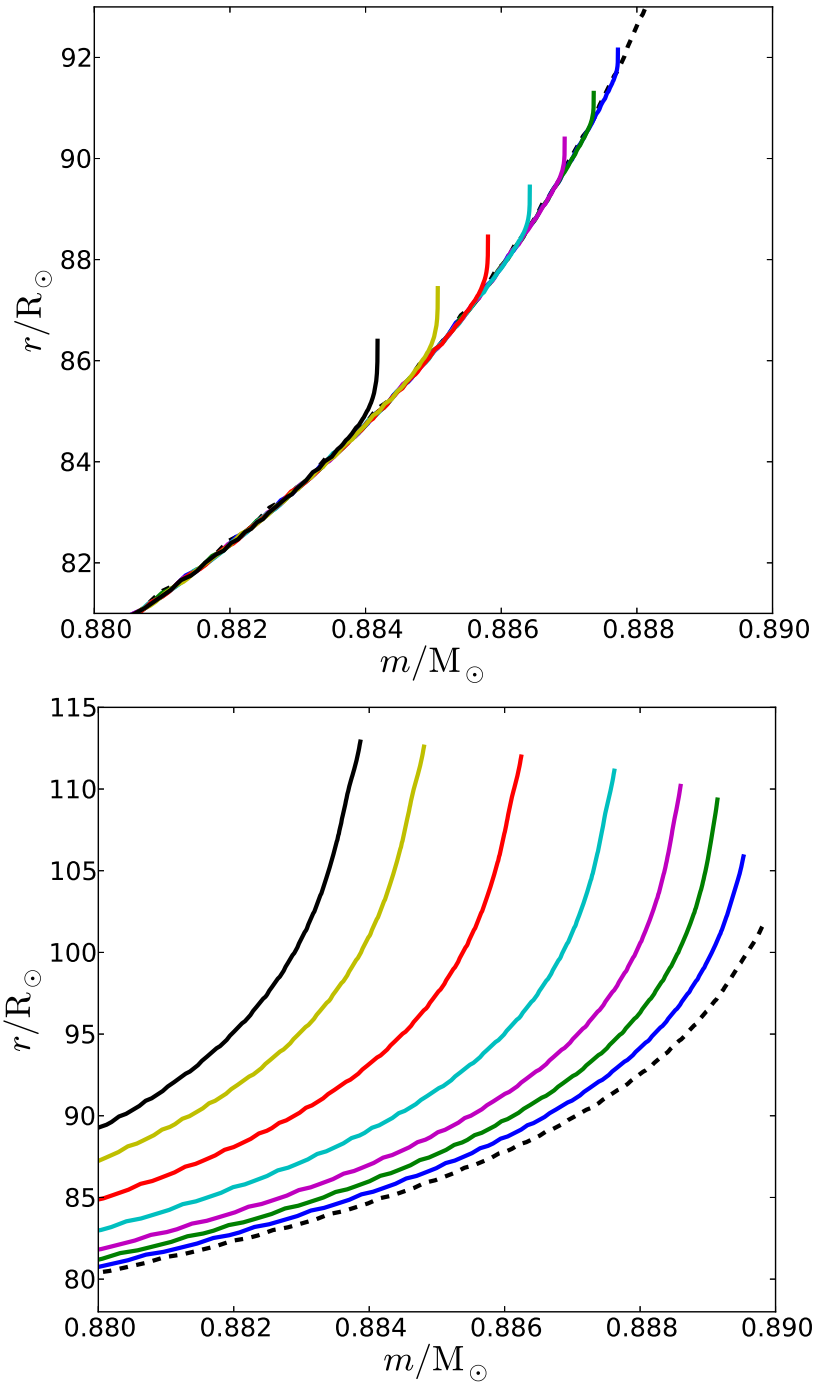

Figure 4.7 Radius profiles at the onset of mass loss (dashed black) and during the early evolutionary phase (solid colors) for the 0.89 $M_\odot$ RGB star and a mass loss rate of 1 $M_\odot$/yr. Both hydrodynamic (top, model 8) and hydrostatic sequences (bottom, model 13) are shown.

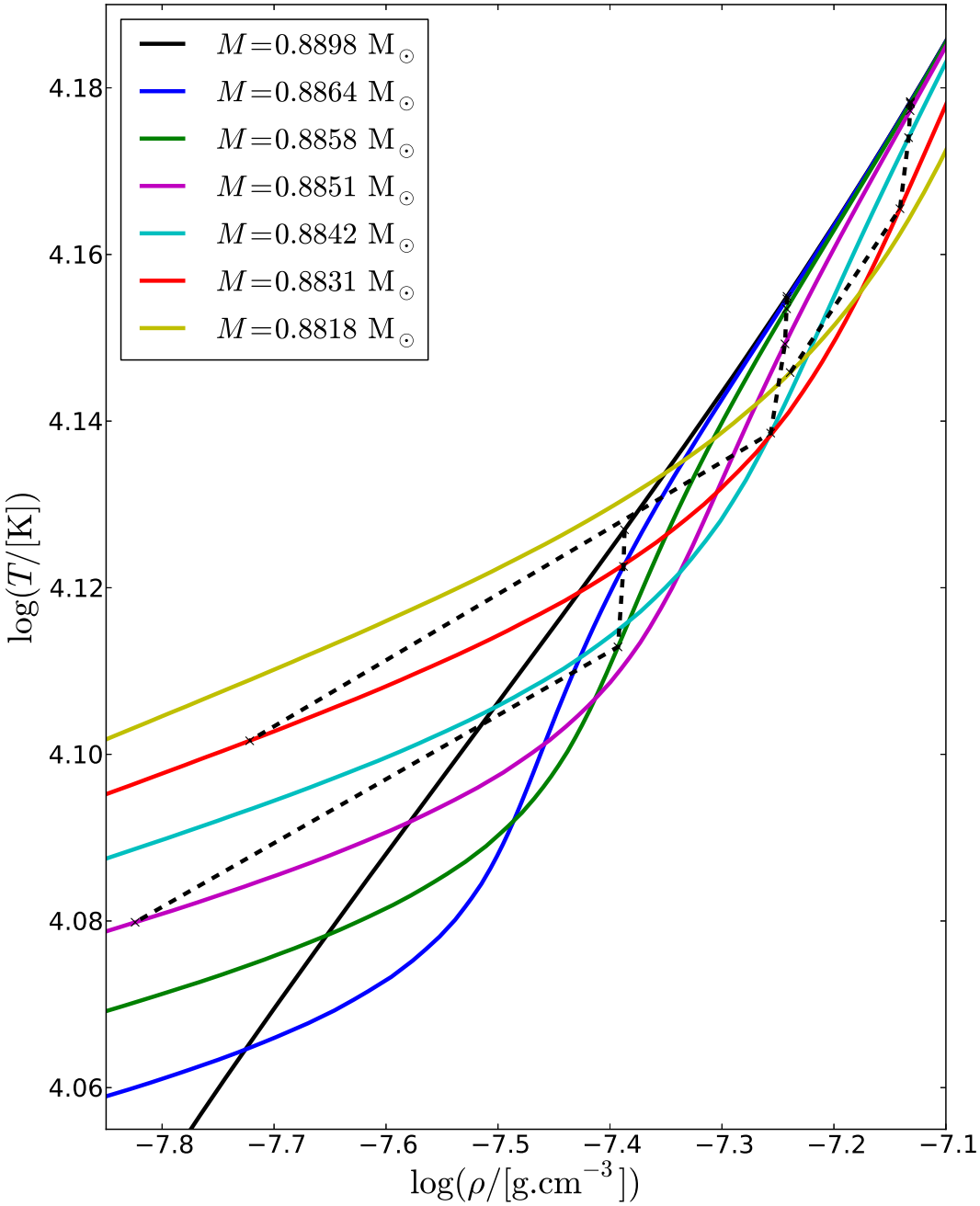

Figure 4.8 Profiles in the $\rho - T$ diagram for the 0.89 $M_\odot$ RGB star ($\dot{M} = 1$ $M_\odot$/yr, model 8) at the onset of mass transfer (solid black) and at different times during the early evolution (colors, the total mass is given in the legend). Also plotted is the location of a fixed mass coordinate (dashed black with crosses, from left to right: 0.885, 0.883 and 0.881 $M_\odot$).

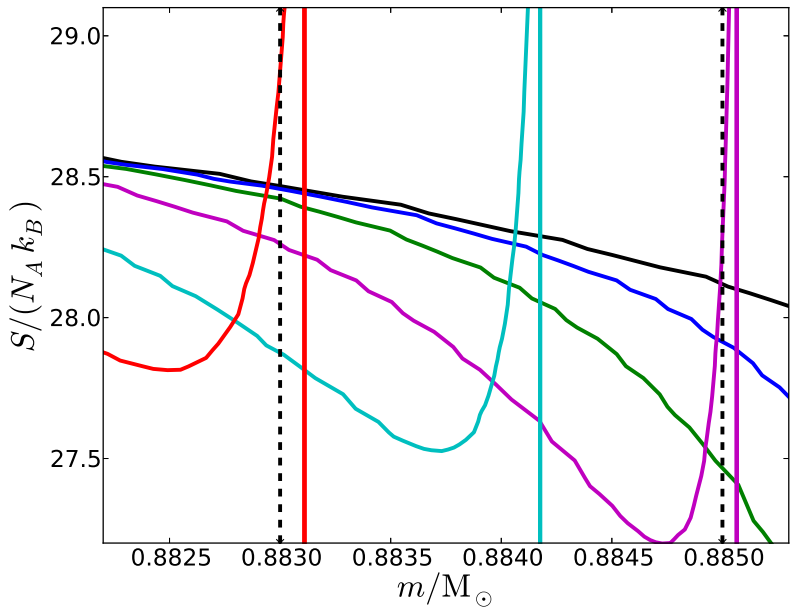

Figure 4.9 Entropy profiles for the 0.89 $M_\odot$ RGB star ($\dot{M} = 1\ M_\odot$/yr, model 8) at the onset of mass transfer (solid black) and at different times during the early evolution (same colors as in Figure 4.8). Also plotted is the location of a fixed mass coordinate (dashed black, from left to right: 0.883 and 0.885 $M_\odot$).

4.5.2 Additional models

We also carry out evolutionary sequences for a 0.74 $M_\odot$ AGB star with two different mass loss rates (models 14 and 15) and for a 5 $M_\odot$ RGB star (models 16, 17 and 18) similar to the one used by Woods & Ivanova (2011) in order to verify that the behavior seen for the 0.89 $M_\odot$ RGB star case is not a special case. The evolution of the radius for both stars is shown in Figure 4.10 and Figure 4.11, respectively. Again, all the models initially shrink in radius. Models suffering a higher mass loss rate then shrink faster. In the particular case of the 5 $M_\odot$ RGB star, our results differ from the findings by Woods & Ivanova (2011). Indeed, their Figure 3 shows that for all mass loss rates except the lowest one ($\dot{M} = 10^{-3}\ M_\odot$/yr), the mass-losing star slightly expands. The higher the mass loss rate, the larger the star expands. This behavior is quite similar to the one seen in Figure 4.4 for the hydrostatic simulations, so it is possible that the results presented in their Figure 3 have been obtained assuming hydrostatic equilibrium. Nevertheless, the stellar radius after 0.6 $M_\odot$ has been lost by the star (see their Figure 2) seems quite consistent with ours, although making a more detailed comparison is difficult as their Figure 3 only shows the evolution until

the star has lost 0.5% of its total mass. Our 5 $M_{\odot}$ RGB model has a smaller core mass fraction (0.122) than their model (0.171), which might also lead to differences.

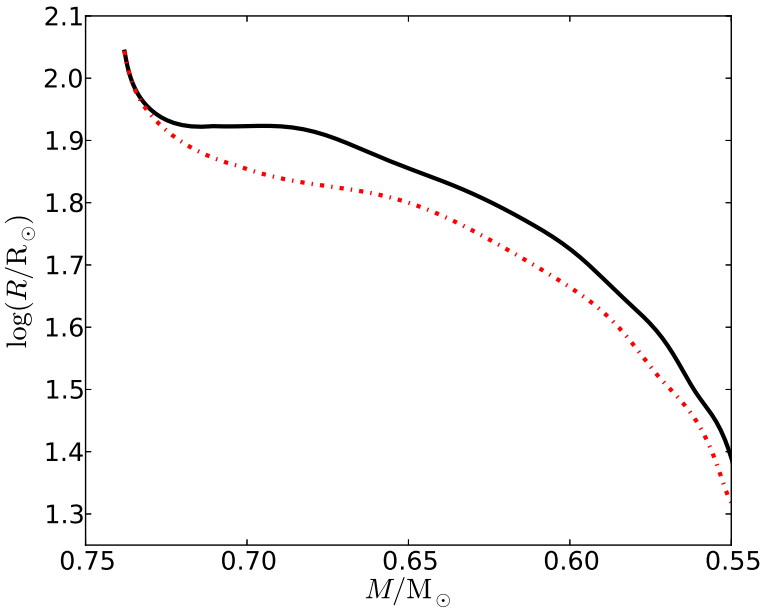

Figure 4.10 Evolution of the stellar radius as a function of stellar mass for the 0.74 $M_{\odot}$ AGB star with mass loss rates of 0.5 $M_{\odot}$/yr (black, model 14) and 1 $M_{\odot}$/yr (dash-dotted red, model 15).

4.6 Summary and Discussion

We used the MESA stellar evolution code to carry out one-dimensional hydrostatic and hydrodynamic simulations of mass-losing stars, either low-mass ZAMS stars between 0.3 and 0.5 $M_{\odot}$, or 1 or 5 $M_{\odot}$ (main sequence mass) giant stars, with several constant and variable mass loss rates up to a few $M_{\odot}$/yr.

We first tested our numerical method against the low-mass ZAMS stars case and reproduced the results of Ge et al. (2010). Therefore, it is correct to assume that the evolution of the star is adiabatic *in this specific case*.

We then investigated the case of a 0.89 $M_{\odot}$ RGB star for five different mass loss rates. We showed that the mass-losing star does not remain in hydrostatic equilibrium for high mass loss rates and that the evolution is not adiabatic, as the outer superadiabatic layer has enough time to thermally relax. Only for low mass loss rates ($\dot{M} \leq 10^{-2}$ $M_{\odot}$/yr) have both the outer superadiabatic layer and the stellar

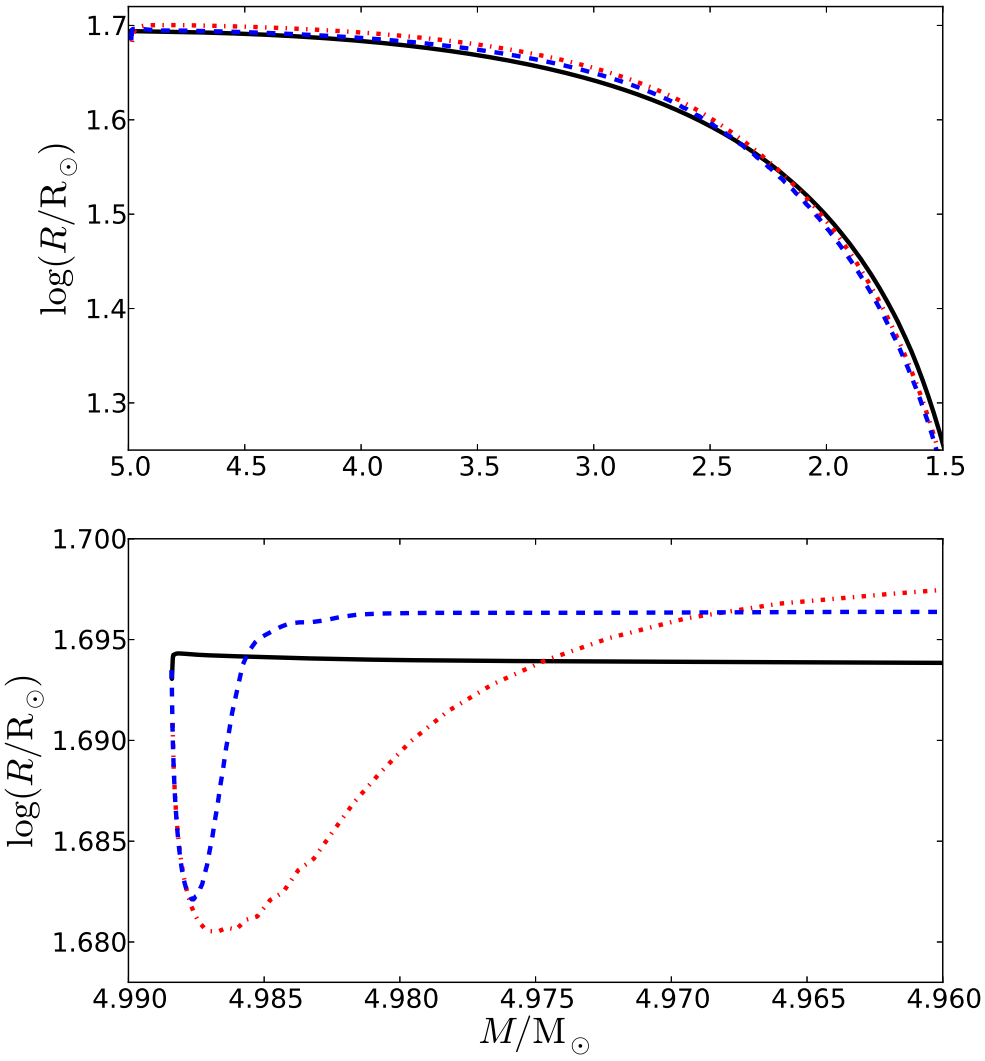

Figure 4.11 Top: evolution of the stellar radius as a function of stellar mass for the 5 $M_\odot$ RGB star with mass loss rates of 10^{-2} $M_\odot$/yr (black, model 16), 1 $M_\odot$/yr (dash-dotted red, model 17), and variable (dashed blue, model 18). Bottom: a close-up of the early evolution.

interior enough time to thermally readjust. The superadiabatic layer progressively reconstructs and survives the entire evolution, making the evolution not adiabatic both locally and globally. For high mass loss rates ($\dot{M} \geq 0.1$ $M_\odot$/yr), the outer part of the star progressively loses its superadiabaticity and the interior does not have enough time to thermally readjust. Even though a fraction of the initial superadiabatic layer might survive, a larger radiative zone emerges below it and the

star keeps shrinking during the entire sequence. The evolution of the star is locally non-adiabatic and hydrodynamic, as some energy that is stored in gravitational form in the hydrostatic models is actually in a kinetic form, leading to the star contracting instead of expanding.

We also carried out additional simulations for a 0.74 $M_{\odot}$ AGB star with a core mass of 0.52 $M_{\odot}$ and a 5 $M_{\odot}$ RGB star. These models are consistent with our previous findings and with the 5 $M_{\odot}$ RGB model in Woods & Ivanova (2011). We have also verified that the outcomes of our simulations depend on neither numerical parameters such as the initial timestep adopted, nor on boundary conditions.

According to our stellar evolution models, giants barely expand, if at all. This result impacts the condition for the onset of the common envelope phase. Using the Eddington luminosity limit, one can estimate the mass loss rate above which a dwarf would be unable to accrete material, to be about 10^{-3} $M_{\odot}$/yr. For higher mass loss rates, the hydrostatic assumption is violated and there is no expansion of the giant's envelope. As a consequence, the positive feedback from the mass-losing giant discussed in Section 4.1, may be reduced. Further investigations are required to quantify how this feedback affects the temporal evolution of the mass transfer rate. Overall, criteria for unstable mass transfer based on adiabatic mass loss models should be re-investigated. Moreover, if giant stars do not expand as a result of mass loss, this process does also not help the envelope ejection during a common envelope interaction, as speculated by De Marco et al. (2011).

Chapter 5

The Common Envelope Phase with Planetary Companions

5.1 On the survival of brown dwarfs and planets engulfed by their giant host star

Originally published as Passy, J.-C., Mac Low, M.-M., & De Marco, O., 2012, ApJ, 759, L30

Abstract

The recent discovery of two Earth-mass planets in close orbits around an evolved star has raised questions as to whether substellar companions can survive encounters with their host stars. We consider whether these companions could have been stripped of significant amounts of mass during the phase when they orbited through the dense inner envelopes of the giant. We apply the criterion derived by Murray et al. for disruption of gravitationally bound objects by ram pressure, to determine whether mass loss may have played a role in the histories of these and other recently discovered low-mass companions to evolved stars. We find that the brown dwarf and Jovian mass objects circling WD 0137-349, SDSS J08205+0008, and HIP 13044 are most unlikely to have lost significant mass during the common envelope phase. However, the Earth-mass planets found around KIC 05807616 could well be the remnant of one or two Jovian mass planets that lost extensive mass during the common envelope phase.

5.1.1 Introduction

The question of survivability of planets during post-main-sequence evolution of the host star has attracted some interest over the past years (Villaver & Livio, 2007; Nordhaus et al., 2010; Spiegel, 2012). Recently, many substellar companions have been discovered in close orbits around evolved stars (Table 5.1). Maxted et al. (2006) detected a 0.053 $M_{\odot}$ brown dwarf orbiting the 0.39 $M_{\odot}$ white dwarf WD 0137–349 with a 1.9-hr period. A likely brown dwarf was discovered in a 2.3-hr orbit around the subdwarf B star SDSS J08205+0008 (Geier et al., 2011). Setiawan et al. (2011) discovered a Jupiter-mass object orbiting the red horizontal branch star HIP 13044 with a 16.2-day period. Finally, Charpinet et al. (2011) reported the detection of two nearly Earth-sized planets orbiting the subdwarf B star KIC 05807616 with orbital periods of 5.8 and 8.2 hr. The existence of these systems for which the radius of the precursor of the primary was larger than today's orbital separation, suggests that they have gone through a common envelope (CE) interaction. During this phase, the companion is engulfed by its host star's envelope when the latter was a giant star (Paczynski, 1976).

Hydrodynamics simulations of this evolutionary phase have been performed with different numerical techniques (Sandquist et al., 1998; Passy et al., 2012; Ricker & Taam, 2012) but questions persist. It is still unclear how the envelope of the donor star gets ejected, and why the final separations obtained by simulations are larger than those observed in post-CE systems (Passy et al., 2012). The resolution reached in these numerical models currently does not suffice to study the complete evolution for a substellar companion that may spiral down to very close to the giant's core.

An important question is therefore whether substellar companions can survive engulfment by the giant's envelope without being totally disrupted. A system with a very low mass companion has a very small orbital energy budget, so we may also plausibly conjecture that a CE in such a system would more likely fail and result in a merger, thus destroying the companion. Is it therefore possible that substellar companions started off as more massive objects, which were then partially disrupted during their engulfment to become the objects we see today? This scenario was actually suggested by Charpinet et al. (2011) to explain the existence of planets around KIC 05807616.

Murray et al. (1993) studied the disruption of gravitationally bound objects by direct action of ram pressure in the context of star formation and galaxy evolution.

However the physics of disruption is scale free, so their results also apply to other astrophysical questions such as the gas stripping occurring in clustered galaxies (Nulsen, 1982; Mori & Burkert, 2000) or here, the disruption of hydrostatic companions captured by the envelope of a giant star. In this contribution we use their theory to determine whether, in the observed systems, the substellar companions could have lost a significant amount of mass during the in-spiral phase. We describe the formalism used in Section 5.1.2 and present the results in Section A.6. We provide a summary in Section 5.1.4.

5.1.2 Analysis

Murray et al. (1993) calculated the conditions for a self-gravitating, hydrostatic, isothermal sphere moving in an ambient medium to be disrupted by ram pressure. The disruption of an object by ram pressure can most simply be understood by the pancake model (Zahnle, 1992; Klein et al., 1994), in which transverse motions are driven by the increased pressure on the front surface of the object compared to the sides. Field & Ferrara (1995) showed that the actual disruption by Kelvin-Helmholtz and Rayleigh-Taylor instabilities with wavelengths comparable to the size of the object reproduces the scalings yielded by this simple model. Murray et al. (1993) confirmed numerically that when self-gravity is strong enough to stabilize the Kelvin-Helmholtz instability, the sphere is stable against catastrophic disruption. This occurs when the gravitational acceleration

$$g \gtrsim g_{\rm crit} \equiv \frac{2\pi\rho_2\rho_1 U^2}{R_2(\rho_2^2-\rho_1^2)} \quad , \tag{5.1}$$

where ρ_1, ρ_2, R_2 and U are the background density, and the density, radius and relative velocity of the companion, respectively. We assume the tidal forces exerted by the giant star on the companion to be negligible compared with the self-gravity of the companion – we discuss this point in Section 5.1.3. Assuming $D \equiv \rho_2/\rho_1 \gg 1$ and taking the gravitational acceleration $g \approx GM_2/R_2^2$, one obtains a critical mass under which disruption occurs (their Equation (2.8)):

$$M_{\rm crit} \sim 9.4 \left(\frac{50}{D}\right)^2 \left(\frac{U}{100\ {\rm km\,s^{-1}}}\right)^3 \times \left(\frac{10^{-4}\ {\rm g\,cm^{-3}}}{\rho_1}\right)^{1/2} {\rm M_J}. \tag{5.2}$$

If the configuration is unstable ($M_2 \lesssim M_{\rm crit}$), the companion is disrupted in a crossing time as the characteristic timescale for destruction is equivalent to its internal dynamical timescale:

$$\tau \sim 1.4 \left(\frac{R_2}{0.1\ \mathrm{R}_\odot}\right)\left(\frac{100\ \mathrm{km\,s^{-1}}}{U}\right)\left(\frac{D}{50}\right)^{1/2}\ \mathrm{hr}. \tag{5.3}$$

We approximate the relative velocity of the companion by the maximum orbital velocity reached during the in-spiral phase, i.e. the final orbital velocity:

$$U \sim \sqrt{\frac{GM_c}{a}} \tag{5.4}$$

where $M_c \gg M_2$ is the mass of the primary's core, and a is the orbital separation at the end of the CE phase. We substitute this relation in Equation (5.2), and obtain the critical background density above which the companion is unstable:

$$\rho_{1,\rm crit} \sim 1.4\ 10^{-3}\ \left(\frac{a}{\mathrm{R}_\odot}\right)\left(\frac{\mathrm{M}_\odot}{M_c}\right)\left(\frac{M_2}{\mathrm{M_J}}\right)^{2/3} \times \left(\frac{\rho_2}{1\ \mathrm{g\,cm^{-3}}}\right)^{4/3}\ \mathrm{g\,cm^{-3}}. \tag{5.5}$$

One should emphasize that if the companion is unstable, the dominant wavelength acting to destroy it is comparable to the sphere radius. The destruction is therefore global and not quasi-static. In other words, the companion is destroyed catastrophically, not ablated by incremental mass-loss due to short wavelength surface instabilities. Thus stability cannot be reached again once disruption starts.

If the companion is stable ($M_2 \gtrsim M_{\rm crit}$), such shorter wavelength instabilities can still occur and strip mass in a more ablative manner, giving a quasi-static mass loss rate. We compute the largest unstable wavelength from Equations (5.1) and (5.4), again assuming $\rho_2 \gg \rho_1$, and substituting $\lambda_{\rm max}$ for R_2. We find

$$\lambda_{\rm max} = 7.8\ 10^{-2}\left(\frac{M_c}{\mathrm{M}_\odot}\right)\left(\frac{\mathrm{R}_\odot}{a}\right)\left(\frac{1\ \mathrm{g\,cm^{-3}}}{\rho_2}\right)^{5/3} \times \left(\frac{\rho_1}{10^{-4}\ \mathrm{g\,cm^{-3}}}\right)\left(\frac{\mathrm{M_J}}{M_2}\right)^{1/3}\ \mathrm{R_J}. \tag{5.6}$$

Murray et al. (1993) suggests that the corresponding mass loss rate can then be approximated to that occurring in laminar viscous flows as described by their Equation 3.5:

$$\dot{M}_{\rm v} \sim 11 \left(\frac{U}{100 \text{ km s}^{-1}} \right) \left(\frac{\rho_1}{10^{-4} \text{ g cm}^{-3}} \right) \times \left(\frac{R_2}{0.1 \text{ R}_\odot} \right)^2 \left(\frac{\lambda_{\rm max}}{R_2} \right) \text{ M}_{\rm J} \text{ yr}^{-1} \tag{5.7}$$

where we have assumed the relative velocity to be of the order of the sound speed of the background. Equation (5.7) should be used with caution as it is valid only for Reynolds numbers $Re \lesssim 30$ (Nulsen, 1982). In our case, the Reynolds number is $Re = 2R_2U/\nu$, where ν is the molecular viscosity. Viscosity in stellar interiors is far too small to allow such low Reynolds numbers on these length scales.

However, such low effective Reynolds numbers might be reached through the turbulent viscosity. Since the largest possible size of the eddies is $\lambda_{\rm max}$ and their largest velocity is the sound speed of the ambient medium c_S, one can use a formalism like that of Shakura & Sunyaev (1973) and parameterize the turbulent viscosity as

$$\nu_{\rm t} = \alpha c_S \lambda_{\rm max} \tag{5.8}$$

where $\alpha \lesssim 1$ is a free parameter. The effective Reynolds number is thus:

$$Re_{\rm t} \sim \frac{2R_2}{\alpha \lambda_{\rm max}} \tag{5.9}$$

where we have still assumed that $U \sim c_S$. Unfortunately, no accepted value of α has been derived for our specific case. We can only calculate the minimum turbulent Reynolds number $Re_{\rm t,min} = Re_{\rm t}(\alpha = 1)$ and see how this number compares to the range required to apply Equation (5.7).

Another approach would be to calculate how much work from the drag acts on the companion during its in-spiral, and compare it to the companion's gravitational binding energy $E_{\rm bin} \sim GM_2^2/R_2$. Assuming for the cross section $S_2 = \pi R_2^2$ and a drag coefficient C_D, the drag force is $F_D = \frac{1}{2} C_D \rho_1 U^2 S_2$. The smaller the companion, the longer the in-spiral phase lasts: for example, the 0.9 $M_\odot$ and 0.1 $M_\odot$ companions complete about 20 and 40 orbits during this phase, respectively (De Marco et al., 2012; Passy et al., 2012). We therefore assume that our companions complete at least

50 orbits, and slice the giant's envelope down to the currently observed separation of the system, in $N_{\rm orbits} = 50$ equally-spaced radii $\bar{R}_i$ corresponding to an average density $\bar{\rho}_i$. Assuming $C_D = 1$, the work provided by drag forces is thus:

$$W_{\rm drag} = \sum_{i \leq N_{\rm orbits}} \frac{1}{2} \bar{\rho}_i U_i^2 S_2 \times 2\pi \bar{R}_i, \tag{5.10}$$

where $U_i = \sqrt{GM_i/\bar{R}_i}$ and M_i is the mass enclosed within $\bar{R}_i$. We will see in Section 5.1.3 that the calculation of $W_{\rm drag}$ does not depend strongly on the number of assumed orbits. If $W_{\rm drag} \gtrsim E_{\rm bin}$ we conclude that the companion could have been destroyed if the drag energy can be coupled to the interior of the companion efficiently, even if it is stable according to Equation (5.1).

5.1.3 Results

In this section we study each system reported in Table 5.1 separately and investigate whether the substellar components are less massive today than they were prior to the CE evolution.

WD 0137–349

Using the *MESA* stellar evolution code (Paxton et al., 2011), we compute a model for the 0.053 $M_\odot$ brown dwarf companion to this white dwarf and obtain a radius $R_2 = 0.079\ R_\odot$ (Figure 5.1). The mean density of the brown dwarf is $\rho_2 = 150\ {\rm g\,cm^{-3}}$ which, substituted in Equation (5.5), yields a critical density $\rho_{1,\rm crit} \approx 27\ {\rm g\,cm^{-3}}$.

We compare this critical density to the density profile of the progenitor and see whether the companion will plunge deep enough into the primary's envelope to encounter a density high enough to destroy it. The most likely progenitor of the white dwarf is a nearly 1 $M_\odot$ main sequence star. We evolve such a model with *MESA* up to the red giant branch until the core mass reaches the observed white dwarf mass. At that time, the radius of the star was 100 $R_\odot$ and its total mass was 0.89 $M_\odot$ due to mass loss. The density profile of this red giant star is displayed in Figure 5.2. The current orbital separation of the system is $a = 0.65\ R_\odot$ which means that the companion has reached a layer of the primary where the density $\rho_{1,\rm max} \sim 2.1 \times 10^{-3}\ {\rm g\,cm^{-3}}$.

At this point, we should emphasize that we have calculated the maximum density encountered by the companion using the *initial* profile of the giant primary. Hydrodynamical simulations suggest that in the deep interior, density at a given coordinate

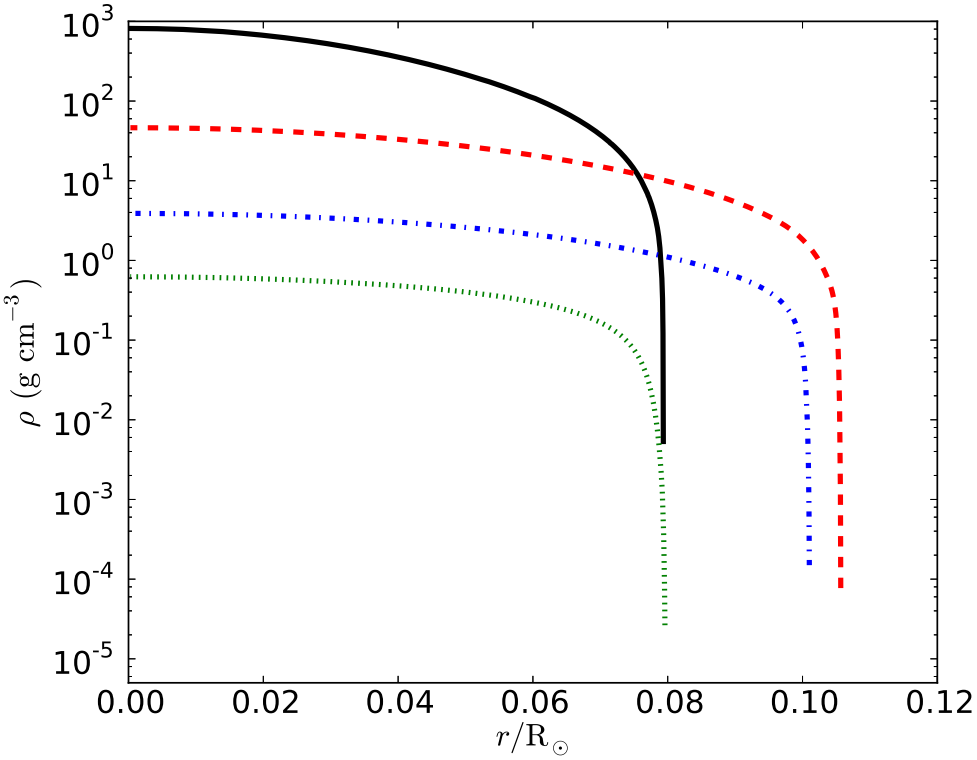

Figure 5.1 Density profiles for the 0.053 $M_\odot$ (solid black), 10 $M_{\rm Jup}$ (dashed red), 1 $M_{\rm Jup}$ (dash-dotted blue) and 0.1 $M_{\rm Jup}$ (dotted green) models.

decreases with time (Passy et al., 2012, Figure 12) although the current resolution does not allow them to give a definitive answer at such small radii. Therefore, $\rho_{1,\rm max}$ should be considered an upper limit.

$\rho_{1,\rm max}$ is four orders of magnitude smaller than the critical density required for instability so we conclude that the companion is stable. Moreover, the mass-loss rate due to viscous stripping is only $\sim 3.8 \times 10^{-2}\ M_{\rm Jup}\,{\rm yr}^{-1}$. Since the dynamical phase of a CE lasts only about one year (Sandquist et al., 1998; Passy et al., 2012), the companion has not lost any significant amount of mass during its in-spiral phase.

SDSS J08205+0008

SDSS J08205+0008 is very similar to WD 0137–349 so we also conclude that the brown dwarf – whose estimated mass ranges from 0.045 to 0.068 $M_\odot$ – has not been affected during the plunge-in phase.

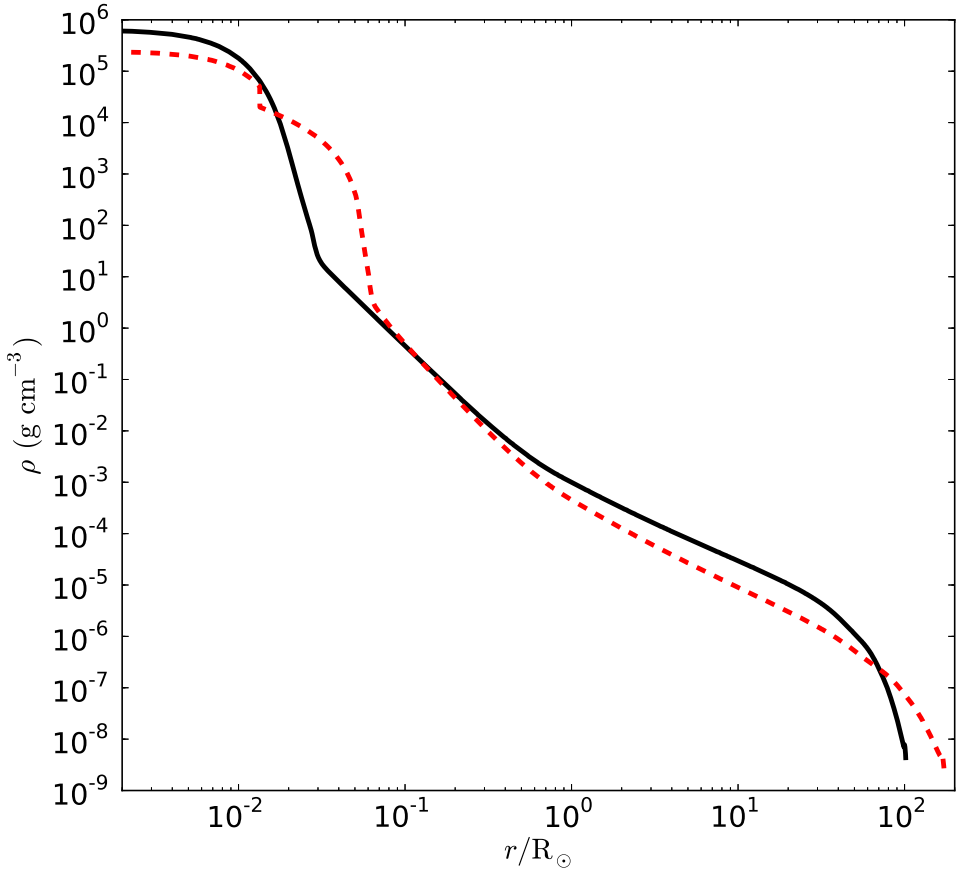

Figure 5.2 Density profile for the 0.89 $M_\odot$ red giant star progenitor of WD 0137–349 (solid black) and a 0.76 $M_\odot$ star at the tip of the red giant branch (dotted red).

HIP 13044

The minimum mass of the planet orbiting HIP 13044 is estimated to be 1.25 M_{Jup} (Setiawan et al., 2011). This system is intriguing, as a plausible formation channel for this system has yet to be found. Indeed, the orbital separation ($\sim 25\ R_\odot$) is much larger than the separations obtained from numerical simulations or observations of post-CE systems (De Marco et al., 2011; Passy et al., 2012). Also, successful CE interactions usually lead to the formation of blue horizontal branch stars with very thin hydrogen-envelopes (Soker, 1998; Han et al., 2002).

Bear et al. (2011) therefore suggested that the helium flash occurring in a 0.9 $M_\odot$ metal-poor red giant star could ignite hydrogen burning in a thick region at the

bottom of the envelope. This deposition of energy would eventually lead to a dramatic inflation lasting about 100 yr, during which the stellar radius could reach 700 $R_\odot$. The planet would then enter a "half-failed, half-successful" CE during which the orbital separation would shrink down to approximately 25 $R_\odot$, only 0.1 $M_\odot$ would be lost by the system and the primary would evolve to the red part of the horizontal branch.

This theory has several problems. First, there is no compelling evidence suggesting that red giant branch stars might suffer such a large and long-lasting expansion after the helium core flash. On the contrary, simulations performed with stellar evolution codes such as *MESA*, show that red giant stars shrink after helium has been ignited explosively. Second, the duration of this suggested post-helium-flash expansion is larger than the duration of a CE phase. Therefore, the in-spiral of the companion could not have been stopped because of the primary contracting below its Roche lobe on a short timescale. Thus, the entire envelope must have been lifted up, mostly in the equatorial plane (Passy et al., 2012; Ricker & Taam, 2012), which raises thus the question of how a red horizontal branch star could eventually form. Finally, the planetary companion would strongly interact with falling back material through gravitational drag. In that regard, the large orbital separation observed is still perplexing. For all these reasons we believe that the scenario suggested by Bear et al. (2011) is unlikely.

A careful investigation of the progenitor of HIP 13044 seems quite complex and beyond the purposes of this paper. Consequently, we simply assume that the companion went through a CE interaction with an unknown progenitor. For the latter, we will consider the same profile as in Section 5.1.3 in order to give an indicative answer on the potential survival of the companion.

For the companion, we consider a 1 $M_{\rm Jup}$ model (Figure 5.1), with a radius $R_2 = 0.101\ R_\odot$ and a mean density $\rho_2 = 1.31\ \mathrm{g\,cm^{-3}}$. We find the critical density for stability $\rho_{1,\rm crit} \sim 6.2 \times 10^{-2}\ \mathrm{g\,cm^{-3}}$. The density in the progenitor's profile corresponding to the observed separations between the subdwarf and the planet is $\rho_{1,\rm max} \sim 10^{-5}\ \mathrm{g\,cm^{-3}}$, almost four orders of magnitude smaller than $\rho_{1,\rm crit}$. We thus conclude that the companion is stable. The viscous mass loss rate is also negligible ($\dot{M}_{\rm v} \sim 1.4 \times 10^{-4}\ M_{\rm Jup}\,\mathrm{yr^{-1}}$) so no mass will be ablated from the companion during the plunge-in phase.

KIC 05807616

The most intriguing system is certainly KIC 05807616, which has two nearly Earth-mass planets orbiting a subdwarf B star with an orbital separation of about 1.5 $R_\odot$. In order to constrain the mass of these planets prior to their engulfment, we use the same method as previously, with four different models ranging from 10 $M_{\rm Jup}$ down to 1 $M_\oplus$ (Figure 5.2). For the Earth-sized model, we use the accepted values for the Earth (see, e.g., Cox, 2000) as listed in Table 5.2. We again assume the primary used in Section 5.1.3 for which we obtain $\rho_{1,\rm max} \approx 10^{-3}$ g cm^{-3}.

The results are summarized in Table 5.2. One can see that the critical density required to catastrophically destroy an Earth-sized companion is about as large as the maximum density $\rho_{1,\rm max}$. In this regard, the 1 $M_\oplus$ companion could still be stable. However $W_{\rm drag} \sim 10^{41}$ erg, which is more than an order of magnitude larger than the gravitational binding energy of the companion (Table 5.2). $W_{\rm drag}$ does not strongly depend on the number of assumed orbits since changing this number to 20 or 100 changes $W_{\rm drag}$ by a factor of 2–3 only. Since the work provided by drag forces exceeds the binding energy of the companion, we conclude that the Earth-sized companion may not survive the engulfment, if the energy can be effectively coupled to the planetary material.

From the same considerations, a 10 $M_{\rm Jup}$ companion is too massive to be affected in any way during its in-spiral phase (Table 5.2). For a 1 $M_{\rm Jup}$ companion, $\rho_{1,\rm max}$ exceeds $\rho_{1,\rm crit}$ by almost an order of magnitude, so the secondary could be stable. However, $E_{\rm bin}$ exceeds $W_{\rm drag}$ by only a factor of three, which suggests that a significant amount of mass could be removed from the surface of the companion. A 0.1 $M_{\rm Jup}$ companion has a critical density an order of magnitude smaller than $\rho_{1,\rm max}$. Moreover, $W_{\rm drag}$ is about 20 times larger than the binding energy of the companion. Together, these suggest that a 0.1 $M_{\rm Jup}$ object probably would be destroyed. Using a more evolved model with a higher core mass $M_c = 0.47$ $M_\odot$ and $N_{\rm orbits} = 100$ (the stellar radius ~ 175 $R_\odot$) yields similar results (Figure 5.2, Table 5.2) We thus conclude that the progenitor of the planets likely had a mass of a few $M_{\rm Jup}$, supporting the suggestion made byCharpinet et al. (2011).

Discussion

A legitimate question is whether mass accretion by the substellar companion is relevant. From a Bondi-Hoyle analysis (see, e.g., Edgar, 2004, Equation (31)), the

accretion rate onto the 1 $M_{\rm Jup}$ object is only

$$\dot{M}_{\rm acc} \sim \frac{\pi G^2 M_2^2 \rho_{1,\rm max}}{\sqrt{2} U^3} = 3.7 \times 10^{-2}\ {\rm M_J/yr}. \quad (5.11)$$

We therefore conclude that mass accretion is negligible on the timescale of the CE interaction. Ricker & Taam (2008) also reached this conclusion in the case of more massive secondaries. They further argued that the mass accretion rate calculated from their simulations is even smaller than the one given by Equation (5.11), mainly because tidal effects dominate the structure of the flow.

Bear & Soker (2012) propose a slightly different scenario for the formation of the two planets around KIC 05807616. Instead of considering the dynamical effects occurring during the CE phase, they suggest that a massive giant planet was tidally destroyed after the end of the in-spiral phase and that the two planets are remnants of the disrupted metallic core. Using their Equation (1) with $C_{\rm tide} = 1$, the values given by Charpinet et al. (2011), and our planetary models (Table 5.2), the tidal radius at which destruction occurs is $R_t = 0.39$ and 0.80 $R_\odot$ for the 10 and 1 $M_{\rm Jup}$ objects, respectively. These qualitative values are still smaller than the observed separations of the planets (see Table 5.1), so it is difficult to conclude whether these objects would be tidally destroyed. They also suggest that evaporation of the companion due to heating from the envelope might be important. They estimate the mass of the planet must be $\gtrsim 5\ M_{\rm Jup}$ in order to survive evaporation. The evaporation timescale depends on the efficiency of heat transfer, which is sensitive to mixing between the planetary atmosphere and the stellar convective envelope. We cannot at present calculate this timescale with sufficient precision. We therefore do not know whether evaporation could dominate the dynamical effects we discuss in this study. Nevertheless, the mass of the progenitor suggested by Bear & Soker (2012) is consistent with ours.

5.1.4 Summary

We have considered evolved stars found to have brown dwarfs or planets around them in close orbits, suggesting that these systems have gone through a CE interaction. Using the criterion developed by Murray et al. (1993), we have investigated the stability of these substellar companions against mass loss induced by Kelvin-Helmholtz and Rayleigh-Taylor instabilities.

We have found that the substellar companions observed in WD 0137–349, SDSS J08205+0008 and HIP 13044 are very unlikely to have been affected during the in-

spiral inside their giant progenitors. Therefore, the masses of these objects currently observed are likely the same as prior to the CE phase. The two planets detected orbiting KIC 05807616, however, are not massive enough to have survived the engulfment unscathed. We have estimated the mass of the progenitor of these planets to be of order 1 $M_{\rm Jup}$. The question that still has to be answered is how such low-mass companions could have successfully unbound the entire envelope of the primary.

Table 5.1. Orbital parameters

Name	M_c ($M_\odot$)	M_2	P	a ($R_\odot$)	References
WD 0137–349	0.39	55.6 $M_{\rm Jup}$	1.93 hours	0.65	Maxted et al. (2006)
SDSS J08205+0008	0.25-0.47	47.1 – 71.2 $M_{\rm Jup}$	2.30 hours	0.60 – 0.72	Geier et al. (2011)
HIP 13044	0.8	$\geq$1.25 $M_{\rm Jup}$	16.2 days	24.95	Setiawan et al. (2011)
KIC 05807616	0.496	0.440 $M_\oplus$	5.7625 hours	1.290	van Grootel et al. (2010); Charpinet et al. (2011)
KIC 05807616	0.496	0.655 $M_\oplus$	8.2293 hours	1.636	van Grootel et al. (2010); Charpinet et al. (2011)

Note. — Reported are the stellar mass (M_c), the companion mass (M_2), the orbital period (P) and the orbital separation (a)

Table 5.2. Parameters of the different companion models investigated

M_2	R_2 ($R_\odot$)	ρ_2 (g.cm^{-3})	$\rho_{1,\mathrm{crit}}$ (g.cm^{-3})	$\lambda_{\max}/R_2$	$Re_{\mathrm{t,min}}$	$\dot{M}_{\mathrm{v}}$ (M_{J} yr^{-1})	W_{drag} (ergs)	E_{bin} (ergs)
10 M_{Jup}	0.106	11.4	0.5	2.0(−3)	9.9(2)	0.6	1.2(43)	3.3(45)
1 M_{Jup}	0.101	1.31	6.0(−3)	1.7(−1)	12	45	1.1(43)	3.4(43)
0.1 M_{Jup}	0.080	0.27	1.5(−4)	–	–	–	7.0(42)	4.3(41)
1 $M_\oplus$	9.16(−3)	5.52	8.8(−4)	–	–	–	1.1(41)	3.7(39)
10 M_{Jup}	0.106	11.4	0.5	1.0(−3)	2.0(3)	0.15	5.3(42)	3.3(45)
1 M_{Jup}	0.101	1.31	6.0(−3)	8.4(−2)	24	12	4.8(42)	3.4(43)
0.1 M_{Jup}	0.080	0.27	1.5(−4)	–	–	–	3.0(42)	4.3(41)
1 $M_\oplus$	9.16(−3)	5.52	8.8(−4)	–	–	–	4.9(40)	3.7(39)

Note. — Values obtained with the 0.89 $M_\odot$ (top) and the 0.76 $M_\odot$ (bottom) models. Quantities relative to viscous stripping are not calculated when the object is found unstable.

5.2 Simulating the common envelope interaction with substellar companions

5.2.1 Introduction

We have addressed in Section 5.1 the question of the survivability of substellar companions during a CE interaction. How substellar companions manage to eject the envelope remains, however, unclear, and requires numerical simulations in order to be explained. Although it is true that this issue has not been solved even for stellar companions (Chapter 3), lower-mass secondaries may enter a different regime of interaction, and studying their case could potentially provide valuable information.

Extending the capabilities of our numerical code *Enzo* (Chapter 3) to model this problem, is non-trivial. The main challenge lies in the various length scales that need to be resolved. One needs a local resolution of at least $\sim 0.1\ R_{\odot}$ in order to resolve the final separations of most systems presented in Section 5.1. Unlike the unigrid simulations presented in Chapter 3, one would also like to have a computational domain large enough such that all the envelope mass would be kept within the domain for the entire duration of the simulation. According to Figure 3.19, the domain should thus be $\sim$ a few thousands $R_{\odot}$. This represents a range in resolutions of at least 4 orders of magnitude, which in three dimensions can only be reached at reasonable cost via the use of adaptive mesh refinement (AMR).

AMR is a feature fully implemented in the *Enzo* code. The user has the choice to locally refine the computational domain according to various criteria, such as baryonic mass, dark matter particle mass (for cosmological simulations), or shocks, to name a few. One of the difficulties of nested-grids simulations including self-gravity is to calculate the gravitational potential field in a consistent manner across the different levels of refinement. We describe this point in detail in the next section.

5.2.2 Self-gravity

The Euler equations (Equations 3.1 to 3.4) are solved numerically using either finite-difference or finite-volume methods. For instance, the Zeus solver used to perform the *Enzo* simulations presented in Chapter 3 is a second order finite-difference advection method, while the third-order piecewise parabolic method (PPM) also implemented in *Enzo*, is based on a finite-volume discretization. More details on these methods,

and others, can be found in Laney (1998). Thus, solving the Euler equations is a *local* problem: the state of a cell at a given time $t + \Delta t$, where Δt is the timestep, only depends on the state of the neighboring cells at t and $t + \Delta t$. This calculation can, as a consequence, be efficiently parallelized to a large number of processes.

Self-gravity is represented by the Poisson equation:

$$\Delta\Phi = 4\pi G\rho \tag{5.12}$$

where Φ its the gravitational potential. The Poisson equation is obtained by combining Gauss' law for gravity:

$$\nabla \cdot \mathbf{g} = -4\pi G\rho \tag{5.13}$$

and expressing the gravitational field, since it is conservative, in terms of a potential Φ:

$$\mathbf{g} = -\nabla\Phi. \tag{5.14}$$

Computing the gravitational potential from Equation (5.12) is a *global* problem: a change in the mass distribution anywhere in the grid will impact the entire domain. Information about the gravitational potential thus need to be communicated between processes, which deteriorates how the code scales. This is one of the reasons why our *Enzo* simulations have been carried out on approximately 200 cores, while some purely hydrodynamical simulations of the He-shell flash convection zone have been performed on 98 000 cores (Falk Herwig 2012, private communication, but see also Woodward et al. 2009). This comparison is not strictly accurate as the codes used and the problems solved are different, but nevertheless shows qualitatively how self-gravity can limit scaling.

Another difficulty of simulations including self-gravity is to compute the gravitational potential accurately, in particular when nested grids are used. In order to reduce the computational resources needed, the default multigrid gravity solver implemented in *Enzo* does not calculate the potential consistently between different levels of refinement. In other words, the gravitational field lines are not continuous at the grids boundaries. While this inaccuracy is negligible in cosmological simulations (because the evolution is driven by gravitational collapse), it significantly affects our simulations, for which the giant star has to be in hydrostatic equilibrium

(Section 5.2.4). We therefore implemented a new gravity solver based on an adaptive particle-mesh (APM) technique that allows a more accurate calculation of the potential. We describe in the next section the fundamental differences between the multigrid and the APM gravity solvers when used in nested-grids simulations.

5.2.3 The different Poisson solvers in Enzo

The Poisson equation in Fourier space

We recall here how to derive the Poisson equation in Fourier space. More details can be found, e.g., in Hockney & Eastwood (1989). By definition, a function f and its Fourier transform $\hat{f}$ follow the relation:

$$f(\mathbf{r}) = \frac{1}{2\pi} \int \hat{f}(\mathbf{k}) e^{i\mathbf{k}\cdot\mathbf{r}} d\mathbf{k}, \tag{5.15}$$

which one can use to rewrite Equation (5.12):

$$-\int \mathbf{k}^2 \hat{\phi}(\mathbf{k}) e^{i\mathbf{k}\cdot\mathbf{r}} d\mathbf{k} = 4\pi G \int \hat{\rho}(\mathbf{k}) e^{i\mathbf{k}\cdot\mathbf{r}} d\mathbf{k}. \tag{5.16}$$

Multiplying both sides by $e^{-i\mathbf{K}\cdot\mathbf{r}}$, integrating over $\mathbf{r}$, and switching the integrals (allowed by Fubini's theorem) leads to:

$$-\int \mathbf{k}^2 \hat{\phi}(\mathbf{k}) \left[\int e^{i(\mathbf{k}-\mathbf{K})\cdot\mathbf{r}} d\mathbf{r} \right] d\mathbf{k} = 4\pi G \int \hat{\rho}(\mathbf{k}) \left[\int e^{i(\mathbf{k}-\mathbf{K})\cdot\mathbf{r}} d\mathbf{r} \right] d\mathbf{k}. \tag{5.17}$$

The Dirac delta function is defined as:

$$\delta(\mathbf{k} - \mathbf{k_0}) = \frac{1}{2\pi} \int e^{i(\mathbf{k}-\mathbf{k_0})\mathbf{r}} d\mathbf{r}, \tag{5.18}$$

which we substitute in Equation (5.17) to obtain the Poisson equation in Fourier space:

$$-\mathbf{K}^2 \hat{\phi}(\mathbf{K}) = 4\pi G \hat{\rho}(\mathbf{K}). \tag{5.19}$$

Let us consider a periodic cubic mesh of period L and spacing H in each direction. The values are defined at points $\mathbf{r}_{i,j,k} = (iH, jH, kH)$ for $(i, j, k) \in [0; N]^3$, where N is the number of mesh points in one direction. Instead of solving the integral version of $\hat{\phi}$ and $\hat{\rho}$ (Equation 5.15), we calculate the finite series version:

$$\hat{f}(\mathbf{k}) = H \sum_{i,j,k} f(\mathbf{r}_{i,j,k}) e^{-i\mathbf{k}\cdot\mathbf{r}_{i,j,k}}, \tag{5.20}$$

where the wavenumber $\mathbf{k}$ takes values $\mathbf{k}_{m,n,p} = (mk_0, nk_0, pk_0)$ with $k_0 = 2\pi/L$. Equation (5.20) is calculated using a fast Fourier transform (FFT) algorithm which offers a $\mathcal{O}(n \log n)$ way to evaluate a set of n^2 sums, where n is the total number of mesh points. The critical point is how boundary conditions on nested grids are handled. This is where the algorithm of the multigrid and the APM solvers differ. We describe these differences in the next two paragraphs.

The multigrid solver

First the potential on the root grid is computed using the FFT algorithm. Then, the basic algorithm followed by the multigrid solver in order to calculate the potential on a fine grid is:

1. copy the density field, or *problem*, on the fine grid onto a working array, or *patch*;
2. recursively replace the problem on the fine patch by an approximation on a coarser patch;
3. solve the Poisson equation on the coarse patch approximately;
4. use the solution of the coarse patch as a starting guess for the fine-patch problem;
5. solve the problem on the fine patch;
6. copy the fine-patch solution onto the fine grid.

The approximation on the coarse grid (step 3) is calculated using the Gauss-Sidel relaxation method (Hockney & Eastwood, 1989). Steps 2 to 5 form what is called a V-cycle (Laney, 1998). A diagram connecting the different steps is showed in Figure 5.3.

The success of the multigrid solver depends on the coarse grid solution being a good approximation to the fine grid solution. The tests presented in Section 5.2.4 will show that this is not necessarily the case because the forces are not continuous through a refinement jump, in particular for a system in equilibrium.

The APM solver

The APM solver is based on the particle-particle particle-mesh method (Hockney & Eastwood, 1989; Couchman, 1991). The basic idea of the algorithm is to split the force to be calculated between the different levels of refinement.

The calculation on the root grid is identical to the one performed by the multigrid solver. On a fine grid, one only calculates the component of the force due to the smallest scales (largest modes), then reconstructs the complete force by adding the components from the parent grids. Different smoothing functions can be used to filter the modes assigned to a given grid resolution. We use the sphere with uniformly decreasing density S_2:

$$S_2(r) = \begin{cases} \dfrac{48}{\pi a^4}\left(\dfrac{a}{2} - r\right) & \text{if} \quad r \leq a/2 \\ \\ 0 & \text{otherwise} \end{cases} \tag{5.21}$$

where a is a positive parameter. The S_2 profile gives better accuracy in three-dimensional schemes (Hockney & Eastwood, 1989). For each grid we take $a = 3.4\,\Delta X$, where ΔX is the grid cell size. This value has been showed empirically to minimize the noise.

Eventually the total force is reconstructed by adding all the different components:

$$F_{\text{tot}} = F_{\text{coarse}} + \sum_{\text{fine grids}} F_{\text{fine}}. \tag{5.22}$$

The decomposition is shown for the particular case of a simulation with one nested grid in Figure 5.4. We now compare the accuracy of both Poisson solvers for different test cases.

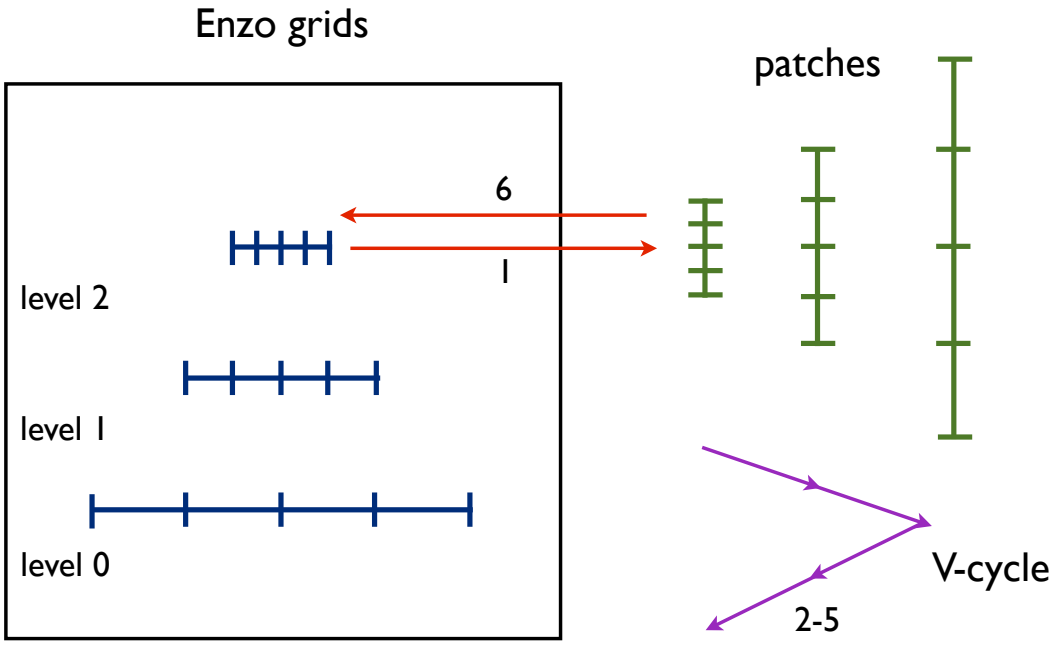

Figure 5.3 The multigrid solver for a simulation with three grids total (blue). The patches are showed in green. The numbers correspond to the different steps described in Section 5.2.3.

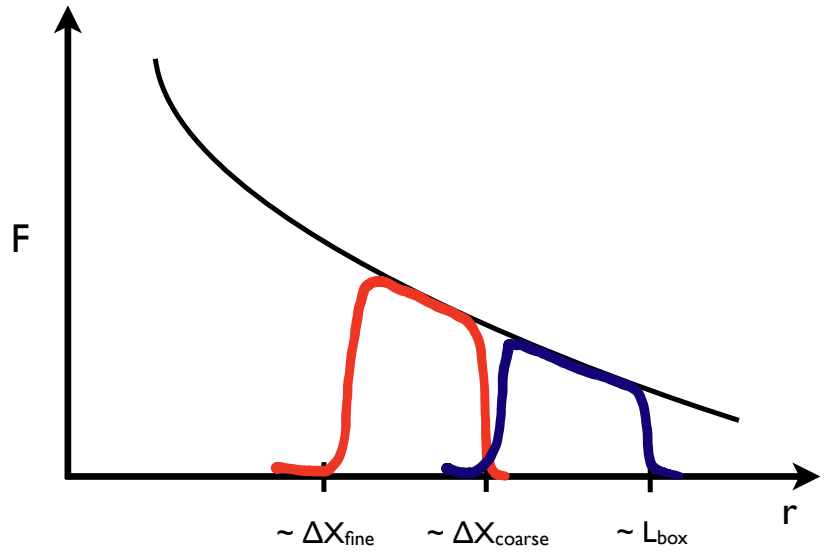

Figure 5.4 Diagram of the APM algorithm for a simulation with a coarse grid of linear size $L_{\rm box}$ and cell size $\Delta X_{\rm coarse}$, and a fine grid of cell size $\Delta X_{\rm fine}$. The total force F (black) is computed adding the component on the coarse grid (blue) and the fine grid (red).

5.2.4 Testing the different Poisson solvers

In this section we perform several tests in order to demonstrate the better accuracy of the APM solver in comparison with the multigrid solver. We assume a three-dimensional computational domain $[0\,;1]^3$, and use gas and *particles*. These particles, also called *dark matter particles*, have their mass deposited into the eight nearest cells and added to the gas density of those cells in order to compute the total density, which is eventually used to solve the Poisson equation.

The TestOrbit problem

We first perform a two-body problem test with two particles initially in a circular orbit, and no gas. The initial conditions are, all in code units:

- Root grid dimensions: $32 \times 32 \times 32$
- Isolated boundary conditions
- Central particle with mass $M_1 = 1.0$
- Test particle with mass $M_2 = 0.1$
- An initial orbital separation $R = 0.3$
- Two levels of adaptive refinement based on the density of the particles when the latter are deposited onto the mesh
- System evolved until $t = 2$

As we can see in Figure 5.5, not even a single circular orbit can be reproduced with the multigrid solver because of the discontinuities across the different refinement levels.

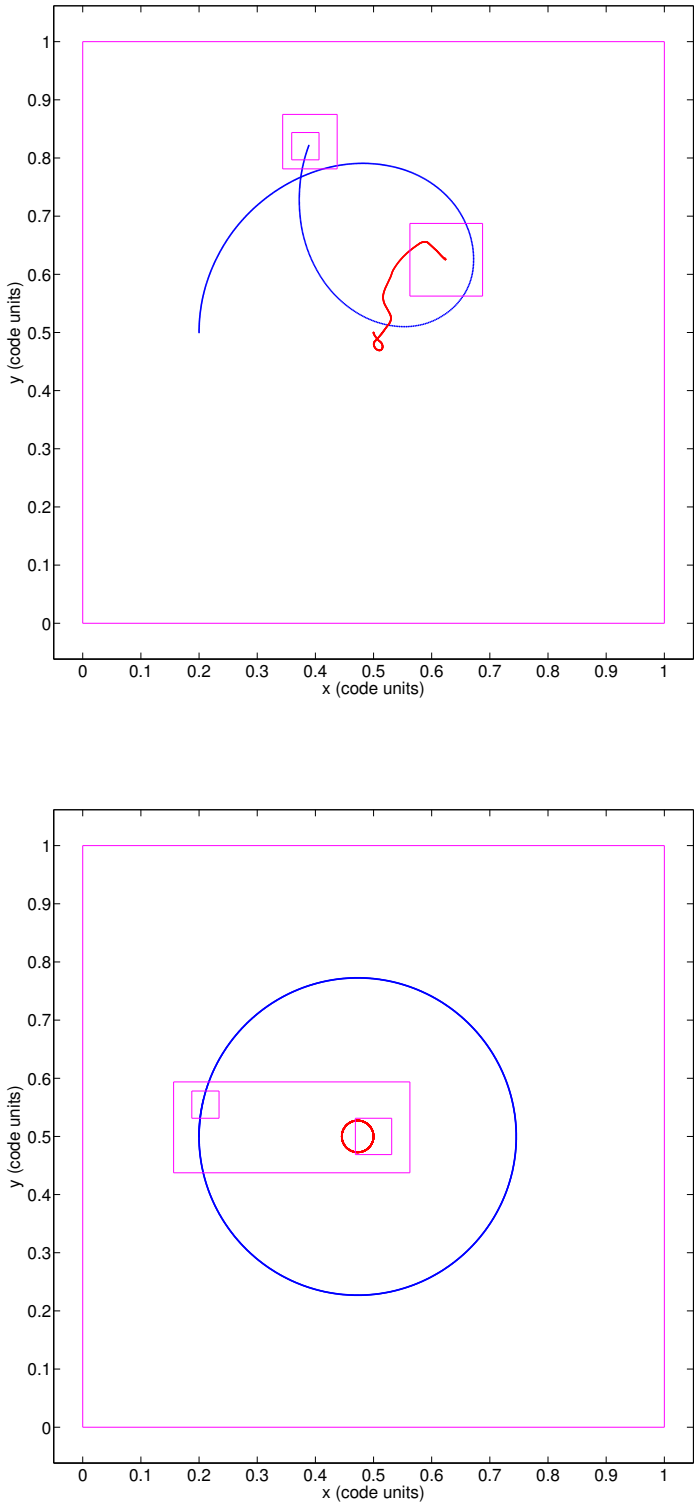

Figure 5.5 Trajectories in the orbital plane of the central particle (red) and the test particle (blue). The different grid levels are showed in magenta. Top: with the Multigrid solver (simulation stopped at $t = 0.64$). Bottom: with the APM solver.

The GravityTest problem

This test verifies the acceleration of nearly massless particles from a single point mass. The initial conditions are, all in code units:

- Root grid dimensions: $32 \times 32 \times 32$
- Isolated boundary conditions
- Central particle with density $\rho = 1.0$
- 5000 test particles placed randomly with mass $m = 10^{-10}$
- One subgrid covering the region $[0.4375\,;0.5625]^3$
- System evolved for one timestep

The tangential component of the force F_{tan} should be zero; the radial component F_{rad} should follow the analytical result $F_{\mathrm{anal}} \propto r^{-2}$, but is softened for radii less than about one cell length. Again, the difference in accuracy between the multigrid solver and the APM solver, is striking (Figure 5.6). For both solvers, the largest inaccuracy in the force calculation is reached at the boundary of the nested grid ($r \approx 2$).

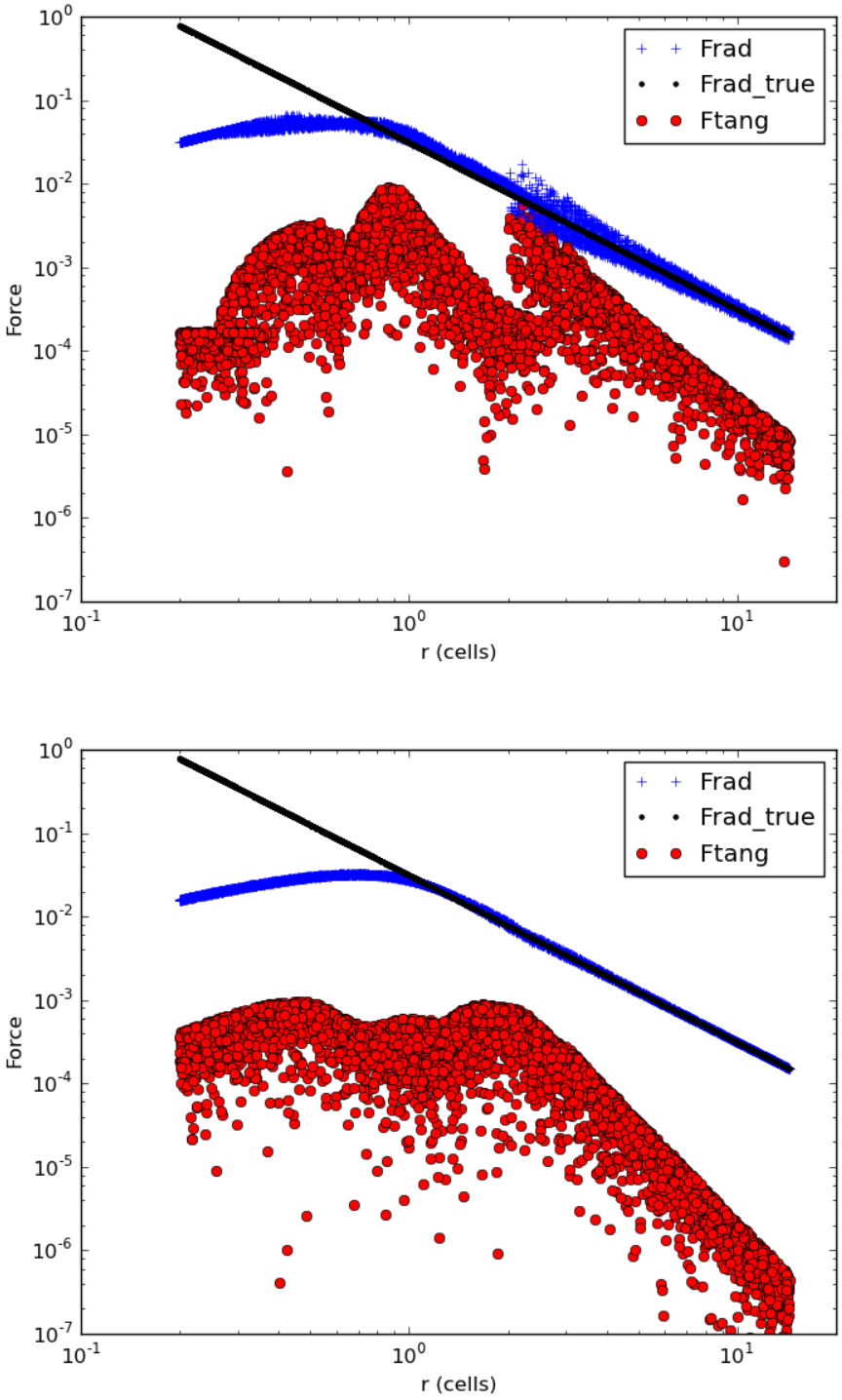

Figure 5.6 Forces on the test particles as a function of the distance to the central particle (in units of the size of a cell in the root grid) obtained with the multigrid (top) and the APM (bottom) solvers. Showed are the analytical force (black), as well as the computed radial (blue) and tangential (red) components.

The SineWaveTest problem

For the final test we set up the gas density to follow a sine distribution. In this particular case, one can directly compare the computed potential with the analytical potential, which according to Equation (5.12), should also be a sine function. The initial conditions are:

- Root grid dimensions: $32 \times 32 \times 32$ or $64 \times 64 \times 64$
- Periodic boundary conditions
- $\rho(x, y, z) = 2 + \sin(\frac{2\pi x}{P})$, where P is the period
- Two levels of refinement in the region $[0.4\ ;\ 0.6]^3$
- Evolved for one timestep

Results are shown in Figure 5.7 and Figure 5.8 for $P = 1.0$ and $P = 0.2$, respectively. Since the gravitational potential is defined to be constant, we display here the values directly output by the code. Note how the accuracy of the computation improves with resolution, in particular for the case $P = 0.2$ (Figure 5.8).

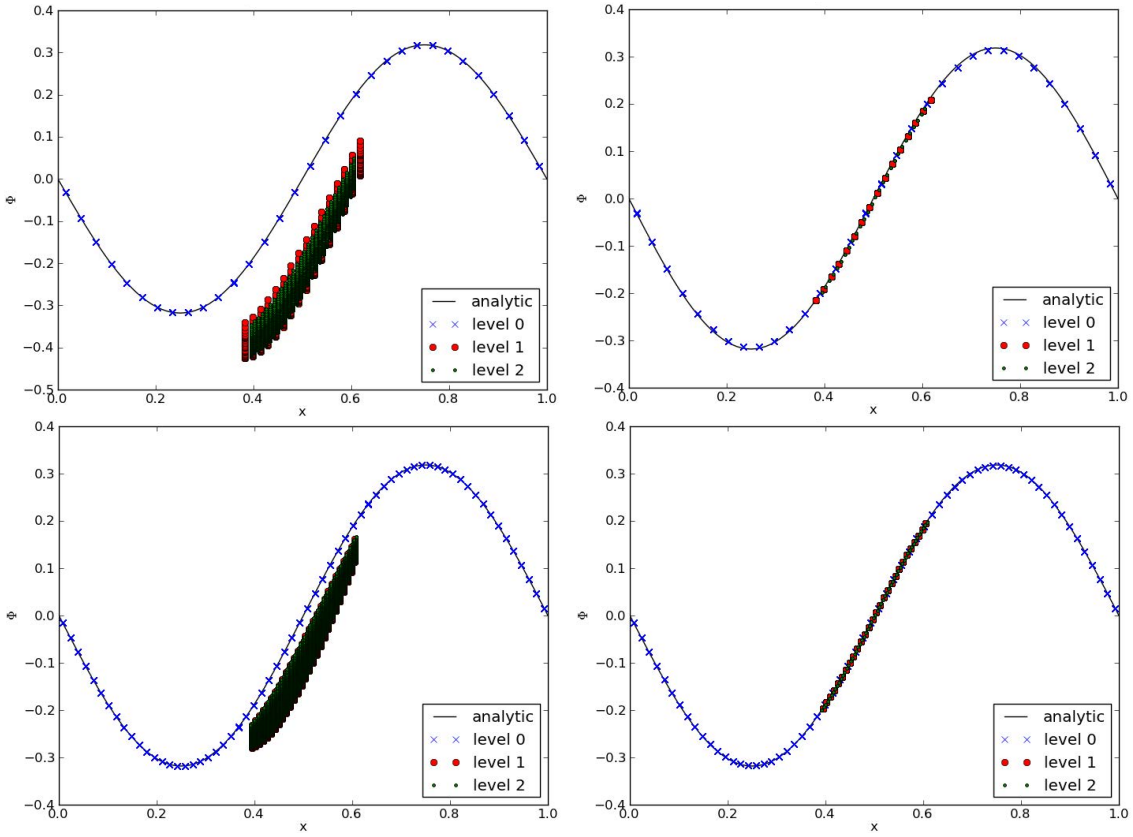

Figure 5.7 Comparison of the potential computed with the multigrid (left) and the APM (right) solver for a sine density wave on a root grid (blue) with $32 \times 32 \times 32$ (top) and $64 \times 64 \times 64$ (bottom) zones, 2 levels of refinement (red and green), and $P = 1.0$.

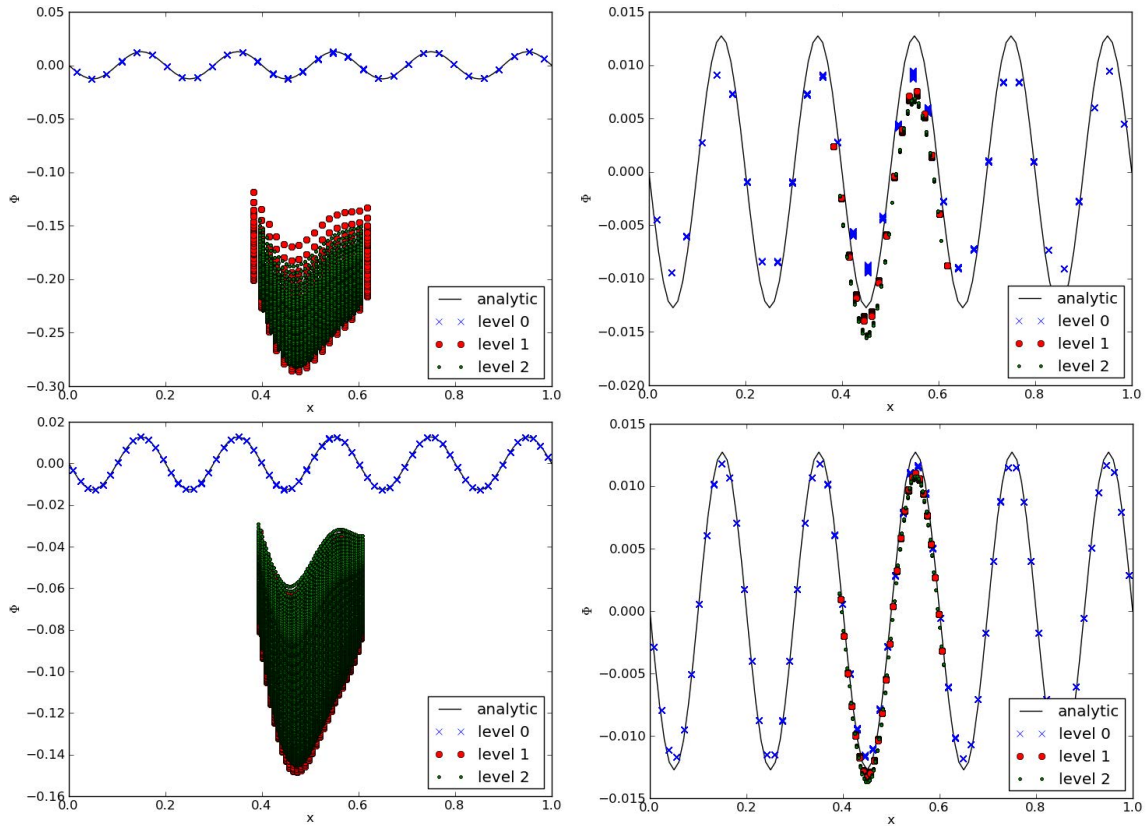

Figure 5.8 Comparison of the potential computed with the multigrid (left) and the APM (right) solver for a sine density wave on a root grid (blue) with $32 \times 32 \times 32$ (top) and $64 \times 64 \times 64$ (bottom) zones, 2 levels of refinement (red and green), and $P = 0.2$.

Prospects

As we showed in the previous section, the APM solver has performed well on a number of test cases. The APM solver is also fully functional in parallel, and we are currently working on generating and relaxing the initial conditions of the simulations that we would like to perform. After having confirmed that our simulations with the 0.15- and 0.1-$M_\odot$ companions are converged (Figure 3.15), we will decrease the companion mass to reach substellar objects.

In that regard, WD 013–349 is of particular interest (Maxted et al., 2006). This system is composed of a 0.053 $M_\odot$ brown dwarf orbiting a 0.39 $M_\odot$ white dwarf with a 0.65 $R_\odot$ orbital separation. This is a clean and well-constrained post-CE system that we could try to model with our hydrodynamical tool.

A local resolution attempt of at least ≈ 0.1 $R_\odot$ is required to study such a short period system. Moreover, the whole computational domain must be $\approx 3\,000$ $R_\odot$ in order to contain the envelope of the giant star until the end of the dynamical phase. Therefore, typical initial conditions that we would like to reach are:

- Root grid dimensions: $64 \times 64 \times 64$
- Domain linear size: $3\,000$ $R_\odot$
- Seven levels of refinement based on the gas mass criterion

A few plots for such conditions are showed in Figure 5.9. Eventually, we are also planning to add another refinement criterion and, at each timestep, refine the regions around the point mass particles, a.k.a the core of the giant star and the companion.

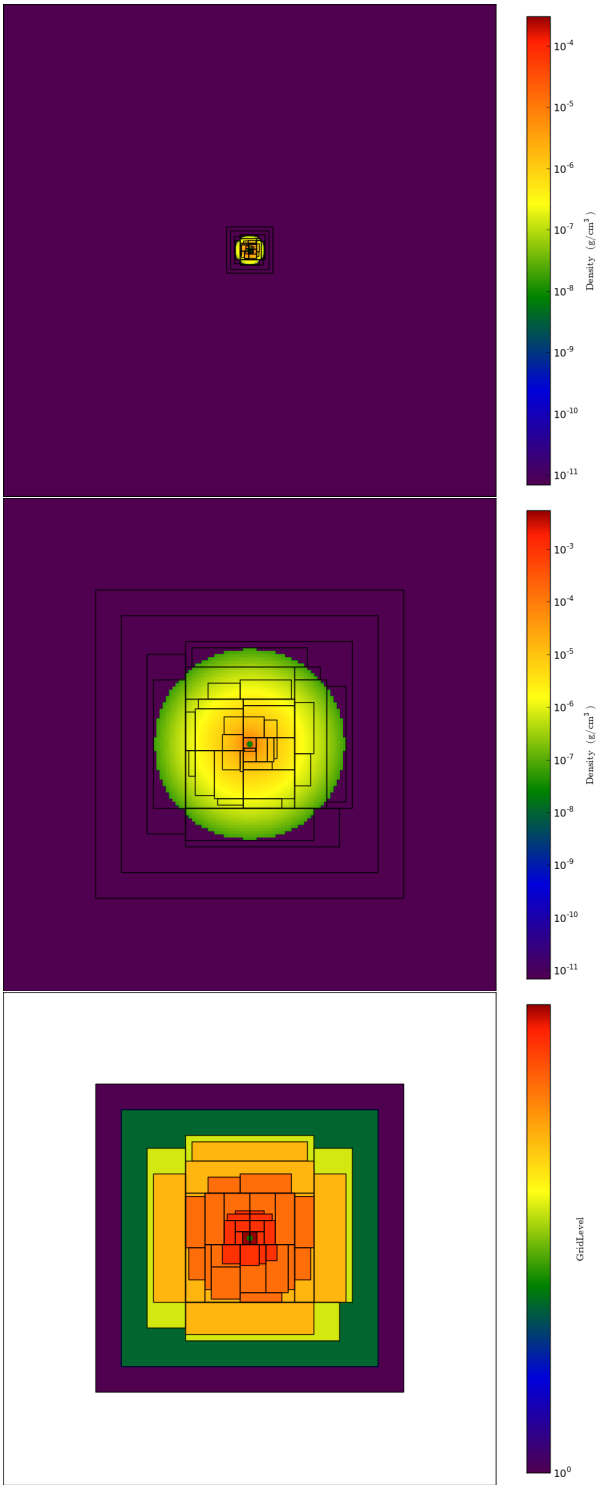

Figure 5.9 Initial conditions described above for a simulation with the progenitor presented in Chapter 3. Top: density slice of the red giant in the entire domain. Middle: Zoom-in on the primary. Bottom: Same region as above but with the refinement level showed instead of density. The black rectangles show the position of the different nested grids.

Chapter 6

Summary and Conclusions

6.1 The common envelope interaction: what's new?

The CE interaction between two stars in a binary system is responsible for some of the most spectacular and important astrophysical objects and phenomena. Although introduced almost forty years ago (Paczynski, 1976), many fundamental questions regarding the CE interaction have yet to be answered. In this thesis, we tackled some of these questions, using mostly analytical and numerical approaches. Here we summarize our findings and emphasize how they have contributed to improving our knowledge of the CE interaction.

Predicting the post-CE interaction orbital period based exclusively on the initial parameters of binary system, is much needed for population synthesis models. We used an analytical/empirical technique in order to statistically predict the final period of a CE interaction. We considered the α-formalism and via a detailed study of the energetics and the use of stellar evolution models, we derived the efficiency α of the CE interaction from a carefully selected and sample of post-CE systems. We suggested a possible inverse dependence of α with the companion to primary mass ratio, and highlighted the significant uncertainties – due to the large degeneracy of the problem – inherent to this type of reconstruction technique.

We then wanted to confirm the predicted efficiency of the ejection with numerical models. Therefore we carried out three-dimensional hydrodynamical simulations of the CE interaction using two different codes. We studied the case of a 0.88 $M_{\odot}$ red giant donor star and companion masses ranging from 0.9 down to 0.1 $M_{\odot}$. The results between the two codes are very consistent, thus verifying that the methods we have

developed to model this problem, are accurate. We were the first to carry out a set of simulations for a range of companion masses, which allowed us to show that the final orbital separation increases with the secondary mass, as expected from an energetic analysis. However, the simulations fail to reproduce systems thought to have gone through a CE interaction. Indeed, most of the envelope of the donor remains bound at the end of the simulations and the final orbital separations are larger than the ones observed. Although these results were also found by Sandquist et al. (1998, 2000), it is the first time that they are connected in a meaningful way to the formation of close binaries. Our conclusions were then confirmed by Ricker & Taam (2012). We suggested that this discrepancy vouches for recombination playing an essential role in the ejection of the envelope and/or significant evolution of the orbit happening in a subsequent phase. Also, a higher local resolution is required in order to prove convergence for the case with secondary masses $\lesssim 0.15\ M_{\odot}$, and to model companion masses down to the substellar regime.

Since most of the giant's envelope is not unbound at the end of the hydrodynamical simulations, we studied whether the mass-losing star would expand as a response to mass loss, therefore facilitating the ejection of the envelope by lowering its binding energy. Using one-dimensional stellar evolution simulations we showed that giants do not evolve adiabatically, nor stay in hydrostatic equilibrium when they lose mass on a dynamical timescale. As a consequence, giant stars actually do not expand when mass is removed from their surface with high mass loss rates, as suggested by previous models in the literature (Hjellming & Webbink, 1987; Ge et al., 2010). Therefore, no stellar expansion that would have helped the envelope ejection, occurs. Moreover, criteria for the onset of the CE interaction based on those previous models, might need to be re-evaluated.

Motivated by several recent observations of brown dwarfs and planets found in close orbits around evolved stars, we finally studied the case where the CE interaction occurs with a substellar companion. Leaving aside the issue of how light companions can eject the envelope, we investigated the dynamical properties of brown dwarf and giant planets while immersed in the common envelope, and whether these substellar companions could be partially or totally destroyed during the in-spiral phase. We concluded that the masses of the companions observed in WD 0137-349, SDSS J08205+0008, and HIP 13044 are most likely the same as prior to the CE phase. However, the planets observed around KIC 05807616 are not massive enough to have survived the engulfment untouched, and we estimated the mass of the progenitor of

these planets to be $\approx 1\ M_{\rm Jup}$.

6.2 Prospects

6.2.1 Reproducing the observations

The immediate first goal should be trying to reproduce the observations for the low- and intermediate-mass systems presented in Chapters 2 and 3. We have suggested two possible explanations for the discrepancy between the outcomes of our numerical simulations and observations of post-CE systems: the missing microphysics and/or the post-dynamical-phase evolution.

Microphysics

In the first scenario, the limited microphysics used in the code – in order to limit computational costs – prevented us from reproducing physical processes that would significantly affect the evolution of the system. One possibility is that as the envelope is ejected, it expands, cools off and recombine, thus releasing enough energy for the envelope to become unbound. We showed qualitatively in Chapter 3 that the use of recombination energy might be sufficient to eject the envelope. The other possibility is related to the initial stratification of the envelope. Because of the use of an ideal gas equation of state (Equation 3.4) in the hydrodynamical simulations, the giant's envelope is not convectively unstable. The convection energy might be the extra energy missing in order to fully unbind the envelope. Different strategies could be adopted to investigate these problems. One could, for instance, try to create a stratification unstable against convection and study whether the CE interaction with this donor star can successfully eject the whole envelope. Recombination could also be included in our simulations, for instance by solving the Saha equations (Equation 3.26) at each timestep. A more definitive option would be to use pre-compiled tables to compute the pressure from the equation of state, which should allow us to treat convection and recombination without having to modify the pressure and density profiles. Finally, one should emphasize that these solutions directly aim to solve the envelope ejection issue, not the fact that the systems are left at too large separations. One would instinctively think that if convection and/or recombination help the ejection, it would not bring to the stellar cores to closer orbits. On the contrary, it might leave the companion at an orbital separation even larger than the ones obtained by the simu-

lations presented in Chapter 3. One should take this reasoning with a grain of salt as intuitive zero-order estimates can be wrong (see Chapter 4) because the equations governing the evolution of the system are non-linear and interlinked. Moreover, we don't know how different the interaction between the companion and a more realistic envelope, would be.

The fall back disk

If the addition of more realistic microphysics is insufficient to eject the envelope and decrease the final orbital separations, one will have to investigate what happens in the post-dynamical phase. The fact that the two jets in NGC6778 (Figure 1.3), moving at ≈ 100 and $400\,\mathrm{km\,s^{-1}}$, are kinematically younger than the nebula (Guerrero & Miranda, 2012) might vouch for strong interactions having taken place after the dynamical phase.

We recall that the extended envelope has, at the end of the simulation, the velocity profile presented in Figure 3.19. Assuming that it evolves ballistically, one can estimate the timescale needed by the envelope to fall back onto the binary. We assume that the profile stays constant in mass coordinates. In other words, a shell is like a particle and does not interact with the shells above and below. A shell i has the the initial profile from Figure 3.19 $[r_i(t=0), v_i(t=0), m_i(t=0)]$, where r_i, v_i, m_i are the position, the radial velocity, and the mass enclosed, respectively. Then for each shell:

- the shell is advanced by δt until $v_i(t) = 0$, which gives us t_{rise};
- $2 \times t_{\mathrm{rise}}$ is the time for the shell to get back to initial configuration but with the velocity oriented downwards;
- the shell is advanced by δt until $r_i(t) \leq r_{\mathrm{final}}$, which gives us t_{collapse};
- the total fallback time is finally $t_{\mathrm{total}} = 2t_{\mathrm{rise}} + t_{\mathrm{collapse}}$.

To advance a shell, we first calculate the local gravitational acceleration

$$g_i(t) = \frac{G m_i(t)}{r_i^2(t)}, \tag{6.1}$$

and compute the position and velocity at the next timestep:

$$\begin{cases} r_i(t+\delta t) = r_i(t) + \epsilon v_i(t)\delta t - \dfrac{1}{2} g_i(t)\delta t^2 \\ \\ v_i(t+\delta t) = v_i(t) - \epsilon g_i(t)\delta t \end{cases} \tag{6.2}$$

with $\epsilon = 1$ if the shell is going upwards, and $\epsilon = -1$ if the shell is going downwards. The different timescales are showed in Figure 6.1 for different time stepping and different $r_{\rm final}$. The typical ballistic timescale of the extended envelope is about a few years. Obviously, such qualitative analysis neglect hydrodynamical effects and radiative transfer, but nevertheless gives a lower-boundary estimate of how long it will take the envelope to fall back and interact with the binary. Hydrodynamical simulations with radiative transfer are required in order to model accurately the evolution of the envelope during the post-dynamical phase.

6.2.2 Different systems and regimes

Another necessary step would be to investigate the evolution for different binary systems. An AGB star has a more loosely bound envelope than a comparable RGB star, and it would be valuable to investigate whether a CE could successfully unbind the envelope in this case. As developed in Chapter 5, the CE interaction with substellar companions is also of particular interest. We have carried out a test simulation with a 10 $M_{\rm Jup}$ secondary (Figure 6.2). As stated earlier, higher resolution is required in order to study the evolution for low-mass and planetary companions, and can only be reached at reasonable costs through the use of adaptive mesh refinement. We therefore implemented an adaptive particle-mesh Poisson solver. This solver should allow us to use nested grids in our codes, a necessary feature to perform simulations with planetary companions. We estimated that a nested grid simulation with initial parameters similar to those showed in Figure 5.9, would require about 200k CPU hours and could scale up to at least 200 cores. Also, the evolution of massive stars is dominated by binary interactions (Bouy, 2011; Sana et al., 2012). Moreover, the most massive stars could very well be in the super-Eddington regime (Shaviv, 2005), thus making the CE evolution with such donors very different from what we have seen in Chapter 3. For these reasons, the evolution of these massive systems through a CE interaction should be investigated. Eventually, all these results should be combined and an exhaustive grid of simulations performed. The results of these simulations could then be easily compiled, for instance in a form of tables, in order

to be efficiently used in population synthesis studies.

6.2.3 Predicting and explaining future observations

Thanks to the recent and coming development of state-of-the-art telescopes, we are now entering a new era in the detection of transient astrophysical phenomena. As an example, the Palomar Transient Factory (PTF, Rau et al., 2009) has already detected more than 1 800 supernovae that have been spectroscopically confirmed[1]. Expected to start running in 2022, the Large Synoptic Survey Telescope (LSST, Ivezic et al., 2008) will survey the sky twice each week and detect a large amount of these time-varying events. In order to explain some of these observations, our numerical simulations could be coupled with a three-dimensional radiative transfer code in order to produce simulated light curves, which could then be used as direct comparisons. Finally, the formation of neutron star/neutron star or neutron star/ black hole systems is thought to result from a CE interaction in a high-mass X-ray binary (Voss & Tauris, 2003). Thus, this work has direct implications for gravitational waves detections such as the Laser Interferometer Gravitational-Wave Observatory (LIGO, Abramovici et al., 1992). Although LIGO was capable to detect about one neutron star/neutron star merger every fifty years, advanced LIGO (aLIGO) should be able to detect about 40 of these objects every year (Voss & Tauris, 2003).

[1]Source: http://www.astro.caltech.edu/ptf/index.php.

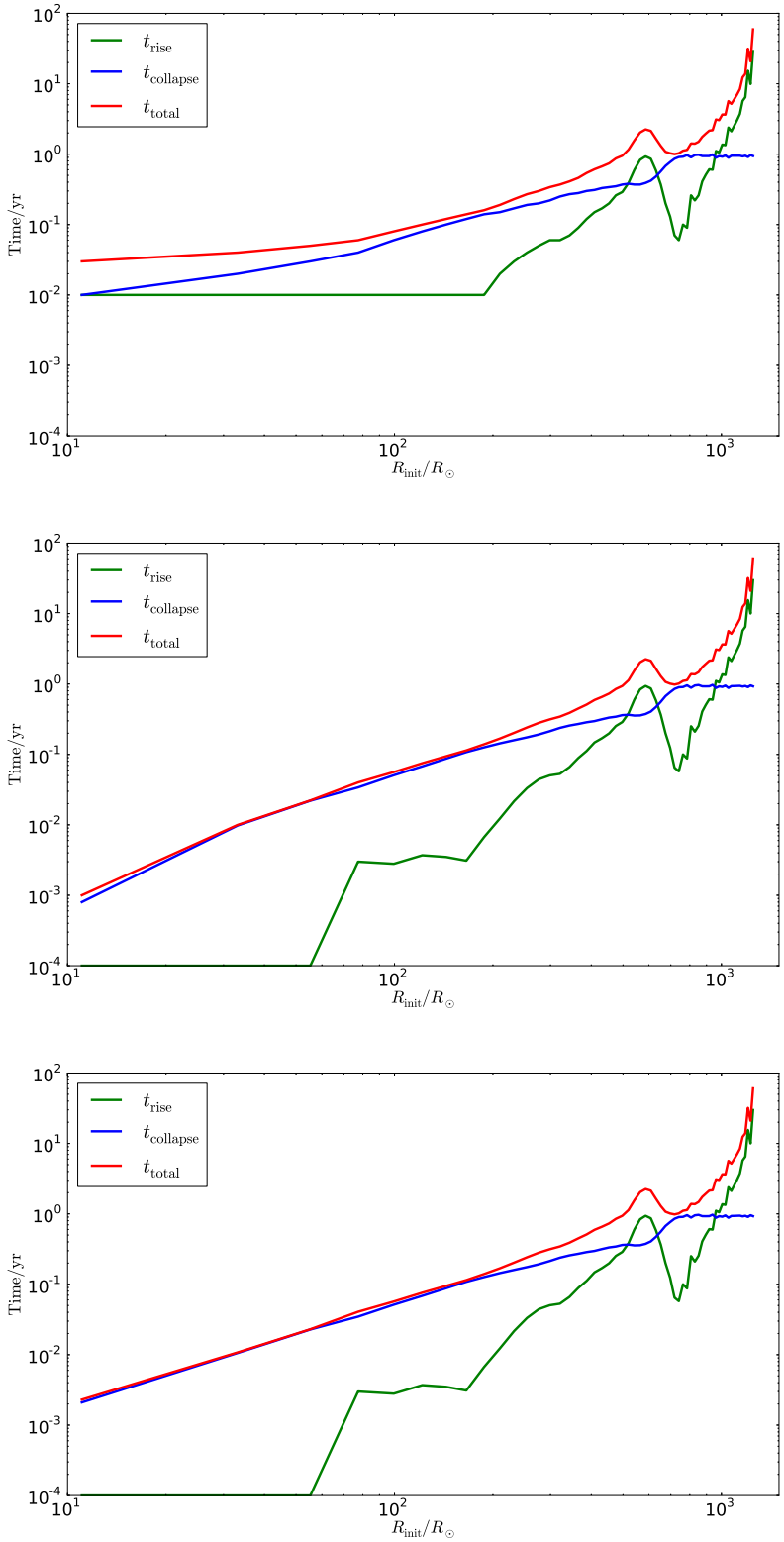

Figure 6.1 Ballistic timescales as a function of the initial position for $\delta t = 10^{-2}$ yr and $r_{\rm final} = 10\ R_\odot$ (top), $\delta t = 10^{-4}$ yr and $r_{\rm final} = 10\ R_\odot$ (middle), and $\delta t = 10^{-4}$ yr and $r_{\rm final} = 1\ R_\odot$ (bottom).

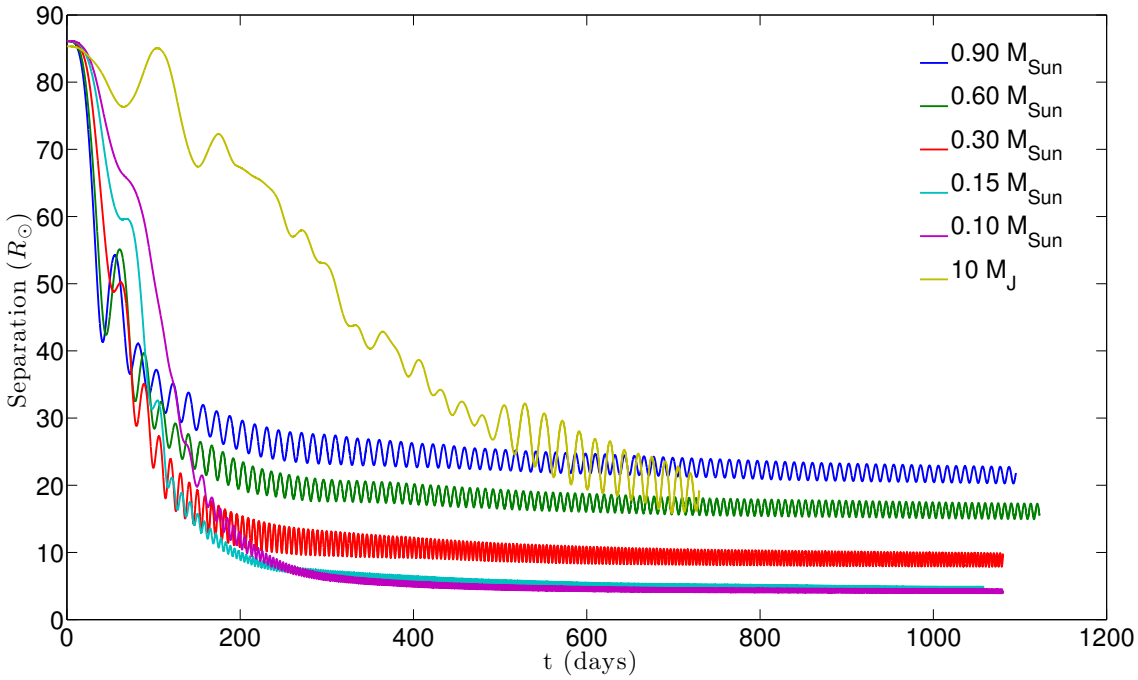

Figure 6.2 Similar to Figure 3.4 but also with the evolution for a 10 $M_{\rm Jup}$ companion. The unigrid resolution is the same between all simulations (256^3 zones).

Bibliography

Abramovici, A. et al. 1992, Science (ISSN 0036-8075), 256, 325

Afşar, M. & Ibanoğlu, C. 2008, Monthly Notices of the Royal Astronomical Society, 391, 802

Agertz, O. et al. 2006, arXiv.org, astro-ph, 963

Artymowicz, P., Clarke, C. J., Lubow, S. H., & Pringle, J. E. 1991, Astrophysical Journal, 370, L35

Bear, E. & Soker, N. 2010, New Astronomy, 15, 483

— 2012, The Astrophysical Journal Letters, 749, L14

Bear, E., Soker, N., & Harpaz, A. 2011, The Astrophysical Journal Letters, 733, L44

Belczynski, K., Bulik, T., & Ruiter, A. J. 2005, The Astrophysical Journal, 629, 915

Belczynski, K., Kalogera, V., Rasio, F. A., Taam, R. E., Zezas, A., Bulik, T., Maccarone, T. J., & Ivanova, N. 2008, The Astrophysical Journal Supplement Series, 174, 223

Benz, W. 1990, in Proceedings of the NATO Advanced Research Workshop on The Numerical Modelling of Nonlinear Stellar Pulsations Problems and Prospects, 269

Bertelli, G., Girardi, L., Marigo, P., & Nasi, E. 2008, Astronomy and Astrophysics, 484, 815

Bevington, P. R. & Robinson, D. K. 2003, Data reduction and error analysis for the physical sciences

Bildsten, L., Shen, K. J., Weinberg, N. N., & Nelemans, G. 2007, The Astrophysical Journal, 662, L95

Bilíková, J., Chu, Y.-H., Gruendl, R. A., Su, K. Y. L., & De Marco, O. 2012, The Astrophysical Journal Supplement, 200, 3

Bloecker, T. 1995a, Astronomy and Astrophysics, 299, 755

— 1995b, Astronomy and Astrophysics, 297, 727

Bodenheimer, P. & Taam, R. E. 1984, Astrophysical Journal, 280, 771

Bondi, H. & Hoyle, F. 1944, Monthly Notices of the Royal Astronomical Society, 104, 273

Bopp, B. W. & Stencel, R. E. 1981, Astrophysical Journal, 247, L131

Bouy, H. 2011, Computational Star Formation, 270, 41

Brüggen, M. & Hillebrandt, W. 2000, arXiv.org, astro-ph, 73

Bryan, G. L., Norman, M. L., Stone, J. M., Cen, R., & Ostriker, J. P. 1995, Computer Physics Communications, 89, 149

Burkert, A. & Bodenheimer, P. 1993, Monthly Notices of the Royal Astronomical Society, 264, 798

Cardelli, J. A., Clayton, G. C., & Mathis, J. S. 1989, Astrophysical Journal, 345, 245

Carney, B. W., Latham, D. W., & Laird, J. B. 2004, arXiv.org, astro-ph, 466

Carroll, B. W. & Ostlie, D. A. 2006, An introduction to modern astrophysics and cosmology / B. W. Carroll and D. A. Ostlie. 2nd edition. San Francisco: Pearson

Casanova, J., José, J., García-Berro, E., Shore, S. N., & Calder, A. C. 2011, Nature, 478, 490

Castellani, M., Castellani, V., & Prada Moroni, P. G. 2006, Astronomy and Astrophysics, 457, 569

Charles, P. A. & Coe, M. J. 2006, Optical, ultraviolet and infrared observations of X-ray binaries

Charpinet, S. et al. 2011, Nature, 480, 496

Clayton, G. C. 2012, The Journal of the American Association of Variable Star Observers, 40, 539

Couchman, H. M. P. 1991, Astrophysical Journal, 368, L23

Cox, A. N. 2000, Irish Astronomical Journal, 27, 234

Darwin, G. H. 1879, The Observatory, 3, 79

Davies, M. B., Ruffert, M., Benz, W., & Muller, E. 1993, Astronomy and Astrophysics, 272, 430

Davis, P. J., Kolb, U., & Willems, B. 2010, Monthly Notices of the Royal Astronomical Society, 403, 179

de Kool, M., van den Heuvel, E. P. J., & Pylyser, E. 1987, Astronomy and Astrophysics, 183, 47

De Marco, O. 2009, Publications of the Astronomical Society of the Pacific, 121, 316

De Marco, O., Hillwig, T. C., & Smith, A. J. 2008, The Astronomical Journal, 136, 323

De Marco, O., Passy, J.-C., Herwig, F., Fryer, C. L., Mac Low, M.-M., & Oishi, J. S. 2012, From Interacting Binaries to Exoplanets: Essential Modeling Tools, 282, 517

De Marco, O., Passy, J.-C., Moe, M., Herwig, F., Mac Low, M.-M., & Paxton, B. 2011, Monthly Notices of the Royal Astronomical Society, 411, 2277

De Marco, O., Sandquist, E. L., Mac Low, M.-M., Herwig, F., & Taam, R. E. 2003, Revista Mexicana de Astronomia y Astrofisica Conference Series, 18, 24

de Medeiros, J. R. & Mayor, M. 1999, Astronomy and Astrophysics Supplement, 139, 433

Deloye, C. J. & Taam, R. E. 2010, The Astrophysical Journal Letters, 719, L28

Dewi, J. D. M. & Tauris, T. M. 2000, Astronomy and Astrophysics, 360, 1043

Diehl, S. & Statler, T. S. 2005, arXiv.org, astro-ph, 497

Dilts, G. A. 1999, International Journal for Numerical Methods in Engineering, 44, 1115

Dorman, B., Rood, R., & O'Connell, R. 1993, arXiv.org, astro-ph, 596

Driebe, T., Schoenberner, D., Bloecker, T., & Herwig, F. 1998, Astronomy and Astrophysics, 339, 123

Dubrulle, B., Morfill, G., & Sterzik, M. 1995, Icarus (ISSN 0019-1035), 114, 237

Duquennoy, A. & Mayor, M. 1991, Astronomy and Astrophysics, 248, 485

Edgar, R. 2004, New Astronomy Reviews, 48, 843

Edgar, R. G., Nordhaus, J., Blackman, E. G., & Frank, A. 2008, The Astrophysical Journal, 675, L101

Eggleton, P. 2006, Evolutionary Processes in Binary and Multiple Stars (Lawrence Livermore National Laboratory, California: Evolutionary Processes in Binary and Multiple Stars)

Eggleton, P. P. 1983, Astrophysical Journal, 268, 368

Farihi, J., Becklin, E. E., & Zuckerman, B. 2005, The Astrophysical Journal Supplement Series, 161, 394

Field, G. B. & Ferrara, A. 1995, Astrophysical Journal, 438, 957

Fontane, J. R. M. & Joly, L. 2008, Journal of Fluid Mechnanics, 612, 237

Fregeau, J. M. 2007a, arXiv.org, astro-ph, 239

— 2007b, arXiv.org, astro-ph, L25

Fregeau, J. M., Ivanova, N., & Rasio, F. A. 2009, The Astrophysical Journal, 707, 1533

Frenk, C. S. et al. 1999, The Astrophysical Journal, 525, 554

Frew, D. J. 2008, PhD Thesis, 109

Frew, D. J. & Parker, Q. A. 2007, "Asymmetrical Planetary Nebulae IV, 68

Fryer, C. L. & Heger, A. 2005, The Astrophysical Journal, 623, 302

Fryer, C. L., Rockefeller, G., & Warren, M. S. 2006, The Astrophysical Journal, 643, 292

Fryxell, B. et al. 2000, The Astrophysical Journal Supplement Series, 131, 273

García-Arredondo, F. & Frank, A. 2004, The Astrophysical Journal, 600, 992

García-Segura, G., Langer, N., Różyczka, M., & Franco, J. 1999, The Astrophysical Journal, 517, 767

García-Segura, G., López, J. A., & Franco, J. 2005, The Astrophysical Journal, 618, 919

Ge, H., Hjellming, M. S., Webbink, R. F., Chen, X., & Han, Z. 2010, The Astrophysical Journal, 717, 724

Geier, S. et al. 2010, Astrophysics and Space Science, 329, 91

— 2011, The Astrophysical Journal Letters, 731, L22

Gesicki, K. & Zijlstra, A. A. 2007, arXiv.org, astro-ph, L29

Girven, J. et al. 2012, Monthly Notices of the Royal Astronomical Society, 425, 1013

Guerrero, M. A. & Miranda, L. F. 2012, Astronomy and Astrophysics, 539, 47

Han, Z., Podsiadlowski, P., & Eggleton, P. P. 1994, Monthly Notices of the Royal Astronomical Society, 270, 121

— 1995, Monthly Notices of the Royal Astronomical Society, 272, 800

Han, Z., Podsiadlowski, P., Maxted, P. L. F., & Marsh, T. R. 2003, arXiv.org, 341, 669

Han, Z., Podsiadlowski, P., Maxted, P. L. F., Marsh, T. R., & Ivanova, N. 2002, arXiv.org, astro-ph, 449

Herwig, F. 2000, Astronomy and Astrophysics, 360, 952

— 2001, arXiv.org, astro-ph

— 2004, The Astrophysical Journal, 605, 425

— 2005, Annual Review of Astronomy and Astrophysics, 43, 435

Herwig, F. 2006, in Proceedings of the International Symposium on Nuclear Astrophysics - Nuclei in the Cosmos - IX. 25-30 June 2006, 206

Hjellming, M. S. & Webbink, R. F. 1987, Astrophysical Journal, 318, 794

Hockney, R. W. & Eastwood, J. W. 1989, Computer Simulation Using Particles (Taylor & Francis)

Holberg, J. B. 2009, Journal of Physics: Conference Series, 172, 2022

Holberg, J. B., Sion, E. M., Oswalt, T., McCook, G. P., Foran, S., & Subasavage, J. P. 2008, The Astronomical Journal, 135, 1225

Hurley, J. R., Aarseth, S. J., & Shara, M. M. 2007, The Astrophysical Journal, 665, 707

Hurley, J. R., Pols, O. R., & Tout, C. A. 2000, Monthly Notices of the Royal Astronomical Society, 315, 543

Hurley, J. R., Tout, C. A., & Pols, O. R. 2002, Monthly Notices of the Royal Astronomical Society, 329, 897

Iben, I. J. & Livio, M. 1993, Astronomical Society of the Pacific, 105, 1373

Iben, I. J. & Tutukov, A. V. 1984, Astrophysical Journal, 284, 719

— 1985, Astrophysical Journal Supplement, 58, 661

— 1993, Astrophysical Journal, 418, 343

Ivanova, N. 2011, arXiv.org, astro-ph.SR

Ivanova, N., Belczynski, K., Fregeau, J. M., & Rasio, F. A. 2005, Monthly Notices of the Royal Astronomical Society, 358, 572

Ivezic, Z. et al. 2008, arXiv.org, astro-ph, 2366

Johansen, A., Henning, T., & Klahr, H. 2005, arXiv.org, astro-ph, 1219

Jorissen, A. & Frankowski, A. 2008, arXiv.org, astro-ph, 1

Junk, V., Walch, S., Heitsch, F., Burkert, A., Wetzstein, M., Schartmann, M., & Price, D. J. 2010, Monthly Notices of the Royal Astronomical Society, 407, 1933

Kahane, C. & Jura, M. 1996, Astronomy and Astrophysics, 310, 952

Kashi, A. & Soker, N. 2011, Monthly Notices of the Royal Astronomical Society, 417, 1466

Kepler, S. O., Kleinman, S. J., Nitta, A., Koester, D., Castanheira, B. G., Giovannini, O., Costa, A. F. M., & Althaus, L. 2007, Monthly Notices of the Royal Astronomical Society, 375, 1315

King, A. R. 1988, Royal Astronomical Society, 29, 1

Kippenhahn, R. & Weigert, A. 1994, Stellar Structure and Evolution (Göttingen, Germany: Stellar Structure and Evolution)

Klein, R. I., McKee, C. F., & Colella, P. 1994, Astrophysical Journal, 420, 213

Knigge, C. 2011, in Evolution of compact binaries. Proceedings of a workshop held at Hotel San Martín, 3

Kraft, R. P. 1962, Astrophysical Journal, 135, 408

Kroupa, P. 2000, arXiv.org, astro-ph, 231

Lajoie, C.-P. & Sills, A. 2011a, The Astrophysical Journal, 726, 66

— 2011b, The Astrophysical Journal, 726, 67

Landolt, A. U. 1992, Astronomical Journal (ISSN 0004-6256), 104, 340

Laney, C. B. 1998, Computational Gasdynamics

Lawrence, A. et al. 2007, Monthly Notices of the Royal Astronomical Society, 379, 1599

Liebert, J., Bergeron, P., & Holberg, J. B. 2005, arXiv.org, astro-ph, 47

Liu, X. W., Barlow, M. J., Blades, J. C., Osmer, S., & Clegg, R. E. S. 1995, Monthly Notices of the Royal Astronomical Society, 276, 167

Mac Low, M.-M. & Zahnle, K. 1994, Astrophysical Journal, 434, L33

Madappatt, N., De Marco, O., Nordhaus, J., & Wardle, M. 2011, in PLANETARY SYSTEMS BEYOND THE MAIN SEQUENCE: Proceedings of the International Conference. AIP Conference Proceedings, Department of Physics and Astronomy, Macquarie University, Sydney, NSW 2109, Australia, 319–323

Maoz, D. & Mannucci, F. 2012, Publications of the Astronomical Society of Australia, 29, 447

Maron, J. L., McNally, C. P., & Mac Low, M.-M. 2012, The Astrophysical Journal Supplement, 200, 6

Mastrodemos, N. & Morris, M. 1998, Astrophysical Journal v.497, 497, 303

— 1999, The Astrophysical Journal, 523, 357

Maxted, P. L. F., Heber, U., Marsh, T. R., & North, R. C. 2001, Monthly Notices of the Royal Astronomical Society, 326, 1391

Maxted, P. L. F., Napiwotzki, R., Dobbie, P. D., & Burleigh, M. R. 2006, Nature, 442, 543

McNally, C. P., Lyra, W., & Passy, J.-C. 2012a, The Astrophysical Journal Supplement, 201, 18

McNally, C. P., Maron, J. L., & Mac Low, M.-M. 2012b, The Astrophysical Journal Supplement, 200, 7

Meng, X. C., Chen, W. C., Yang, W. M., & Li, Z. M. 2011, Astronomy and Astrophysics, 525, 129

Meyer, F. & Meyer-Hofmeister, E. 1979, Astronomy and Astrophysics, 78, 167

Mikołajewska, J. 2007, Baltic Astronomy, 16, 1

Milone, A. P. et al. 2012, Astronomy and Astrophysics, 540, 16

Miranda, E. N. 2001, European Journal of Physics, 22, 483

Miszalski, B., Acker, A., Moffat, A. F. J., Parker, Q. A., & Udalski, A. 2009, Astronomy and Astrophysics, 496, 813

Miura, A. & Pritchett, P. L. 1982, J. Geophys. Res., 87, 7431

Moe, M. & De Marco, O. 2006, arXiv.org, astro-ph, 916

— 2011, Asymmetric Planetary Nebulae 5 conference, 107P

Monaghan, J. 1992, In: Annual review of astronomy and astrophysics. Vol. 30 (A93-25826 09-90), 30, 543

Montez, R. J., De Marco, O., Kastner, J. H., & Chu, Y.-H. 2010, The Astrophysical Journal, 721, 1820

Morales-Rueda, L., Maxted, P. L. F., & Marsh, T. R. 2004, Astrophysics and Space Science, 291, 299

Morales-Rueda, L., Maxted, P. L. F., Marsh, T. R., North, R. C., & Heber, U. 2003, Monthly Notice of the Royal Astronomical Society, 338, 752

Mori, M. & Burkert, A. 2000, The Astrophysical Journal, 538, 559

Murray, S. D., White, S. D. M., Blondin, J. M., & Lin, D. N. C. 1993, Astrophysical Journal, 407, 588

Nelemans, G., Verbunt, F., Yungelson, L. R., & Portegies Zwart, S. F. 2000, Astronomy and Astrophysics, 360, 1011

Nelson, B. & Young, A. 1970, Publications of the Astronomical Society of the Pacific, 82, 699

Nordhaus, J. & Blackman, E. G. 2006, arXiv.org, astro-ph, 2004

Nordhaus, J., Blackman, E. G., & Frank, A. 2006, arXiv.org, astro-ph, 599

Nordhaus, J., Spiegel, D. S., Ibgui, L., Goodman, J., & Burrows, A. 2010, Monthly Notices of the Royal Astronomical Society, 408, 631

Norman, M. L., Bryan, G. L., Harkness, R., Bordner, J., Reynolds, D. R., O'Shea, B. W., & Wagner, R. 2007, arXiv.org, 0705, 1556

Nulsen, P. E. J. 1982, Monthly Notices of the Royal Astronomical Society, 198, 1007

Ofman, L. & Thompson, B. J. 2011, arXiv.org, astro-ph.SR

O'Shea, B. W., Bryan, G. L., Bordner, J., Norman, M. L., Abel, T., Harkness, R., & Kritsuk, A. 2004, arXiv.org, astro-ph, 3044

Paczynski, B. 1976, in Structure and Evolution of Close Binary Systems; Proceedings of the Symposium, 75

Parker, Q. A. et al. 2006, Monthly Notices of the Royal Astronomical Society, 373, 79

Passy, J.-C. et al. 2012, The Astrophysical Journal, 744, 52

Paxton, B., Bildsten, L., Dotter, A., Herwig, F., Lesaffre, P., & Timmes, F. X. 2011, The Astrophysical Journal Supplement, 192, 3

Perets, H. B. 2010, arXiv.org, astro-ph.EP

Podsiadlowski, P. 2001, Evolution of Binary and Multiple Star Systems; A Meeting in Celebration of Peter Eggleton's 60th Birthday. ASP Conference Series, 229, 239

Politano, M., van der Sluys, M., Taam, R. E., & Willems, B. 2010, The Astrophysical Journal, 720, 1752

Politano, M. & Weiler, K. P. 2007, arXiv.org, astro-ph, 663

Price, D. J. 2008, Journal of Computational Physics

— 2012, Journal of Computational Physics, 231, 759

Quinlan, N. J., Basa, M., & Lastiwka, M. 2006, International Journal for Numerical Methods in Engineering, 66, 2064

Raghavan, D. et al. 2010, The Astrophysical Journal Supplement, 190, 1

Rau, A. et al. 2009, Publications of the Astronomical Society of the Pacific, 121, 1334

Rauch, T. & Deetjen, J. L. 2003, Stellar Atmosphere Modeling, 288, 103

Rauch, T., Ziegler, M., Werner, K., Kruk, J. W., Oliveira, C. M., Vande Putte, D., Mignani, R. P., & Kerber, F. 2007, Astronomy and Astrophysics, 470, 317

Read, J. I., Hayfield, T., & Agertz, O. 2010, Monthly Notices of the Royal Astronomical Society, 405, 1513

Reimers, D. 1975, Mémoires of the Société Royale des Sciences de Liège, 8, 369

Ricker, P. M. & Taam, R. E. 2008, The Astrophysical Journal, 672, L41

— 2012, The Astrophysical Journal, 746, 74

Robertson, B. E., Kravtsov, A. V., Gnedin, N. Y., Abel, T., & Rudd, D. H. 2009, arXiv.org, astro-ph.CO, 2463

Rodríguez, M., Corradi, R. L. M., & Mampaso, A. 2001, Astronomy and Astrophysics, 377, 1042

Rosswog, S. 2009, arXiv.org, astro-ph.IM, 78

Ruffert, M. 1993, Astronomy and Astrophysics, 280, 141

Ryan, S. G., Beers, T. C., Kajino, T., & Rosolankova, K. 2000, arXiv.org, astro-ph

Sana, H. et al. 2012, Science, 337, 444

Sandquist, E. L., Taam, R. E., & Burkert, A. 2000, The Astrophysical Journal, 533, 984

Sandquist, E. L., Taam, R. E., Chen, X., Bodenheimer, P., & Burkert, A. 1998, Astrophysical Journal, 500, 909

Schonberner, D. 1993, in Planetary nebulae: proceedings of the 155 Symposium of the International Astronomical Union; held in Innsbruck; Austria; July 1317; 1992. Edited by Ronald Weinberger and Agnes Acker. International Astronomical Union. Symposium no. 155; Kluwer Academic Publishers; Dordrecht, 415

Schreiber, M. R. et al. 2009, Journal of Physics: Conference Series, 172, 2024

Schreiber, M. R. & Gänsicke, B. T. 2003, Astronomy and Astrophysics, 406, 305

Schreiber, M. R., Gänsicke, B. T., Southworth, J., Schwope, A. D., & Koester, D. 2008, Astronomy and Astrophysics, 484, 441

Setiawan, J., Klement, R., Henning, T., Rix, H.-W., Rochau, B., Schulze-Hartung, T., & Rodmann, J. 2011, in PLANETARY SYSTEMS BEYOND THE MAIN SEQUENCE: Proceedings of the International Conference. AIP Conference Proceedings, Max-Planck-Institut für Astronomie, Königstuhl 17, 69117 Heidelberg, Germany, 182–189

Shakura, N. I. & Sunyaev, R. A. 1973, Astronomy and Astrophysics, 24, 337

Shaviv, N. J. 2005, The Fate of the Most Massive Stars, 332, 180

Sills, A. 2010, arXiv.org, astro-ph.SR

Sills, A., Karakas, A., & Lattanzio, J. 2009, The Astrophysical Journal, 692, 1411

Soker, N. 1992, Astrophysical Journal, 386, 190

— 1997, Astrophysical Journal Supplement, 112, 487

— 1998, arXiv.org, astro-ph, 1308

— 2006, The Publications of the Astronomical Society of the Pacific, 118, 260

Soker, N. & Harpaz, A. 2003, Monthly Notices of the Royal Astronomical Society, 343, 456

Solheim, J.-E. 2010, Publications of the Astronomical Society of the Pacific, 122, 1133

Sollima, A., Lanzoni, B., Beccari, G., Ferraro, F. R., & Pecci, F. F. 2008, arXiv.org, astro-ph, 701

Spiegel, D. S. 2012, arXiv.org, astro-ph.EP, 2276

Springel, V. 2011a, arXiv.org, physics.flu-dyn, 2218

— 2011b, arXiv.org, astro-ph.CO, 391

Stone, J. M., Gardiner, T. A., Teuben, P., Hawley, J. F., & Simon, J. B. 2008, The Astrophysical Journal Supplement Series, 178, 137

Stone, J. M. & Norman, M. L. 1992, Astrophysical Journal Supplement, 80, 753

Sweigart, A. V. 1997, The Third Conference on Faint Blue Stars (1997), 3

Taam, R. E., Bodenheimer, P., & Ostriker, J. P. 1978, Astrophysical Journal, 222, 269

Taam, R. E. & Ricker, P. M. 2010, New Astronomy Reviews, 54, 65

Taam, R. E. & Sandquist, E. L. 2000, Annual Review of Astronomy and Astrophysics, 38, 113

Tarbell, T., Ryutova, M., Covington, J., & Fludra, A. 1999, The Astrophysical Journal, 514, L47

Tasker, E. J., Brunino, R., Mitchell, N. L., Michielsen, D., Hopton, S., Pearce, F. R., Bryan, G. L., & Theuns, T. 2008, arXiv.org, astro-ph, 1267

Tauris, T. M. & Dewi, J. D. M. 2001, Astronomy and Astrophysics, 369, 170

Terman, J. L. & Taam, R. E. 1996, Astrophysical Journal, 458, 692

Tody, D. 1986, in IN: Instrumentation in astronomy VI; Proceedings of the Meeting, 733

Tody, D. 1993, Astronomical Data Analysis Software and Systems II, 52, 173

Tout, C. A. & Eggleton, P. P. 1988, Monthly Notices of the Royal Astronomical Society (ISSN 0035-8711), 231, 823

Tutukov, A. & Yungelson, L. 1979, in In: Mass loss and evolution of O-type stars; Proceedings of the Symposium, Akademiia Nauk SSSR, Astronomicheskii Sovet, Moscow, USSR, 401–406

Tylenda, R. et al. 2011, Astronomy and Astrophysics, 528, 114

Vacca, W. D., Garmany, C. D., & Shull, J. M. 1996, Astrophysical Journal v.460, 460, 914

van Grootel, V. et al. 2010, The Astrophysical Journal Letters, 718, L97

van Leer, B. 1977, Journal of Computational Physics, 23, 276

Vassiliadis, E. & Wood, P. R. 1994, The Astrophysical Journal Supplement Series, 92, 125

Villaver, E. & Livio, M. 2007, arXiv.org, astro-ph, 1192

— 2009, The Astrophysical Journal Letters, 705, L81

Voss, R. & Tauris, T. M. 2003, arXiv.org, astro-ph, 1169

Walker, M. F. 1954, Publications of the Astronomical Society of the Pacific, 66, 230

Wallerstein, G. et al. 1997, Reviews of Modern Physics, 69, 995

Wang, L. F. & Ye, W. H. 2010, Wang: Combined effect of the density and velocity... - Google Scholar (Physics of Plasmas)

Warner, B. 1995, Cataclysmic variable stars., Vol. 28 (Camb. Astrophys. Ser.)

Warren, M. & Salmon, J. 1993, in Supercomputing '93. Proceedings, 12–21

Weaver, T. A., Zimmerman, G. B., & Woosley, S. E. 1978, Astrophysical Journal, 225, 1021

Webbink, R. F. 1984, Astrophysical Journal, 277, 355

— 2008, Short-Period Binary Stars: Observations, 352, 233

Weidemann, V. 2000, Astronomy and Astrophysics, 363, 647

Werner, K., Deetjen, J. L., Dreizler, S., Nagel, T., Rauch, T., & Schuh, S. L. 2003, Stellar Atmosphere Modeling, 288, 31

Woods, T. E. & Ivanova, N. 2011, The Astrophysical Journal Letters, 739, L48

Woodward, P. R., Porter, D. H., Herwig, F., Pignatari, M., Jayaraj, J., & Lin, P.-H. 2009, arXiv.org, astro-ph.SR, 1414

Woosley, S. E., Heger, A., & Weaver, T. A. 2002, Reviews of Modern Physics, 74, 1015

Yorke, H. W., Bodenheimer, P., & Taam, R. E. 1995, Astrophysical Journal, 451, 308

Yungelson, L. R., Tutukov, A. V., & Livio, M. 1993, Astrophysical Journal, 418, 794

Zahn, J.-P. 1989, Astronomy and Astrophysics (ISSN 0004-6361), 220, 112

Zahn, J.-P. & Bouchet, L. 1989, Astronomy and Astrophysics (ISSN 0004-6361), 223, 112

Zahnle, K. J. 1992, Journal of Geophysical Research (ISSN 0148-0227), 97, 10243

Zanstra, H. 1929, Publications of the Dominion Astrophysical Observatory Victoria, 4, 209

Zorotovic, M., Schreiber, M. R., Gänsicke, B. T., & Gómez-Morán, A. N. 2010, arXiv.org, astro-ph.SR, 86

Zuckerman, B., Becklin, E. E., & McLean, I. S. 1991, ASP Conference Series, 14, 161

Appendix A

The binary fraction of planetary nebula central stars I. A high-precision, *I*-band excess search

From De Marco, O., Passy, J.-C., Frew, D. J., Moe, M., & Jacoby G. H. 2013, MNRAS, 428, 2118

A.1 Introduction

A single star may be incapable of generating non-spherical planetary nebulae (PN). Models that can reproduce elliptical and bipolar PN shapes (e.g. García-Segura et al., 1999, 2005) have traditionally assumed the constancy of magnetic fields over the high mass-loss period (known as the superwind phase) that characterizes the end of the asymptotic giant branch (AGB) evolution. However, even a weak magnetic field during the end of the AGB can act to slow down the differential rotation that generates the field in the first place: today we have no viable theory to sustain a magnetic field during the superwind phase in a single AGB star (Soker, 2006; Nordhaus et al., 2006). An alternative theory, that a binary companion might be responsible for the shaping action, has become central in the study of PN and formed the core of the *binary hypothesis* which postulates that PN form more readily around binaries, where by binary we mean a star accompanied by another star, a brown dwarf, or even a

planetary system. For a review, see De Marco (2009).

There are several ways in which binary companions as light as planets can alter the shape of the AGB superwind and the subsequent PN (Mastrodemos & Morris, 1999; Edgar et al., 2008; Passy et al., 2012). However, this does not prove that all non-spherical PN (about 80% of the entire sample; Parker et al. 2006) derive from a binary interaction. In order to determine the impact of binarity on PN formation a first, fundamental step is to determine the binary fraction of central stars of PN.

Binary detection methods for central stars of PN have centered on the light variability technique, where a central, unresolved binary, undergoes eclipses, suffers ellipsoidal distortion or where the cool companion is irradiated by the luminous hot one. This technique is responsible for the detection of almost all the known central star binaries (Miszalski et al., 2009). The binary fraction determined in this way is $\sim$15–20%. This technique is biased against binaries with periods smaller than about 2 weeks, against binaries with the orbital plane near the plane of the sky, and against companions with small radii (De Marco et al., 2008).

To determine the binary fraction for binaries with any orbital separation we need a technique that is free of separation biases, such as the detection of red and infrared excess from photometry or spectroscopy. So far only Zuckerman et al. (1991) and Frew & Parker (2007) have carried out such studies. Zuckerman et al. (1991) detected definitive K-band excess in 50% of 30 central stars but concluded that only in three cases this could be ascribed to a companion, while in the others the emission may be due to hot dust. Frew & Parker (2007) analyzed 32 objects with 2-micron All Sky Survey (2MASS) or Deep Near Infrared Survey of the Southern Sky (DENIS) near-IR photometry and deduced that >53% of PN have a cool companion (the completeness limit of that survey and the error limits were not quantified).

Key to the success of such survey are (i) extremely accurate photometry with well quantified uncertainties in at least two blue colors (e.g., B and V, to determine the reddening) and in at least one red color (I or J, to detect the excess flux due to the companion); (ii) a sufficiently large sample ($\gtrsim$150 objects) covering the majority of a volume-limited sample and (iii) the use of a red band that is not contaminated by dust, practically leaving only the I or J bands as feasible. Here we present the first study in a series that uses I band photometry (and J where possible) to detect a red or near-IR excess. The I band is not as sensitive as the J band, but, if photometric errors can be limited to 1%, this method can be a very practical way to observe a substantial number of objects in a relatively short time.

The binary fraction of the progenitor population has recently been measured to be (50±4)% (Raghavan et al., 2010). This includes *all* companions down to the planetary regime out to all separations with primary stars in the spectral range F6V to G2V. We therefore expect a PN binary fraction of approximately 10 points lower. Clearly, if we are to explain 80% of all PN (those with non-spherical shapes) with a binary interaction, either the binary fraction of PN is higher than for the main sequence, and close to 80%, or, if it is not, a fraction of PN should be explained by planetary interactions. While testing for the presence of planets around central stars is not generally within reach yet, we start here with determining the *stellar-companion*, PN binary fraction.

The goal of this survey is to determine accurate B, V and I band photometry of the ∼200 central stars closest to the Sun. This sample has been recently compiled using the best available data from the literature supplemented by an improved Hα surface brightness–radius relation which allows one to obtain distances accurate to ∼20% in most cases (Frew, 2008). Obtaining the J band magnitude of the central stars is also desirable but much less practical for such a large sample.

In § A.2 we describe our sample. In § A.3 we present our observations and data reduction, while in § A.4 we present our measurements of the photometric magnitudes and their uncertainties. In § A.5 we give the details of the technique to detect I and J band excess flux and the predicted accuracies and biases that derive from it. In § A.6 we report our results, including a discussion of objects that were detected to be variable in the course of our observations. A comparison between our results and the prediction for the single and binary scenarios follows in § A.7. We summarize and conclude in § A.8.

A.2 The sample

Ideally, we would like to derive the binary fraction and period distribution in separate samples, such as the non-spherical and the spherical subsets of PN. The need for a larger sample as well as the lack of a clear definition of morphological classes lead us to simplify this test: we simply derive the binary fraction (by which, hereafter, we mean the *stellar* binary fraction) among a volume limited sample of central stars of PN and compare it with that of the presumed main sequence progenitor population. The expectation from the current scenario, whereby PN derive from stars in the mass range ∼1-8 $M_{\odot}$, whether they are single or in binaries, is that the PN binary fraction

should be slightly smaller than that of intermediate mass main sequence stars, if companions down to the brown dwarf limit and at all separations can be sampled. A small difference between the binary population on the main sequence and during the PN phase is justified by the expectation that very close binary main sequence stars suffer a strong interaction on the red giant branch (RGB) and do not ascend the AGB; also, it is expected that some binary interactions on the RGB or AGB could result in mergers.

The sample presented here consists of 27 central stars of PN which were selected solely based on their low PN surface brightness (radius of the PN is larger than $\sim$25 arcsec in most cases) as well as on the faint V magnitudes of their central stars. The first criterion allows us to reduce the measurement error; the second insures that fainter companions can be detected because, although faint V magnitudes can imply intrinsically bright, distant objects, the large PN radius tends to select for closer objects whose faint V brightness indicates that the stars are intrinsically faint. The sample comprises 27 objects studied in the I band of which 11 have additional J-band photometry.

A.3 Observations and Data Reduction

The observations were acquired during 8 nights between the 30th of October and the 6th of November, 2007 at the 2.1-m telescope at Kitt Peak National Observatory. However, the data from nights 2 and 8 were not photometric. The weather conditions during the other nights were mostly photometric.

The detector was a 2048×2048 pixel Tetronix CCD, which was binned 2×2 (to achieve a faster read-out and reduce the read noise level). The pixel size was 24 μm, and the field of view was $10.2' \times 10.2'$ (the platescale is 0.60 arcsec per (binned) pixel). The electronic gain of the camera was 3.1 e^-/ADU (Analog-to-Digital Unit), which minimally samples the system noise of 6 e^-, while providing a maximum signal of about 200,000 e^- before saturating.

The observations were made through the B,V,R and I Johnson-Cousins astronomical bandpasses. Ten bias frames per nights were obtained as well as ten dome flats per filter. Their medians were used to de-bias and flat field the exposures. Standard stars were selected from the list of Landolt (1992), so as to encompass the colours and brightnesses of our targets as well as to sample a range of air masses. They are listed in Table 4 alongside with the nights when they were used. We applied a shutter

correction of -0.001 sec to the header exposure times, very low for even our shortest exposure times.

A.4 The determination of the photometric magnitudes and uncertainties

Instrumental magnitudes were measured with the APPHOT package in IRAF[1] (Tody, 1986, 1993). The radius of the aperture that samples the flux was estimated to be 8 binned pixels by measuring bright stars through increasingly larger apertures. The background was sampled between 8 and 13 binned pixels from the position of the star. Targets were measured using apertures of 3 binned pixels and then aperture-corrected. However, it was noticed that the final result was not very different from that obtained by measuring targets through an 8-binned pixel aperture directly with no aperture correction.

The instrumental magnitudes b, v, r and i, were then converted to observed magnitudes, B, V, R and I on the standard system, by making the following first order transformation:

$$\begin{aligned} B &= O_B + b + C_B(B-V) - K_B * Z_B \\ V &= O_V + v + C_V(B-V) - K_V * Z_V \\ R &= O_R + r + C_R(V-R) - K_R * Z_R \\ I &= O_I + i + C_I(R-I) - K_I * Z_I \end{aligned} \tag{A.1}$$

where O_B, O_V, O_R, O_I are the instrumental offsets, C_B, C_V, C_R, C_i are the colour terms, K_B, K_V, K_R, K_I are the extinction coefficients, and Z is the airmass (where the Z values are all the same and the subscripts are there for clarity). There can be a second order correction due to the atmosphere, and therefore zenith distance because the atmosphere acts as a broadband colour filter. This second order correction was negligible. Although the airmass of our observations varied, it was never higher than 2.1 and generally very close to unity.

Our standard stars were used to calculate the needed coefficients. Each standard star was observed through each filter at several values of the airmass, Z, and its instrumental magnitudes b, v, r and i were determined. Then, for each filter, we solved

[1] IRAF is distributed by the National Optical Astronomy Observatories, which are operated by the Association of Universities for Research in Astronomy, Inc., under cooperative agreement with the National Science Foundation.

the system of equations in (A.1) using a least squares method, where the unknowns are K, C and O. We finally plot $Y_1 = V - O_V - v - C_V(B - V)$ as a function of Z, and $Y_2 = I - O_I - i + K_I * Z$ as a function of $R - I$. In Figure A.1, we show the importance of obtaining observations of several standards at different airmass values. When there are few stars (less than $\sim$25 stars), the fits tend to be noticeably poorer. The values obtained for each coefficient as well as the total number of stars in each filter are summarised in Table 5.

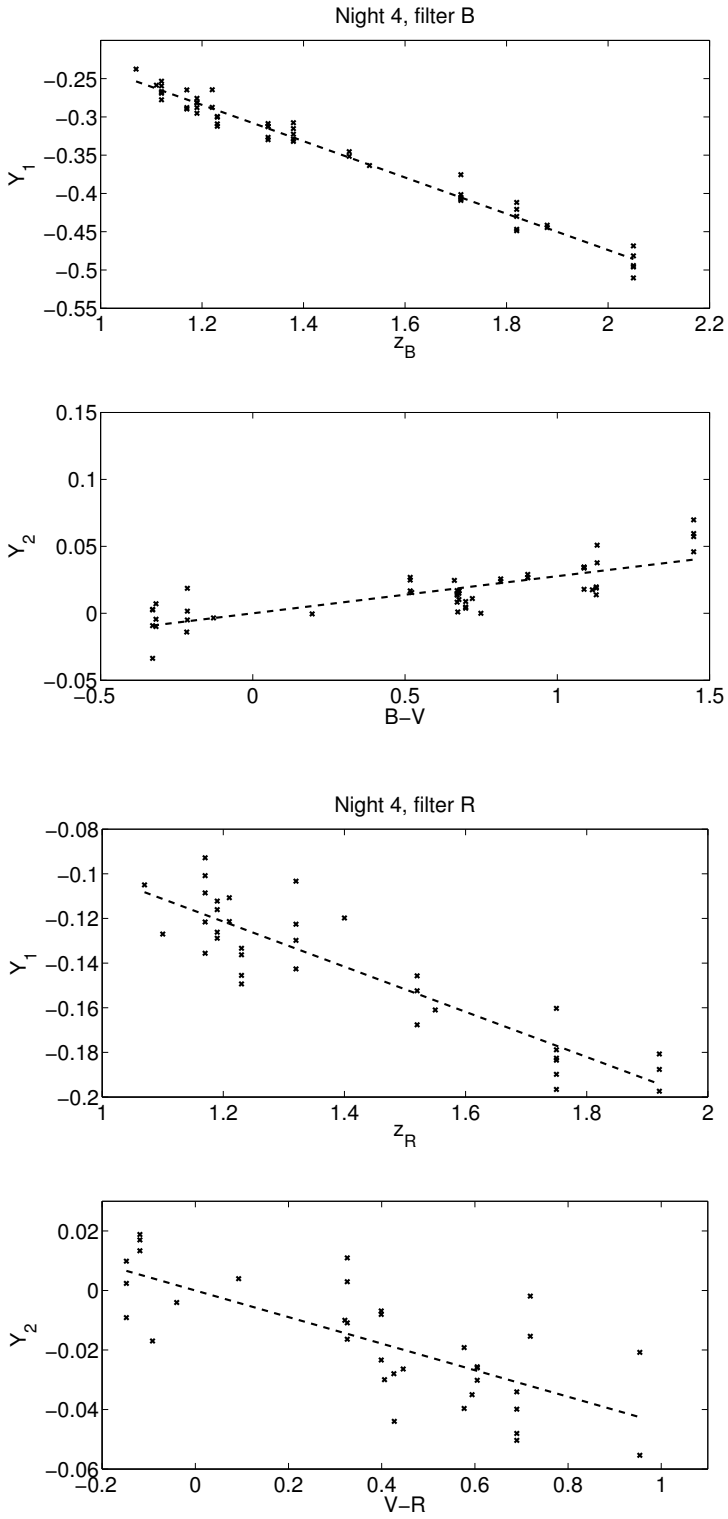

Figure A.1 Example of fits to standard stars to estimate conversion coefficients. Note the small range on the y-axis of the R band fit.

Several precautions are taken to minimise the uncertainty. First, the targets' signal-to-noise ratio is $\gtrsim$100. Second, multiple observations of each target are taken on different nights. This guards against possible mistakes in estimating the photometric conditions. Finally, most of our targets have faint, large PN (>25 arcsec), which reduces the error due to background subtraction.

The uncertainties on the instrumental magnitude measurements (σ_b, σ_v, σ_r, and σ_i) provided by IRAF include the photon statistics and the uncertainty on the sky measurement. While the shutter correction was included, we did not include a shutter correction error because it was deemed negligible. By adding the uncertainties in quadrature we have, e.g., in the case of the error on the B-band magnitude:

$$\sigma_B^2 = \sigma_{O_B}^2 + \sigma_b^2 + (B-V)^2\sigma_{C_B}^2 + C_B^2\sigma_{B-V}^2 + Z_B^2\sigma_{K_B}^2 + \sigma_{apco}^2$$

where $\sigma_{apco} \approx 0.004$ mag is the error on the aperture correction, calculated as the standard deviation of the aperture correction for the 5 reference stars used to calculate the aperture correction itself. By adopting the approximation $\sigma_{B-V}^2 = \sigma_B^2 + \sigma_V^2 \approx 2\sigma_V^2$, we obtain the following equations for the errors on the B and V bands:

$$\sigma_B^2 = \left(\sigma_{O_B}^2 + \sigma_b^2 + (B-V)^2\sigma_{C_B}^2 + Z_B^2\sigma_{K_B}^2 + \sigma_{apco}^2\right)/(1-2C_B^2) \qquad \text{(A.2)}$$

$$\sigma_V^2 = \left(\sigma_{O_V}^2 + \sigma_v^2 + (B-V)^2\sigma_{C_V}^2 + Z_V^2\sigma_{K_V}^2 + \sigma_{apco}^2\right)/(1-2C_V^2) \qquad \text{(A.3)}$$

which we solve simultaneously to derive the values of σ_B and σ_V. Similarly, we derive the uncertainties on R and I.

When more than one independent observation was taken for a given target, the weighted mean was calculated:

$$\mu = \Sigma_{i=1}^{N} p_i x_i, \qquad \text{(A.4)}$$

where N is the number of observations, x_i is a given measurement and p_i is its associated probability ($p_i = (1/\sigma_i)/\Sigma_j(1/\sigma_j)$, where σ_i is the error on that measurement and σ_j is the error on the j$^{\text{th}}$ measurement). The error on the mean was calculated in the following way:

$$\sigma = \sqrt{\Sigma_{i=1}^{N} p_i (x_i - \mu)^2}. \qquad \text{(A.5)}$$

The photometric magnitudes and their errors thus obtained are reported in Table A.1, along with the number of measurements that were used in obtaining these values.

Name	B	V	R	I
A 7	15.190 ± 0.003 (3)	15.495 ± 0.004 (3)	15.632 ± 0.013 (3)	15.818 ± 0.011 (2)
A 16	18.517 ± 0.015 (3)	18.714 ± 0.018 (3)	18.733 ± 0.020 (3)	18.686 ± 0.016 (3)
A 20	16.216 ± 0.002 (3)	16.466 ± 0.006 (3)	16.559 ± 0.007 (3)	16.701 ± 0.016 (3)
A 28	16.280 ± 0.008 (3)	16.557 ± 0.009 (3)	16.691 ± 0.008 (3)	16.877 ± 0.014 (3)
A 31	15.201 ± 0.007 (2)	15.544 ± 0.001 (2)	15.693 ± 0.009 (2)	15.831 ± 0.016 (2)
A 57	17.903 ± 0.001 (2)	17.734 ± 0.011 (2)	17.451 ± 0.010 (2)	17.210 ± 0.002 (2)
A 71	19.384 ± 0.015 (3)	19.335 ± 0.006 (3)	19.253 ± 0.010 (3)	19.185 ± 0.056 (3)
A 72	15.761 ± 0.021 (3)	16.070 ± 0.028 (3)	16.237 ± 0.091 (3)	16.381 ± 0.043 (3)
A 79	17.825 ± 0.013 (3)	16.965 ± 0.005 (3)	16.397 ± 0.026 (3)	15.743 ± 0.085 (3)
A 84	18.366 ± 0.012 (3)	18.584 ± 0.013 (3)	18.613 ± 0.020 (3)	18.671 ± 0.020 (3)
DeHt 5	15.268 ± 0.018 (1)	15.495 ± 0.019 (1)	15.568 ± 0.018 (1)	15.631 ± 0.018 (1)
EGB 1	16.308 ± 0.007 (2)	16.439 ± 0.005 (2)	16.452 ± 0.007 (2)	16.482 ± 0.022 (2)
EGB 6	15.692 ± 0.002 (2)	15.999 ± 0.002 (2)	16.137 ± 0.008 (2)	16.300 ± 0.009 (2)
HaWe 5	17.321 ± 0.014 (2)	17.439 ± 0.005 (2)	17.471 ± 0.004 (2)	17.528 ± 0.011 (2)
HDW 3	17.084 ± 0.003 (3)	17.187 ± 0.004 (3)	17.218 ± 0.039 (3)	17.234 ± 0.019 (3)
HDW 4	16.310 ± 0.011 (1)	16.540 ± 0.013 (1)	16.638 ± 0.017 (1)	16.739 ± 0.017 (1)
IsWe 1	16.374 ± 0.017 (3)	16.523 ± 0.007 (3)	16.576 ± 0.016 (3)	16.644 ± 0.013 (3)
IsWe 2	18.142 ± 0.026 (5)	18.160 ± 0.033 (5)	18.118 ± 0.026 (5)	18.098 ± 0.022 (5)
JnEr 1	16.775 ± 0.005 (2)	17.128 ± 0.013 (2)	17.288 ± 0.001 (2)	17.501 ± 0.023 (2)
K 1-13	18.051 ± 0.013 (3)	18.425 ± 0.006 (3)	18.592 ± 0.019 (3)	18.846 ± 0.044 (3)
K 2-2	13.977 ± 0.007 (3)	14.263 ± 0.010 (3)	14.390 ± 0.008 (3)	14.553 ± 0.013 (3)
NGC 3587	15.414 ± 0.001 (3)	15.777 ± 0.009 (3)	15.960 ± 0.006 (3)	16.194 ± 0.029 (3)
NGC 6720	15.405 ± 0.016 (2)	15.769 ± 0.023 (2)	15.901 ± 0.003 (2)	16.062 ± 0.012 (2)
NGC 6853	13.749 ± 0.026 (3)	14.089 ± 0.010 (3)	14.247 ± 0.006 (3)	14.405 ± 0.010 (3)
PuWe 1	15.291 ± 0.008 (2)	15.545 ± 0.006 (2)	15.662 ± 0.011 (2)	15.792 ± 0.008 (2)
Sh 2-78	17.633 ± 0.012 (2)	17.660 ± 0.005 (2)	17.608 ± 0.025 (2)	17.543 ± 0.027 (2)
Sh 2-176	18.489 ± 0.086 (3)	18.559 ± 0.019 (3)	18.570 ± 0.016 (3)	18.545 ± 0.029 (3)
Sh 2-176[1]	18.442 ± 0.018 (2)	18.551 ± 0.016 (2)	18.562 ± 0.009 (2)	18.531 ± 0.010 (2)
Sh 2-188	17.424 ± 0.013 (3)	17.447 ± 0.004 (3)	17.398 ± 0.009 (3)	17.376 ± 0.011 (3)
Ton 320	15.379 ± 0.007 (2)	15.725 ± 0.006 (2)	15.890 ± 0.010 (2)	16.105 ± 0.018 (2)
WeDe 1	16.958 ± 0.007 (3)	17.226 ± 0.004 (3)	17.338 ± 0.010 (3)	17.489 ± 0.016 (3)

[1]These measurements are obtained by excluding the observations taken in night 3.

Table A.1 The photometric magnitudes of our targets rounded to 3 decimal places. Formal errors lower than 1% were set at 1%. In brackets are the number of independent exposures (taken on different nights) used to calculate the final photometric magnitude and the uncertainty.

A.5 Binary detection technique by red and IR excess flux

The ideal spectral location for this technique is the J band. This is the best compromise between companion brightness and the elimination of contamination from hot dust. However, procuring J band data has proven more challenging than optical data because IR instruments are often associated with larger telescopes which tend to allocate shorter observing runs and because of the need for photometric conditions. In addition, for most of our sample we also need to obtain B- and V-band photometry because the values in the literature tend not to be sufficiently accurate, thus generating the need for parallel proposals to more than one telescope. As a result, we have found it more practical to use the I band to detect companion-generated flux excess as our work horse, accompanied by the J band when available (we used UKIRT, Infrared Deep Sky Survey (UKIDSS; Lawrence et al. 2007) data, or the most reliable 2MASS values – see Table 2). Below we discuss the technique and its biases.

Most of our targets have reasonably well determined effective temperatures either via stellar spectrum modelling or using the Zanstra technique (Zanstra, 1929). Those that were modelled also have known gravities. For those stars with only a Zanstra temperature estimate, we determine the gravity using the most common central star mass, namely 0.6 $M_{\odot}$, selecting the corresponding stellar evolutionary track of Vassiliadis & Wood (1994) and choosing the larger of the possible gravity values, appropriate for our sample of evolved PN. Once the temperatures are obtained, single star colours ($B-V$, $V-I$ and $V-J$) can be predicted. The predicted $B-V$ colour is used together with the measured one to determine the reddening, $E(B-V)$. If the reddening thus determined has a negative value, possible because of random errors, we set the value to zero. As we will see in § A.6, all negative reddening values we derive in this way are very small and within the uncertainty, reassuring us that the uncertainties have been assessed reasonably. With the reddenings thus derived we obtain values of $A_{\lambda}/E(B-V)$ using the reddening law of Cardelli et al. (1989), where λ represent the bandpass central wavelengths. The central wavelengths for the filter bandpasses are obtained by convolving the bandpasses with a synthetic stellar atmosphere with $T_{\rm eff}$=100 kK, $\log g = 7$ and solar abundance. This decreases the central wavelengths by approximately 10 Å, compared to the values obtained for un-convolved bandpasses, but yields only a very small change in the final results.

The $V-I$, or $V-J$ observed dereddened colours are then compared with the

predicted ones so as to determine if a flux excess exists. An I (J) band excess is detected every time the observed (dereddened) and predicted colours are different by more than the combined uncertainties. While a high confidence result can already lend substantial weight towards a binary interpretation, a lower sigma result needs to be confirmed by additional photometry or spectroscopy.

To predict the $B-V$, $V-I$, $V-J$, $R-I$ and $J-H$ colours of single post-AGB stars, we use theoretical stellar atmosphere models calculated with the simulation code TMAW, the web interface to TMAP (Werner et al., 2003; Rauch & Deetjen, 2003), or the German Astrophysical Virtual Observatory grid calculations TheoSSA[2].

The uncertainties on the measurements (see § A.4) are combined with the uncertainty on the predicted colours to derive an uncertainty on the colour excess. The uncertainty on the theoretical colours reflect solely the uncertainty on the temperature. We assume that additional sources of uncertainty are far smaller and do not play a role. The uncertainty in colours derived from the uncertainty on the temperature is quite small, in particular for stars hotter than ∼50 kK, which is the case for most of our sample. Systematic uncertainties on the theoretical, single star colours are estimated to be below 1% (e.g., Rauch et al., 2007). In fact, the observational uncertainties dominate the error budget.

To further exemplify the technique, we present in Fig. A.2 the predicted I- and J-band excess as a function of primary star absolute V magnitude (M_V) and main sequence companion mass/spectral type. This plot gives a good idea of the ability of the I- and J-band methods to detect companions, although it must be pointed out that this figure is only valid for those stars that have already entered the cooling track. To generate Fig. A.2, we created a grid of M_V absolute stellar brightness for the hot central stars using the effective temperatures to determine both bolometric luminosities and bolometric corrections. The former was determined using the average of the cooling track temperature-luminosity relations of Schonberner (1993), Vassiliadis & Wood (1994) and Bloecker (1995b) (for a 1.5 $M_\odot$ main sequence star, but the scatter is very small). The latter was determined using the average of the relation determined by Vacca et al. (1996) and a blackbody curve. To each hot central star we added the flux of a range of main sequence companions. We thus created a grid of binaries. Next we calculated the total (binary) $B-V$ colour for each primary-secondary combination and compared it to that of the primary alone. A difference is only present when the companion contributes flux in the V or even B and V bands,

[2]dc.zah.uni-heidelberg.de/theossa/

which is the case for companions brighter than K0-5V. Any difference is interpreted as reddening and used to deredden all bands. We then subtract the primary I band flux from the binary (dereddened) one and any difference is labelled as excess (this is the value reported on each contour line).

As can be seen in Fig. A.2, a measured I or J band excess corresponds to two distinct companion spectral types. This is due to the contribution of the brightest companions to the V and even B bands, resulting in too high a predicted reddening, too blue a de-reddened spectral energy distribution (SED) and therefore smaller I or J-band excess. This effect is less pronounced for the J band, because reddening effects are smaller in that band. The $R-I$ colour provides an approximate way to distinguish between the two companion spectral types allowed by a given I band excess, while the $J-H$ colour is not as discriminating (see dashed contours in Fig. A.2).

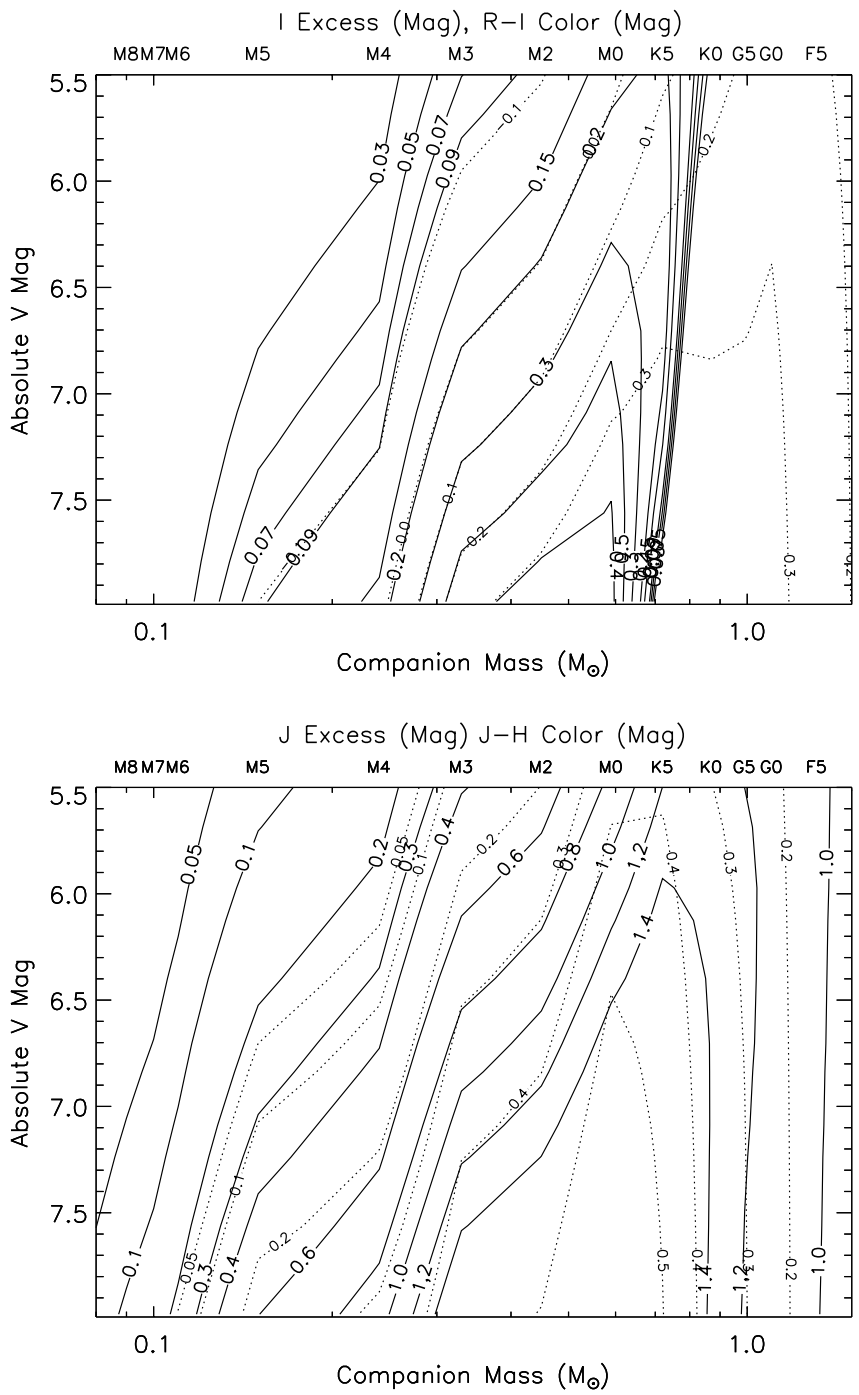

Figure A.2 The I and J band excess (solid contours) and $I-R$ and $J-H$ colours (dotted contours) that are produced by main sequence companions (M9V to F5V) as a function of companion mass and primary's absolute V magnitude. These plots are obtained by assuming that the central stars are on the cooling-curve part of the HR diagram and cannot be used to determine the spectral type of the companion of objects which have not yet turned the "knee" on the post-AGB evolutionary track. The I and J band excess correspond to the $\Delta(V-I)$ and $\Delta(V-J)$ listed in Tables A.2 and A.3

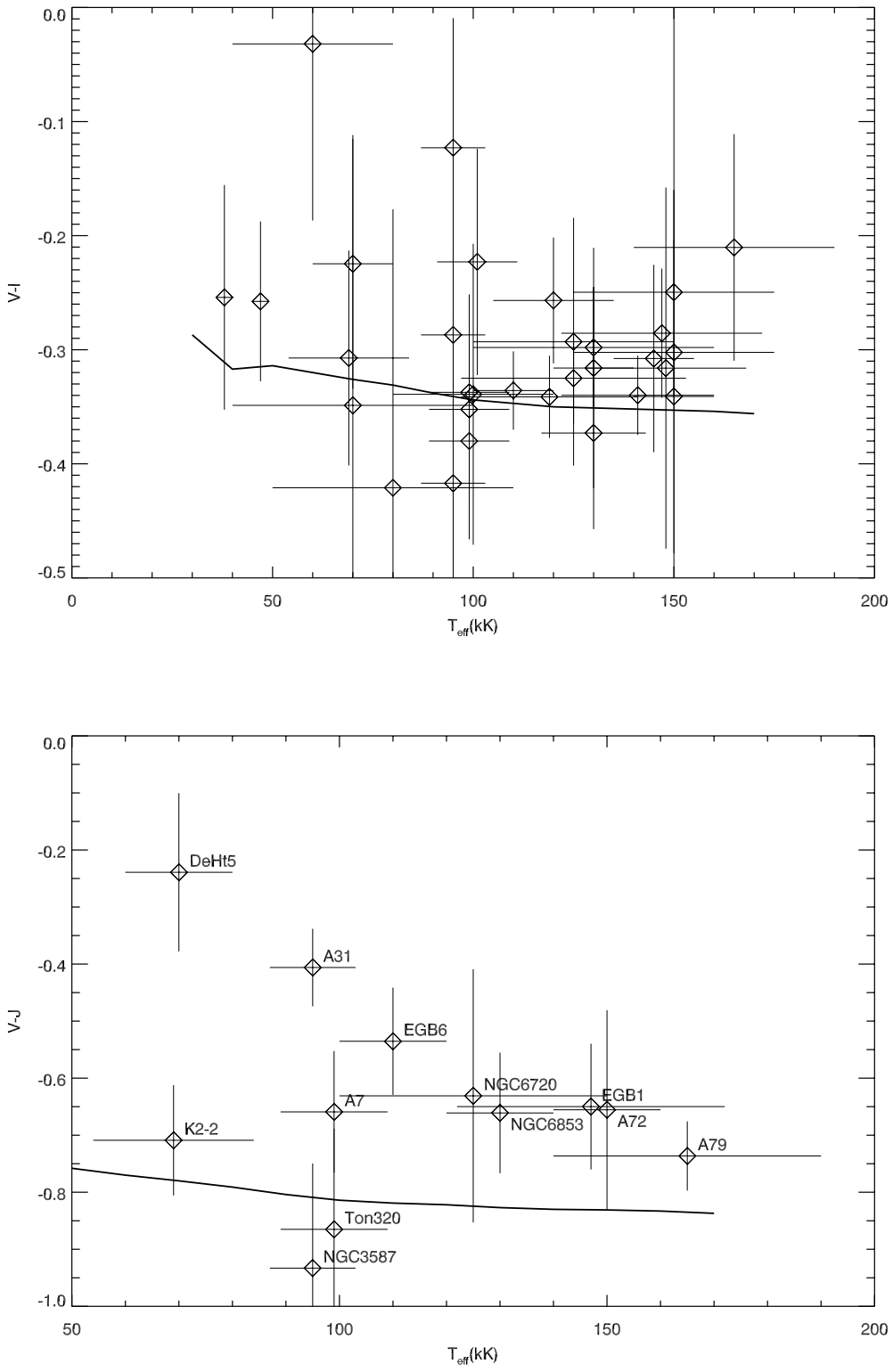

Figure A.3 Top: the observed (dereddened) $V-I$ colours of our targets (symbols; see Table A.2) compared with the predicted $V-I$ colours of single stars as a function of effective temperature (for a $\log g = 7.0$ – solid line). Bottom: same but for the J-band.

Name	$E(B-V)$	$(V-I)_0$	$(R-I)_0$	$\Delta(V-I)$	M_{I2}	Comp. spec. type
A 7	0.02 ± 0.02	-0.35 ± 0.08	-0.19 ± 0.06	-0.01 ± 0.08	> 9.60	Later than M4V
A 16	0.13 ± 0.03	-0.12 ± 0.11	0.02 ± 0.09	0.22 ± 0.11	8.30 [9.24 – 7.73]	M3V [M3V – M1V]
A 20	0.07 ± 0.02	-0.32 ± 0.08	-0.16 ± 0.06	0.02 ± 0.08	> 7.29	Later than M0V
A 28	0.02 ± 0.07	-0.35 ± 0.24	-0.19 ± 0.18	-0.02 ± 0.24	> 8.18	Later than M2V
A 31	0.00 ± 0.02	-0.29 ± 0.08	-0.14 ± 0.06	0.06 ± 0.08	> 9.14	Later than M3V
A 57	0.46 ± 0.04	-0.03 ± 0.15	0.15 ± 0.12	0.29 ± 0.15	5.51 [6.56 – 4.79]	K3V [K7V – G8V]
A 71	0.38 ± 0.02	-0.31 ± 0.08	-0.01 ± 0.07	0.05 ± 0.08	> 10.56	Later than M5V
A 72	0.04 ± 0.04	-0.35 ± 0.14	-0.15 ± 0.14	0.01 ± 0.14	> 6.84	Later than K8V
A 79	1.20 ± 0.01	-0.21 ± 0.10	0.42 ± 0.10	0.15 ± 0.10	3.12 [4.44 – 2.66]	F6V [G6V – F3V]
A 84	0.11 ± 0.03	-0.22 ± 0.10	-0.08 ± 0.08	0.12 ± 0.10	10.00 [11.91 – 9.28]	M4V [M6V – M3V]
DeHt 5	0.07 ± 0.03	-0.22 ± 0.11	-0.08 ± 0.09	0.10 ± 0.11	> 9.28	Later than M3V
EGB 1	0.20 ± 0.01	-0.29 ± 0.06	-0.07 ± 0.05	0.07 ± 0.06	10.05 [11.96 – 8.91]	M4V [M6V – M3V]
EGB 6	0.03 ± 0.01	-0.34 ± 0.03	-0.17 ± 0.03	0.01 ± 0.03	> 9.79	Later than M4V
HaWe 5	0.14 ± 0.03	-0.25 ± 0.10	-0.08 ± 0.08	0.06 ± 0.10	> 11.21	Later than M5V
HDW 3	0.23 ± 0.01	-0.32 ± 0.04	-0.06 ± 0.05	0.03 ± 0.04	> 10.35	Later than M4V
HDW 4	0.04 ± 0.02	-0.24 ± 0.07	-0.11 ± 0.06	0.07 ± 0.07	13.05 [16.87 – 12.30]	M7V [M8V – M6V]
IsWe 1	0.19 ± 0.03	-0.35 ± 0.09	-0.11 ± 0.08	0.01 ± 0.10	> 9.77	Later than M4V
IsWe 2	0.32 ± 0.04	-0.32 ± 0.16	-0.04 ± 0.12	0.04 ± 0.16	> 9.38	Later than M4V
JnEr 1	0.00 ± 0.01	-0.37 ± 0.06	-0.21 ± 0.05	-0.01 ± 0.06	> 10.86	Later than M5V
K 1-13	0.00 ± 0.07	-0.42 ± 0.24	-0.25 ± 0.19	-0.09 ± 0.24	> 8.85	Later than M3V
K 2-2	0.02 ± 0.02	-0.31 ± 0.09	-0.17 ± 0.07	0.01 ± 0.09	> 7.40	Later than M1V
NGC 3587	0.00 ± 0.04	-0.42 ± 0.15	-0.23 ± 0.12	-0.07 ± 0.15	> 8.96	Later than M3V
NGC 6720	0.00 ± 0.03	-0.29 ± 0.11	-0.16 ± 0.08	0.06 ± 0.11	> 7.99	Later than M2V
NGC 6853	0.00 ± 0.03	-0.32 ± 0.11	-0.16 ± 0.08	0.04 ± 0.11	> 8.42	Later than M3V
PuWe 1	0.08 ± 0.02	-0.34 ± 0.09	-0.14 ± 0.07	0.01 ± 0.09	> 10.46	Later than M4V
Sh 2-78	0.31 ± 0.01	-0.26 ± 0.06	0.00 ± 0.06	0.10 ± 0.06	10.22 [11.32 – 9.72]	M4V [M5V – M4V]
Sh 2-176	0.26 ± 0.09	-0.30 ± 0.32	-0.03 ± 0.25	0.05 ± 0.32	> 8.91	Later than M3
Sh 2-176[1]	0.23 ± 0.02	-0.25 ± 0.09	-0.01 ± 0.07	0.11 ± 0.09	10.68 [12.87 – 9.95]	M5V [M6V – M4V]
Sh 2-188	0.31 ± 0.01	-0.30 ± 0.05	-0.04 ± 0.04	0.05 ± 0.05	10.46 [14.33 – 9.71]	M4V [M8V – M4V]
Ton 320	0.00 ± 0.03	-0.38 ± 0.10	-0.21 ± 0.08	-0.04 ± 0.10	> 9.36	Later than M4V
WeDe 1	0.06 ± 0.01	-0.34 ± 0.03	-0.16 ± 0.03	0.01 ± 0.03	> 11.36	Later than M5V

[1]These measurements are obtained by excluding the observations taken in night 3

Table A.2 I-band excesses ($\Delta\ (V-I)$), companion absolute I-band magnitudes (M_{I2}) and spectral types (or limits) of our targets

A.6 Results

Those objects for which $\Delta(V-I) > \sigma_{\Delta(V-I)}$ (or, equivalently, $\Delta(V-J) > \sigma_{\Delta(V-J)}$) are considered as cases where a companion is detected. We note that this difference is the same as what we call the I (J) band excess in Fig. A.2, because the theoretical colours are normalised to the observed (dereddened) V magnitudes. Reddenings, intrinsic $V-I$ ($V-J$) and $R-I$ ($J-H$) colours, I (J) band excesses ($\Delta(V-I)$ or $\Delta(V-J)$), companions' absolute I (J) band magnitudes and companions' spectral types are listed in Tables A.2 (A.3). The I (J) band excesses are plotted as a function of stellar temperature in Fig. A.3 (A.3).

Most reddenings derived by comparing observed and (single star) predicted $B-V$

Name	$E(B-V)$	$(V-J)_0$	$(J-H)_0$	$\Delta(V-J)$	M_{J2}	Comp. spec. type
A 7	0.02 ± 0.02	-0.66 ± 0.11	-0.07 ± 0.20	0.15 ± 0.11	9.65 [11.07 – 8.95]	M5V [M8V – M5V]
A 31	0.00 ± 0.02	-0.41 ± 0.07	0.15 ± 0.03	0.40 ± 0.07	8.26 [8.57 – 7.98]	M4V [M4V – M4V]
A 72	0.04 ± 0.04	-0.68 ± 0.17	–	0.16 ± 0.17	> 6.57	Later than M1
A 79	1.20 ± 0.01	-0.74 ± 0.06	0.02 ± 0.07	0.10 ± 0.06	4.05 [5.17 – 3.45]	G7V [K5V – G1V]
DeHt 5	0.07 ± 0.03	-0.24 ± 0.14	–	0.54 ± 0.14	8.80 [9.30 – 8.37]	M5V [M5V – M4V]
EGB 1	0.20 ± 0.01	-0.65 ± 0.11	–	0.18 ± 0.11	9.43 [10.52 – 8.80]	M5V [M6V – M5V]
EGB 6	0.03 ± 0.01	-0.54 ± 0.09	0.38 ± 0.10	0.28 ± 0.09	9.15 [9.67 – 8.76]	M5V [M5V – M5V]
K 2-2	0.02 ± 0.02	-0.71 ± 0.09	-0.06 ± 0.08	0.01 ± 0.09	> 7.84	Later than M4V
NGC 3587	0.00 ± 0.04	-0.93 ± 0.18	–	-0.12 ± 0.18	> 10.12	Later than M6V
NGC 6720	0.00 ± 0.03	-0.63 ± 0.22	–	0.19 ± 0.22	> 7.97	Later than M4V
NGC 6853	0.00 ± 0.03	-0.66 ± 0.11	0.05 ± 0.06	0.17 ± 0.11	8.81 [10.05 – 8.12]	M5V [M6V – M4V]
Ton 320	0.00 ± 0.03	-0.87 ± 0.18	–	-0.05 ± 0.18	> 9.97	Later than M6V

Table A.3 J-band excesses ($\Delta\ (V-J)$), companion absolute J-band magnitudes (M_{J2}) and companion spectral types (or limits) of our targets. All detections and limits are consistent with the results of the I-band excess (Table A.2)

colours compare well. The five exceptions are A 57 and A 79, whose high derived stellar reddenings are likely due to bright companions affecting the B and V bands, A 71, EGB 1 and Sh 2-78 for which we suspect the nebular reddenings have uncertain values.

We have 9 detections or marginal detections in the I band: A 16 (at the 2-σ level), A 57 (at the 1.9-σ level), A 79 (at the 1.5-σ level), A 84 (at the 1.2-σ level), EGB 1 (at the 1.2-σ level), HDW 4 (at the 1-σ level, but this is a PN mimic), Sh 2-78 (at the 1.7-σ level), Sh 2-176 (at the 1.2-σ level, only for the measurement excluding night 3) and Sh 2-188 (at the 1-σ level). A 79 was already known to have a F0V companion (Rodríguez et al., 2001). The spectral type determined with our method is cooler because the reddening was overestimated due to the strong contribution of the companion in the V band (see § A.5). We have therefore 8 detections out of 27 objects.

In the J band we detected A 7 (at the 1.4-σ level), A 31 (at the 4.7-σ level), A 79 (at the 1.7-σ level), DeHt 5 (at the 3.8-σ level, but this is a PN mimic), EGB 1 (at the 1.6-σ level), EGB 6 (at the 3.1-σ level) and NGC 6853 (at the 1.5-σ level). We have therefore 6 detections out of 11 central stars with data.

The spectral types of the companions implied by the detected excesses as well as limits of the non-detections are also listed in Tables A.2 and A.3. When a companion was not detected, we summed the I (J) band excess with the upper error bars to create an upper limit to the flux excess and determined an upper limit for the companion mass/spectral type in this way. We note that all limits and detections are fully consistent across the two detection techniques.

The I band binary fraction is determined by the ratio of 8 objects over 27 central stars, or 30%. Only companions brighter than the spectral type M3-4V can be detected by our survey, where this limit was estimated by taking the median of the limits in Table A.2. Within the J band group, the detection rate is 6 out of 11, or 54%, in line with the study of Frew & Parker (2007). A look at Table A.3 shows that most detections in the J band were fainter, in line with the expectation that the J band is a more sensitive method. Based on the detection and limits of Table A.3 we guesstimate that this limit is M5-6V. The binary fraction for the entire sample, obtained from either the I or J band excess methods is 44% (12 out of 27 bona fide PN), to a limit intermediate between the two methods.

Before comparing our results with predictions, we would like to remark on the asymmetry of the distribution of $V - I$ colours of our sample about the single star

prediction line (Fig. A.3). Even eliminating from that plot the 9 detections, which are all above the prediction, the non-detections (21 objects) still preferentially lie above the single star prediction line (15 vs. 6 objects). We speculate that this points to the detection of a binary signal which is higher than the fraction we determined from individual objects above. To determine whether this is significant we would need a Monte Carlo simulation. One could counter argue that this asymmetry is caused by an incorrect placement of the prediction line, or, in other words, that the predicted colours are too blue. To shift the prediction line so that the non-detected data points scatter symmetrically about it, would require a systematic shift of the synthetic $V-I$ colours of about $\sim$5% which is excluded by the comparison of synthetic spectra with data carried out over the years (Rauch, private communication; Rauch et al. 2007).

Finally, we have demonstrated that the I band excess method necessitates extraordinary accuracy, such as that achieved for the current dataset, but is not usually encountered in unvetted data from the literature. For example, in Fig. A.4 we compare the I-band excesses obtained by using the B, V and I data compilation of Bilíková et al. (2012) with our dataset. Using all of their data and determining the stellar temperatures in the same way we have done for our sample, we see how the scatter around the single star prediction is dramatic. While their compilation was not aimed at detecting binarity, it can easily be seen that data from the literature is not generally suitable for this type of work.

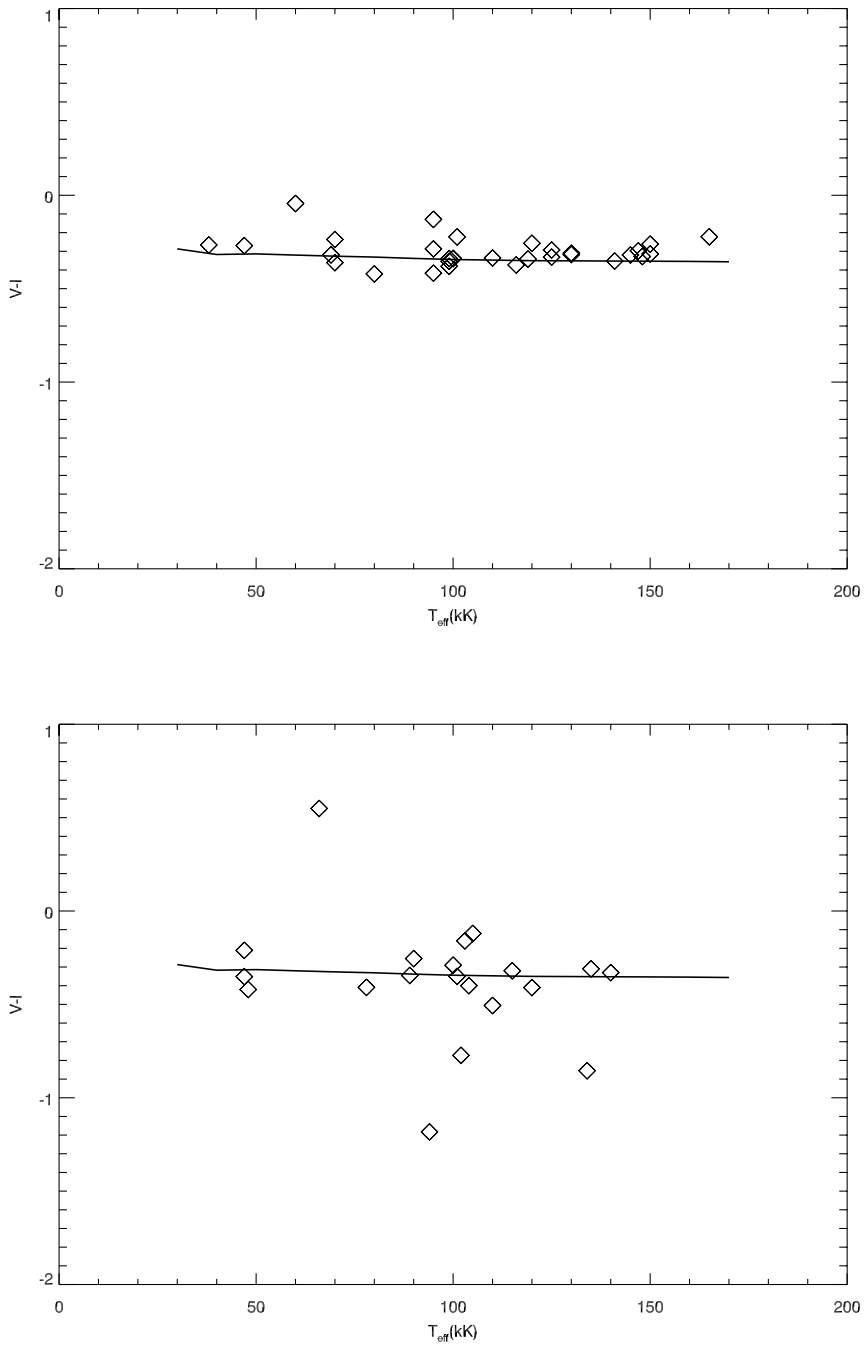

Figure A.4 The same figure as Fig. A.3, except here we compare our results (top) with no error bars, for clarity, with results obtained using the data compiled by (Bilíková et al., 2012, bottom panel), showing how unvetted data has much larger random errors.

A.7 Comparison of the overall PN binary fraction with the overall main sequence binary fraction

We recognise that the binary fraction determined here is preliminary, because of the small sample size. However, here we compare it with the prediction from the current PN evolution scenario, whereby PN derive from *all* ∼1-8- $M_{\odot}$ stars, whether they are single stars or are in binaries. As already explained, it is this prediction that we are testing. We expect that if PN derive from a binary interaction more often than for the current evolutionary scenario, we would find a larger fraction of short- and intermediate-period binaries in the central star population. This leads to the prediction that the *overall* binary fraction, i.e., where we consider binaries at any period, should also be larger in the *binary hypothesis* than in the standard scenario.

The progenitor population of the PN from which we have drawn our targets is the main sequence stars with masses between ∼0.9 and 8 $M_{\odot}$. We can then use the main sequence population binary fraction of Raghavan et al. (2010) to represent the binary fraction of the progenitor population of our PN. We use (50±4)%, which is the percentage of double and multiple star systems with primaries in the spectral type range F6V-G2V (masses in the range 1.27 – 1.03). This is reasonable on the grounds that the median progenitor mass of today's PN is 1.2 $M_{\odot}$ (Moe & De Marco, 2006). This fraction is lower than that determined by Duquennoy & Mayor (1991, 57%) who accounted for a larger incompletion bias, but is likely to be more accurate. This fraction includes *any main sequence companion down to the planetary regime at any separation.*

A.7.1 Accounting for completion effects

Before we can carry out a comparison we need to increase the PN binary fraction to (i) include the companions that have not been detected because they are too faint; (ii) include wide companions, because our observed sample does not contain resolved binaries by design. Finally, we need to (iii) account for the fact that some main sequence close binaries go through a common envelope interaction on the RGB. Those systems will become short period binaries with very low mass envelopes (the primary will become a subdwarf O or B star; Morales-Rueda et al. 2003) and are unlikely to ever ascend the AGB on the grounds of low envelope masses (Dorman et al., 1993); if they do, they will suffer a second common envelope almost immediately which would

result in a sub-luminous object, highly unlikely to ever make a visible PN.

(i) To account for companions with an M3-4V spectral type or fainter (mass $\leq$0.33-0.24 $M_{\odot}$), we use Table 18 of Raghavan et al. (2010) that lists all the companion spectral types of the detected binaries. We determine that the fraction of main sequence binaries with a companion spectral type of M3-4V or later is 41-31% (73-56 of 179 main sequence binaries for which the companion spectral type is known, where we count as undetectable also 4 hot and evolved companions). We therefore increase our I-band derived PN binary fraction (30%) by a factor of 1.69-1.45 to account for the undetected faint companions.

To account instead for companions with brightness equal to, or fainter than M5-6V (the limit we estimated for the J band dataset) we would have to multiply the J-band-derived PN binary fraction (54%) by a factor of 1.28-1.19.

(ii) The ground-based spatial resolution of our observations is probably only slightly smaller than the median seeing of 1.3 arcsec corresponding to a projected separation of $\sim$1040 AU for the median distance of our sample of 0.80 pc. To de-project this separation we would have to divide the projected separation by a factor of 0.8, which accounts for the systems' random phase *and* random orientation. However, if we also account for an eccentricity distribution similar to the main sequence's, this factor approaches unity, because systems spend more time near apastron in eccentric systems. Not knowing the eccentricity distribution of central star binaries but presuming a degree of circularisation to have taken place, we de-project the projected separation using a range of factors (0.8-1.0). The median separation is then converted to a period in the range $\sim$13 000–18 000 years (log(P/days)=7.11-7.25), using Kepler's third law and a total system mass of 0.9 $M_{\odot}$. This period limit is then decreased to $\log(P/\mathrm{days}) = 6.71 - 6.85$, to account for the fact that, due to mass-loss and angular momentum conservation, the orbit of a typical binary will widen by a factor of 2-3 (we used 2.5) and so some of the main sequence binaries of Raghavan et al. (2010) will become resolved central star binaries in our sample because of orbit widening.

A similar argument can be applied to the J-band sample of 11 bona fide PN, which have a median distance of 0.65 kpc, with a resulting median projected separation of 845 AU, resulting in a period corrected for orbit widening of $\log(P/\mathrm{days}) = 6.57-6.71$.

(iii) Finally, the main sequence binary population with orbital period shorter than $\log(P/\mathrm{days}) = 2.43$ never ascend the AGB. This value was calculated using a radius on the RGB of 100 $R_{\odot}$(see, e.g., see figure 5 of De Marco et al. (2011)), and a maximum tidal capture radius of 2 stellar radii (using a total system mass of 1.5 $M_{\odot}$).

The maximum tidal capture radius for the RGB was obtained from Villaver & Livio (2009) and Madappatt et al. (2011). At this point we integrate under the normalised main sequence binary period distribution of Raghavan et al. (2010, their Fig. 13) using log(P/days)=2.43 - 6.78 as limits (or 2.43 – 6.65 for the J-band sample; where we have taken the average of the period separation ranges to determine the upper limits), obtaining a fraction of 0.65 of the total (or 0.64, for the J band sample): these are the systems we detect. This translates into a second factor of 1.54 (or 1.56), which we multiply by the central star binary fraction so as to include binaries at all separations and thus make it comparable to the main sequence one.

(iv) The only bias that is impossible to account for, is that due to central stars whose companions are bright enough to contribute to the V and even B bands. As we have explained in § A.5, these will result in reddenings that are artificially large, because the bright companions tend to make their system's colours redder. Once this over-large reddening is applied to all the bands, the binary SED is rendered bluer than it should be and the I or J band excess is necessarily reduced. The mismatch between reddening curve and SED of the companion can decrease the red/IR flux excess below detectability or reduce it such that it is impossible to match it to a companion spectral type. Interestingly, only 6 objects have stellar-derived reddening values that are larger than the nebular-derived values, the most noticeable being A 79, a known binary and A 57 which has a large I band excess. For the other 4 objects (A 7, A 16, A 28 and Sh 2-188), these discrepancies are however always within the uncertainties. We therefore conclude that either the reddening comparison is not reliable due to high errors in nebular-derived reddenings, or that our sample tends not to include companions much hotter than spectral type K0V. This makes sense in view of the fact that only a minority of companions are expected to be that hot). We leave this bias unquantified in the knowledge that it would be at most a few percent. A spectroscopic follow-up will resolve this issue.

A.7.2 The debiased PN binary fraction and its uncertainties

The de-biased central star binary fraction obtained through the I band photometry of our sample is 67-78%. Using the J band data alone we obtain a fraction of 100-107%. The ranges account for the uncertainty on the factor to account for the unobservable faint companions. The error bars on these estimates are difficult to estimate for the moment and we defer this exercise to the next paper in this series, which will increase

the sample. However, if all limits were accurately accounted for then the I- band and J-band fractions should be the same. We therefore tentatively estimate a 10-30% error bar. We preliminarily conclude that the PN binary fraction is higher than the main sequence binary fraction of (50±4)%.

We can also estimate the PN binary fraction after eliminating from each of the I and J samples the one detection with the smallest statistical relevance. By doing so, we would obtain I and J binary fractions of 58-68% and 84-90% respectively.

A.7.3 Comparison of the short-period PN binary fraction with the main sequence binary fraction

The fraction of PN that surround short-period, post-common envelope binaries is 15-20% (Miszalski et al., 2009). This is a very large fraction when we consider that only a very small minority of main sequence binaries would suffer a common envelope on the AGB.

The fraction of main sequence binaries that go through a common envelope on the AGB, resulting in post-common envelope central stars of PN should be quite small: only those companions that escape capture on the RGB, but then are successfully captured on the AGB will become post-common envelope central stars. These are companions that, while on the main sequence, have periods in the range $\log(P/\mathrm{days}) > 2.7 - 2.8$ and therefore account for only ∼1% of all main sequence binaries. The lower period limit was calculated in § A.7, while the higher period limit was obtained by considering that for a successful AGB capture the orbital separation has to be smaller than approximately twice the maximum AGB radius (Villaver & Livio, 2009; Nordhaus et al., 2010; Madappatt et al., 2011). The maximum AGB stellar radius for a 1.2- $M_{\odot}$ star was calculated to be ∼300 $R_{\odot}$ (De Marco et al. 2011, with the usual adjustment for the orbital widening due to mass loss, see § A.7). Even exaggerating the maximum AGB radius (600 $R_{\odot}$) and the maximum capture radius to 5 stellar radii, we get $\log(P/\mathrm{days}) = 3.9$ and a fraction of 5%. We would therefore predict a similar fraction of post-common envelope central stars, contrary to the observations.

A.7.4 Comparison of the PN binary fraction with the white dwarf binary fraction

We note finally that the PN binary fraction, even before detection biases are accounted for, appears to be higher than the white dwarf binary fraction of 25% (Holberg, 2009, the WD binary fraction should be a few points higher, if we could readily detect white dwarfs around bright main sequence stars - Sirius-like systems). One reason could be that the white dwarfs derive from a population that includes lower mass stars, those that do not develop a PN due to long transition times. Such lower mass population would naturally have a lower binary fraction (Raghavan et al., 2010). Another reason could be that PN form preferentially around binaries, the hypothesis we are trying to test. To discern between the two explanations of the discrepancy between the white dwarf and PN binary fractions we need better constraints on white dwarfs and central stars masses (Liu et al., 1995; Liebert et al., 2005; Gesicki & Zijlstra, 2007).

A.8 Conclusions and discussion

In this work we have started a survey of the 2-kpc, volume limited sample to determine the binary fraction via a technique able to detect I and J band flux excess due to the presence of a cool companion. For this first survey we have selected 30 central stars of PN, of which we later determined three to be PN mimics. Of the remaining 27 central stars we have detected 8 with a possible I-band excesses (of which one was a previously known binary). For 12 of these objects we collected the best J band photometry from the literature and determined that 6 out of 11 bona fide central stars have a flux excess. In total we have detected an excess in 11 of the 27 central stars in either of the two bands.

For the I band survey we calculate a detected fraction of 30%, which when de-biased to account for undetected objects, to result in an unbiased binary fraction of 67-78%. There are three principal de-biasing factors. The first to account for the fact that we do not detect companions fainter than M3-4V. The second, to account for the fact that we do not detect wide binaries by design. The third, to account for the fact that main sequence binaries that go through a common envelope on the RGB do not ascend the AGB and do not become PN. These factors have to be included in order to compare the PN binary fraction with the main sequence one.

From the J band survey we calculate a binary fraction of 54% which, when de-

biased to account for binaries at any period and all companions, becomes 100-107%, clearly showing that the error bar due to the low number statistics is high. The discrepancy between the I and J band fractions is likely an effect of the low number statistics. Since the binary fraction determined using I band photometry relies on more data than using the J band photometry, it is likely that the I band fraction is more accurate (even if the I band is less sensitive). However the J band fraction agrees with the preliminary work of Frew & Parker (2007), who used 34 objects (although their detection limits were poorly quantified).

Thus debiased we can compare these fractions with that of main sequence star binaries of (50±4)% (Raghavan et al., 2010). We preliminarily conclude that there may be an overabundance of central star binaries, compared to the putative parent population.

We have also noticed how, starting from the main sequence binary fraction and period distribution we would expect only a few percent of central stars of PN to be post-common envelope binaries, whereas previous surveys detected 15-20%. This discrepancy can only be reconciled within the *binary hypothesis*.

Here we have demonstrated that the binary fraction is an elusive quantity. Even the best, most accurate observations cannot easily detect faint companions and the only way to reduce the error is by analysing a much larger sample with similarly accurate photometry. Such high accuracy observations are extremely hard to obtain because of the need of photometric weather and the importance to obtain several observations on different nights. In the second instalment of this paper we will use the same technique with an additional dataset and combine the results. Our goal is to analyse with similar accuracy the entire 2.5-kpc volume-limited sample of Frew (2008), comprising approximately 250 central stars.

Finally, we compare the binary fraction determined here with two alternative predictions. The first one was done on the basis of PN morphology alone. De Marco et al. (2011), revising the scheme of Soker (1997), predicted that about 60% of all central stars have interacted with a stellar companion. Here we measured that 48% of central stars have a companion closer than 1300 AU (30% × 1.45-1.69, where we took the middle of the range; § A.7.1). These two numbers are easily the same within the uncertainty, but only if all of the companions we detected (and those we did not detect but accounted for) are closer than ∼100 AU, i.e., have interacted with the central star. The comparison is possibly closer using the J band sample, whereby 67% of all central stars are binaries with any separation to a distance of ∼1000 AU.

Another prediction was that of Moe & De Marco (2011) who used a population synthesis analysis to predict a fraction of 70% of all central star derives from a binary interaction. This fraction is even higher and more discrepant with the fraction detected here for the I band sample but more in line with that derived from the J band sample. All these comparisons will need to be carried out again, once the PN binary fraction is finalised and a period distribution is obtained.

Appendix B

A Well-Posed Kelvin-Helmholtz Instability Test and Comparison

From McNally, C. P., Lyra, W., & Passy, J.-C. 2012, ApJS, 201, 18

B.1 Introduction

Kelvin-Helmholtz instability (KHI) is the name given to the primary instability that occurs when velocity shear is present within a continuous fluid or across fluid boundaries. The shear is converted into vorticity that, subject to secondary instabilities, cascades generating turbulence. The KHI is one of the most important hydrodynamical instabilities and plays a significant role in various parts of astrophysics. It is believed to be responsible for additional mixing in differentially rotating stellar interiors (Brüggen & Hillebrandt, 2000), and to keep a finite-thickness layer of dust around the midplane of protoplanetary disks (Dubrulle et al., 1995; Johansen et al., 2005). It also contributes to convective mixing in any deep stellar interior at the stiff convective boundaries, for instance in asymptotic giant stars (Herwig, 2006) or novae (Casanova et al., 2011). Moreover, KHI can lead to the destruction of cool gravitationally bound objects moving in a hot ambient medium (Murray et al., 1993) such as galaxies in the intracluster medium (Nulsen, 1982; Mori & Burkert, 2000), substellar companions engulfed by a giant star (Chapter 5) and comets entering a planetary atmosphere (Mac Low & Zahnle, 1994). KHI plays a role in the interactions of the magnetopause and solar wind (Miura & Pritchett, 1982) and has been observed in the solar corona (Ofman & Thompson, 2011). In order to understand these phenom-

ena and their implications, it is therefore important to define a well-posed method to quantify how accurately KHI can be modeled by different numerical techniques.

Verifying the correct treatment of KHI has attracted increased interest following the conclusions made by Agertz et al. (2006) including vigorous discussions of KHI in Lagrangian schemes. The main conclusion reached was that Smoothed Particle Hydrodynamics (SPH) fails to resolve KHI due to a surface tension effect between the SPH particles at the shear interface. However, the test was done at a sharp shear and contact discontinuity. Price (2008) attempted to address the problem with KHI growth from a sharp contact discontinuity in Agertz et al. (2006) by adding an artificial thermal conductivity to SPH. Read et al. (2010) pointed out the zeroth-order inconsistency in SPH, and designed a kernel to minimize these effects, achieving better qualitative results on a sharp contact discontinuity KHI test. Zeroth-order inconsistency is the inability of SPH interpolation to reproduce a constant function at any finite resolution (Dilts, 1999; Quinlan et al., 2006). One of the only well posed convergence tests for KHI was done in Robertson et al. (2009), but that was in a study of Galilean invariance restricted to fixed-mesh schemes. The test by Springel (2011b) is a well posed problem influenced by Robertson et al. (2009), but the evaluation of the SPH result was done by comparison to an analytic solution for a sharp transition initial condition and incompressible flow in an infinite domain, not for the problem posed with a softened transition in compressible flow in a finite periodic domain.

We give the problem setup in Section B.2 and list the different codes used in this study in Section B.3. We discuss in Section B.4 which quantity is measured and how to obtain a reference compressible solution. The results and comparison from several codes with different underlying algorithms and discretizations are presented in Section B.5. We discuss the various results and implications in Section B.6. In Section B.7 we discuss secondary instabilities arising from the problem setup in this work, and the difficulty of determining if they are produced in a physically meaningful manner. Our conclusions are summarized in Section B.8.

B.2 Setup

Our motivation in choosing the initial conditions is that they should be smooth, reflect as closely as possible a configuration that can be treated analytically, and be represented easily in a wide variety of codes. In all codes, we will solve the inviscid compressible Euler equations. The setup we use is chosen to be a periodic version

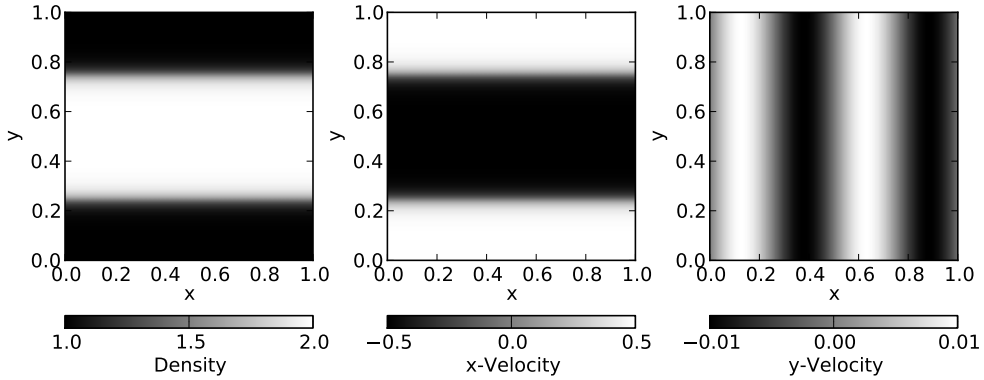

Figure B.1 Density and velocity initial conditions used for the KHI test in this work.

of that used in the analysis of Kelvin-Helmholtz instability in Wang & Ye (2010): the domain is 1 unit by 1 unit in the x and y directions if two-dimensional, and an arbitrary thickness in the z direction if needed for the three dimensional code. Runs with resolutions of 128×128, 256×256, and 512×512 cells, or equivalent were used in the comparison. All boundaries are periodic. The initial condition is smooth and periodic, as illustrated in Figure B.1. The density is given by:

$$\rho = \begin{cases} \rho_1 - \rho_m e^{\frac{y-1/4}{L}} & \text{if } 1/4 > y \geq 0 \\ \rho_2 + \rho_m e^{\frac{-y+1/4}{L}} & \text{if } 1/2 > y \geq 1/4 \\ \rho_2 + \rho_m e^{\frac{-(3/4-y)}{L}} & \text{if } 3/4 > y \geq 1/2 \\ \rho_1 - \rho_m e^{\frac{-(y-3/4)}{L}} & \text{if } 1 > y \geq 3/4 \end{cases} \tag{B.1}$$

where

$$\rho_m = (\rho_1 - \rho_2)/2 \tag{B.2}$$

with $\rho_1 = 1.0$, $\rho_2 = 2.0$, and the smoothing parameter $L = 0.025$. The x-direction velocity is given by:

$$V_x = \begin{cases} U_1 - U_m e^{\frac{y-1/4}{L}} & \text{if } 1/4 > y \geq 0 \\ U_2 + U_m e^{\frac{-y+1/4}{L}} & \text{if } 1/2 > y \geq 1/4 \\ U_2 + U_m e^{\frac{-(3/4-y)}{L}} & \text{if } 3/4 > y \geq 1/2 \\ U_1 - U_m e^{\frac{-(y-3/4)}{L}} & \text{if } 1 > y \geq 3/4 \end{cases} \tag{B.3}$$

where

$$U_m = (U_1 - U_2)/2 \tag{B.4}$$

with $U_1 = 0.5$, $U_2 = -0.5$, and L as in the density so that the smooth transition in density and velocity occurs over the same interval. The background shear is perturbed in order to start the KHI by adding some velocity in the y-direction with the form

$$V_y = 0.01 \sin(4\pi x). \tag{B.5}$$

An ideal gas equation of state with $\gamma = 5/3$ is used. The internal energy is set such that pressure is initially uniform with value 2.5. The problem is run until at least time $t = 1.5$. Analysis is done on snapshots spaced at a minimum of $\Delta t = 0.02$. However, in most cases the snapshots will not be spaced exactly as codes often do output or analysis on an approximate interval, e.g. at the first time step after the specified snapshot or analysis time. The test can be run in two dimensions in a structured grid code, but for unstructured meshes or mesh free methods two dimensional and three dimensional simulations may yield slightly different results depending on how the resolution elements are arranged in the initial condition. For unstructured mesh methods and meshless methods the results will differ for a disordered node distribution and a regularly gridded one.

B.3 Codes

In this paper, we compare the results from six codes to the reference solution, which itself is produced with the Pencil code.

The Pencil code[1] is a fixed Eulerian mesh, non-conservative, finite-difference, MHD code that uses sixth order centered spatial derivatives and a third order Runge-Kutta time-stepping scheme, being primarily designed for weakly compressible turbulent hydromagnetic flows.

The other codes, Enzo, Athena, NDSPMHD and Phurbas are introduced below.

Enzo is a three-dimensional, Eulerian adaptive mesh refinement hybrid (hydrodynamics + N-body) grid-based code (Bryan et al., 1995; O'Shea et al., 2004)[2]. For this problem the Euler equations are solved using a third-order piecewise parabolic method (PPM) with the two-shock approximate Riemann solver. Time-stepping is

[1] See `http://www.nordita.org/software/pencil-code`

[2] `http://enzo-project.org/`

constrained by a Courant condition for the gas with a Courant factor C=0.4. The run-time PPM diffusion, flattening, and steepening parameters were set to zero. Enzo version 1.5 was used.

Athena is a three dimensional Eulerian grid code that (among other algorithms) implements a higher order Godunov method for hydrodynamics (Stone et al., 2008). Specifically, we have used the third-order cell reconstructions with the HLLC approximate Riemann solver and the unsplit corner-transport-upwind (CTU) second order time integration algorithm. Otherwise the options used were as specified in the two-dimensional test problem supplied with the code, with a Courant number $C = 0.8$. We used Athena version 4.1 obtained from the project website[3].

NDSPMHD is a one, two, and three dimensional reference implementation of SPH and a platform for experimentation (Price, 2012). We obtained NDSPMHD version 1.0.1 from the author's website[4]. NDSPMHD was run on this problem in two dimensions, using both the cubic and quintic kernel options. The cubic kernel is the conventional choice for SPH, whereas the quintic kernel delivers higher accuracy at the cost of computational expense. Price (2012) describes the NDSPMHD implementation of SPH as converging as higher order kernels are used. That is, the result on the test problem shown here should converge with the combination of using more particles and using a higher order kernel. NDSPMHD also supports the artificial thermal conductivity described in Price (2008). The results of SPH simulations may depend strongly on the initial particle distribution used, which is described in McNally et al. (2012a). The number of particles used at each resolution matched the number of cells or points used for the grid code (128^2, 256^2, 512^2). Otherwise, the code was run with the default parameters used in Test 6 of the NDSPMHD examples package.

Phurbas is a meshless, adaptive, Lagrangian code for magnetohydrodynamics (Maron et al., 2012; McNally et al., 2012b). Phurbas uses third order least square fits to derive spatial derivatives, and a second order scheme for time integration. Stabilization is achieved through an artificial bulk viscosity. It is run here in three dimensions, using volumes with height 1/64, 1/128, and 1/256 in thickness in the z-direction. Phurbas does not use a grid, so instead we use spatially constant resolution and set the resolution parameter λ to the cell size used in the grid codes. The generation of initial conditions is described in McNally et al. (2012a).

[3] `https://trac.princeton.edu/Athena/`

[4] `http://users.monash.edu.au/~dprice/ndspmhd/index.html`

Table B.1. Simulation Prefixes and Codes

Prefix	Code	Variation
Pe	Pencil	6th order space, 3rd order time accuracy, 6th-order hyperviscosity
Ep	Enzo	3rd order reconstruction, directionally split, two-shock Riemann solver
At	Athena	3rd order reconstruction, unsplit integrator, HLLC Riemann solver
Ne	NDSPMHD	2D cubic kernel
Nc	NDSPMHD	2D cubic kernel, no artificial conductivity
No	NDSPMHD	2D quintic kernel
Ph	Phurbas	3D, λ = cell length in 2D codes

B.4 Analysis

To quantitatively describe the growth of the Kelvin-Helmholtz instability, one of the measurements used is the maximum y-direction kinetic energy density. This quantity is useful as it is very sensitive to noise in the computed velocity field. It is simply the maximum value of $1/2\rho V_y^2$ computed for all resolution elements (cells, points, or particles) in the computation volume at each time. In the non-periodic, incompressible limit, the growth of this quantity should be $\propto \exp(2 \times 4.384 \times t)$ (Wang & Ye, 2010, Equation 18). In practice, the growth will start from a finite perturbation, will reflect erroneous velocities occurring both at the interface due to unbalanced pressures at the cell scale, and any velocity and density noise in the bulk flow. It is also important that the test posed here, and those commonly used in other works, are actually posed in a periodic domain with a compressible flow. To obtain a basis for comparison we use a numerical reference solution to the problem as posed and establish the uncertainty on this reference solution in a rigorous manner, as described below.

To produce a solution to the full nonlinear, periodic, compressible case as run in this work, we performed an extensive convergence study with the Pencil Code. This convergence study allows us to establish not only a very high quality reference solution, but also a notion of the uncertainty in this reference solution. The importance of the unusual step of establishing the uncertainty of the reference result is that we can then assert with confidence that the differences seen between other lower quality results and this reference result are overwhelmingly due to errors in the lower quality solutions. In the results in Section B.5 the Pencil Code is shown to be well suited to the smooth, subsonic problem posed here. We use grids of 128×128, 256×256, 512×512, 1024×1024, 2048×2048, and 4096×4096 points, specified so that every

second grid coordinate overlaps on successive refinements, and with the time stepping scheme in the Pencil Code modified to provide outputs at exact $\Delta t = 0.02$ time unit intervals. This set of outputs enables a resolution study at each output time for the convergence of the mode amplitude, a smooth and global quantity described in McNally et al. (2012a). Establishing the empirical rate of convergence of the mode amplitude allows a Richardson extrapolation based estimate of the uncertainty in the most resolved measurement. Hence, we are able to make comparisons of the results from other codes to the highest resolution Pencil Code result while knowing in a rigorous manner that the errors in this reference result are negligible. A more detailed description of the convergence study can be found in McNally et al. (2012a).

To demonstrate more explicitly the convergence behavior, and the magnitude of the changes between successive resolutions we have plotted the differences in the y-velocity values between successive resolutions in one quadrant of the domain in Figure B.2. The greatest changes between successive resolutions are localized to the density change interface, and show not suggestion of the presence of secondary instabilities.

B.5 Results

The simulations are identified by a two letter prefix as outlined in Table B.1 and the resolution (128^2, 256^2, 512^2).

Maximum y-direction specific kinetic energy histories are shown for all simulations in Figure B.3. Here the velocity noise in SPH resulting from pressure force errors can be seen clearly in the overview figure, while all other codes behave in a roughly similar manner. The convergence study does not establish an uncertainty on the maximum y-direction kinetic energy, but the highest resolution Pencil Code result plotted as the reference curve can be taken as a useful indicator of the correct nonlinear solution.

In Pencil, Enzo, Athena, and Phurbas, at late times at low resolution the maximum y-direction kinetic energy is low. This is the opposite of the situation found in NDSPMHD, where at late times at low resolution the maximum y-direction kinetic energy is too high.

At lower resolutions in Phurbas the influence of velocity noise at the interface can be clearly seen. At early times the maximum y-direction kinetic energy is too high. Pencil does not suffer from this to the same extent. Enzo and Athena have the best initial behavior at the interface as they are finite-volume schemes and hence the initial

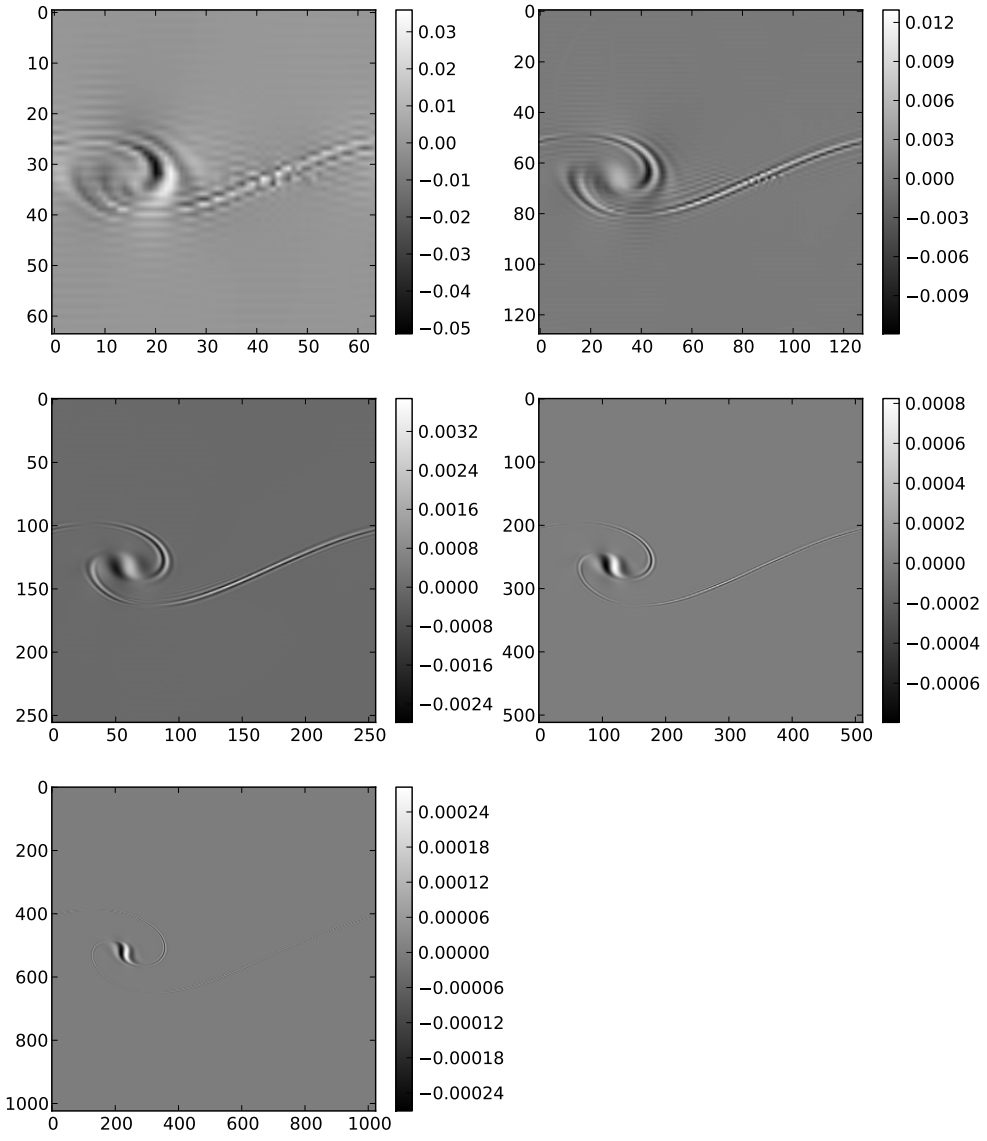

Figure B.2 Differences in y-velocity between successively finer resolutions in one quadrant of the convergence study performed with the Pencil Code at time $t = 1.5$. Color bars show range of y-velocity differences, and axes are in units of grid points in the lower resolution for each plot. Differences shown are: *Upper Row:* 128^2-256^2 and 256^2-512^2 *Middle Row:* 512^2-1024^2 and 1024^2-2048^2 *Lower Row:* 2048^2-4096^2

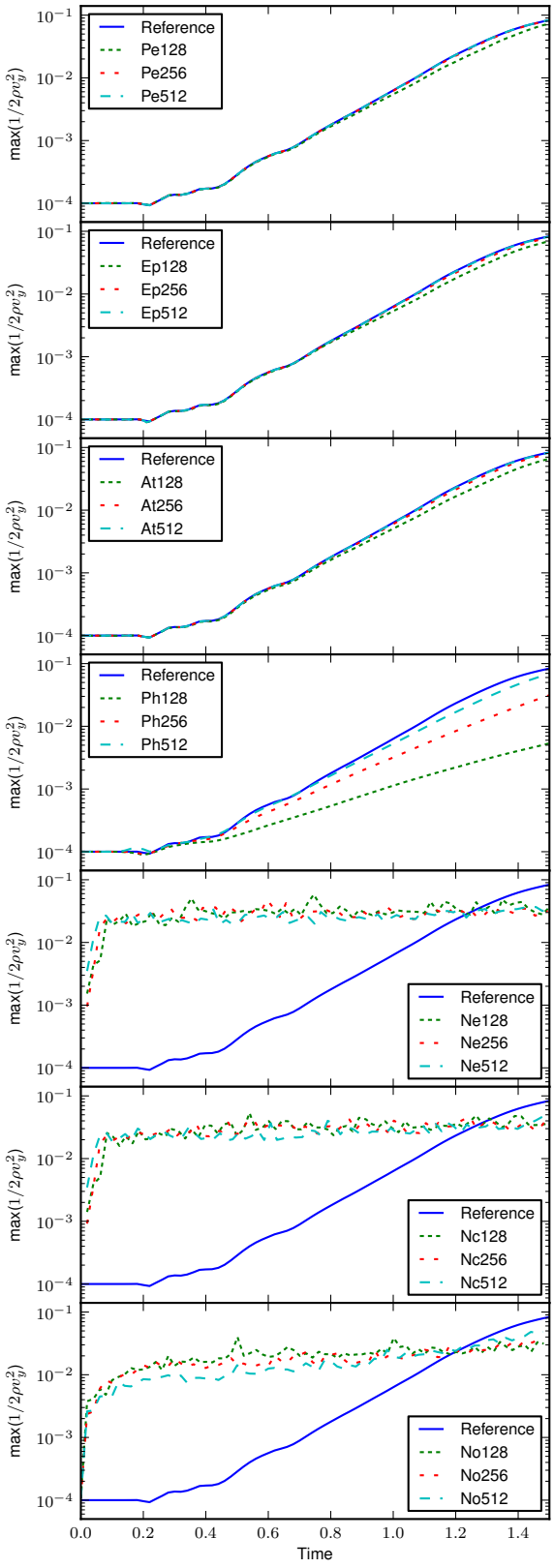

Figure B.3 Maximum y-direction kinetic energy in all codes.

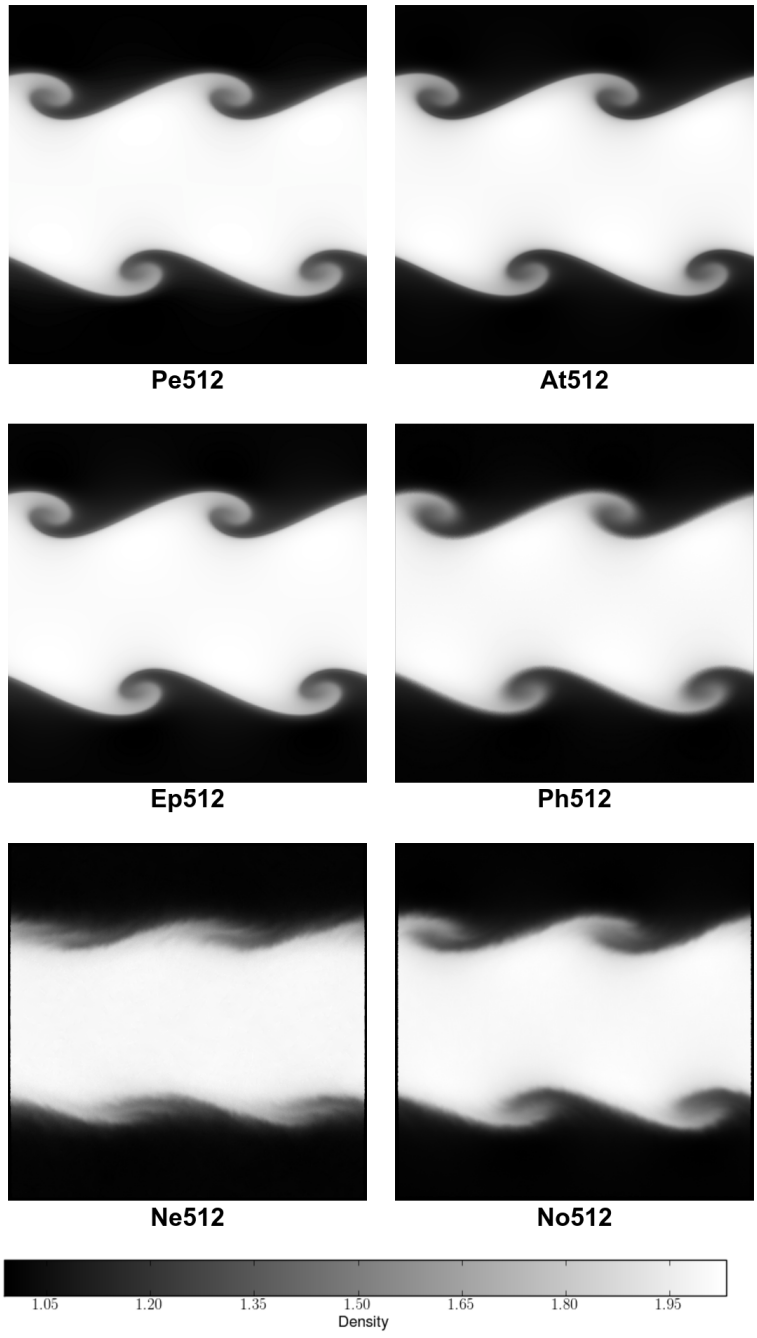

Figure B.4 Density at resolution 512^2 and time $t = 1.5$. *Upper Row:* Pencil, Athena *Middle Row:* Enzo, Phurbas *Lower Row:* NDSPMHD cubic kernel, NDSPMHD quintic kernel

pressure equilibrium is well represented across the interface. The initial maximum kinetic energy and the initial mode amplitude are both to low at low resolution in these codes.

The resolution dependence of the velocity noise is illustrated for the cubic-kernel SPH with artificial conductivity (Ne). Neglecting the artificial conductivity yields virtually the same result as shown in Figure B.3 (simulation Nc). Quintic kernel SPH, with smaller zeroth-order inconsistency errors than cubic-kernel SPH, does show smaller velocity noise, but it is still very large (simulation No).

We show gray scale slices of the density field at $t = 1.5$ in Figure B.4. All the images have the same limits on the grey scale between density of 0.9883 and 2.0320, the density extremes in the highest resolution result in the Pencil Code convergence study. The results for Pencil, Enzo, and Athena are largely similar, as at high resolution these codes agree well with each other and with the reference result. Though the result with Phurbas strongly resembles the reference result although it clearly shows more diffusion. The SPH results from NDSPMHD (only Ne and No shown) reflect the slow growth of the unstable y-velocity mode already discussed. The simulation No result using quintic-kernel SPH shows less diffusion than simulation Ne using cubic-kernel SPH. Especially in simulation Ne, secondary features of a filamentary appearance can be seen along the interface, and these are less apparent in the simulation No result. The quintic kernel result (No) overall shows better agreement with the reference than the cubic kernel result (Ne).

B.6 Discussion

Overall, the grid based codes Pencil Code, Athena, and Enzo had very similar performance. For these codes, the test problem in this work (run to $t = 1.5$) confirms their correctness. This shows that the test as outlined here can be used to discriminate among numerical schemes. In this test, we demonstrated that Phurbas and NDSPMHD, while both using meshless Lagrangian schemes, give significantly different convergence behaviors. Though Phurbas was run in three dimensions, and NDSPMHD in two, the strikingly different qualitative behavior bears some explanation. A primary observation is that Phurbas differs from NDSPMHD in that Phurbas uses a third order accurate and consistent spatial discretization, while NDSPMHD uses an SPH discretization which has zeroth-order inconsistency. We also note that no code developed obvious signs of secondary instabilities in the solution

by time $t = 1.5$, in agreement with the findings of the convergence study performed on the reference result. How, and when, secondary instabilities may arise in a KHI test such as this is discussed in Section B.7.

B.7 Secondary Instabilities

We have shown that given a convergence test stated in a well posed manner, all the methods tested appear to converge towards the correct result for the growth of the primary instability. Recent discussion of Kelvin-Helmholtz tests has broadened to include secondary instabilities. Springel (2011a) shows secondary instabilities developing from a similar initial condition. The reference solution we compute shows no indication of these structures. Springel (2011a) suggested that their moving-mesh code is able to resolve secondary KHI billows which cannot be resolved in their fixed-mesh code because it was too diffusive. Though the solution in a fixed mesh and moving mesh code should not be expected to by equivalent at any finite resolution, that a given code does not develop secondary Kelvin-Helmholtz instabilities is not simply a function of the diffusivity of the code, it is also a dependent on the seeding of such instabilities.

For our problem, we can show that the secondary instabilities that do develop are of a purely numerical origin. To demonstrate this we have performed a test with Athena. We ran the KHI test at resolutions of 1024^2, 2048^2 and 4096^2 until $t = 4$. In Figure B.5 the density in a region centered on a single primary KHI billow is shown at time $t = 3$. Secondary KHI billows can be seen growing in the 1024^2 case, and this pattern is successively suppressed at the higher resolutions, suggesting it is an artifact of the finite resolution and is converging away. However, in the 2048^2 resolution, a different set of secondary instabilities can be seen growing at much shorter wavelengths in the central winding of the primary billow. As the resolution is increased, the numerical seeding of the secondary instabilities changes, and the secondary modes which are excited change. Figure B.6 shows the same region at time $t = 3.2$. By this point, the secondary instabilities in the 4096^2 resolution simulation have become apparent. Surprisingly, a new set of secondary billows has appeared on the outer winding of the primary billow. We cannot reach well justified conclusions about a particular mode of the secondary instability from this study as we cannot reproduce the same instability at two different resolutions.

Though the growth of secondary instabilities is likely a physical reality at the

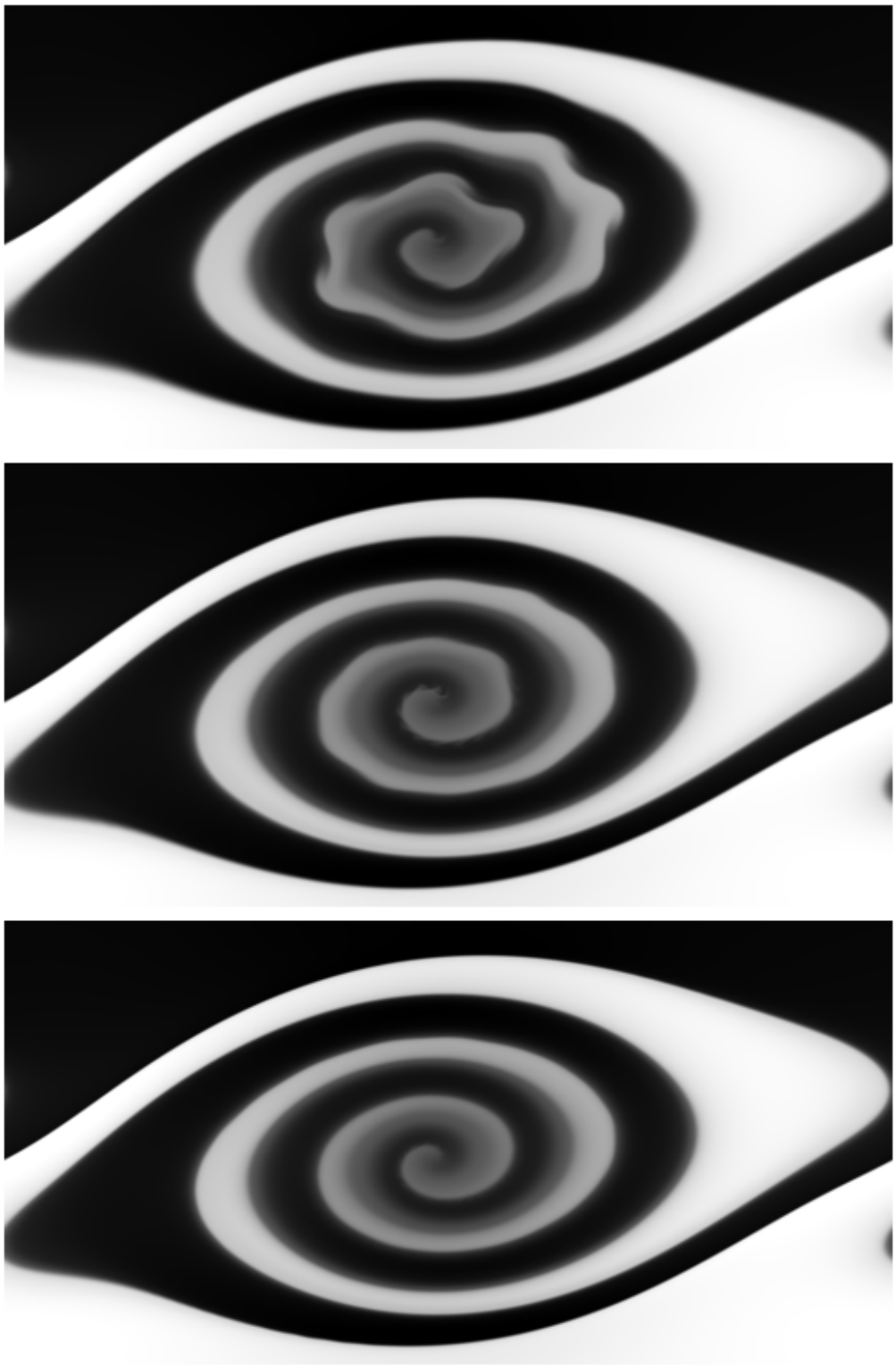

Figure B.5 Density in Athena at time $t = 3.0$ at three resolutions, zoom-in on one primary KHI billow. Greyscale same as Figure B.4. *Top:* 1024^2 *Middle:* 2048^2 *Bottom:* 4096^2

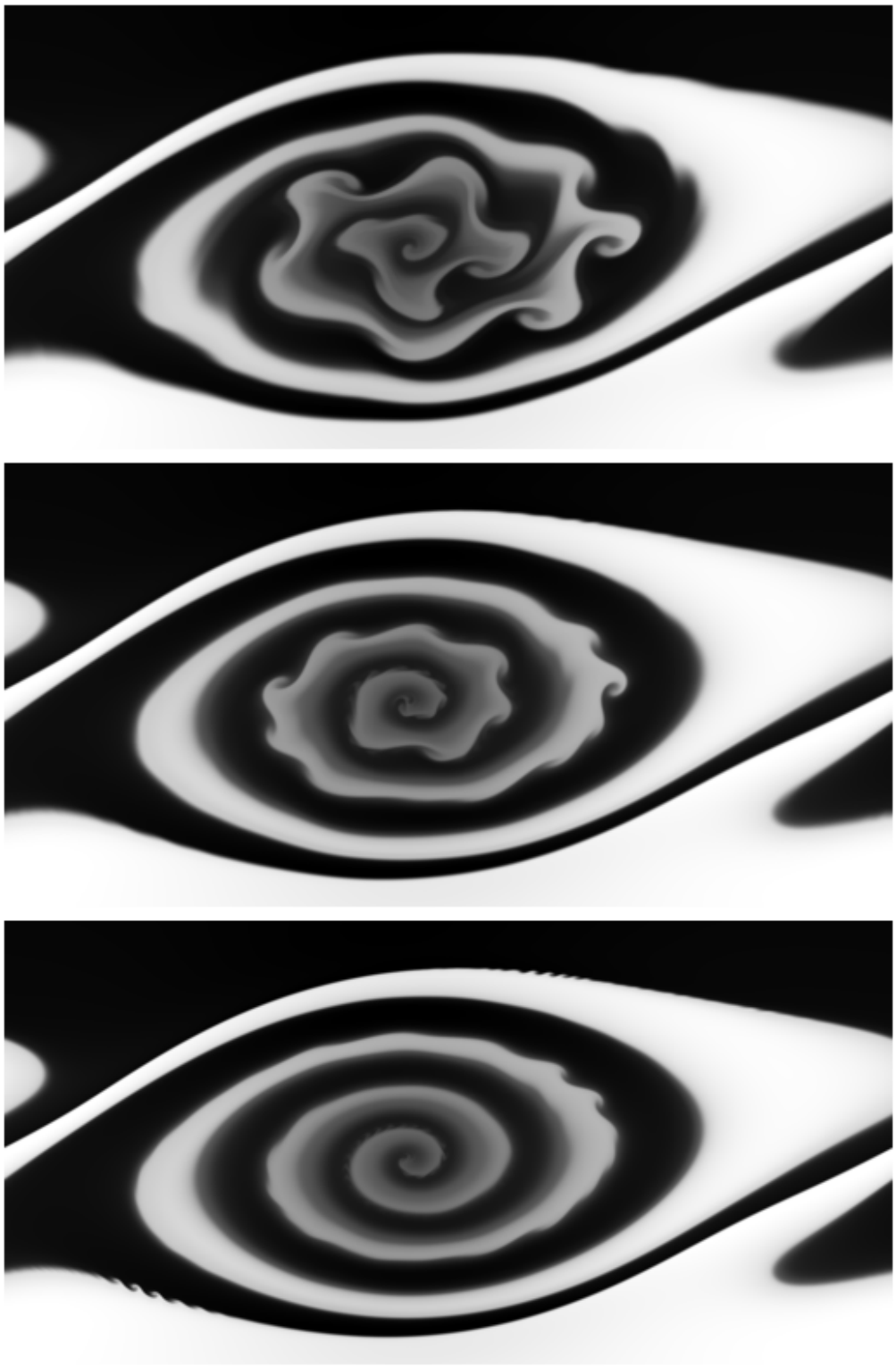

Figure B.6 Density in Athena at time $t = 3.2$ at three resolutions, zoom-in on one primary KHI billow. Greyscale same as Figure B.4. *Top:* 1024^2 *Middle:* 2048^2 *Bottom:* 4096^2

Reynolds numbers involved in astrophysical problems, relying on numerical effects to seed them will not result in a true physical model of the phenomena as the seeding, and hence growth of these instabilities, will be inherently dependent on parameters such as resolution. From the results of the convergence study in Section B.4 we propose that if a code develops secondary Kelvin-Helmholtz billows in this test by $t = 1.5$, it is due to the growth of numerical perturbations.

The less rigorous study performed with Athena suggests that development of secondary Kelvin-Helmholtz instability after $t = 1.5$ is likely due to the presence of spurious noise in the solution, and that this conclusion should hold to at least $t = 2.5$. For example, in the preparation of this work, we discovered that the evolution of the test problem here differed greatly at high resolution (4096^2) between Enzo versions 1.5 and 2.0. In Enzo 2.0, a bug existed that caused slightly incorrect pressure reconstructions. This caused small sound waves to launch from the interface, and propagate though the periodic domain interacting with themselves and forming small short-wavelength perturbations. The discovery of this bug was fortuitous however, because it demonstrates again how artificial, numerical perturbations can give rise to secondary Kelvin-Helmholtz in this test problem if they are able to overwhelm the dissipation of the scheme. In the limit of infinite resolution, any convergent code should reproduce the correct result. However, if at finite resolution a code shows a tendency to produce secondary instabilities, then the scheme can be improved by adding a diffusive operator to damp the noise leading to the the instability.

The underlying cause of the tendency of many schemes to develop secondary KHI in this test problem is that the shear interface becomes increasingly steep as it stretches in the primary KHI billow. Eventually, the width of the interface approaches the grid scale and it become susceptible to numerically seeded secondary instabilities. This behavior is also commonly seen in the initial evolution of grid-aligned sharp transition versions of the KHI test. Two examples are Junk et al. (2010, Figure 13) and Springel (2011a, Figure 8, upper right panel). We suggest then that even fixed-grid finite volume Godunov schemes may be improved in pathological cases of unresolved shear interfaces by the addition of a diffusive flux. This flux should be chosen to spread the interface over enough grid cells to suppress the numerically seeded instabilities.

Another lesson to be derived here is a cautionary one. Not all new instabilities seen as resolution is increased when solving the discretized Euler equations are physically real. New numerical instabilities can reveal themselves as resolution is increased,

as the flow can enter into new regimes where it is more sensitive to the inevitable numerical noise in a method. One route around this difficulty can be to solve the Navier-Stokes equations instead with a fixed viscosity. Since these equations have a physical scale where diffusion dominates dynamics, the reliable elimination of numerically generated instabilities for arbitrarily long run times can be obtained by fixing the physical diffusive scale and reducing the grid scale far below the diffusive scale.

Finally, we suggest that it is possible to produce a controlled test of the growth of secondary billows from definite perturbations, similar to the study performed by Fontane & Joly (2008) in an incompressible flow. Such a setup could be useful in determining the appropriate and minimal diffusion to add to a scheme to suppress the numerical seeding of secondary instabilities in given conditions.

B.8 Conclusions

We have constructed a reference solution with a well characterized uncertainty, along with defining a general manner in that the test can be analyzed. This methodology was applied to example codes from the major families of numerical techniques used in astrophysics. All codes tested showed convergence towards the reference result when the resolution was increased in the appropriate manner. For SPH, the use of an artificial thermal conductivity does not significantly effect the results, but using a higher-order kernel (and hence a larger number of neighbors) does improve the results. We conclude then that the fundamental reason for poor performance of SPH in KHI is the zeroth-order inconsistency of SPH interpolation. Visually, to time $t = 1.5$ in the test problem there are no secondary instabilities that arise in the reference solution. By examining the relative behavior of different types of code, we argue that the presence of secondary instability on this test is caused by having a numerical diffusion that is very low compared to the grid noise in the method. Hence, we propose that it is advantageous in some methods, particularly moving-mesh tessellation methods, but also in fixed-grid Godunov schemes, to include an extra diffusion operator to smooth the solution such that grid noise does not drive small scale instabilities.